8-1-2016

Seismic Response of an Older Bridge in Nevada under Maximum Considered Earthquake

Ryan Thomas Isaac
University of Nevada, Las Vegas, isaacrt915@gmail.com

SEISMIC RESPONSE OF AN OLDER BRIDGE IN NEVADA UNDER MAXIMUM CONSIDERED EARTHQUAKE

By

Ryan T. Isaac

Bachelor of Science – Civil Engineering
University of Nevada, Reno
2009

A thesis submitted in partial fulfillment
of the requirements for the

Master of Science in Engineering – Civil and Environmental Engineering

Department of Civil and Environmental Engineering and Construction
Howard R. Hughes College of Engineering
The Graduate College

University of Nevada, Las Vegas
August 2016

UNLV | GRADUATE COLLEGE

Thesis Approval

The Graduate College
The University of Nevada, Las Vegas

July 14, 2016

This thesis prepared by

Ryan Isaac

entitled

Seismic Response of an Older Bridge in Nevada under Maximum Considered Earthquake

is approved in partial fulfillment of the requirements for the degree of

Master of Science in Engineering – Civil and Environmental Engineering
Department of Civil and Environmental Engineering and Construction

Ying Tian Ph.D.
Examination Committee Chair

Kathryn Hausbeck Korgan, Ph.D.
Graduate College Interim Dean

Samaan G. Ladkany, Ph.D.
Examination Committee Member

Aly Said, Ph.D.
Examination Committee Member

Zhiyong Wang, Ph.D.
Graduate College Faculty Representative

ABSTRACT

Given the aging infrastructure in the United States, a study was conducted on an older bridge in Nevada to determine its performance under the maximum considered earthquake. A suite of eight synthetic site-specific ground motions, including a spectrum-matched "RSP" record, were applied along both the longitudinal and transverse axes of Bridge G-953 in Las Vegas, Nevada. A detailed model, including the effects of column nonlinearity, material degradation such as shear keys, abutment soil stiffness, and restrainers at the in-span hinges of the superstructure (which were not part of the original design), was developed to capture both local demands and the global response of the structure. Comparison of the average demand of the seven regular ground motions ("Avg 1-7") with "RSP" was made to determine if the "RSP" record can be a computationally efficient estimation of seismic demand to a structure. Analysis results indicate that while the "RSP" record adequately predicted some force demands, it failed to capture extensive nonlinear deformation such as plastic hinge rotation demand. Displacement-controlled shear failure caused by excessive plastic hinge rotations and flexural distress in the concrete and longitudinal steel were found to be the governing limit states for the average response, creating a possibility of collapse. Localized failures, including rupture of the restrainers, cracking of the shear keys, and large permanent abutment displacements, are also possible. The primary vulnerability of the bridge is in the substructure, where the spacing of transverse reinforcement is too large and the pinned bases of some piers allow large lateral drifts.

ACKNOWLEDGEMENTS

This research would not be possible without the contributions of numerous individuals. Many thanks are due to my committee chair, Dr. Ying Tian, for inspiring this work and providing his guidance, mentorship, and editing services. Additionally, the assistance and commentary from my other committee members, Dr. Aly Said, Dr. Samaan Ladkany, and Dr. Zhiyong Wang helped to substantially increase the quality of this work. Site-specific ground motions were developed for Bridge G-953 by Dr. Barbara Luke and Dr. Suchan Lamichhane; their help in increasing the accuracy of this research is greatly appreciated. NDOT is acknowledged for providing the Original Drawings as well as some original construction material specifications. The facilities and financial aid from the University of Nevada, Las Vegas (UNLV) was of great assistance in making this research possible. Also, the guidance of the academic and administrative faculty at UNLV was crucial to moving this research through to completion. Appreciation is also given to the University of Nevada, Reno, the place of my undergraduate studies, for challenging me to push my limits and learn my discipline. My professional experience in the structural engineering field, attained first from Atkins Global under Jaime Chang and now Kordt Engineering Group with Stephan Kordt, has helped me bridge the divide between theory and practice to gain a more complete understanding of the field of civil engineering. Finally, the support, guidance, and patience of my family and friends, especially my parents, is forever remembered. This has been my greatest academic achievement so far, and none of it would be possible without the above mentioned persons and any other not mentioned here.

DEDICATION

This research was completed to address the serious consequences of seismicity on structural systems, mainly older bridges. Healthy infrastructure is critical in providing a stable, thriving economy and ensuring the safety of the citizenry. With funds for retrofitting and rehabilitation limited, it is important to understand where these limited resources are best spent. A greater understanding of the structural performance of older systems can help grow the database of seismic research and continue to advance the ever-important field of earthquake engineering. This work is dedicated to the many lives lost in earthquakes, in that their loss will continue to inspire research in this field which can help to continue to reduce the casualties that result from these disasters. Finally, this work is motivated by my Creator, that through this work and continued research, I may find purpose and strive to gain a deeper understanding of His magnificent creation and help make the world a better and safer place.

TABLE OF CONTENTS

LIST OF TABLES

LIST OF FIGURES

CHAPTER 1

INTRODUCTION

1.1 BACKGROUND

A reinforced concrete highway bridge with short-to-medium spans can be classified as a precast girder bridge (Figure 1-1a) or monolithically constructed, cast-in-place girder bridge (Figure 1-1b). Precast girder bridges are widely used in non-seismic regions. The superstructure of this type of bridge contains concrete decks on girders that are simply supported by piers or abutment seats, preventing superstructure-substructure bending moment transfer.

(a) (b)

Figure 1-1 Two types of concrete highway bridge: (a) precast girder bridge (www.fhwa.dot.gov), and (b) cast-in-place girder bridge (www.derrpainting.com)

Cast-in-place girder bridges have continuous decks capable of spanning two or more supports and are constructed monolithically with the piers. Because the girders and the columns are rigidly framed to transfer bending moment between each other, this type of bridge is stiffer and thus predominantly used for new bridges in high-seismic regions in the U.S., especially in California. As stated by Nielson and DesRoches (2007), ground motion excitations applied on a cast-in-place girder bridge not only cause higher force demand compared to precast bridges but

also require higher ductility capacity in the columns. Additionally, the continuous nature produces larger pounding forces due to the higher masses of interconnected frame systems. These tradeoffs are worthwhile to produce a bridge structure that is more stable and resistant to earthquake loadings, especially unseating risks. Severe earthquakes are a serious threat to structures in general and have been responsible for the collapse of many bridges during past earthquakes such as the 1964 Alaska, 1989 Loma Prieta, and 1995 Kobe earthquakes. Before the 1970s, earthquake design adopted a simple static procedure that utilized a severely-underestimated 6% of the gravity load as the design lateral force (Seible and Priestley 1999). Following the 1971 San Fernando Earthquake, considerable efforts were undertaken to improve the seismic design of structures. As a result, earthquake loads were greatly increased and detailing requirements became much more stringent. Despite the advances made in the seismic design for new bridges, there is a large inventory of existing bridges designed and built in accordance with the older design codes. The seismic performance of these bridges is of particular concern.

Some of Nevada's older bridges have been classified as "structurally deficient" or "functionally obsolete" (Nevada Department of Transportation [NDOT] 2015 State Highway Preservation Report). Bridge G-953 (Figure 1-2), as designated by NDOT, is the Carey Avenue overpass crossing the I-15 freeway in North Las Vegas, Nevada (Figure 1-3), which is located at approximately 36°12'12" latitude and -115°8'4" longitude. This bridge is a reinforced concrete, cast-in-place girder bridge designed following the 1969 specifications developed by the American Association of State and Highway Transportation Officials (AASHTO) and constructed in 1971. The superstructure of this bridge contains multicell box girders, offering a higher strength-to-weight ratio and thus significantly reduced seismic weight and inertial forces. Even though most box girder bridges are now prestressed or post-tensioned, this is not the case for Bridge G-953.

Saad (2009) conducted an extensive seismic evaluation of five older bridges in the greater Las Vegas area, including G-953. A simplified model was used to conduct nonlinear static (i.e. pushover) analyses. It was found that G-953 likely has unacceptable plastic hinge rotation capacity.

Figure 1-2 Bridge G-953.

Figure 1-3 Geographical location of Bridge G-953 in the U.S. (photo courtesy of Google Maps).

1.2 OBJECTIVE

The overall goal of this research is to further study the seismic performance of Bridge G-953. The Federal Highway Administration (FHA) *Seismic Retrofitting Manual for Highway Structures: Part I – Bridges* by Buckle et al. (2006) can be consulted for guidance on this topic. Specific objectives include:

- Identify the shear and flexural failure potential of the piers;
- Identify the likelihood of superstructure damage caused by pounding;
- Understand the effects of bi-directional ground motion; and
- Understand the effects of abutments on the overall seismic performance of this bridge.

1.3 RESEARCH METHOD

To achieve the aforementioned goal and objectives, the following research components are implemented:

- A literature review is conducted to summarize the seismic response of various bridge components (Chapter 2);
- Incorporating recent research outcomes, a detailed finite element model for Bridge G-953 is developed to effectively capture the seismic response of critical components, including the deck, expansion joints at abutments and in-span-hinges, pounding, piers, restrainers, and abutments (Chapter 3); and
- Time-history analyses are conducted using site-specific ground motions (Chapter 4).

Finally, the findings obtained from this study and suggestions for future research are summarized in Chapter 5.

CHAPTER 2

LITERATURE REVIEW

2.1 SEISMIC RESPONSE OF SUPERSTRUCTURE

2.1.1 General Behavior of Superstructure

A bridge's superstructure, its main travel surface, transmits gravity and seismic loads to the substructure. The massive deck is expected to behave elastically and is generally designed with high stiffness and strength. However, the deck can experience pounding, unseating, shear key damage, and restrainer failure, which will be described later in Sections 2.1.2 to 2.1.5.

The deck of a bridge is prevailingly assumed as linear elastic under seismic lateral loading and often modeled as a rigid single line element spanning the bents. However, according to Yi Meng and Lui (2000), neglecting deck flexibility can underestimate column forces and displacements (especially axial) as well as the bridge's natural period (as much as 21% in the second vibration mode). McCallen and Romstad (1994) compared simplified "stick" and full deck models (Figure 2-1), finding a maximum 12% difference in frequencies for the transverse vibration mode that could significantly affect the pier-abutment force distributions. Additionally, a single line element with a single lumped mass for each deck segment cannot accurately represent the rigidity and inertial forces of the deck in the vertical direction. Thus, if one wishes to model the effects of a vertical ground motion, the full width of the deck with distributed masses needs to be modeled. This was verified by Wakefield et al. (1991) who compared the simple line element with a built-up plate model.

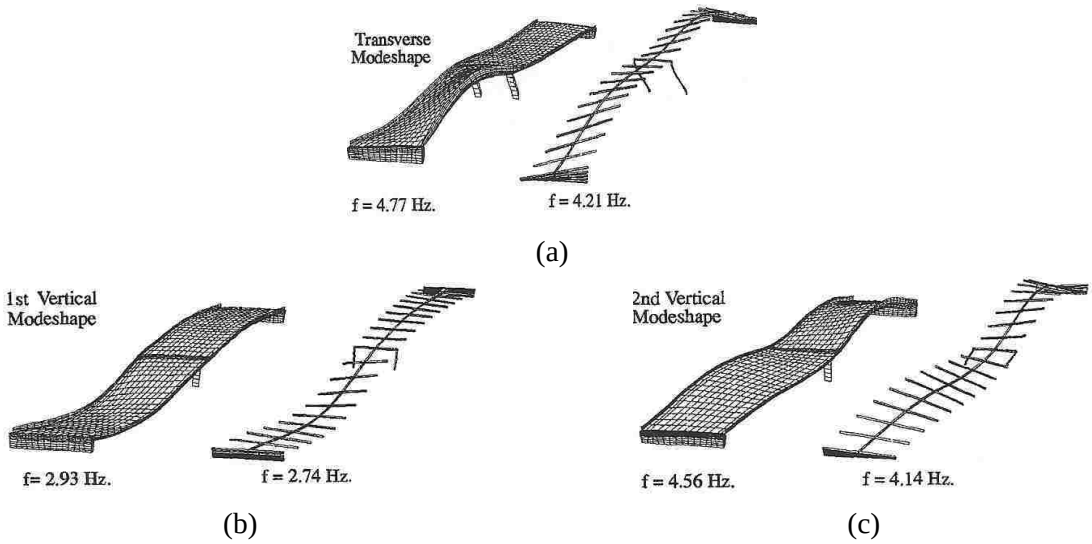

Figure 2-1 Calculated frequencies based on full deck and stick models (McCallen and Romstad 1994).

2.1.2 Seismic Damage Due to Pounding and Unseating

Expansion joints (Figure 2-2) with gaps, often referred to as in-span hinges in bridges, are used to accommodate thermal expansion of the superstructure of a bridge. Factors such as the ratio of natural periods of the adjacent frames determine their interactions at the joints. Seismic pounding between adjacent decks occurs when the gap is closed, which is highly-probable for out-of-phase frames. The deck can be damaged by pounding at expansion joints when the bearing strength is exceeded and the contacted concrete spalls.

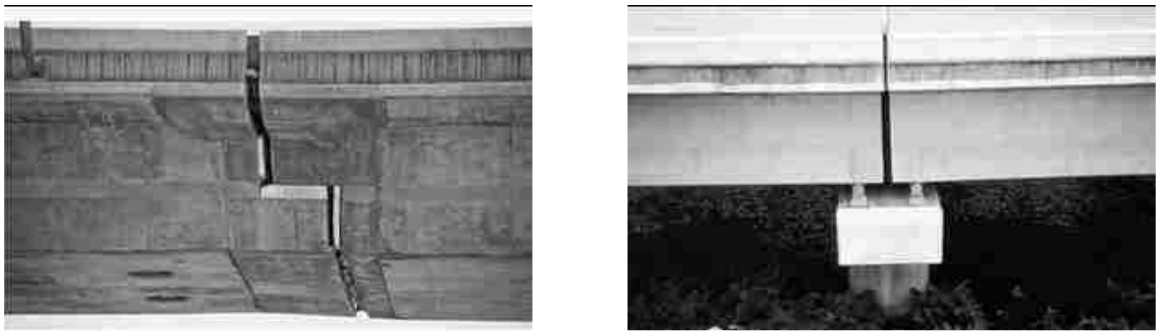

(a) (b)

Figure 2-2 Expansion joint types: (a) between supports (in-span-hinge) (www.worldofstock.com), and (b) at support (www.transportation.njit.edu).

Even though pounding can prevent the buildup of resonance in the structure (Muthukumar 2003), the sudden impulse can cause severe complications. Pounding creates sudden force and acceleration spikes that can amplify drifts or overload structural members. Consequently, pounding can fail girder ends, dislocate the superstructure, damage bearings, and cause spalling (Muthukumar and DesRoches 2006). In an extreme case, it can fail expansion joints and lead to catastrophic unseating. Force spikes and the extra ductility demand (Vlassis et al. 2004) could lead to other failure modes such as shear in the substructure. Figure 2-3 shows the severe damages of bridge superstructures caused by pounding.

(a) (b)

Figure 2-3 Damage due to seismic pounding: (a) In-span hinge seat failure causing unseating (Muthukumar 2003), and (b) near-collapse of Copper River railroad bridge in 1964 Alaskan Earthquake (United States Geological Survey [USGS]).

The worst case scenario is unseating-induced bridge collapse (Figure 2-4) when the relative displacement between adjacent deck segments cannot be accommodated by the available seat width at abutment expansion joints or in-span hinges. Unseating was a relatively-common failure mode before the 1971 San Fernando earthquake (Vlassis et al 2004). As a result, Caltrans has tried to reduce or eliminate the use of in-span Hinges after the 1994 Northridge earthquake to mitigate the risk of unseating (Seible and Priestley 1999).

Figure 2-4 Superstructure failure due to unseating (Andrawes and DesRoche 2005).

2.1.3 Seismic Behavior of Bearing Pads

Bearing pads transferring vertical bearing stresses are installed between adjacent deck segments or between deck end diaphragms and an abutment seat. The most common type of bearing pad uses elastomeric rubber material reinforced with steel plate layers. Bearing pads are fairly soft in the lateral directions, having little effect on the global bridge response under seismic loading.

Elastomeric bearing pads rely on static friction to remain in place and are not anchored directly into the deck. Sliding failures (Figure 2-5) have been investigated by McDonald et al. (2000). Wax coating from the manufacturing process was found to be responsible for the failure. Crushing and delamination are other noted failure types.

Figure 2-5 Sliding failure of bearing pads (Pamuk et al. 2005).

2.1.4 Seismic Response of Shear Keys

Shear keys in a bridge are used to prevent excessive transverse displacement of its superstructure relative to that of the substructure or abutment. The interior type of shear key (Figure 2-6a) consists of a small block of concrete that extends from the expansion joint/in-span hinge, while the exterior types are larger and rest on the outside edges of the seat. Shear keys normally have a small gap (surrounded by elastomeric material for in-span hinges) to prevent activation under small displacements. Exterior shear keys (Figure 2-6b) are much more common for modern bridges because they are easy to design and replace.

(a) (b)

Figure 2-6 Shear key types: (a) interior (www.bridgeofweek.com), and (b) exterior (www.tensar.co.uk).

Shear keys, normally anchored by rebar, have a certain amount of resistance, but are usually designed as sacrificial, breaking off in order to prevent excessive force transmission that can damage the abutments or foundations. In general, shear keys have little ductility (Degenkolb 1977) and experience brittle shear failure (Megally et al. 2002). Figure 2-7 shows the failure of exterior and interior shear keys. Kaviani et al. (2012) found that shear keys are critical components to control the global superstructure rotation and corresponding column drift amplification,

especially when installed at the abutments. ACI (American Institute of Concrete) Monograph No. 10 (1977) deemed shear keys essential for earthquake mitigation.

(a) (b)

Figure 2-7 Failure of shear keys: (a) exterior key, and (b) interior key (Megally et al. 2002).

2.1.5 Seismic Response of Restrainers

One of the most catastrophic bridge failure modes results from span unseating at expansion joints/in-span hinges (Figure 2-4), which can be prevented by the use of restraining devices. Steel cables are the most common approach, linking together adjacent deck segments across the joint. Restrainers act only in tension, with a slack to prevent activation under normal thermal expansions and contractions. Restrainer types and methods of construction are shown in Figure 2-8.

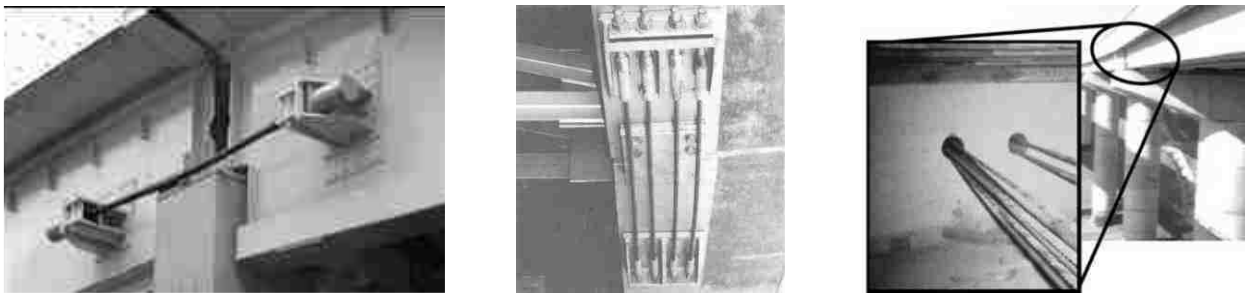

(a) (b) (c)

Figure 2-8 Restrainer types: (a) cable and shock absorber (Raheem 2009), (b) external installation (Muthukumar 2003), and (c) internal in-span hinge/joint installation (Pamuk et al. 2005).

The tests conducted by Vlassis et al. (2004) indicated that, when restrainers were used, the separation at expansion joints/in-span hinges was dramatically reduced and the threat of unseating eliminated. Additionally, when the restrainer stiffness is similar to that of the joined frames, the link provided by restrainers controls the out-of-phase vibrations of the connected adjacent frames, a major cause of unseating, limits pounding, and creates in-phase motion. The length of slack was found by Vlassis et al. (2004) to be significant. Even though larger slack reduces the possibility of restrainer yielding, it creates higher impact accelerations and relative displacements. In contrast, less slack leads to better pounding mitigation but with restrainers yielding under only a moderate ground motion. Therefore, a restrainer design that uses a balanced approach with the right amount of slack is likely the most effective solution.

Generally speaking, the restrainers can be effective as long as they do not yield. Failure of restrainers involves cable fracture (Figure 2-9a) and punching shear failure at the connected diaphragms (Figure 2-9b). Additionally, bearing failure was observed on the plates and nuts of the restrainer assembly (Selna et al. 1989a). The current design practice permits, for extreme cases, restrainer yielding to prevent punching failure caused by excessive force in the restrainer, along with the benefit of earthquake force absorption.

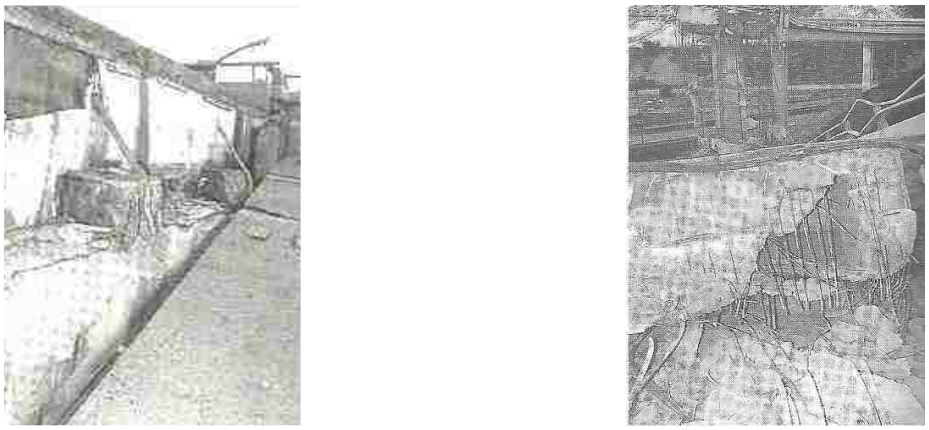

(a) (b)

Figure 2-9 Restrainer failure modes: (a) fracture, (b) diaphragm punching shear (Priestley et al. 1996).

2.2 SEISMIC RESPONSE OF ABUTMENT

Abutments support the bridge's superstructure and act as retaining walls for the embankment soil. Abutments can be integral (monolithic, Figure 2-10a, in Las Vegas) or non-integral (seat-type), which G-953 has and is shown in Figure 2-10b. Integral abutments are generally only used in single span or very short bridges; seat-type abutments are used much more widely and will therefore be the focus of the following discussions.

(a) (b)

Figure 2-10 Abutment types: (a) integral (Las Vegas), and (b) seat (Bridge G-953) (Google Maps).

An abutment consists of a backwall, wingwalls, embankment/backfill soil, and foundation. A gap exists between the seat-type abutment backwall and superstructure to accommodate thermal expansion and prevent engagement under normal loads. During an earthquake, the deck end diaphragms may fill the gap, pound against the backwall, and engage the passive stiffness of the backfill, thereby limiting the longitudinal displacement of the superstructure. The wingwalls act in a similar matter but in the transverse direction and without a gap. The study by Mylonakis et al. (1999) showed a 100% change in the longitudinal dynamic response when considering the contribution of abutments. For skewed bridges, Dimitrakopoulos (2011) found that superstructure-abutment pounding can amplify deck rotations. The embankment provides mass, vertical stiffness,

and passive resistance for the backwalls and wingwalls. The foundation for a seat-type abutment consists of a spread footing that often rests on piles, providing stability against excessive translation or rotation.

While the rotational stiffness of non-integral abutments is generally considered negligible, the translational stiffness of an abutment can be beneficial in controlling superstructure rotations in skewed bridges (Kaviani et al. 2012). Mitoulis (2012) also identified reductions in the longitudinal displacement (20-33%) and rotation ductility (29-43%) demands, natural period, and pier bending moment (21-24%) when abutment participation is considered. Overall, if the abutments' shear keys do not fail, modeling abutment stiffness is needed to accurately estimate displacement and base shear demands (Aviram et al. 2008a). Detailed abutment modeling can also result in a cost-effective design if they are utilized as a second line of defense against earthquake resistance (Mitoulis 2012).

The main concern for abutments is excessive displacement or passive soil pressure demand (Priestley et al. 1996) that can separate the abutment from the roadway, thereby cutting off emergency response routes. Siddharthan and El-Gamal (1999) observed embankment settlements in 80% of bridges during the 1994 Northridge earthquake. Caused by slope failure, grainslip excitation, and backfill settlement from abutment displacement, settlements in the range of 7.8 to 11.8 in. were recorded, enough to restrict bridge accessibility. A more serious consequence of backfill settlement is the redistribution of vertical loads in the bridge and possible unexpected failure modes (Papazoglou and Elnashai 1996).

2.3 SEISMIC RESPONSE OF SUBSTRUCTURE

2.3.1 General Behavior of Substructure

The substructure of a concrete bridge consists of the column bents with cap beams and footings. Opposite to the linear-elastic response of the deck superstructure, the columns behave inelastically in a moderate to severe ground motion. The complex behavior of reinforced concrete, combined with coupled flexure-shear-axial-torsion demands, stresses the importance of good modeling and strict reinforcement detailing. Inadequate design and detailing can lead to catastrophic collapse. Figure 2-11 shows the collapse of the Hanshin Expressway caused by poor shear strength and ductility during the 1995 Hyogo-Ken Nanbu Earthquake in Japan.

Figure 2-11 Collapse of Hanshin Expressway due to substructure failure (Chen and Scawthorn 2003).

2.3.2 Failure Modes of Columns

The flexural behavior of a bridge's columns is well understood. Damage due to flexure (Figure 2-12a) involves initial cracking, yielding of longitudinal reinforcement, spalling of cover concrete with plastic hinge formation that can propagate along the column, transverse reinforcement

fracture and buckling of longitudinal steel, and finally disintegration of the concrete core with low residual strength or total loss of load-carrying capacity.

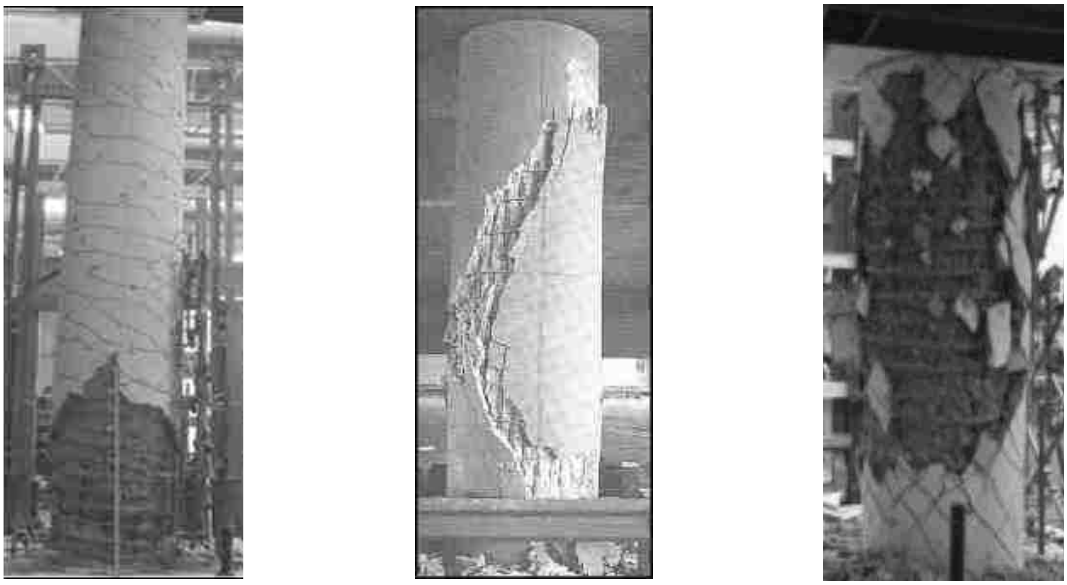

(a) (b) (c)

Figure 2-12 Failure modes of bridge columns: (a) flexural failure (Prakash et al. 2010), (b) shear failure (Priestley et al. 1996), and (c) torsional failure (Belarbi et al. 2009).

Shear is a more brittle and complex behavior than flexure for reinforced concrete members. Shear failure (Figure 2-12b) begins with diagonal cracks on one face of the member and then on the opposite side with cyclic loading. Lateral load reversals reduce the contribution of concrete to shear resistance. Brittle shear failure may occur when the cracks spread across the entire member. The presence of compressive axial force in a column can delay its concrete-shear-strength loss through aggregate interlock. Alternatively, tensile loads are detrimental to the shear strength provided by concrete due to its low strength in tension and the loss of the aggregate interlock effect. The shear strength of a column in seismic zones depends heavily on transverse reinforcement and its spacing.

A rarer but less-understood force demand in bridge columns, caused by twisting of their longitudinal axes, is torsion. Torsion can be a significant problem in skewed bridges where shear keys are not provided or have failed, allowing large deck rotations about the bridge's vertical axis that can damage or even fail the piers (Figure 2-12c). Other causes of torsion can be bidirectional earthquake loadings, bridge horizontal curvature, and unequal column heights or spans. Torsion, always coupled with other actions, can create early spalling of concrete cover, soften the concrete core (Prakash et al. 2010), and damage both flexural strength (Tirasit and Kawashima 2006) and shear strength (Tsuchiya et al. 2007). Consequently, flexure-only column designs may be inadequate with the presence of torsion (Belarbi et al. 2009). Tied columns are more vulnerable than spiral-reinforced members due to their inferior confinement effects. Otsuka et al. (2003) found that axial compression increased torsional capacity by about 10%; this effect, however, diminishes with increasing column twist (Tirasit and Kawashima 2006).

2.3.3 Geometrical Parameters Affecting Substructure Behavior

The aspect ratio of a column, the ratio of its unbraced length to its diameter, is a major parameter controlling its response. Moustafa et al. (2011) tested columns with aspect ratios ranging from 2.5 to 6.4. It was observed that shear dominated the response of columns with low aspect ratios. For the column with an aspect ratio of 4.3, the acceptable ductility of 4.0 recommended by Priestley et al. (1996) was barely met. The slender columns, or those with higher aspect ratios, however, are flexure-dominated, showing more stable hysteresis but yielding under smaller earthquake demands compared to more squat columns. Additionally, Prakash et al. (2010) found that the flexural and torsional capacities of a column are not affected by its aspect ratio.

The number of columns at a bent can also affect the global response of a bridge. While single column bents can be aesthetically-pleasing and meet space constraints, they can lead to more

stress in the shear keys (Kaviani et al. 2012). This is due to a reduced bent torsional stiffness that cannot mitigate deck rotations as well as those with multiple-column bents, forcing the shear keys to compensate (Yi Meng and Lui 2000).

2.3.4 Seismic Response of Footing

Poor footing design can result in rebar pullout at the column-footing joint (Figure 2-13a). Xiao et al. (1999) stated that shear failure of such a joint was common for pre-1971 bridges, where joint cracking (Figure 2-13b) and straightening of longitudinal reinforcement hooks (Figure 2-13c) have been observed.

(a) (b) (c)

Figure 2-13 Column-footing joint failures: (a) pullout of longitudinal reinforcement due to insufficient development length, (b) column-footing joint cracking (c) straightening of hooks with penetration through bottom of footing (Priestley et al. 1996).

2.3.5 Seismic Detailing of Substructure

Seible and Priestley (1999) noted that the transverse reinforcement ratios in current design are eight to ten times that of the pre-1971 specifications. Figure 2-14 (Moustafa et al. 2011) compares the current substructure design with the typical design in the 1960s. Rebar discontinuity along columns in older designs, especially in plastic hinge zones, creates a critical section and has led to some column failures during the 1995 Nanbu earthquake (Taylor 1999). This practice prevents the proper formation of plastic hinges and is discouraged in modern design. Another outdated practice

had longitudinal and transverse bars that did not extend into the cap beams and footings, which can strengthen the joints (Moustafa et al. 2011).

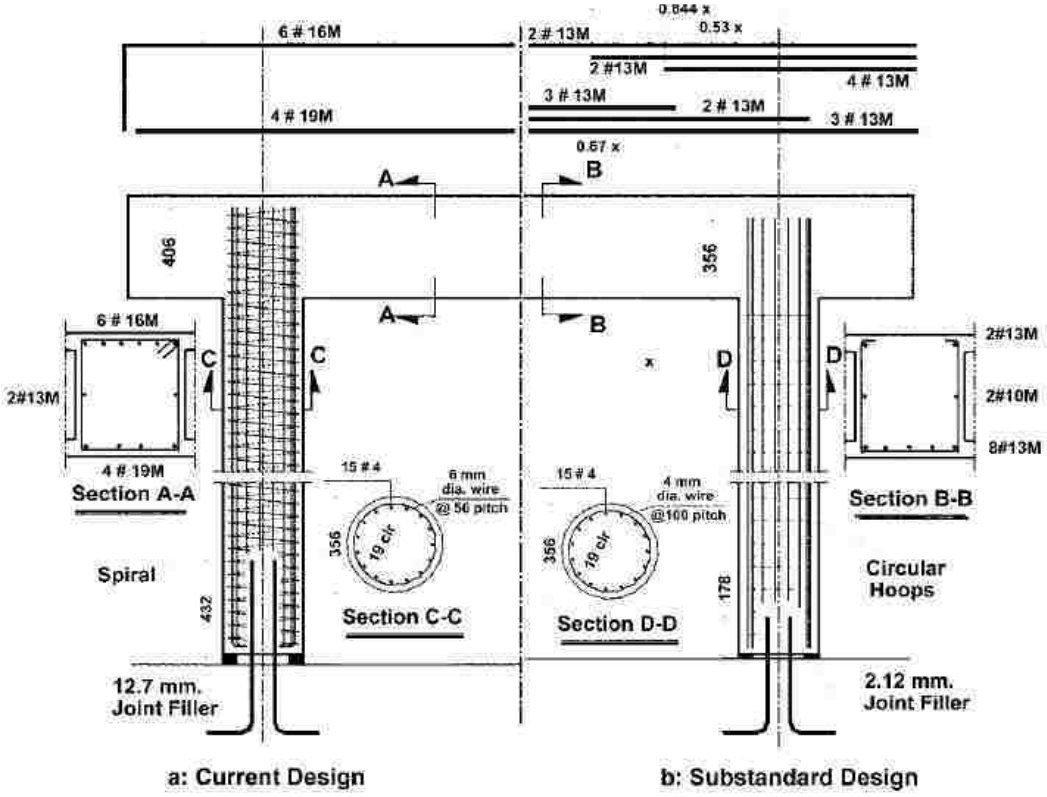

Figure 2-14 Current vs. substandard substructure design (Moustafa et al. 2011).

It has been well accepted that transverse reinforcement, with its confinement effects, has the most beneficial contribution to column integrity and ductility. Adequate transverse reinforcement prevents premature shear failure in the plastic hinge zones (Prakash et al. 2010), enhances resistance against coupled actions involving axial load, flexure, shear, and torsion (Belarbi et al. 2009), delays longitudinal bars from buckling, and strengthens the concrete core. Spacing of transverse hoops or spirals is critical. For instance, doubling their spacing results in a 50% drop in torsional strength (Tsuchiya et al. 2007). A 1% volumetric ratio for the transverse reinforcement is considered adequate for high-risk seismic design (Prakash et al. 2010) because yielding and fracture can be avoided (Moustafa et al 2011). While spirals are more expensive and

difficult to manufacture than conventional hoops or ties, the benefits often outweigh the costs for bridges resisting seismic loads.

Another detailing issue that affects the seismic performance of a bridge is the splicing and development length of flexural reinforcement. The cap beams should be adequately confined with full ties, have continuous longitudinal reinforcement across the joint region (Moustafa et al. 2011), and remain elastic under seismic loads. Splicing of longitudinal bars in the plastic hinge zone can result in a premature splicing failure (Figure 2-15a) with unexpectedly-reduced flexural strength and reduced ductility. Additionally, if close spacing of dowel bars exists at the column-footing joint, Moustafa et al. (2011) pointed out that excessive slip in the longitudinal bars can occur due to low bond strength. They also stressed that longitudinal bars anchored into the footing must be kept straight at the joint to avoid deep spalling (Figure 2-15b).

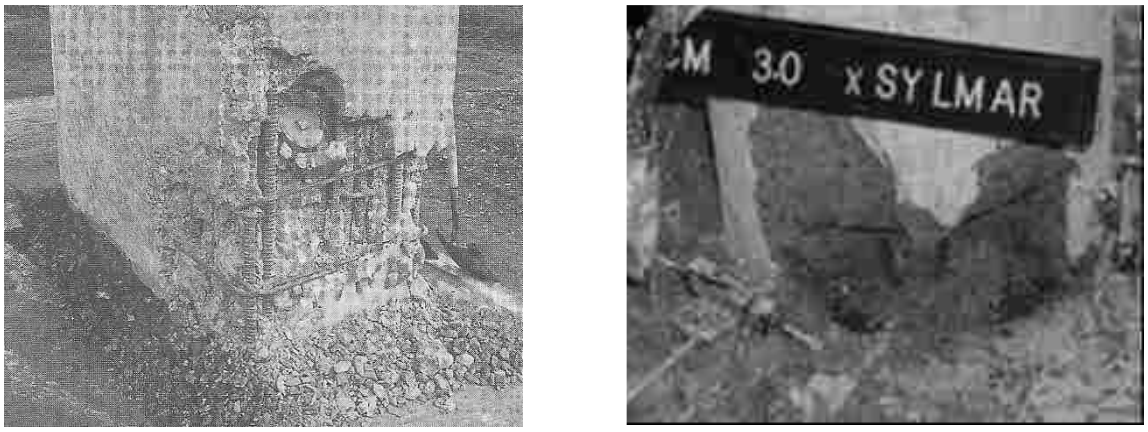

(a) (b)

Figure 2-15 Detailing-caused failures: (a) bond failure of lap splices in the 1989 Loma Prieta Earthquake (Priestley et al. 1996), (b) base hinge spalling from non-straight longitudinal bars (Moustafa et al. 2011).

In the tests on older bents by Moustafa et al. (2011), ductility was a barely-acceptable value of 4.23 compared to the standard of 4.0 proposed by Priestley et al. (1996). However, Memari et al. (2011) stated that poorly-detailed columns have a minimum ductility of 1.5 but could be as high

as 4 to 6 if the longitudinal reinforcement is continuous across the plastic hinge region. Such a level of ductility can be sufficient for minor to moderate earthquakes, implying that insufficient transverse reinforcement may not be enough to justify seismic retrofit of such columns.

2.3.6 Seismic Response of Joints

Connections and joints must be well designed to ensure their integrity and achieve the designed-for behavior and performance. Proper design and detailing is critical to ensuring proper stiffness and force transfer between the super- and sub-structures. On the other hand, poorly designed or detailed connections and joints can cause reduced system stiffness, undesired force distribution, and the formation of a collapse mechanism. Loads on joints come from two main sources, tension in longitudinal bars and cap beam overhang forces (Moustafa et al. 2011). Timosidis and Pantazopoulou (2007) formulated joint deformations at different loading stages including first cracking, first yielding of joint reinforcement, and final failure. In the knee joints cracks can be created by high tension in the transverse reinforcement; fortunately, this can help relieve strain at the same time (Moustafa et al 2011). Deep spalling occurs in T-joints near ultimate load. A joint failure caused by the 1989 Loma Prieta Earthquake is shown in Figure 2-16.

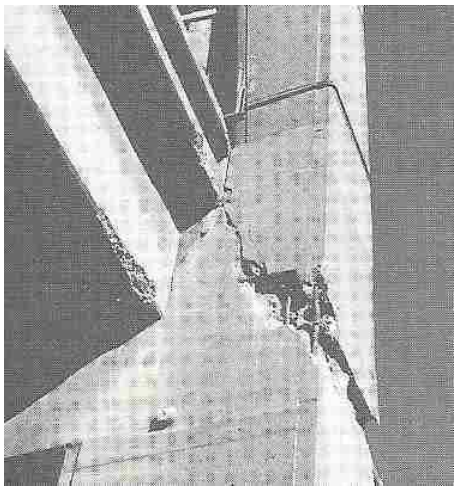

Figure 2-16 Joint failure caused by the 1989 Loma Prieta earthquake (Priestley et al. 1996).

2.4 EFFECTS OF BRIDGE SKEW

The main effect of skew on the seismic response of a bridge is superstructure in-plane rotation about its vertical axis (Figure 2-17a), resulting in torsion and increased shear demand in the columns (Yi Meng and Lui 2000). As discussed in Section 2.3.2, column torsion can interact with other forces and degrade capacities. McCallen and Romstad (1994) illustrate the skew effect on mode shapes and frequency, as shown in Figure 2-17b. The study by Yi Meng and Lui (2000) of the Foothill Boulevard Overcrossing, a skewed bridge subjected to the 1971 San Fernando earthquake, indicated that three out of the four central bents were inadequate for torsion. Torsional rotation dominated the first modes of the structure, inducing the twist demands. This also caused additional transverse displacement demands but had little effect in the longitudinal direction. Their analysis also recorded a larger natural period than non-skewed superstructures and higher skews led to an increase in the transverse displacement component and column torsion and shear demand. Contrary to popular belief, the skew of a bridge with monolithically constructed piers was found to have no effect on bending moment demand (Attarchian et al. 2012).

Additional causes of superstructure in-plane rotation are eccentric segment masses (Wakefield et al. 1991), abutment skew, uneven column elevations, and asymmetric column damage (Kaviani et al 2012). Arrangements of spans and differences in column stiffness have little effect (Yi Meng and Lui 2000). Shorter and stiffer bridges without good abutment connections were found to be more sensitive to rotation (Wakefield et al. 1991).

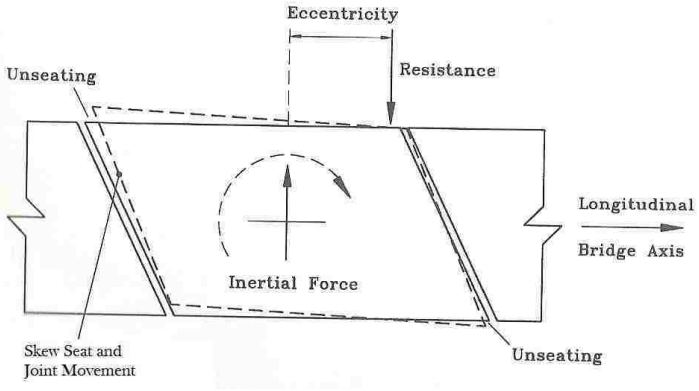

(a)

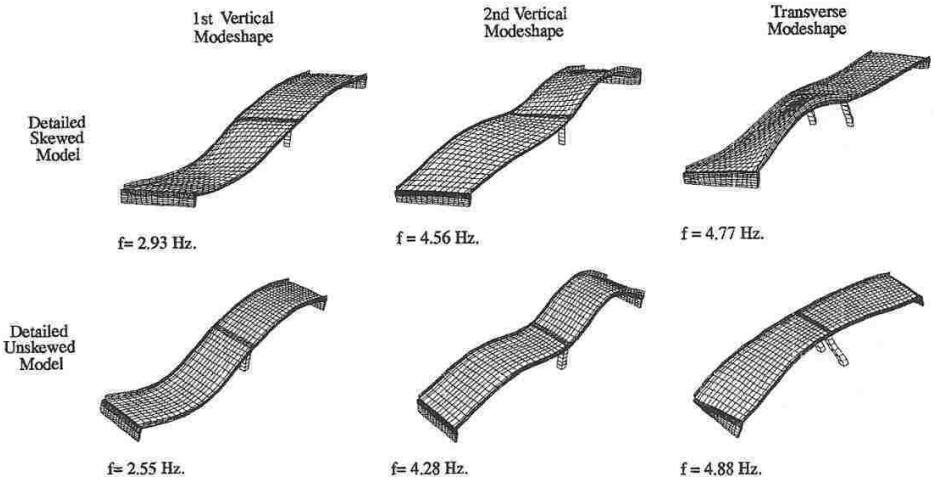

(b)

Figure 2-17 Effects of bridge skew: (a) in-plane deck rotation (Priestley et al. 1996), and (b) mode shape and frequency (McCallen and Romstad 1994).

Generally speaking, skewed bridges are more prone to failure than their non-skewed counterparts according to Kaviani et al. 2012. They also found that ground motions with sudden pulses affected skewed bridges greatly. The risk of unseating for skewed bridges is higher; this is due to the higher in-plane deck rotations which also failed columns by shear amplification in a study by Yi Meng and Lui (2000) (Figure 2-18). Permanent residual rotations can render the bridge unserviceable. For instance, Jennings et al. (1971) identified a deck in-plane rotation of 0.9×10^{-3} radians that increased the deck displacement 2.95 in. in addition to the purely-translational component. While bridge skew is often an unavoidable design constraint, its effects can be

mitigated. Kaviani et al. (2012) found that the abutment shear keys play a significant role in controlling deck rotations. Additionally, Caltrans has enacted measures to reduce the skew angle at expansion joints due to the many unseating failures of bridges in the 1994 Northridge earthquake, where skew angles were as high as 66° (Seible and Priestley 1999).

Figure 2-18 Column failure of Foothill Boulevard Undercrossing caused by effects of skewed superstructure (Earthquake Engineering Research Center, University of California-Berkeley).

2.5 Effects of Ground Motion

Ground motions travel in *p*- and *s*-waves, causing both horizontal and vertical excitations. The vertical s-wave travels much faster but diminishes quickly as it spreads out from the epicenter. Thus, for structures more than 60 km away from a fault, the effects of vertical ground motion can be neglected (Button et al. 2002). Additionally, as stated by Siddharthan and El-Gamal (1999), while the vertical component, having a higher frequency than the horizontal, can be large in magnitude, it is not in phase with the horizontal motion. This reduces the chance of any interaction or amplification of demands.

While most analyses of bridges have neglected the vertical acceleration components, increasing evidence and studies are pointing to its detrimental effects on structures near an earthquake's epicenter. Button et al. (2002) found that when most of the modal mass is near the

peak of the vertical response spectrum, the effects can be significant. Underestimation of the vertical/horizontal spectral acceleration ratio for near-field motions and overestimation for far-field accelerations was identified by Papazoglou and Elnashai (1996). The ratio can be as high as 1.7, with the average of recorded earthquakes above unity and thus 30% higher than the current 2/3 code scaling factor.

Vertical ground motion can cause sudden changes in axial loads in the columns, which can crush concrete in compression or easily destroy it in tension. Papazoglou and Elnashai (1996) studied the failure of the Bull Creek Canyon Channel Bridge (Figure 2-19a), which was near the epicenter of the 1994 Northridge earthquake. The columns of this bridge suffered fracture of transverse reinforcement, buckling of longitudinal bars, core disintegration, and axial shortening. Based on the damage pattern, it was believed that the vertical ground motion was responsible for the failure of this bridge. The Hanshin Expressway damage from the 1995 Kobe earthquake (Figure 2-19b) is another possible example of vertical acceleration damage.

(a) (b)

Figure 2-19 Bridge failure likely caused by vertical ground motions: (a) Bull Creek Canyon Channel Bridge during the 1994 Northridge earthquake (www.eeri.org), and (b) Hanshin Expressway during the 1995 Kobe earthquake (EQE International).

Axial force fluctuation in the columns can lead to a tensile state which can completely eliminate the aggregate interlocking; this reduces both the torsional and shear resistances provided by concrete. Papazoglou and Elnashai (1996) believed that the vertical ground motion explained the shear failure of a column of the La Cienega-Venice Undercrossing Collector Distributor 36 (Figure 2-20). They believe that the column's shear strength was severely reduced by a momentary state of tension in conjunction with high shear demand.

Figure 2-20 Shear failure of La Cienega-Venice Undercrossing Collector Distributor 36 possibly caused by axial tension (Papazoglou and Elnashai 1996).

Another property of ground motions is the spatially-varying effect, which considers how the variations in the arrival time of excitations at each support can change the bridge response. Chouw and Hao (2008) studied the practice of designing adjacent frames to have identical vibration periods to limit pounding and how nonuniform excitations can affect this assumption. They found that, for a period ratio T_1/T_2 greater than 0.6, spatially-varying effects and soil-structure interaction can amplify pounding. Generally, only longer bridges are affected since the ground motion travels so fast that shorter-spaced spans can be assumed to be excited nearly at the

same time. For long bridges that are affected, the effect diminishes with an increase in the natural period of the structure.

2.6 SOIL-STRUCTURE INTERACTION

A significant but debatable contributor to the global stiffness of a bridge system is soil-structure interaction (SSI). Highly idealized boundary conditions, either fixed or pinned supports, are assumed for columns and abutments. However, the soil properties and foundation design create support conditions that offer stiffnesses somewhere between purely rigid and rotation-free. The general belief is that considering SSI lowers the global stiffness of the bridge system, reducing the natural period and, thus, seismic loads. Some design codes consider SSI to be beneficial and assume that neglecting it will produce a simplified but conservative design.

Elgamal et al. (2008) found SSI beneficial in reducing maximum acceleration applied to the structure but detrimental in creating residual loads due to soil lateral deformation. Saadeghvaziri and Yazdani-Motlagh (2008) found that the increased displacement demand from SSI almost unseated the simply-supported bridge they analyzed. Mylonakis and Gazetas (2000) challenged what they called a “dogma of design philosophy” concerning SSI with three concerns. These are 1) response spectra that decrease monotonically with an increase in the natural period, 2) modification factors that are constant or increase with an increase in the natural period, and 3) foundation impedances with homogeneous halfspace soil conditions that tend to over-predict structural damping. Their work questioned the ever-growing practice of neglecting SSI as a conservative design choice. Additionally, they believed that SSI was directly or partially involved in structure collapses during several earthquakes, such as the 1985 Mexico City event.

CHAPTER 3

BRIDGE MODELING

3.1 DESCRIPTION OF BRIDGE

3.1.1 General Properties

Figure 3-1 schematically shows the plan and elevation views of Bridge G-953 based on its Original Drawings (Appendix A). This bridge is slightly curved and each end is supported on gravity seat-type abutments without piles. Each abutment has four slots accommodating interior shear keys built into the deck diaphragms. The overall length along the bridge centerline, L_{Bridge}, is 487 ft. The span lengths given in Figure 3-1 are measured along the curve of the bridge. The width of the main deck, w_{Bridge}, perpendicular to the bridge centerline, is 69.7 ft, with additional 2.75 ft cantilevers on either side for pedestrians. The bridge has a skew angle of approximately 34.6° relative to the transverse direction, leading to a skewed width ($w_{Bridge,skew}$) of 84.7 ft. The expansion joints, which allow for thermal effects, split the superstructure into five segments, as shown in Figure 3-1. The expansion joints are either at the abutments, discussed in Section 3.1.4, or between bents (in-span hinges as labeled in Figure 3-1). All dimensions, material properties, and other information for Bridge G-953 cited in this work are taken from the Original Drawings (Appendix A) unless otherwise noted.

Concrete compressive strength was specified as 3000 psi for all structural members except for 5000 psi at the columns of Pier 1. Grade 60 steel is specified and will be considered for the longitudinal and transverse reinforcing bars. Plain elastomeric material, without steel reinforcing plates, is assumed for all bearing pads. The bearing pads are placed at the expansion joints at abutments and at the in-span hinges, which are expansion joints between adjacent deck segments.

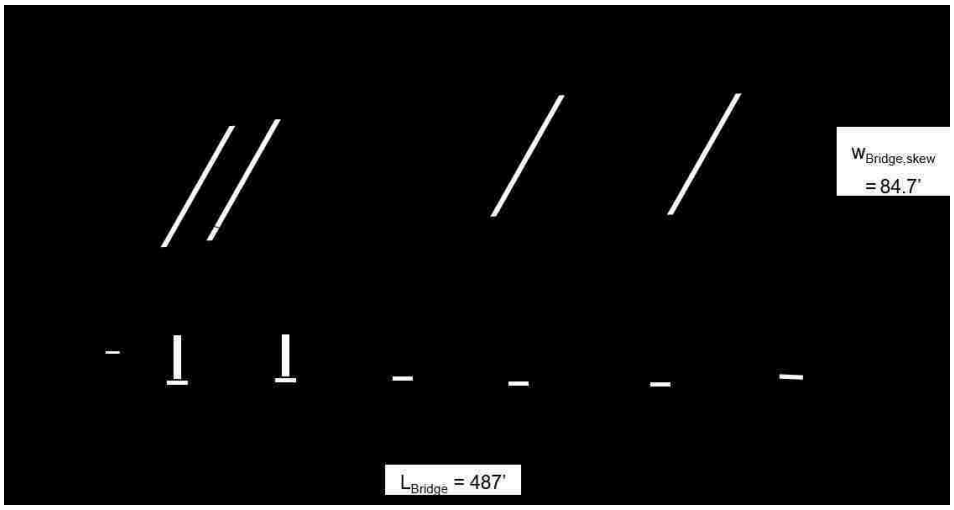

Figure 3-1 Bridge plan and elevation.

3.1.2 Superstructure

As shown in Figure 3-2, the superstructure cross-section consists of ten cast-in-place concrete box-girders oriented in the longitudinal direction. Since the bridge has a horizontal curve, there is a slight slope of 2% in the deck. The deck thickness varies along the longitudinal direction of the bridge. Between Abutment A and Pier 3, denoted in Figure 3-1, the deck thickness is 48 in. However, it is gradually increased to 60 in. from Pier 3 to Pier 4, beyond which the deck thickness stays constant at 60 in. The webs have an 8 in. width, with 4 in. fillets flaring out at the top and bottom. The top and bottom flanges are 7 in. and 6 in. thick, respectively.

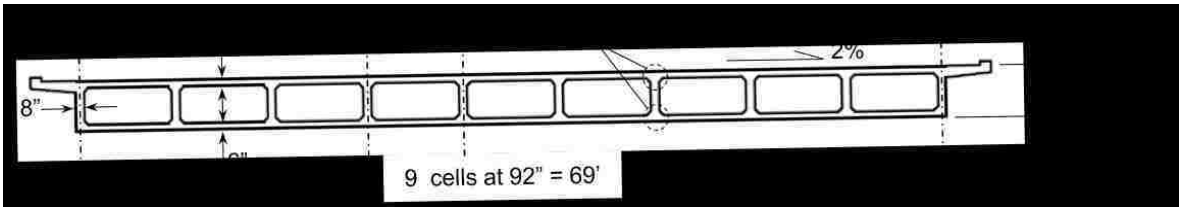

Figure 3-2 Superstructure/deck cross section in transverse direction.

Diaphragms oriented in the transverse direction, including those at the ends at the abutments, at in-span hinges, pier cap beams, and intermediate diaphragms between cap beams, were used to obtain high in- and out-of-plane stiffness. Figure 3-3 shows the cross section parallel

to the bridge longitudinal axis for all deck segments. All dimensions are measured along the curve of the bridge. The locations and dimensions of diaphragms are illustrated in this figure. Segment 3 (S3) is the longest and thus most massive deck segment.

The cap beams with the wider webs (Figure 3-3) are constructed monolithically with the deck, transferring bending moment, shear, torsion, and axial force to the columns. All diaphragms intersect the longitudinal girders in a waffle-style arrangement of webs for high deck rigidity. Depending on the span length, either one or two intermediate diaphragms are used between two cap beams. However, no intermediate diaphragm is used between Abutment A and Pier 1. The web thickness for the diaphragms is the same as that for the girders shown in Figure 3-2.

3.1.3 In-Span Hinges

The in-span hinges split the superstructure into five segments as shown in Figure 3-3 (Segment 1 [S1] to Segment 5 [S5]). As shown in the Original Drawings (Appendix A), both abutment expansion joints and in-span hinges were changed from a filler-type material with a waterstop to a strip-seal model. Figure 3-4a shows a cross section of a typical in-span hinge. The gap width is 1.5 in. for In-Span Hinges 1 and 4 and 2.0 in. for In-Span Hinges 2 and 3, which are given by the restrainer plans in the Original Drawings (Appendix A) and are larger than the gaps shown in the original construction plans. These gaps are larger than the 1 in. specified in the original bridge plans; this is likely due to concrete shrinkage from years of curing between the time of original construction and installation of the restrainers. The seat at an in-span hinge, where a deck segment bears against another one, has a total design width of 17 in, as shown in Figure 3-4a. However, due to the gap, the usable seat width should be considered as 15.5 in. for In-Span Hinges 1 and 4, and 15 in. for In-Span Hinges 2 and 3.

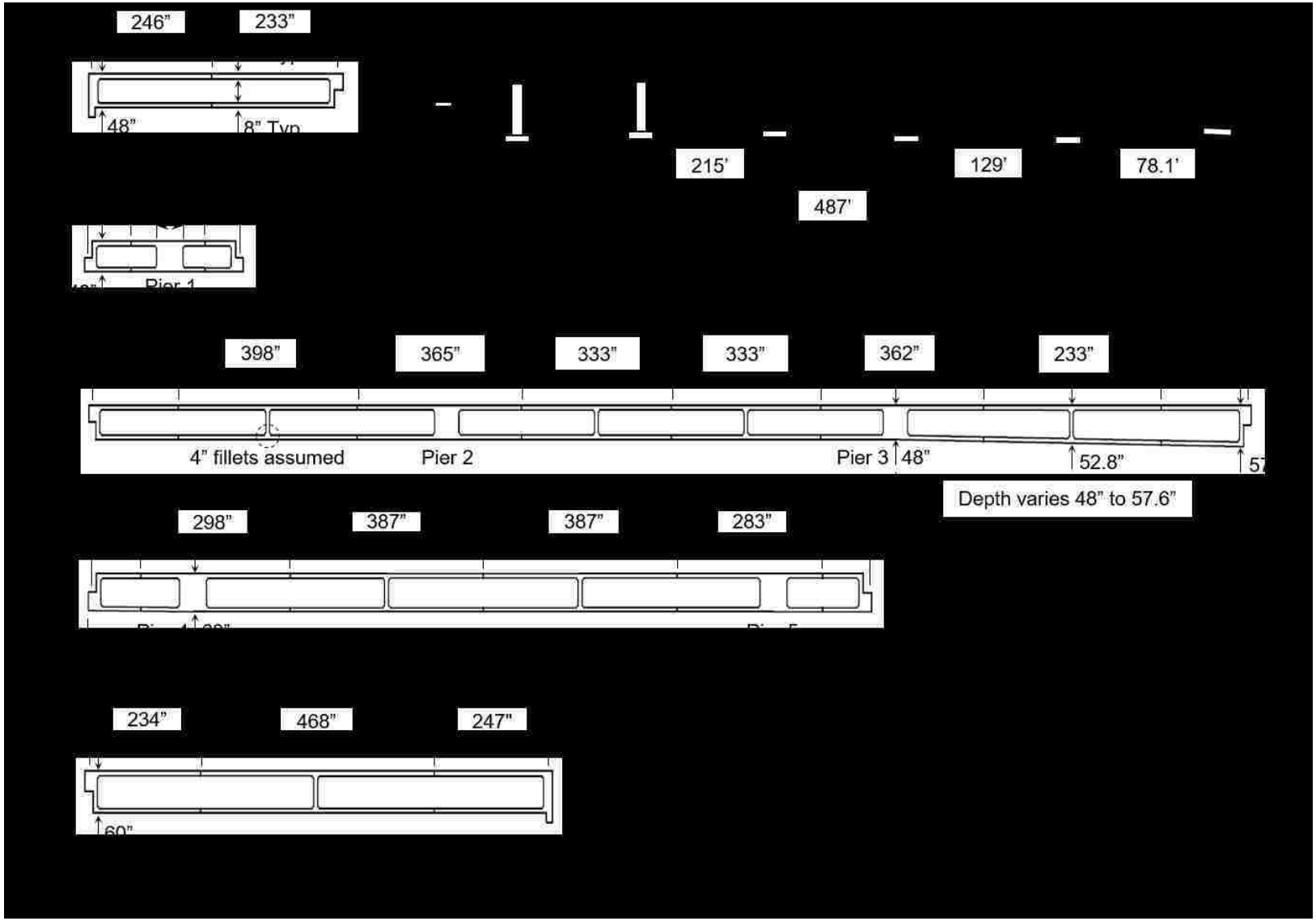

Figure 3-3 Superstructure/deck cross section in longitudinal direction.

Bearing pads are placed 1 per girder at the abutments and 2 per girder at the in-span hinges (Figure 3-4b). These bearing pads are vertically stiff but horizontally soft. Table 3-1 summarizes the dimensions and mechanical properties of the bearing pads at the in-span hinges and abutment expansion joints. The Young's Modulus, E_{BP}, is assumed as 10 ksi based on AASHTO (1968) and the shear modulus, G_{BP}, is given by NDOT as 0.13 ksi.

(a) Cross section of a typical in-span hinge (restrainers and shear key not shown)

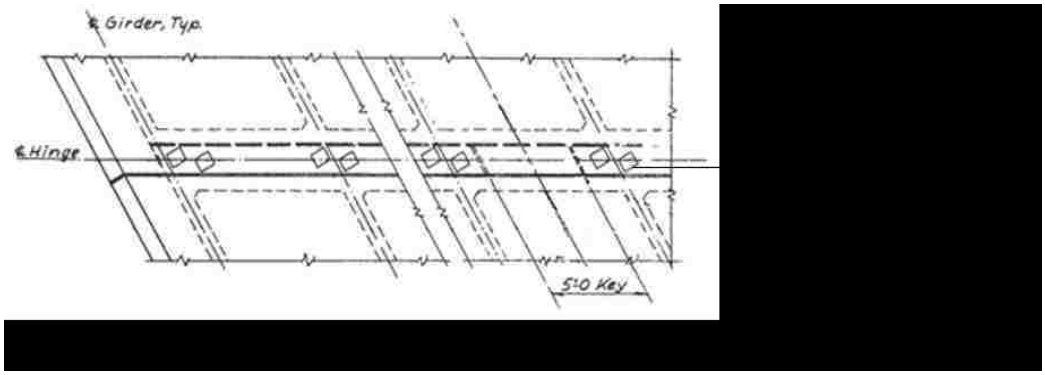

(b) Plan view for bearing pads at in-span hinges (Original Drawings, Appendix A)

Figure 3-4 In-span hinge details.

Table 3-1 Bearing pad parameters (dimensions are for a single bearing pad)

Location	Width (in.)	Length (in.)	Thickness (in.)	E_{BP} (ksi) (AASHTO 1968)	G_{BP} (ksi) (NDOT)
In-Span Hinges 1 to 3	10	6	1	10	0.13
In-Span Hinge 4	10	8			
Abutment A	12	10			
Abutment B	14	12			

A 16 x 60 x 12 in. interior shear key was installed in the middle of each in-span hinge (Figure 3-5). The shear key restrains only the relative transverse displacement along the skew between two sides of an in-span hinge. For each in-span hinge, a shear key was built into the diaphragm at one side of the in-span hinge and accommodated by a slot on the diaphragm on the opposite side of the in-span hinge. Steel reinforcement for anchorage of each key is provided. A 0.25 in. gap on either side prevents activation under low lateral loads and contains a soft elastomer.

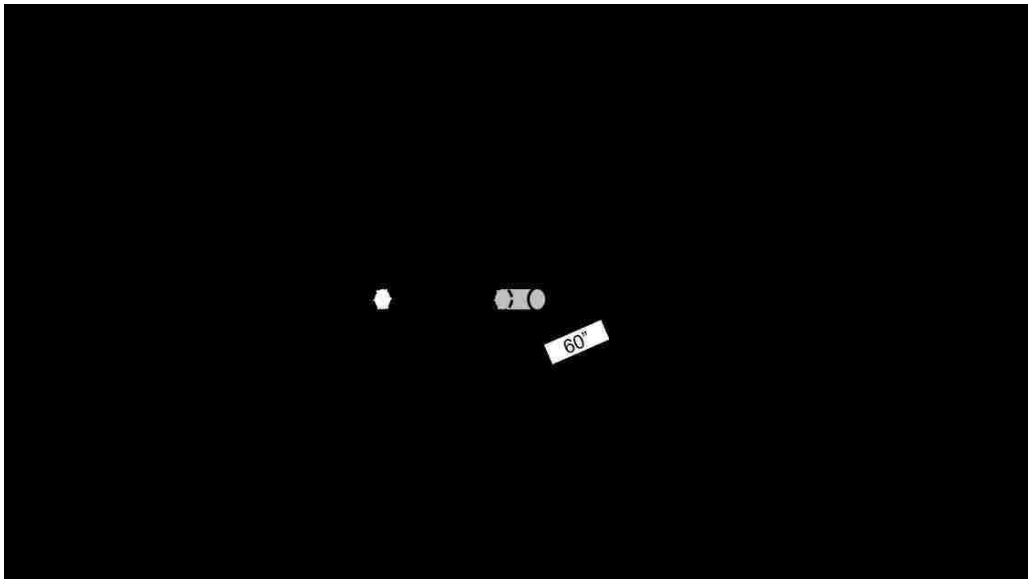

Figure 3-5 Shear key at an in-span hinge.

For seismic retrofitting, cable restrainers connecting adjacent deck segments were installed at the in-span hinges (Appendix A). A cross section of the typical assembly, taken from the Original Drawings (Appendix A), is shown in Figure 3-6. Totally 9 restrainers, each located at the center of a cell between longitudinal girders, are installed at each in-span hinge (Figure 3-5). For each restrainer, as shown in Figure 3-6, a cable was threaded through both sides of an in-span hinge and secured to the diaphragms with bolts and nuts. Restrainers typically have a slack to prevent activation under low displacements, assumed for Bridge G-953 as 0.5 in. This amount of

slack is identical to that which caused the maximum restrainer response in tests by Johnson et al. (2008) and was an average of slack values tested by Vlassis et al. (2004).

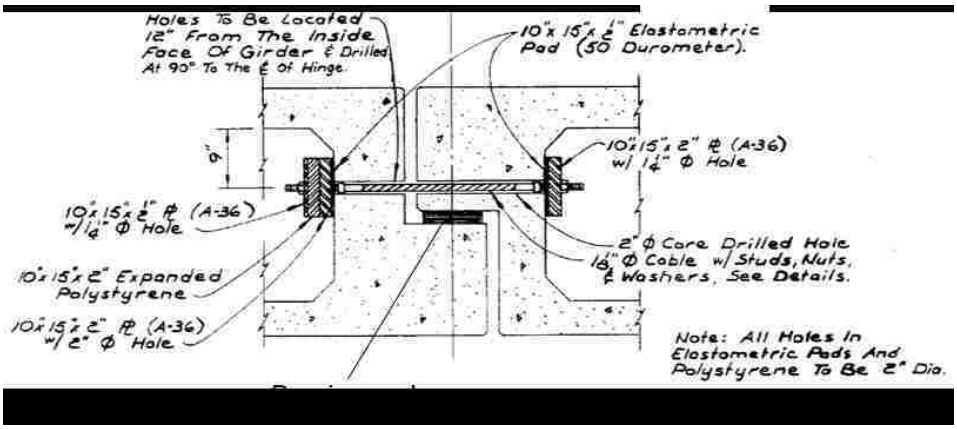

Figure 3-6 Cross section of an in-span hinge with restrainers (Original Drawings, Appendix A).

3.1.4 Abutments

The abutments are seat-type (Figure 3-7a) and do not allow moment transfer between the superstructure and the abutments. Each abutment consists of a backwall, two wingwalls, and a spread footing while providing a 25.5 in. wide seat for the superstructure. The effective seat width is 24.0 in. after deducting the 1.5 in. expansion joint gap given by the restrainer plans in the Original Drawings (Appendix A). Once again, the increase in this gap from 1 in. specified in the original bridge plans is likely due to concrete shrinkage from curing. Bearing pads, identical to those installed at the in-span hinges but with larger size (Table 3-1), were used at the abutments to support the deck. As previously mentioned, only one bearing pad was used at each girder web for both abutments. Totally four shear keys, each with identical dimensions of 12 x 59.5 x 13 in., were built into both end diaphragms of the superstructure. These shear keys fit into slots formed in the abutment seat. Just as with the in-span hinges, each slot has a 0.25 in. gap, filled with soft elastomer

on either side, to prevent activation under low lateral loads. Figures 3-7b and 3-7c show the layout of the bearing pads and shear keys.

Likely due to the relatively large seat size of the abutments (24.0 in. effective), restrainers were not installed here during the seismic retrofit. A new bridge was constructed that frames into the backfill of Abutment B, but any possible effect on the global stiffness of Bridge G-953 is neglected in this study.

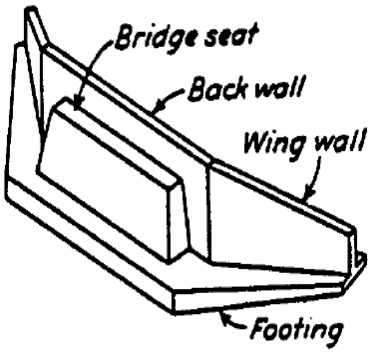

(a) General layout (Xanthakos 1996)

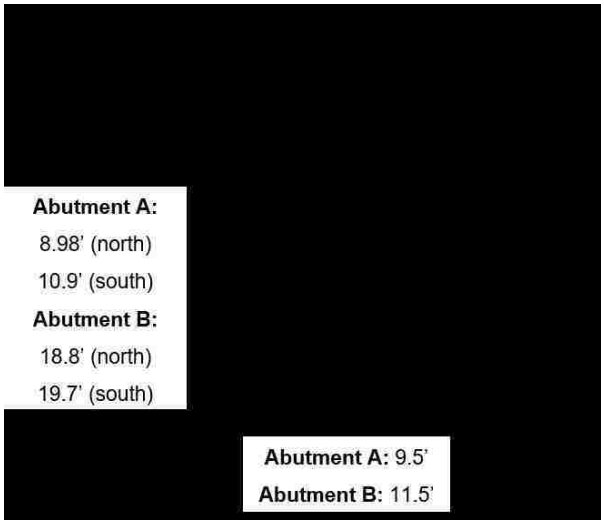

(b) Cross section

(c) Plan view

Figure 3-7 Abutment details.

3.1.5. Substructure

The substructure consists of five piers. Figure 3-8 shows an elevation view of the substructure as well as the reinforcing details of a typical section for the columns for Pier 1 (Figure 3-8a) and Piers 2 to 5 (Figure 3-8b). Each pier has four circular columns supported on rectangular spread footings. The columns have a diameter of 44 in. for Pier 1 and 42 in. for Piers 2 to 5. The height of the four columns at each pier varies slightly due to the 2% transverse slope in the deck.

Table 3-2 gives the dimensions of columns and footings, where H_F is the transverse dimension (with respect to the bridge), W_F is the longitudinal dimension, and D_F is the thickness of a footing, respectively. There is a large change in average column height from Pier 1 to Pier 5 due to the vertical curve of the bridge. Pier 1 has the tallest columns at 349 in. on average, while the shortest Pier 5 columns have only a 216 in. average height. Longitudinal reinforcement consists of varying numbers of No. 11 bars for each section, except for No. 8 at the top of the interior columns of Pier 1 and No. 10 for the exterior columns at Piers 2 and 3.

Table 3-2 Geometry of columns and footings

Pier	Column diameter (in.)	Average column height (in.)	Exterior footing (Col 1 and 4) size (H_F x W_F x D_F, ft)	Interior footing (Col 2 and 3) size (H_F x W_F x D_F, ft)	Bottom of footing elevation (ft)
1	44	349	19 x 14 x 3	19.8 x 14 x 3	1921
2	42	340	12 x 12 x 3	13.3 x 13.3 x 3	1921
3		318			1918
4		272	14.3 x 14.5 x 3	15.5 x 15.3 x 3	1916
5		216			1915

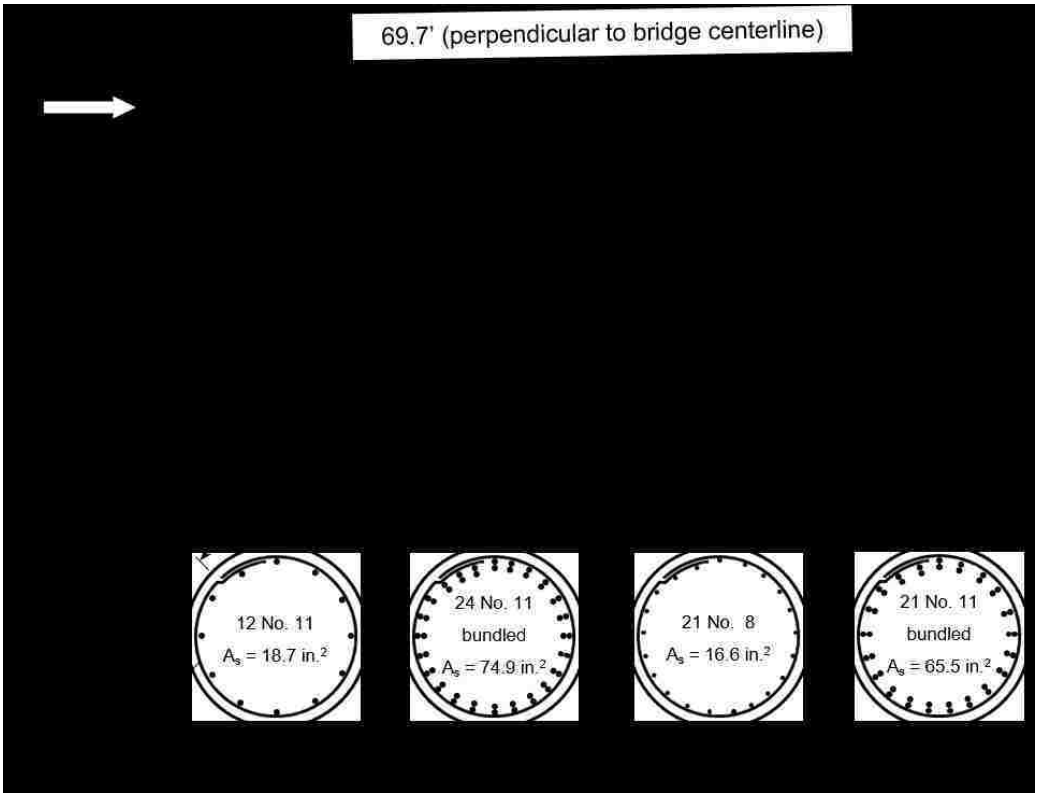

(a) Pier 1

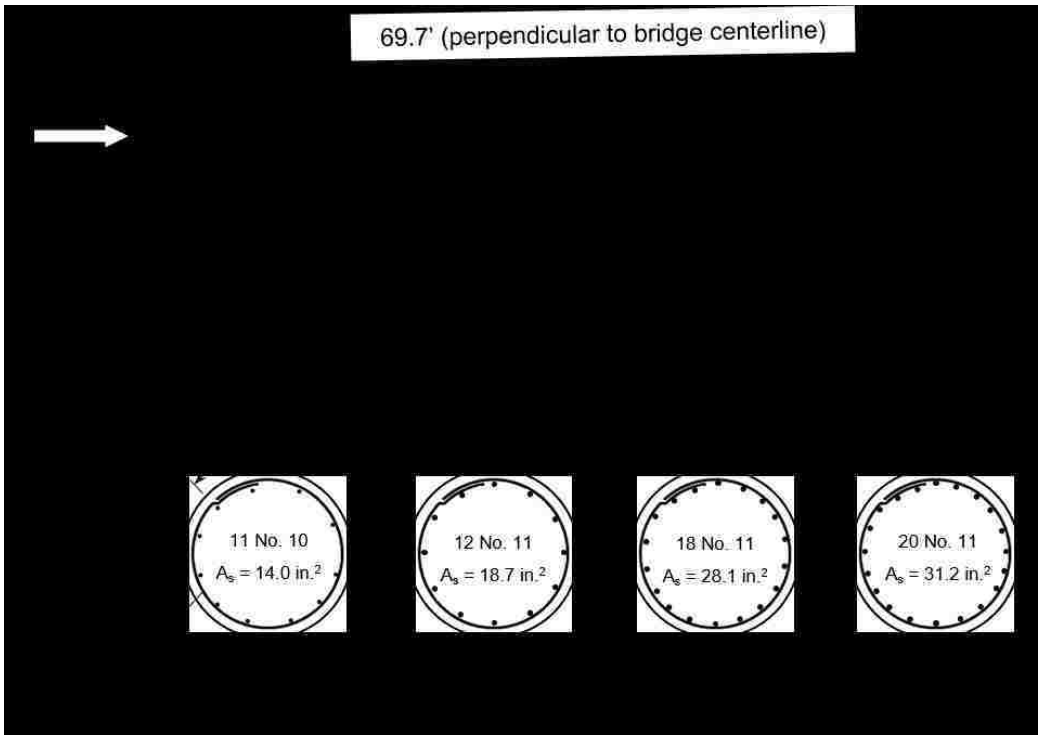

(b) Piers 2 to 5 (approximate height for Pier 5 is shown)

Figure 3-8 Substructure details.

The columns of Pier 1 were designed substantially stronger than those of the other piers, having higher reinforcement ratios (especially on their bottom halves), larger diameters, and higher concrete compressive strength. This can be seen in the substructure details in Figure 3-9. For Pier 1, a lap splice is located near column midheight (Figure 3-9a), having a length of 43 in. for the exterior columns and 30 in. for the interior columns. The longitudinal bars are continuous for the columns of Pier 2 to Pier 5. No. 5 circular hoops, with a center-to-center spacing of 12 in., were used as transverse reinforcement for every column. While the Original Drawings (Appendix A) give spirals as an option, it is conservatively assumed that hoops were provided. Each hoop has a splice of 40 in. for Pier 1 and 38 in. for Pier 2 to Pier 5, which is assumed to be welded to prevent opening upon spalling of the cover concrete (Taylor 1999). While the specified hoops are minimal according to current standards (recommended spacing today would be 1/3 to 1/4 of what has been specified), they provide the columns with some confinement effects and shear strength.

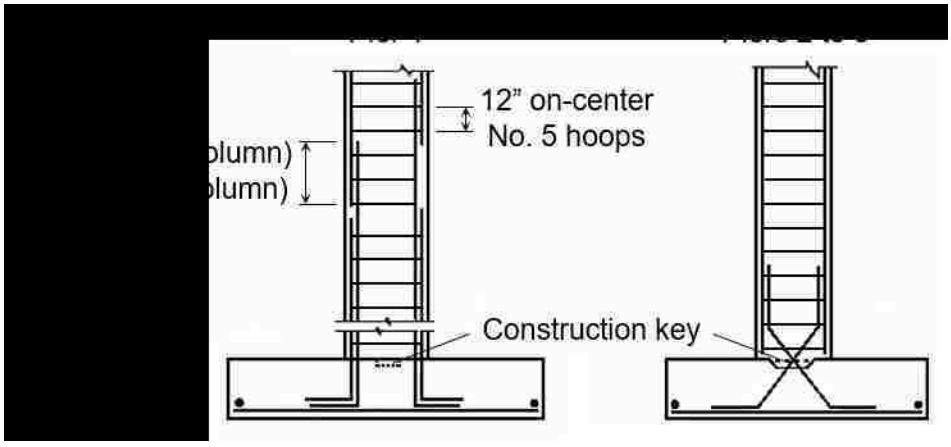

a) Fixed connection with footing b) Pinned connection with footing

Figure 3-9 Connection between column and footing (based on Original Drawings, Appendix A).

All columns were designed with fixed, monolithic connections with the cap beams. The columns of Pier 1 were designed with fixed connections with the footings (Figure 3-9a). The longitudinal bars in these columns were extended into the footings with sufficient development length. However, as shown in Figure 3-9b, the columns for all other piers were designed with pinned connections to the footings; this was done by bending and crossing the longitudinal bars near the column-footing interface.

3.1.6 Concerns for the Seismic Performance

Bridge G-953 is classified as "structurally deficient/functionally obsolete" in the 2015 State Highway Preservation Report (NDOT 2015). This bridge was designed prior to the modern seismic design and detailing approaches for bridges as well as buildings in the U.S., which were not implemented until the mid-1970s after the 1971 San Fernando earthquake. Even though the original design calculations are not available, it appears that some seismic loads have been considered based on the flexural design of columns (especially the heavily reinforced Pier 1 columns), the spacing of circular hoops less than half of column diameters, Pier 1 longitudinal bar splices away from plastic hinge zones, and the use of shear keys at in-span hinges and abutments. Additionally, the retrofitting of the bridge with restrainers at the in-span hinges should help prevent unseating and control the global displacement response.

Since the 1970s, the design loads in seismic regions have been significantly increased and seismic detailing requirements have become much more stringent. Additionally, a recent study by Lamichhane et al. (2014) indicated that the current seismic risk in Southern Nevada, as determined by the national seismic hazard model developed by the United States Geological Survey (USGS, usgs.gov), is possibly underestimated. Given that higher seismic load can be expected during a future major earthquake than that possibly considered in the initial design of Bridge G-953, there

are a series of prominent and pertinent questions to be answered concerning the seismic performance of this bridge:

(1) If the bridge behaves inelastically under strong ground motions, will the plastic hinge regions of columns (top/base of Pier 1, top of Piers 2 to 5) have sufficient deformation capacity?

(2) Do the columns have sufficient shear strength to avoid premature failure?

(3) Will the interaction between different deck segments due to the longitudinal ground motion component cause large axial forces in restrainers beyond their strength?

(4) Will a strong ground motion cause damage to the interior shear keys that are extremely difficult and expensive to repair?

(5) Will a strong ground motion cause damage due to pounding at the in-span hinges and/or abutments?

To answer the aforementioned questions, a series of nonlinear time-history analyses are performed using detailed finite element models described in the next section.

3.2 FINITE ELEMENT MODELING

3.2.1 General

Due to the special properties of Bridge G-953, such as slight vertical and horizontal curvature, considerable span length and number, and skewed design, a detailed modeling approach is chosen to study the seismic response of this bridge. The *Guidelines for Nonlinear Analysis of Bridge Structures in California* (Aviram et al. 2008b), prepared by the Pacific Earthquake Engineering Center (PEER), is adopted to determine appropriate mechanical models for the various types of structural members. Additionally, OpenSEES (McKenna et al. 2010), the Open System for Earthquake Engineering Simulation, is employed in this study. The program has various elements

and uniaxial materials to serve as an analysis platform due to its wide variety of element types suitable for accurately simulating the nonlinear response of structural components. Anything from OpenSEES (McKenna et al. 2010) used to define the model (elements, materials, etc.) of Bridge G-953 will be italicized for the remainder of this document. Since this is an analysis of an existing bridge, strength reduction, load amplification, or safety factors normally considered for design will not be used.

Figure 3-10 shows the overall model for Bridge G-953. Details for modeling each type of structural component are provided in Sections 3.2.2 to 3.2.10. A global coordinate system is defined by the horizontal X-axis along the line connecting the centers of the two abutments, the Y-axis orthogonal to the X-axis and in the horizontal plane, and the vertical Z-axis. P-delta effects are accounted for by adopting the *geomTransf PDelta* command for the geometric transformation of the main superstructure and column frame elements. Elastic response is assumed for the deck. Since the model will be used for future studies of the effects of vertical ground motion, the deck is modeled by a grid of line elements simulating the longitudinal and transverse girders and diaphragms. At the in-span hinges, bearing pads, restrainers, shear keys, and pounding are simulated to capture the load transfer across the gap and the interaction between deck segments. Figure 3-11 schematically shows the arrangement of the various elements that model the in-span hinges.

Figure 3-10 Schematic illustration of modeling Bridge G-953.

Figure 3-11 Modeling of an in-span hinge.

At an abutment, both the backwall and wingwalls rely on passive pressure to resist the longitudinal and transverse movements of the superstructure. This is simulated by exterior springs with strength limited by the ultimate passive pressure of the backfill soil. According to Maroney

and Chai (1994), the backfill is effective mainly in compression, where the superstructure bears against it or the abutment participating mass engages it, and will be modeled as such. The wingwalls are assumed effective in both tension and compression since the wingwalls on either end of the abutment engage the passive stiffness of the backfill. The bearing pads and shear keys for the abutments are defined in the same manner as those for the in-span hinges. Figure 3-12 shows the arrangement of various types of elements at the abutments. The bridge columns are modeled using line elements rigidly connected with the superstructure. Fixed end supports for Pier 1 and pin supports for Piers 2 to 5 are assumed. Bond slip of longitudinal bars is modeled because it may account for near 30% of lateral drift prior to column yielding (Zhao and Sritharan 2007).

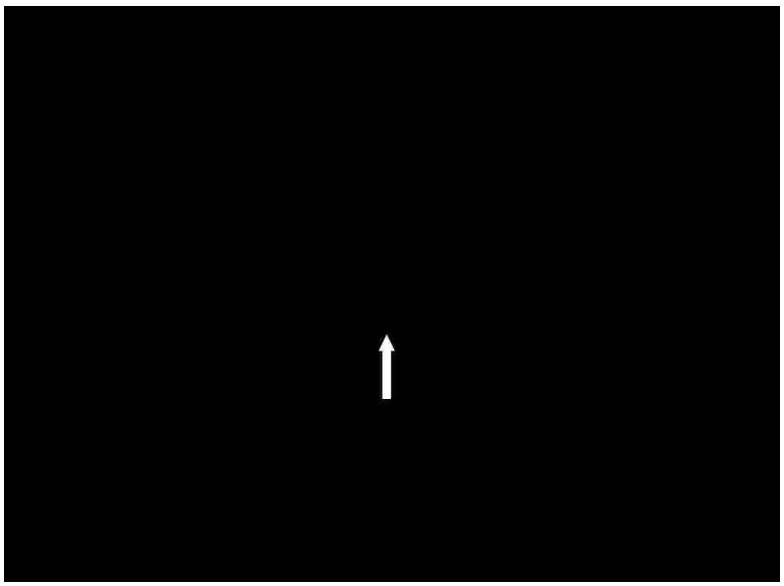

Figure 3-12 Modeling of elements at abutments (Abutment B shown).

3.2.2 Modeling of Material Properties for Reinforcing Steel and Concrete

The material properties are defined based on the original design, correspondence with NDOT engineers, research papers, and current design standards and specifications. Since the deck is assumed to behave elastically, the steel reinforcement in the deck is not explicitly considered. The

properties of longitudinal reinforcement in the columns are defined using the *ReinforcingSteel* material. This material model has incorporated the Giuffré-Menegotto-Pinto model (Menegotto and Pinto 1973) without isotropic hardening and has a defined yield plateau. Figure 3-13 plots the stress-strain response of the *ReinforcingSteel* material under tensile (Figures 3-13a and 3-13c) and compressive (Figures 3-13b and 3-13d) loadings. The actual recorded cyclic response for the first (northernmost) column of Pier 5 from the OpenSEES (McKenna et al. 2010) model of Bridge G-953 is shown. The 100X-30Y seismic loading of Ground Motion 3 (GM3) was used to generate these cyclic responses for the longitudinal steel.

Material properties of the longitudinal steel, such as the tensile strength and strain needed to define the *ReinforcingSteel* material, are determined based on the *Caltrans Seismic Design Criteria* (SDC) (2013) and listed in Table 3-3. In Figure 3-13a, $f_{s,u}^{+}$ is the maximum tensile stress, $f_{s,y}$ is the yield stress, $\varepsilon_{s,u}$ is the ultimate tensile strain, and $\varepsilon_{s,y}$ is the yield stress of the steel reinforcement. The initial strain hardening stiffness, E_{sh} (E_s is the elastic stiffness), is defined as $5\times(f_{s,u}^{+} - f_{s,y})/(\varepsilon_{s,u} - \varepsilon_{s,y})$. This is approximated by measuring the slope of a representative stress-strain plot for reinforcing steel provided by Wight and MacGregor (2009), where E_{sh} was approximately five times greater than the slope measured from the onset of strain hardening to the failure point. E_{sh} is approximately 7.5% of E_s. Post-processing will determine if the longitudinal bars fracture in tension.

Given the relatively large spacing of the transverse hoops (12 in. on-center for all columns for Bridge G-953), buckling of the longitudinal reinforcement in the columns could be a limit state (Figures 3-13b and 3-13d). The compressive stress-strain behavior in the *ReinforcingSteel* material model is modified using the *GABuck* command based on Gomes and Appleton (1997). The buckling response is shown in Figure 3-13b. This command requires a slenderness ratio, defined

as s/d_b, where s is the spacing of the transverse reinforcement and d_b is the diameter of a longitudinal reinforcing bar. Additionally, an amplification factor, β_b, taken as 1, a reduction factor, r_b, taken as 0.4 (shown as "r" in Figure 3-13b), and buckling constant, γ_b, taken as 0.5, are defined for the *GABuck* command.

(a) Tensile loading

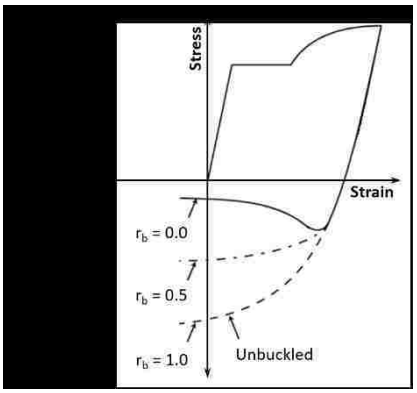

(b) Compressive loading with buckling by Gomes an Appleton (1997) (McKenna et al. 2010)

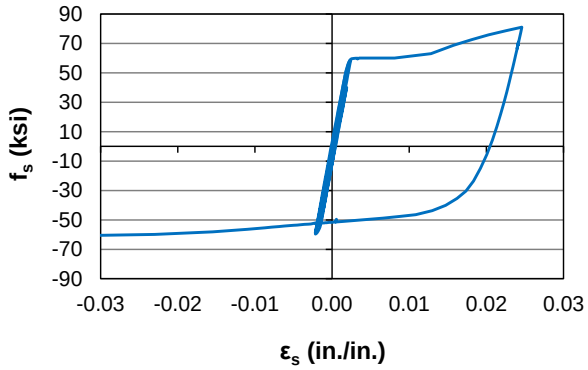

(c) Cyclic loading of Pier 5 Column 1 (GM3 100X-30Y) from the Bridge G-953 model with high tension and strain-hardening

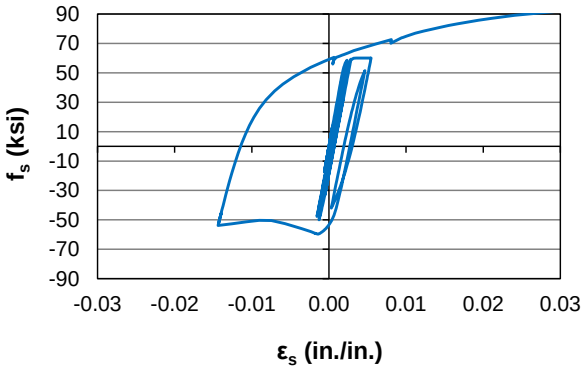

(d) Cyclic loading of Pier 5 Column 1 (GM3 100X-30Y) from the Bridge G-953 model with high compression and buckling (r_b = 0.4)

Figure 3-13 Stress-strain behavior of *ReinforcingSteel* material.

Urmson and Mander (2012) developed ultimate compressive stress and strain limits, based on crippling buckling, for longitudinal bars. Equations 3-1 to 3-5 summarize the calculation of the ultimate compressive stress and strain for longitudinal bars and Table 3-3 lists all important

buckling properties of the longitudinal bars. Post-processing will determine if a buckling failure is possible.

$$f_{s,u}^{-} = f_{s,u}^{+}\left(1 + \varepsilon_{s,u}\right)^2 \tag{3-1}$$

$$f_{s,cb} = f_{s,u}^{-}\left(\sqrt{1 + \frac{\pi^2}{1.47 \times 10^6 \times \varepsilon_{s,y}^{1.5}}} - \frac{\pi}{1200\varepsilon_{s,y}^{0.75}}\right) \tag{3-2}$$

$$\left(\frac{s}{d_b}\right)_{cb} = \frac{2.34}{\sqrt{\varepsilon_{s,u}}} \times \sqrt{\frac{f_{s,u}^{-}}{f_{s,cb}} - \frac{f_{s,cb}}{f_{s,u}^{-}}} \tag{3-3}$$

$$f_{s,cr} = f_{s,u}^{+}\left(1 + \varepsilon_{s,u}\right)^2 \left(\frac{f_{s,cb}}{f_{s,u}^{-}}\right)\left[\frac{(s/d_b)_{cb}}{s/d_b}\right]^{0.5/\beta_{s,cr}} \tag{3-4}$$

$$\varepsilon_{s,cr} = \frac{0.405}{(s/d_b)^2}\left[\frac{f_{s,u}\left(1 + \varepsilon_{s,u}\right)^2}{f_{s,cr}} + 1.52\right]\left[\frac{f_{s,u}\left(1 + \varepsilon_{s,u}\right)^2}{f_{s,cr}} - 2.82\right] \tag{3-5}$$

where $f_{s,u}^{-}$ is the ultimate compressive stress of the longitudinal reinforcement, s is the center-to-center spacing of the transverse hoops, d_b is the nominal diameter of one longitudinal reinforcing bar, $f_{s,cb}$ is an axial stress used in the empirical relationship developed by Urmson and Mander (2012), $f_{s,cr}$ and $\varepsilon_{s,cr}$ are the crippling buckling stress and strain of the longitudinal reinforcement, respectively, and $\beta_{s,cr} = 1 + 1000\varepsilon_{s,y}$ is an empirical constant.

The actual conditions for anchorage and splices of column longitudinal reinforcement are shown in Figure 3-14. The interior Column 3 of Pier 1 is shown for Figure 3-14a; the reinforcement detailing varies slightly for the exterior Column 1 and 4. As shown in this figure, splices were assumed to be placed near the mid-height of the columns in Pier 1. Additionally, provided development length varies due to different column heights and rebar length as specified in the Original Drawings (Appendix A). ACI 318-14 (2014) was employed to determine the required

rebar development length in tension and compression. Only the maximum required development length, either tension or compression, was used to determine rebar development for each section (seismic load reversals can put the bars in tension or compression). The longitudinal bars are found to have adequate development for most columns, with exceptions at certain critical sections (topmost section of column near moment-resisting joint) for tension development length listed in Table 3-4. Accordingly, the yield strength of reinforcement in these sections is proportionately reduced and no strain hardening is considered.

Table 3-3 Material properties of longitudinal reinforcing steel

Column Section	Bar No.	$f_{s,y}$ (ksi)	$f_{s,u}^{+}$ (ksi)	f_{cr} (ksi)	E_s (ksi)	$\varepsilon_{s,y}$	$\varepsilon_{s,u}$	$\varepsilon_{s,cr}$
Pier 1 bottom	11 2-bar bundle	60	95	85.7	29000	0.00207	0.09	-0.0476
Pier 1 interior top	8			79.0			0.12	-0.0112
Pier 1 exterior top	11			81.0			0.09	-0.0232
Piers 2,3 interior top	11			81.0			0.09	-0.0232
Piers 2,3 exterior top	10			82.1			0.12	-0.0185
Piers 4,5 all top	11			83.5			0.09	-0.0230

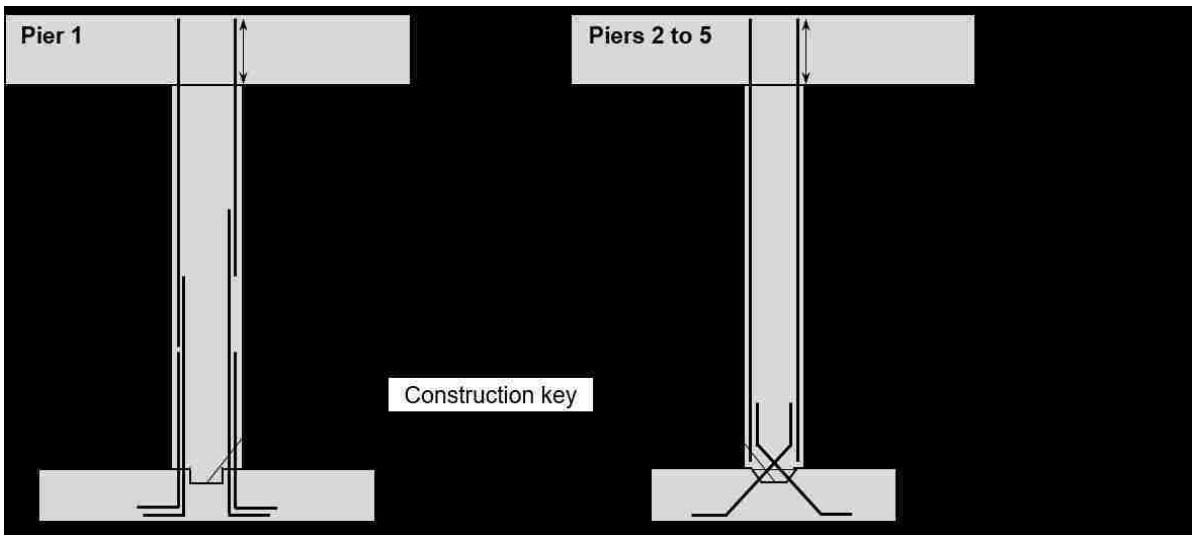

Figure 3-14 Provided development lengths of longitudinal reinforcement in columns.

Table 3-4 Properties of undeveloped longitudinal reinforcement at column tops

Pier #	Column #	Provided L_d	Required L_d (governed by tension)	% Developed	$f_{s,y}$ (ksi)
3	2	40.9	42.8	95.4	57.3
	3	40.9	42.8	95.4	57.3
4	2	47.9	51.0	94.0	56.4
	3	46.4	51.0	91.0	54.6
	4	45.0	45.8	98.4	59.0
5	3	48.7	51.0	95.5	57.3

The *Concrete04* material, which defines the hysteretic behavior of concrete (Figure 3-15a) and accounts for its tensile capacity, is used to model concrete in the columns. The stress and strain in the concrete are denoted as f_c and ε_c, respectively. The actual recorded cyclic response for the first (northernmost) column of Pier 5 from the OpenSEES (McKenna et al. 2010) model of Bridge G-953 is shown. The 100X-30Y seismic loading of Ground Motion 3 (GM3) was used to generate this cyclic response of the concrete core at the outermost fiber.

Concrete compressive strength was specified in the Original Drawings (Appendix A) as the 28 day strength. Because the strength of concrete beyond this age can increase gradually, Equation 3-6 (ACI Committee 209 1982) is adopted to estimate the current strength of the unconfined concrete.

$$f_c' = f_{c(28)}' \left[\frac{t}{(4 + 0.85t)}\right] \tag{3-6}$$

where f'_c is the unconfined concrete compressive strength considering time strength gain, $f'_{c(28)}$ is the concrete compressive strength at 28 days, and t is the age of the concrete in days.

The compressive strength of unconfined concrete is determined from Equation 3-6 as 5880 psi for Pier 1 columns and 3520 psi for the columns of Piers 2 to 5 and all other components (superstructure, abutment, shear keys, etc.). The Young's modulus for concrete used in the

superstructure and the concrete tensile strength for the substructure are defined based on ACI 318-14 (2014) provisions. The Poisson's ratio for concrete is assumed as 0.2.

Confining concrete in compression can enhance its strength and ultimate strain and mitigate strength degradation after reaching peak stress. The confinement effect provided by the No. 5 hoops at a spacing of 12 in. on the concrete core of the columns is considered using the model by Mander et al. (1988) (Figure 3-15b). In addition to maximum concrete compressive strength, $f'_{c,c}$, and the respective strain, $\varepsilon_{c,c}$, the ultimate strain, $\varepsilon_{c,u}$, and corresponding stress, $f'_{c,u}$, need to be specified for the *Concrete04* material. These properties are defined for the unconfined concrete cover and confined concrete core of the columns and are summarized in Table 3-5. Note that "top" and "bottom" designate the top and bottom halves of a column, respectively. Also, "exterior" denotes the northern/southernmost columns 1 and 4 while "interior" specifies the inner columns 2 and 3 (Figure 3-8). Figure 3-15c shows the typical stress-strain response for the confined concrete, as defined by the Mander et al. (1988) model, of the columns. A very large number is specified for $\varepsilon_{c,u}$ (1.0×10^{10}) in the *Concrete04* material, as the reduction in concrete stress to zero upon reaching $\varepsilon_{c,u}$ can cause numerical errors during analysis. The degradation in stress with increasing strain in the concrete core is still captured, however.

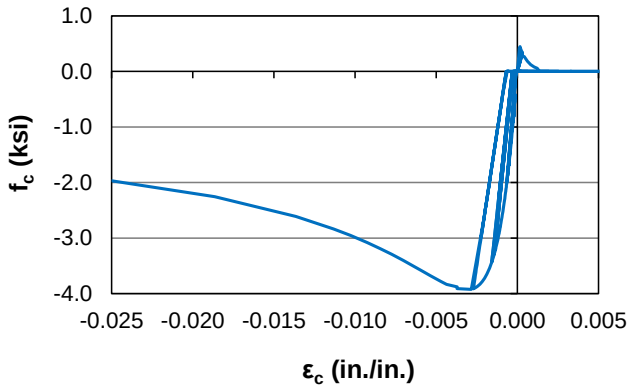

(a) *Concrete04* example cyclic loading from model

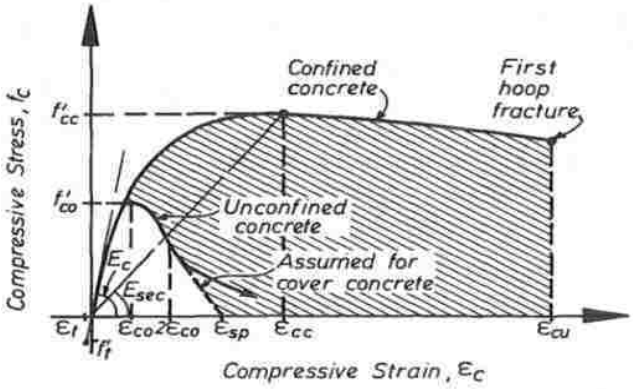

(b) Mander et al. (1988) model

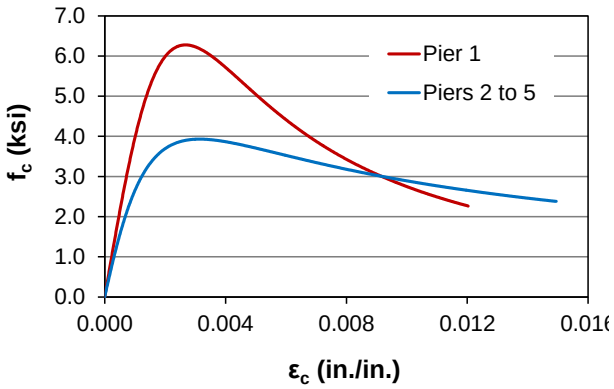

(c) Confined concrete stress-strain relationship

Figure 3-15 *Concrete04* material model for columns.

Table 3-5 Concrete material properties for columns

Pier	Section	$f'_{c,c}$ (psi)	$\varepsilon_{c,c}$	$f'_{c,u}$ (psi)	$\varepsilon_{c,u}$
1	Exterior Bottom	6290	0.00270	3870	0.00720
	Exterior Top	6270	0.00267	2340	0.0116
	Interior Bottom	6290	0.00270	3670	0.00761
	Interior Top	6270	0.00267	2260	0.0120
	Cover	5880	0.002	0	0.005
2 and 3	Exterior	3930	0.00314	2370	0.0149
	Interior	3930	0.00314	2470	0.0138
4 and 5	Exterior	3930	0.00315	2640	0.0122
	Interior	3930	0.00315	2690	0.0118
2 to 5	Cover	3520	0.002	0	0.005

3.2.3 Modeling of Superstructure

The superstructure of Bridge G-953 is modeled by a grid of elastic beam-column elements aligned according to the location and orientation of longitudinal girders and transverse diaphragms. For each superstructure element, axial, shear, flexural and torsional stiffness are evaluated based on the geometry of the web and flanges of that element located within a tributary area. The effects of the 4 in. fillets, except on weight and mass, are neglected.

The PEER guidelines (Aviram et al. 2008b) suggested a stiffness reduction to account for deck cracking. The effective moment of inertia, $I_{G,Cr}$, was assumed between $0.5I_{G,z}$ to $0.75I_{G,z}$, depending on the extent of cracking, where $I_{G,z}$ is the gross moment of inertia of a superstructure girder/diaphragm about its local z-axis (local z-axis lies in the horizontal plane of the superstructure while the local y-axis is parallel to the global-Z axis). The seismic analysis of Bridge G-953 is first performed with uncracked superstructure elements to compare the moment demand on a superstructure girder, M_G, with the cracking moment, $M_{G,Cr}$, calculated by Equation 3-7.

$$M_{G,Cr} = \frac{f_r I_{G,z}}{y_t} \tag{3-7}$$

where f_r is the modulus of rupture of the concrete, taken as $7.5\sqrt{f'_c}$, $I_{G,z}$ is the gross moment of inertia about the local z-axis of the girder cross-section, and y_t is the distance from the centroid of the cross-section to the extreme tension fiber, taken simply as half of the deck thickness at each girder (deck thickness is 48 in. from Abutment A to Pier 3, 48-60 in. from Pier 3 to Pier 4 [take average thickness in this area for each longitudinal girder], and 60 in. from Pier 4 to Abutment B).

If the bending moment demand on a superstructure girder is found to have exceeded its cracking moment, $M_{G,Cr}$ (Equation 3-7), at a beam section, then its moment of inertia is modified to an assumed value of $I_{G,Cr} = 0.75I_G$ for simplicity. Since the bridge satisfies the "Ordinary

Standard Bridge" requirements of the *Caltrans SDC* (2013) and does not have a high degree of in-plane curvature, the torsional, shear, and axial stiffnesses of the superstructure elements are not reduced.

3.2.4 Modeling of In-Span Hinges

At an in-span hinge, adjacent decks interact due to the contact caused by pounding and the forces transmitted through bearing pads, restrainers, and shear keys. Figure 3-16a illustrates these interactions and the directions in which they act. As shown in Figure 3-11, nodes are defined on each side of an in-span hinge. The *Elastic* and *Steel01* materials define the behavior of the bearing pads, which are assigned to the *twoNodeLink* element. The *elasticPPGap* (elastic perfectly-plastic gap) material is assigned to the *twoNodeLink* elements for the restrainers in tension, *twoNodeLink* elements for pounding in compression, and a *twoNodeLink* element for the shear key in both tension and compression (*parallel* material). Elements simulating bearing pads and pounding are defined in parallel as separate elements due to their identical location in the model (no *Parallel* material used, Figure 3-16b). The orientation of the restrainer *twoNodeLink* elements is identical to their actual arrangement on Bridge G-953, being perpendicular to the skew of the superstructure (Figure 3-11). However, the restrainer length in the model is shortened from the actual length in order to allow the restrainer nodes to be collinear with the other in-span hinge diaphragm nodes (Figure 3-11). The *twoNodeLink* element simulating the single shear key at each in-span hinge is defined in parallel with the middle restrainer (Restrainer 5, where Restrainer 1 is the northernmost), as shown in Figure 3-16c, but again as separate elements with no *Parallel* material used. Sections 3.2.5 to 3.2.8 discuss the modeling details of each in-span hinge component. Note that the general modeling approach for the shear keys and bearing pads is applied to both the in-span hinges and the abutment expansion joints.

3.2.5 Modeling of Bearing Pads

The 60-durometer bearing pads (Appendix A) are considered to have resistance in all 6 DOF (degrees of freedom) and are simulated using the *twoNodeLink* element. Except for horizontal shear, linear elastic response is assumed for all other actions (Figure 3-17a) and their stiffness properties are defined based on pad geometry and the elastic modulus, E_{BP}, and shear modulus, G_{BP}, given in Table 3-1. Since two pads per girder are used at the in-span hinges, composite properties of the bearing pads will be used in the determination of the area and moment of inertia.

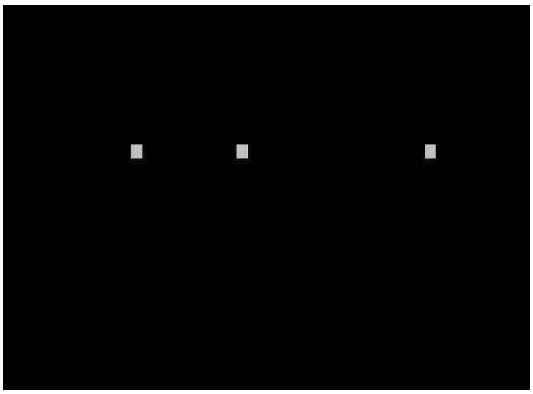

1: Bearing pad (all 6 DOF)
2: Pounding (longitudinal compression)
3: Restrainer (longitudinal tension)
4: Shear key (transverse translation)

(a) Actions modeled at an in-span hinge (DOF = degrees of freedom)

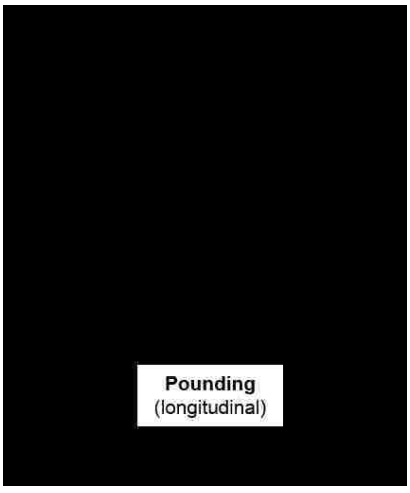

(b) Bearing pad and pounding

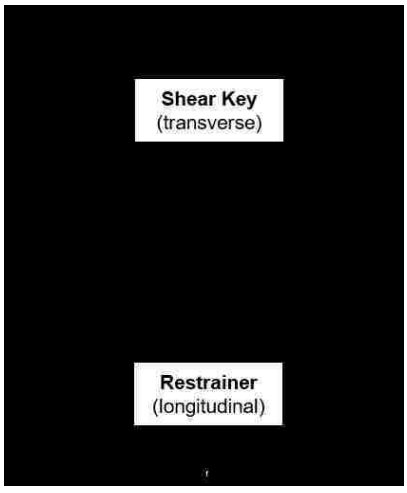

(c) Restrainer and shear key

Figure 3-16 Overview of in-span hinge modeling.

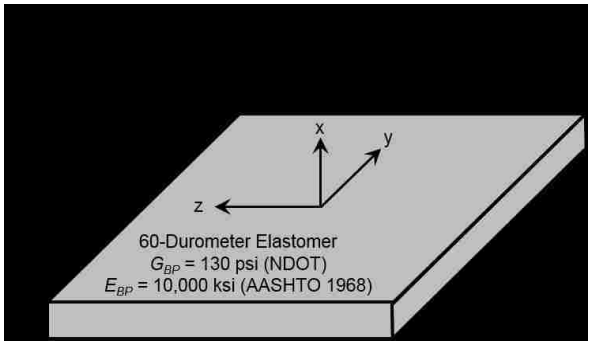

a) Resistance in 6 DOFs

b) Modeling for shear in horizontal plane

Figure 3-17 Modeling for bearing pads.

To simulate the nonlinearity associated with horizontal shear in the bearing pads, Naeim and Kelly (1999) developed a model (Figure 3-17b) based on the tests by Roeder et al. (1987). The model is incorporated by using the S*teel01* material. The elastic shear stiffness of the bearing pads, $K_{BP,t}^{(1)}$ (*t* denotes the transverse stiffness in the local-y/z axes of the bearing pad element, local-x is the vertical axis), is calculated by Equation 3-8. Equation 3-9 calculates the post-yield shear stiffness of the bearing pads, $K_{BP,t}^{(2)}$. These elastic and post-yield shear stiffnesses are derived assuming yielding of the bearing pads at 10% of the ultimate shear strain (Muthukumar 2003). Ultimate shear strain of the bearing pads is given as $\gamma_{BP,t}^{(u)} = \delta_{BP,t}^{(u)}/t_{BP}$ (Naeim and Kelly 1999), where $\delta_{BP,t}^{(u)}$ is the ultimate lateral displacement of the bearing pads in either the local-y or local-z axis and t_{BP} is the thickness of the elastomer. The thickness of the elastomer, given as 1 in., is used to define $\delta_{BP,t}^{(u)}$ (Muthukumar 2003). Thus, the plain elastomeric pads should yield at a lateral displacement of 0.1 in. and fail at 1.0 in. Equation 3-10 calculates the yield force for the bearing pads in shear, $F_{BP,t}^{(y)}$. Equations 3-11 through 3-13 calculate all other bearing pad stiffnesses, including vertical stiffness, $K_{BP,x}$ (Equation 3-11), flexural stiffness in either local axis, $R_{BP,t}$ (Equation 3-12), and torsional stiffness, $R_{BP,x}$ (Equation 3-13).

$$K_{BP,t}^{(1)} = 3.0K_{BP,t}^{(2)} \tag{3-8}$$

$$K_{BP,t}^{(2)} = \frac{G_{BP}A_{BP}}{1.2t_{BP}} \tag{3-9}$$

$$F_{BP,t}^{(y)} = 0.1t_{BP}K_{BP,1} \tag{3-10}$$

$$K_{BP,x} = {E_{BP}A_{BP}}/{t_{BP}} \tag{3-11}$$

$$R_{BP,t} = {E_{BP}I_{BP,x/y}}/{t_{BP}} \tag{3-12}$$

$$R_{BP,x} = {G_{BP}J_{BP}}/{t_{BP}} \tag{3-13}$$

where G_{BP}, $I_{BP,x/y}$, J_{BP}, A_{BP}, and t_{BP} are the shear modulus, moment of inertia in either local horizontal axis, polar moment of inertia taken as $I_{BP,y} + I_{BP,z}$, plan area, and thickness of a bearing pad, respectively.

Bearing pads may fail in several modes, including slip and exceedance of shear strain, rotation, and axial force capacities. No failure type for the bearing pads is explicitly modeled; post-processing can be used to determine if a failure is possible. According to the model by Naeim and Kelly (1999), bearing pads should fail in shear rather than slip. The slip force, F_{slip}, can be determined as the maximum static friction force, calculated using a dynamic coefficient of friction, $\mu_{s,BP}$ = 0.4 (Aviram et al. 2008a), and the axial force at a bearing pad, N_{BP}. The rotation and axial load capacities are evaluated based on recommendations from Chen and Duan (2000). Table 3-6 lists all types of loading capacities for the bearing pads.

Table 3-6 Failure criteria of plain elastomeric bearing pads

Pad Type	$\delta_{BP,t}^{(y)}$ (in.)	$\delta_{BP,t}^{(u)}$ (in.)	Lateral slip load	Ultimate axial compression (kips)	Ultimate rotation (radians)
Plain	0.1	1	$0.4N_{BP}$	101.2	0.01

3.2.6 Modeling of Pounding

Pounding (Figure 3-18) is often modeled using a compression-only elastic gap element with a high stiffness. As shown in Figure 3-16b, the pounding spring can be modeled with the *ElasticPPGap* material assigned to a *twoNodeLink* element. However, the work by Muthukumar (2003) indicated that using linear impact springs can overestimate the global system response by as much as 15%. To overcome this problem, Muthukumar (2003) developed a bilinear model based on the Hertz law and restitution and validated it against other common methods of modeling pounding (Muthukumar and DesRoches 2006). The force-displacement behavior of this mechanical model is shown in Figure 3-18a, where g_{ISH} is the gap width for the in-span hinge and $\delta_{Pen,max}$ is the maximum deck penetration, or overlap, at an in-span hinge, illustrated by Figure 3-18b.

The linear pounding spring is used during the initial analysis, having an elastic stiffness, K_{Imp}, of 25,000 k/in. as suggested by Muthukumar (2003). The maximum penetration, $\delta_{Pen,max}$, is recorded (Figure 3-18b) and then used to change the behavior of the linear pounding spring to bilinear. Penetration will always occur in the model with the pounding spring, with 1 in. or less desired. The required modeling parameters for pounding are defined in Equations 3-14 to 3-17.

(a) Bilinear force-deformation response (b) Maximum deck penetration

Figure 3-18 Modeling for pounding at in-span hinges.

$$K_{Imp,eff} = K_{Imp}\sqrt{\delta_{Pen,max}} \tag{3-14}$$

$$\Delta E = \frac{K_{Imp,eff}\left(\delta_{Pen,max}\right)^{(n+1)}(1-e^2)}{n+1} \tag{3-15}$$

$$K_{Imp,1} = K_{Imp,eff} + \frac{\Delta E}{a\left(\delta_{Pen,max}\right)^2} \tag{3-16}$$

$$K_{Imp,2} = K_{Imp,eff} - \frac{\Delta E}{(1-a)\left(\delta_{Pen,max}\right)^2} \tag{3-17}$$

where K_{Imp} is the impact spring elastic stiffness equal to 25,000 k/in., n is the Hertz model coefficient taken as 1.5, e is the coefficient of restitution equal to 0.6, a is the yield parameter taken as 0.1, and ΔE is the energy loss during impact.

Bearing capacity can be exceeded by pounding forces at in-span hinges and abutment expansion joints. Since ten pounding springs are modeled, it is assumed that the bearing area, A_B, is equal to one-tenth of the deck cross-sectional area. The approximate bearing capacity is determined based on ACI 318-14 (2014) as $0.85f'_cA_B$. Bearing failure at pounding locations is not explicitly modeled, and post-processing will be required to determine if this failure type is possible.

3.2.7 Modeling of Restrainers

All of the nine restrainers at an in-span hinge are modeled (Figures 3-11 and 3-19). Each restrainer cable is modeled using a *truss* element assigned with the *ElasticPPGap* material. This material model, shown in Figure 3-19a, permits simulating the effects of slack and the bilinear tensile response of the cable. The actual material properties of the restrainers are unavailable. Therefore, properties will be assumed from the tests by Selna et al. (1989a,b). The effective area of the cables is given as $A_R = Fd_R^2$ in Section 2 of the Nobles Catalogue (2016), where d_R is the diameter of the restrainer given by the Original Drawings (Appendix A) and F is a compactness factor listed as

0.38 for 6x7 cable construction. Table 3-7 lists all restrainer parameters required to develop the bilinear stress-strain relationship in Figure 3-19a. The *eta* term in the *ElasticPPGap* material is the ratio of the plastic to elastic branches in Figure 3-19a, defined as $(f_{R,u} - f_{R,y})/(\varepsilon_{R,u} - \varepsilon_{R,y})$, where $f_{R,u}$ and $f_{R,y}$ are the ultimate and yield stress and $\varepsilon_{R,u}$ and $\varepsilon_{R,y}$ are the ultimate and yield strain of the restrainer cable, respectively.

Because the restrainers are oriented perpendicular to the skew of the in-span hinges, nodes are defined in the model specifically to accommodate the *truss* elements for restrainers connecting each side of an in-span hinge (Figure 3-19b, 3-16c). Since the distance between the two nodes (1.5 to 2.0 in.) is shorter than the actual length of the restrainers (36 in.), the stiffness assigned to the truss elements is adjusted to equivalently simulate the stress-strain response of the restrainers. Additionally, the assumed 0.5 in. restrainer slack is converted into a strain, $\varepsilon_{R,gap}$ (Figure 3-19a), for use in the truss element. Restrainer failure is explicitly modeled using the *MinMax* material. When the strain capacity of the restrainer is recorded in the *truss* restrainer element, the stress will drop to zero and the displacement record for the element will be locked at the failure displacement.

Table 3-7 Restrainer properties

Restrainer type	1-1/8" 6x7 Regular Lay Houlage Rope Galvanized	Original Drawings (Appendix A)
Actual length (in.)	36.0	Original Drawings (Appendix A)
Modeled length (in.)	1.5 (In-Span Hinges 1,4) 2.0 (In-Span Hinges 2,3)	Johnson et al. (2008), Vlassis et al. (2004)
Slack (in.)	0.5	Johnson et al. (2008), Vlassis et al. (2004)
Nominal cable diameter, d_r (in.)	1.13	Original Drawings (Appendix A)
Elastic stiffness, K_R (ksi)	10,000	Selna et al. (1989b)
Yield force, $F_{R,y}$ (kips)	39.0	Selna et al. (1989a)
Ultimate force, $F_{R,u}$ (kips)	53.0	Selna et al. (1989a)
Design ultimate strain (%)	5.0	Selna et al. (1989a)

(a) Modeling for nonlinear response of restrainers with adjusted parameters

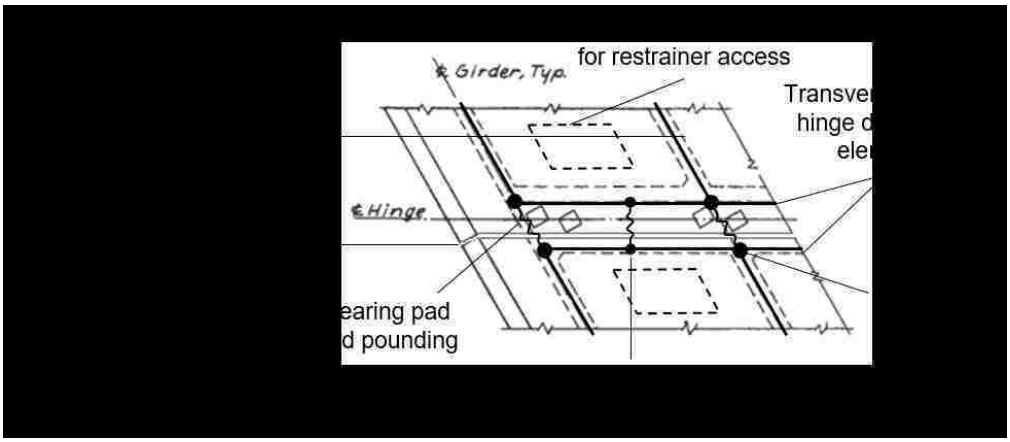

b) Location of truss element for restrainer in model (drawn over Original Drawings, Appendix A)

Figure 3-19 Modeling for restrainers.

3.2.8 Modeling of Shear Keys

The shear keys are assumed to provide transverse resistance only in the direction of the bridge skew. This resistance is simulated by a model developed from the tests by Megally et al. (2002). Figure 3-20 shows the assumed monotonic loading response. The *Hysteretic* material is used to define the normal response of the shear key up to its maximum strength (solid line in Figure 3-20), which quickly degrades to zero with further displacement. Once the shear key is loaded to its maximum strength, $V_{SK,u}$, another *Hysteretic* material (dashed line in Figure 3-20) represents the residual shear key force-displacement response. This second backbone has a significantly reduced

stiffness and strength, $V_{SK,r}$, compared to the initial shear key stiffness, to account for cracking that occurs when the shear key is loaded to its maximum resistance. The force deformation response of this second backbone is mainly based on residual sliding friction up to a 4.5 in. ultimate displacement. At this ultimate displacement, it is assumed that cracking has propogated across the entire shear key and a total loss of shear key resistance occurs. Initial and residual shear key strength are given by Equations 3-18 and 3-19, respectively.

$$V_{SK,u} = \text{minimum}\begin{cases} 3.6\pi\sqrt{f'_c}A_{SK} \\ 800A_{SK}\ \left(\frac{A_{s,SK}}{A_{SK}} < 0.006\right) \\ 0.2A_{SK}f'_c\ \left(\frac{A_{s,SK}}{A_{SK}} \geq 0.006\right) \end{cases} \tag{3-18}$$

$$V_{SK,r} = V_{SK,u}\left[1.5\left({}^{h_{SK}}/_{d_{SK}}\right) - 0.25\right] \tag{3-19}$$

where A_{SK} is the cross-sectional area of the shear key in the horizontal plane (i.e. interface between shear key and in-span hinge or abutment), $A_{s,SK}$ is the total cross-sectional area of steel crossing the horizontal shear key interface (i.e. the anchoring bars), h_{SK} is the height of the shear key (i.e. the amount the shear key protrudes from the horizontal interface), and d_{SK} is the larger horizontal dimension of the shear key interface (i.e. dimensions used to calculate A_{SK}).

In Figure 3-20, since the springs representing the normal and residual response of the shear keys will be in parallel, the strength shown for $V_{SK,u}$ is the ultimate strength calculated by Equation 3-18 reduced by the residual strength, $V_{SK,r}$, calculated by Equation 3-19. Otherwise, the strength of the shear key would be overestimated, as both springs are active upon initial loading (i.e. reduction of the normal shear key response [solid line] has not yet been reduced to zero).

Figure 3-20 Shear key force-displacement behavior.

Figure 3-21 shows how the *Hysteretic* materials defined in Figure 3-20 can be modeled by an assembly of springs in series and parallel. Gaps of 0.25 in. exist between the shear keys (Figure 3-5), denoted as g_{SK} in Figures 3-20 and 3-21. These gaps are filled with soft elastomeric material that covers the slots for the shear keys for the in-span hinges and abutment seats. Based on the study by Megally et al. (2002), it is assumed that 95% of this gap is closed before a shear key activates ($0.95g_{SK}$ in Figures 3-20 and 3-21) and a shear key reaches its maximum strength when the remaining 5% of the gap closes ($0.05g_{SK}$ in Figure 3-20). These gaps are modeled using the *ElasticPPGap* material. Because gaps exist on each side of a shear key, tension and compression gaps are combined in parallel with the *Parallel* material (Figures 3-16c and 3-21).

The original and residual shear key force-deformation response, shown in Figures 3-16c and 3-21, can both be defined with the *Hysteretic* material and then combined with the *Parallel* material. In this way, upon reloading of the shear key, after $V_{SK,u}$ is exceeded, the residual *Hysteretic* shear key material will govern the response. These two sets of *Parallel* materials, one set for the gap and the other set for the shear key force-displacement response, are then combined

in series using the *Series* material. This *Series* material is then applied to the *twoNodeLink* (in-span hinges) and *zeroLength* (abutments) elements. In this way, the approximate stiffness, strength, weakening, and ultimate failure of the shear keys are modeled. The locations of the shear keys in the analysis model have been shown in Figures 3-11 and 3-12.

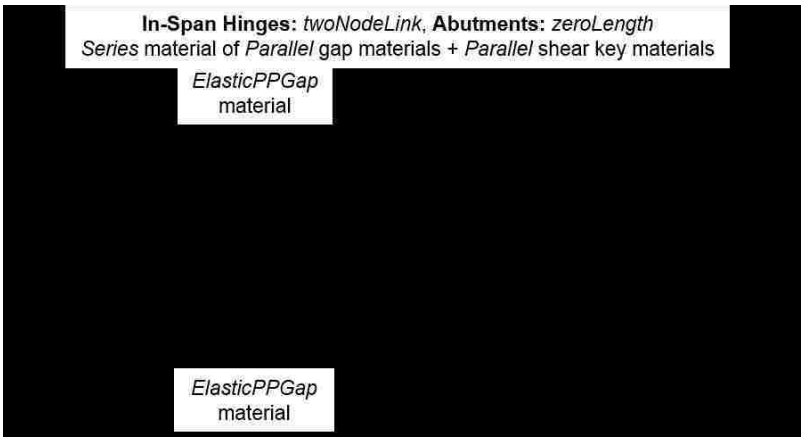

Figure 3-21 Modeling for shear key.

3.2.9 Modeling of Abutments

Abutments can significantly affect the overall stiffness of bridges, especially those with shorter spans under severe earthquakes (Aviram et al. 2008a). The "spring" type abutment model, proposed by Aviram et al. (2008a), is used to model the abutment of Bridge G-953. This type of model uses a series of rigid elements to simulate the abutment seat. These elements are connected to the deck end diaphragm and embankment by springs (Figures 3-10 and 3-12). The resistances of an abutment, including the vertical elastic embankment, longitudinal bilinear backwall, and transverse bilinear wingwall, are modeled using *zeroLength* elements at the extreme ends of the rigid *elasticBeamColumn* elements that are the abutment seat. At the extreme ends of this rigid element, *zeroLength* elements model the longitudinal backwall and transverse wingwall

resistances together. Separate *zeroLength* elements (Figure 3-10) are used to model the vertical stiffness of the embankment, longitudinal friction resistance and pounding, transverse resistance of the shear keys, and stiffnesses of the bearing pads in all DOF.

Abutments can restrain the horizontal translation of the bridge in the longitudinal and transverse directions by passive soil pressure applied by the backwall and wingwalls, respectively. This pressure provides resistance up to an ultimate load of P_{BW} for the backwalls and P_{WW} for the wingwalls. Figures 3-22a and 3-22b show the assumed force-displacement response for the backwall and wingwalls, respectively.

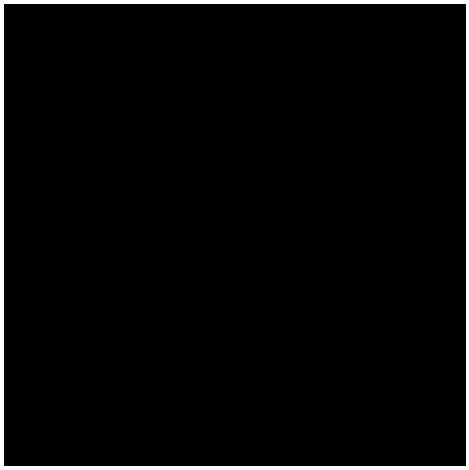

(a) Backwall modeled by *ElasticPPGap* material

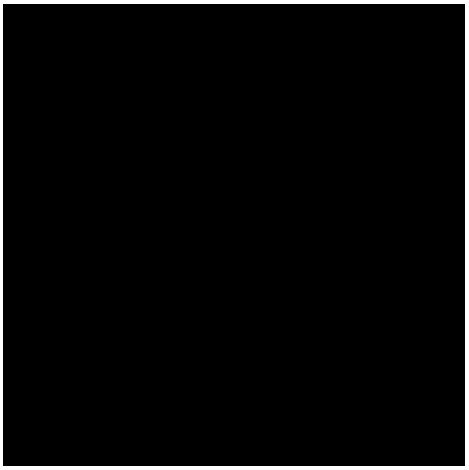

(b) Wingwall modeled by *Steel01* material

Figure 3-22 Force-displacement response for backwall/wingwall lateral resistance.

The wingwalls are assumed effective in both tension and compression; the *Steel01* material is used. The backwall, however, is effective only in compression, that is, when the superstructure overcomes the assumed 1.5 in. gap from the Original Drawings (Appendix A) and bears directly against the backwall. Two *ElasticPPGap* materials will be used, one to simulate this pounding and another to ensure the backwall responds only in compression. The backwall stiffness and loading capacity are determined based on the *Caltrans SDC* (2013).

The *Caltrans SDC* (2013) also determines the stiffness and strength of the wingwalls, but modification factors suggested by Maroney and Chai (1994) are required. The width of the top of a wingwall, w_{ww}, is altered by a factor of 2/3 to account for its different shape compared to the rectangular backwall. Additionally, the net stiffness and strength of a wingwall, calculated using this modified width, is modified by an effectiveness coefficient of 4/3. This coefficient accounts for the passive strength of the soil between the wingwalls being fully utilized while only 1/3 of the soil outside a wingwall is effective (total effectiveness is, therefore, 1 + 1/3 = 4/3). The total lateral stiffness for the backwall, K_{BW}, and wingwalls, K_{WW}, at an abutment is calculated using Equations 3-20 and 3-21, respectively. The total lateral strength provided by the backwall, P_{BW}, and wingwalls, P_{WW}, is evaluated using Equations 3-22 and 3-23, respectively. Note that the aforementioned modification factors have already been incorporated into Equations 3-21 and 3-23. Note that, as shown in Figure 3-22, the backwall and wingwall springs at the ends of each abutment have half of the total stiffness and strength calculated from Equations 3-20 to 3-23 (to account for two springs, one at each end of the rigid abutment seat element).

$$K_{BW} = \frac{K_{Abut} w_{BW} t_{Deck}}{5.5} \tag{3-20}$$

$$K_{WW} = \frac{K_{Abut} w_{WW} t_{Deck}}{6.188} \tag{3-21}$$

$$P_{BW} = \frac{w_{BW} t_{Deck}^2}{1.1} \tag{3-22}$$

$$P_{WW} = \frac{w_{WW} t_{Deck}^2}{1.238} \tag{3-23}$$

where K_{Abut} is the stiffness of the abutment backfill taken as 20 k/in./ft from the *Caltrans SDC* (2013) (non-standard backfill conservatively assumed, unable to determine if standard

specification applicable), w_{BW} is the effective, non-skewed backwall width perpendicular to the centerline of the bridge, and t_{Deck} is the backwall height above the abutment seat equal to the deck thickness (48 in. for Abutment-A, 60 in. for Abutment-B). The capacity of the abutment is limited by a suggested displacement, D_u, of 2.4 in. by Chen and Duan (2000), after which the backfill soil can experience a permanent softening and reduction in force capacity.

The total vertical stiffness of the embankment, K_{Emb}, is evaluated by multiplying a stiffness parameter, k_{Emb}, suggested by Wilson and Tan (1990) with a critical length, L_c, recommended by Aviram et al. (2008a). The critical length is calculated as an average of values from Zhang and Makris (2002, $L_{c,Z\&M} = 0.7\sqrt{[S_{Emb}w_{BW}H_{Emb}]}$) and Werner (1994, $L_{c,W} = 0.25L_{Bridge}$). Equations 3-24 to 3-26 formulate the parameters for the vertical elastic stiffness of the abutment.

$$k_{Emb} = \frac{2E_{Emb}}{S_{Emb} \cdot \ln[1 + (2H_{Emb}/S_{Emb}w_{BW})]} \tag{3-24}$$

$$L_c = \left(0.7\sqrt{S_{Emb}w_{BW}H_{Emb}} + 0.25L_{Bridge}\right)/2 \tag{3-25}$$

$$K_{Emb} = k_{Emb}L_c \tag{3-26}$$

where E_{Emb} is the elastic modulus of the embankment soil, assumed as an average value of 7.5 ksi for dense sand (Das 2006), S_{Emb} is the slope of the backfill (formatted as S_{Emb}-to-1) as given in the Original Drawings (Appendix A) and illustrated in Figure 3-29, H_{Emb} is the height of the embankment from original ground, and L_{Bridge} is the length of the bridge between abutments along the roadway centerline, taken as 492 ft.

As previously stated, the backwall is effective only in compression and requires more detailed modeling than the wingwall (Figure 3-23). Prior to gap closure, the deck transmits longitudinal forces to the abutment through the bearing pads. After closure, however, the

superstructure bears/pounds against the abutment seat, utilizing the full backwall pressure and thus rendering the longitudinal bearing pad resistance negligible. This behavior is modeled, as shown in the left parallel spring assembly in Figure 3-23, by using the *ElasticPPGap* material that is assigned to a *zeroLength* element. This behavioral model contains an elastic, compression-only gap element with a stiffness of 25,000 k/in., the original pounding stiffness discussed in Section 3.2.6. The bilinear pounding model proposed by Muthukumar (2003) was not considered for superstructure-abutment pounding interaction. This is due to the focus of that work being primarily on the pounding interaction between adjacent bridge frames (i.e. at the in-span hinges) and not between an abutment and the superstructure. This pounding spring is in parallel with a *zeroLength* element for the bearing pad. The backwall *ElasticPPGap* element contains a small compression gap (1.0×10^{-5} in.) to prevent activation under tension, and is activated in compression once the *ElasticPPGap* pounding element, which is in parallel with the bearing pad *zeroLength* element, is activated.

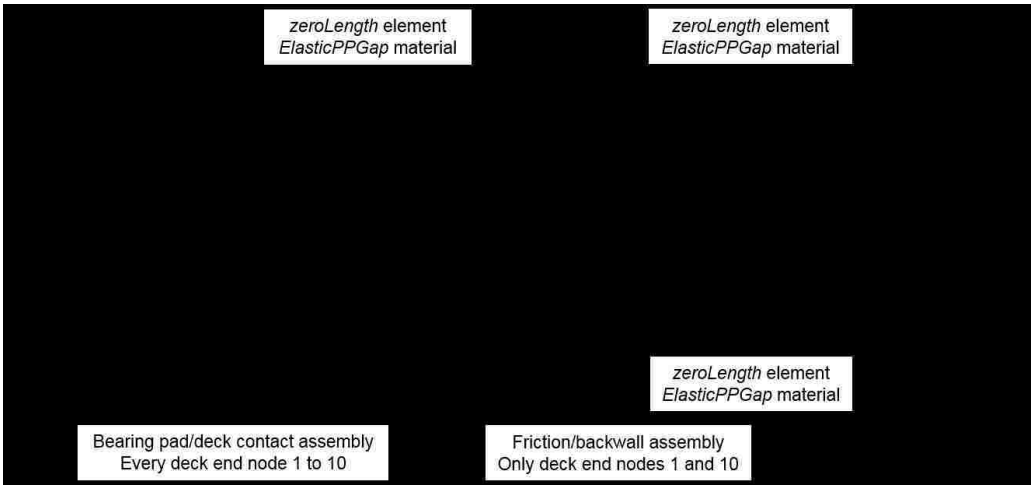

Figure 3-23 Modeling of longitudinal response at abutments (north end of Abutment B shown).

Some longitudinal tensile resistance can be expected through friction, and a simple model can consider this. In Figure 3-23, the right parallel spring assembly models the backwall and friction responses. Tensile forces are caused by the superstructure "pulling away" from the abutment seat and transmitting this force through the bearing pads. Additionally, the abutment participating mass (Section 3.4.2) can cause the abutment to slide away from the backfill soil. The static friction force is determined using a conservative static friction coefficient, $\mu_{s,Abut}$, of 0.4 for concrete on wet sand (i.e. recent rainfall). The normal force considered for tensile friction resistance is conservatively assumed as the minimum compressive force experienced at the abutment during the seismic analysis (if a positive axial force [i.e. uplift] is detected at the abutment, no friction force will be modeled). Half of this friction force defines the capacity of both *ElasticPPGap* springs at either end of the abutment rigid element. Both friction springs have a very small tension gap (1.0×10^{-5} in.) to prevent engagement in compression (backwall stiffness will govern the longitudinal compression response). The force-displacement response of the friction springs is similar to that of the wingwalls (Figure 3-22b), but with a very high stiffness.

At both abutment seats, there is only one bearing pad for each girder. Each abutment bearing pad is modeled in an identical manner to that described in Section 3.2.5. Abutment shear keys are modeled in the same way as those for the in-span hinges as discussed in Section 3.2.8, except that a *zeroLength* instead of a *twoNodeLink* element is used. Figure 3-24 shows the cross section of a superstructure end diaphragm. The gray nodes in this figure (Nodes 2, 4, 7 and 9, where Node 1 is the northernmost girder-diaphragm intersection node) show where the *zeroLength* elements that model the shear key will be attached. The abutment *zeroLength* elements for the shear keys will be attached between these nodes on the deck end diaphragm and identically placed nodes on the rigid *elasticBeamColumn* element for the abutment seat (Figure 3-12).

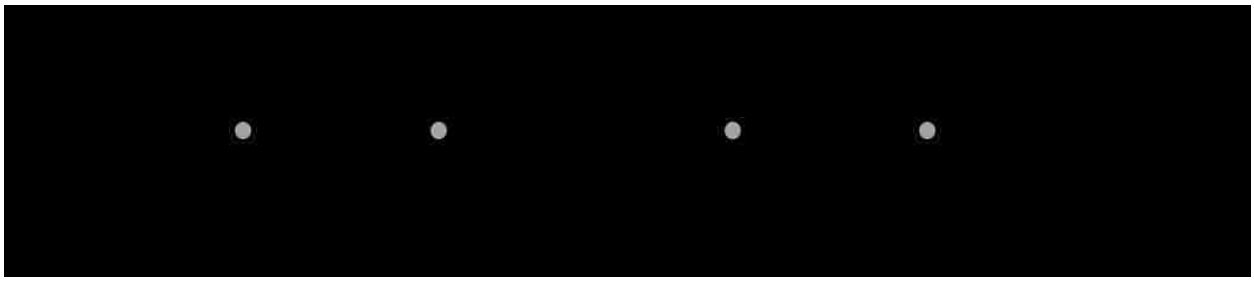

Figure 3-24 Location of shear keys at abutments in the model.

3.2.10 Modeling of Substructure

3.2.10.1 Substructure Modeling Breakdown

Since the columns of a bridge are subjected to a complex state of stress, the columns of Bridge G-953 need to be modeled with sufficient detail. A schematic of the column model considered in this study is shown in Figure 3-25. The modeling of a column involves three types of elements: (1) force-based beam-column (*forceBeamColumn*) elements defined with fiber sections to simulate the response under bending, shear, torsion, and axial force; (2) a *zeroLengthSection* element to simulate bond-slip between reinforcing bars and concrete at plastic hinge regi**o**ns; and (3) a *zeroLength* element with rigid shear and torsion stiffness in parallel with the bond slip element. In addition, rigid line elements are used at the column-cap beam joint.

Several *forceBeamColumn* elements, three for the columns of Pier 1 and two for Piers 2 to 5, are each assigned with various fiber sections. The shorter elements define the approximate plastic hinge length, taken as D_{col}, while the single longer element represents the portion of the column expected to remain mostly linear-elastic. Five integration points are considered for the plastic hinge elements and seven are used for the single longer element; this should ensure acceptable accuracy.

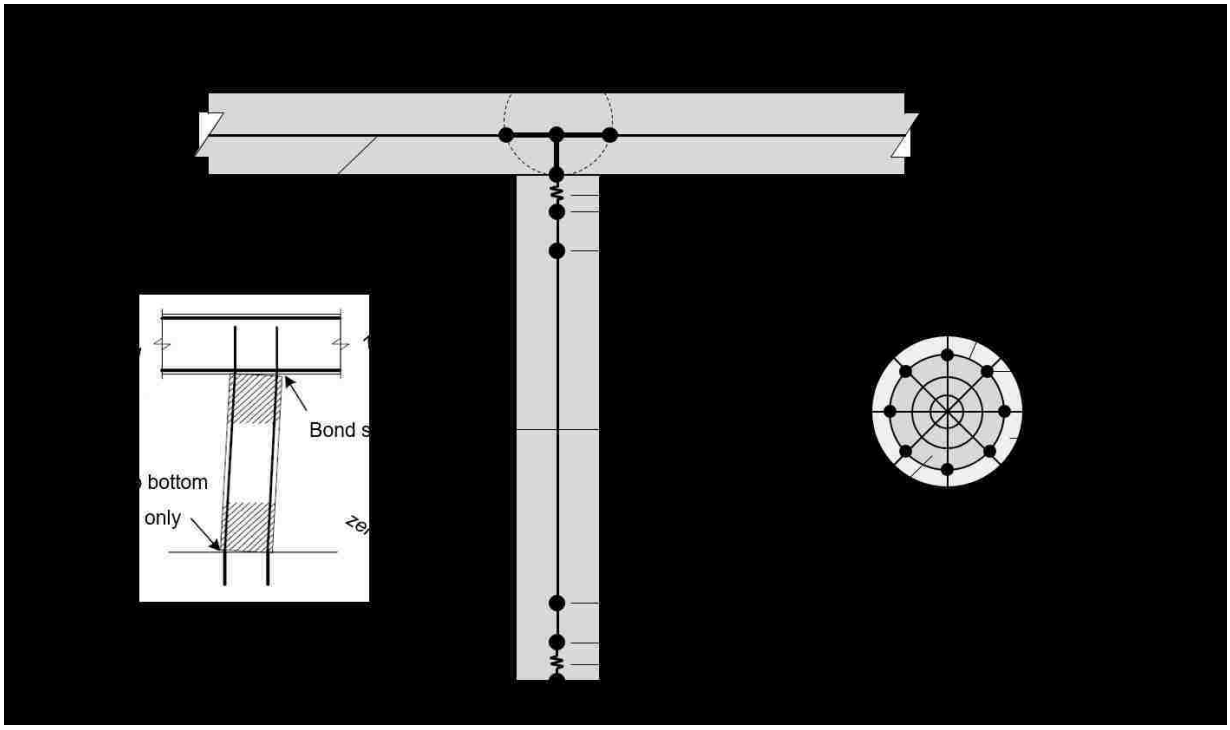

Figure 3-25 Schematic illustration of column modeling (pinned base for Piers 2-5).

Fiber sections are used to simulate the response of columns under axial load and bending moment. Using fiber sections can conveniently simulate the (1) spalling of cover, (2) confinement effects of transverse reinforcement on the concrete core, (3) flexural response of columns due to bi-directional lateral loading, (4) flexure-axial force interaction, and (5) spread of yielding in the column. As per recommendations by Berry and Eberhard (2008), the core concrete fibers are defined using the *patch circ* command with 20 circumferential (*numSubdivCirc*) and 10 radial (*numSubdivRad*) divisions, ensuring good accuracy and minimal computational effort (Section A-A in Figure 3-25 schematically visualizes dividing a section into fibers). The cover concrete is similarly modeled with the recommended 20 circumferential divisions but just one radial division per Berry and Eberhard (2008). The stress-strain relationships, discussed in Section 3.2.2 for unconfined and confined concrete, are applied to the cover and core concrete, respectively. The

mechanical properties of reinforcing steel discussed in Section 3.2.2 are defined for the longitudinal reinforcement and applied to the fiber sections using the *layer circ* command.

3.2.10.2 Shear and Torsion Aggregators for Columns

Fiber sections can only simulate the flexural and axial behavior of a column; therefore, the *section Aggregator* command is employed to define shear and torsion. For the elements assigned with fiber sections, shear and torsion are assumed as linear elastic. The shear modulus is taken as $G_{cc}A_{Col,g}/k$ (Berry and Eberhard 2008), where G_{cc} is the confined concrete shear modulus taken as $\gamma_G E_{cc}$, where E_{cc} is the confined concrete Young's modulus and $\gamma_G = 0.4$ as recommended by Park and Paulay (1975), $A_{Col,g}$ is the gross cross-sectional area of the column, and $k = 4/3$ for circular sections. The torsional modulus is calculated as $0.2G_{cc}J_{Col}$ (Aviram et al. 2008b), where J_{Col} is the polar moment of inertia of a column and the 0.2 factor accounts for the severe reduction in torsional stiffness for a cracked concrete column section.

3.2.10.3 Bond Slip/Strain Penetration of Columns

The bond between reinforcing bars and concrete at moment-resisting connections degrades under cyclic loading. Consequently, the overall flexural stiffness of a column is less than that with perfect bonding. Additionally, consideration of bond slip can prevent overestimation of section curvatures in the columns (Zhao and Sritharan 2007). Bond-slip is considered by adopting the model by Zhao and Sritharan (2007), which defines longitudinal bars using the *Bond_SP01* material. To apply this model, deformations of rebar due to bond-slip at yielding, S_y, and ultimate strength, S_u, need to be defined based on Equations 3-27 and 3-28, respectively. Additionally, the ultimate tensile strength of the rebar, $f_{s,u}$ (95 ksi per *Caltrans SDC* (2013), an initial strain hardening ratio, b_{BS} (0.3 to 0.5), and a pinching factor, R_{BS} (0.7 to 1.0), must also be specified. The parameters b_{BS} and R_{BS} are defined herein as 0.5 and 0.7, respectively. This *Bond_SP01* material is assigned to the steel fibers

in a column fiber section (*section Fiber*), which is then applied to the *zeroLengthSection* elements located at the moment-resisting connections for the columns (Figure 3-25), which are located at the top and bottom of Pier 1 columns but only at the tops of columns for Piers 2 to 5. Note that the rigid shear-torsion *zeroLength* elements, shown in Figure 3-25, constrain these *zeroLengthSection* elements in the shear and torsion degrees-of-freedom; this is due to the *zeroLengthSection* element only having axial and flexural stiffness.

$$S_y = 0.1\left[\frac{d_b}{4000}\cdot\frac{f_{s,y}}{\sqrt{f'_{cc}}}\cdot(2\alpha_{BS}+1)\right]^{1/\alpha_{BS}} + 0.013 \tag{3-27}$$

$$S_u = 35S_y \tag{3-28}$$

where d_b is the longitudinal bar diameter, $f_{s,y}$ is the yield strength of the longitudinal bars, f'_{cc} is the confined compressive strength of the concrete, and α_{BS} is a parameter used in the local bond-slip relation taken as 0.4 (CEB-FIP Model Code 1990).

3.2.10.4 Shear Failure of Columns by Force/Rotation-Based Effects

Figure 3-26 displays the possible shear failure modes for a column with an idealized force-displacement relationship. First, there is the case where the column reaches maximum shear strength, $V_{u,Force}$, before the column yields in flexure (Figure 3-26a). This is a brittle, force-based shear failure mode, with a low column drift at failure, $\Delta_{v,Force}$. Flexural yielding that prevents $V_{u,Force}$ from being reached is classified as a ductile, displacement-based shear failure, where the ultimate shear capacity, $V_{u,Disp}$, occurs at a much higher column drift, $\Delta_{v,Disp}$, and is defined by an ultimate total rotation across the plastic hinge zone, θ_f, rather than a limiting column drift (Elwood 2004, Elwood and Moehle 2008), $\Delta_{v,Disp}$, as shown in Figure 3-26b. Force-based shear failure will be discussed first. Both force-based and displacement-based shear failure are not explicitly modeled, and post-processing is required to determine if either failure is possible.

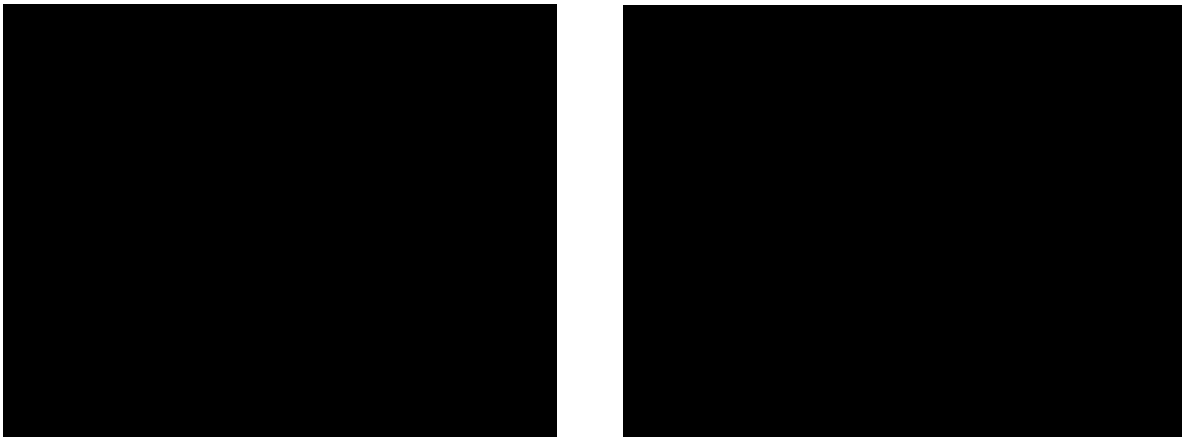

(a) Force-based (b) Displacement-based

Figure 3-26 Shear failure modes.

The constant load reversals of an earthquake significantly deteriorate the concrete component of shear strength, making the seismic shear strength of a section much lower than the shear capacity for a typical static loading case. Two methods for the calculation of $V_{u,Force}$ will be considered: AASHTO (2011) and Kowalsky and Priestley (2000).

The first force-based shear strength model considers that provided in the *AASHTO Guide Specifications for LRFD Seismic Bridge Design, 2nd Edition* (2011). This document will be referenced as AASHTO (2011) for the remainder of this document. The shear capacity is given as $V_{u,1} = V_{c,1} + V_{s,1}$, where "1" denotes the capacities determined by the AASHTO (2011) method, $V_{c,1}$ is the concrete contribution (Equations 3-29 to 3-31, $V_{c,1} = 0$ if the column is in tension), and $V_{s,1}$ is the steel component (Equation 3-32).

$$V_{c,1} = 0.8A_{Col,g}\nu_c \tag{3-29}$$

$$\nu_c = 0.032\alpha'\sqrt{f'_{cc}}\left(1 + \frac{P}{2A_g}\right) \leq min\left[0.11\sqrt{f'_{cc}} \;\; OR \;\; 0.047\alpha'\sqrt{f'_{cc}}\right] \tag{3-30}$$

$$\alpha' = \frac{f_s}{0.15} + 3.67 - \mu_D, \;\; where \;\; f_s = \frac{4A_{Hoop}f_{t,y}}{sD'} \leq 0.35 \tag{3-31}$$

$$V_{s,1} = \frac{\pi n A_{Hoop} f_{t,y} D'}{2s} \leq \; 0.2A_{Col,g}\sqrt{f'_{cc}} \tag{3-32}$$

where $A_{Col,g}$ is the gross cross-sectional area of the column, v_c is the concrete stress, α' is the concrete shear strength adjustment factor, P is the compressive axial load on the section, A_{Hoop} is the cross-sectional area of a transverse reinforcement hoop, $f_{t,y}$ is the yield strength of a hoop, s is the spacing of the hoops, D' is the diameter of the column core measured from the center of the hoop, and n is taken as 1 for a non-interlocking hoop section. The variable μ_D is equal to 2 for Seismic Design Category B, which was determined for Bridge G-953 using methods supplied in the AASHTO (2011) code.

The second force-based shear failure criterion was suggested by Kowalsky and Priestley (2000). This shear strength model is a revised version of the original model developed at the University of California, San Diego (Priestley et al. 1994) that can calculate the seismic shear strength for circular concrete columns with good accuracy. Additionally, Kowalsky and Priestley (2000) claimed a reduced spread in their results for predicted vs. actual shear strengths for various column sections as compared to other methods. The transverse steel contribution to shear strength is based on a crack that extends the width of the concrete core and mobilizes the transverse reinforcement, being the circular hoops in the case of Bridge G-953, in tension. In the compression zone, however, the crack is assumed closed and thus shear cannot be transferred across it by tension in the hoops. This creates a smaller steel shear strength contribution than traditional capacity equations. Available column shear strength suggested by Kowalsky and Priestley (2000) is given as $V_{u,2} = V_{c,2} + V_{s,2} + V_p$, where the subscript "2" denotes the capacities as determined by this

method. The individual shear strength components are concrete, $V_{c,2}$ (Equation 3-33), steel, $V_{s,2}$ (Equation 3-34), and axial load, V_p (Equation 3-35, $V_p = 0$ for axial tension).

$$V_{c,2} = \alpha\beta_{V2}\gamma\sqrt{f'_{cc}}(0.8A_{Col,g}) \tag{3-33}$$

$$V_{s,2} = \frac{\pi A_{Hoop} f_{t,y} \cot(\theta_{V2}) \times (D_{col} - c - cov)}{2s} \tag{3-34}$$

$$V_p = \frac{P(D_{col} - c)}{2L_{V2}}, P > 0 \quad OR \quad V_p = 0, \ P < 0 \ (axial\ tension) \tag{3-35}$$

where θ_{V2} is the angle of the shear failure crack with respect to the vertical axis of the column assumed as 30°, c is the depth of the compression zone, cov is the column clear cover given as 2 in., s is the center-to-center spacing of the transverse reinforcement given as 12 in, P is the axial load demand on the column (positive P is compression), L_{V2} is the length from the shear-critical section to the point of contraflexure on the column equal to half the column height for Pier 1 and the full column height for Piers 2 to 5, f'_{cc} is the compressive strength of the confined concrete core, and α, β_{V2}, and γ are parameters that account for the aspect ratio, longitudinal steel, and ductility of the column, respectively. Details can be found by referencing the paper by Kowalsky and Priestley (2000).

The second type of shear failure discussed is displacement-based shear failure. Leborgne and Ghannoum (2012) developed a model that compares the total rotation across the plastic hinge zone, θ, to an ultimate capacity, θ_f, given by Equation 3-36:

$$\theta < \theta_f = 0.027 - \frac{0.033P}{A_g f'_{cc}} - \frac{0.01s}{D'} \geq 0.006 \tag{3-36}$$

where θ_f is the plastic hinge rotation at which shear failure occurs and the 0.006 limit prevents shear failure from occurring prior to inelastic behavior.

Equation 3-37 is used in post-processing to determine if rotation-based shear failure is possible for Bridge G-953. The total hinge rotation was calculated using the difference in total rotation between the nodes that bound the plastic hinge zone, including the rotation caused by bond slip. According to Figure 3-25, the two considered nodes would be the outermost node of the *zeroLengthSection* element and the extreme end node of the *forceBeamColumn* plastic hinge zone element. If the calculated total hinge rotation exceeds θ_f in Equation 3-36 at any point during the ground motion, rotation-based shear failure is possible.

3.2.10.5 Torsional Capacity of Columns

Generally, pure torsion is not a problem, but can be significant when combined with other responses, such as flexure and shear, where twist in column sections can degrade other capacities. Only the columns of Pier 1 are subject to torsion since the other bents are pinned at their bases with hinges and cannot resist torsional loadings. Since the fiber sections only monitor the flexure-axial force interaction, ACI 318-14 (2014) (Equation 3-37) determines the pure torsional capacity of the columns. Given the large spacing and small size of the transverse reinforcement (No. 5 at 12 in.), torsion could be a possible failure mode since torsional resistance mainly depends on the size and spacing of the transverse reinforcement. Additionally, a simple interaction equation for the effects of combined torsion and shear is considered (Equation 3-38). Failure in torsion is not explicitly modeled, and post-processing is used to determine the likelihood of any torsional failure.

$$T_u = \frac{2A_o A_{Hoop} f_{t,y} \cot\theta_T}{s} \tag{3-37}$$

$$\frac{T}{T_u} + \frac{V}{V_u} \leq 1.0 \tag{3-38}$$

where $A_o = 0.85A_{oh}$ and A_{oh} is the column cross-sectional area enclosed by the hoops, A_{Hoop} is the area of torsional reinforcement taken as the area of one hoop, θ_T is the crack angle for torsion given as 45° for nonprestressed concrete, and V and T are the shear and torsion demand on the section, respectively.

3.2.10.6 Axial Strength of Columns

Post-processing can determine the potential for axial failure in the columns, considering both the normal capacity and residual strength following a shear failure. Normally, pure axial failure is not a problem for bridges; the columns are usually only loaded to 10-20% of their regular capacity, that is, the capacity calculated assuming no shear failure. Normal compressive axial capacity of the columns, P_n, is calculated by Equation 3-39 (ACI 318-14). Residual axial strength can be assumed as $0.1P_n$ (Flores 2004).

$$P_n = 0.85f'_{cc}\left(A_{Col,g} - A_s\right) + f_{s,y}A_s \tag{3-39}$$

where A_s and $f_{s,y}$ are the total area and yield stress of longitudinal reinforcement, respectively.

3.3 GRAVITY LOADS

3.3.1 Dead Load

The dead loads acting on the superstructure are defined as uniformly distributed line loads (Figure 3-27) determined from the self-weight of the deck and asphalt pavement. Volumetric unit weights of asphalt and concrete are multiplied by the cross-sectional area of the respective material to calculate a distributed load. This distributed load is then applied to the various girders and diaphragms on the superstructure. The different line thicknesses for the distributed loads shown in Figure 3-27 indicate which girder it is applied to, which are shaded differently (girder 1 is the northernmost). The self-weight of bearing pads, restrainers, shear keys, elastomeric lining at in-span-hinges and abutment expansion joints, pedestrian rails, bolts, and any other secondary

component was ignored due to simplicity and negligible contribution. The 4 in. fillets of the box girder deck contribute to the dead line loads applied on the longitudinal elements. The dead loads applied on the transverse elements are determined only from the self-weight of the webs of the diaphragms. This is because the dead load contribution from the flanges is already accounted for in the dead loads of the longitudinal girders. The dead loads for the columns are determined from their self-weight. However, only half of the total dead load of a column is assumed to act as a concentrated load at its top node, while the other half goes into the ground and is not modeled.

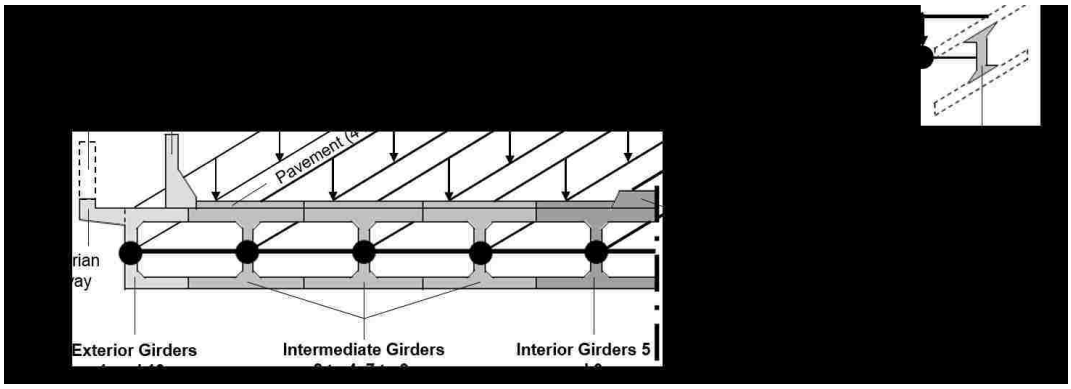

Figure 3-27 Dead load distribution on superstructure girders.

3.3.2 Live Load

Based on the recommendations by Wibowo et al. (2012), 50% of design live loads are considered. From the recommendations by the *NDOT Structures Manual* (2008) and O'Connor and Shaw (2000), the design live loads of a bridge consist of a uniform lane load representing a train of HS 20-35 trucks (Figure 3-28) as well as a standard HS 20-44 concentrated truck loading. However, for the sake of simplicity and due to the relatively-negligible weight compared to the bridge dead load, the HS 20-44 truck live load is ignored. The HS 20-35 lane load (Figure 3-28) of 0.64 k/ft/ft-of-lane is considered to act on a lane width of 10 ft. Bridge G-953 has four traffic

lanes and all but the exterior longitudinal girders (northernmost/southernmost) are assumed to equally support the live load. Thus, the live area lane loading can be converted to a distributed load. Additionally, the 85 psf pedestrian load, which is applied to the 5 ft wide walkway overhangs, is converted into a uniformly distributed load and applied on only the exterior longitudinal girders (girders 1 and 10).

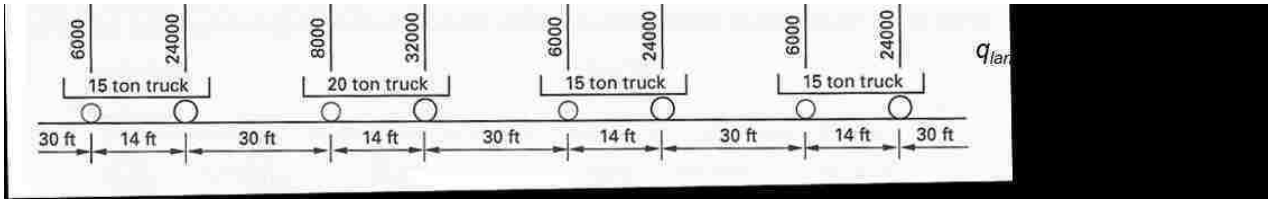

Figure 3-28 AASHTO HS 20-35 truck train lane loading (AASHTO 1996, 1998).

3.4 MASS

3.4.1 Superstructure and Substructure

Lumped masses are defined at the nodes on the primary superstructure and column elements. Since the mass is distributed over the full deck width, there is no need to define rotational mass (Dowell 2004). The nodal masses are specified only in the global X and Y translational DOF. Only the dead loads, which are permanently attached to the structure, are considered effective in defining the lumped masses at the nodes of the bridge deck. For each main superstructure node, a lumped mass is determined from the distributed dead load, calculated in Section 3.3.1, applied to its respective tributary width. The total dead weight on this tributary width is then converted to a lumped mass. The nodal mass of each column is calculated directly from the concentrated dead load for its self-weight (half goes into ground and is not modeled) and applied to the respective column top node.

3.4.2 Abutments

The participating mass of the abutments, associated with the structural concrete, M_{Conc}, and a trapezoidal portion of the embankment engaged by the backwall, M_{Soil}, is considered for use in the spring abutment model proposed by Aviram et al. (2008a). The total lumped mass for each abutment ($M_{Abut} = M_{Conc} + M_{Soil}$), having only global X- and Y-axis components, is evenly distributed among the ten nodes of the rigid abutment element shown in Figure 3-12. The total mass of concrete for an abutment includes the masses of the seat, wingwalls, backwall, and footing. A trapezoidal volume of backfill soil (bold outline in Figure 3-29) having a height equal to that of the backwall, h_{BW}, a length equal to the critical length L_c (Equation 3-25), a top width equal to b_{BW}, and a bottom width determined using the given 2-to-1 slope from the Original Drawings (Appendix A), $b_{Soil,Bot}$, defines the embankment soil contribution to the participating mass of the abutment. Note that the wingwalls have been omitted from Figure 3-29 for clarity. The density of the assumed "dense soil" embankment, γ_{Soil}, is taken as 100 lb/ft^3 (Das 2006). Table 3-8 summarizes the gross mass of each bridge segment and the abutments. As can be seen in Table 3-8, the abutment participating masses are similar to the mass of the largest deck segment, S3 (In-Span Hinge 2 to In-Span Hinge 3).

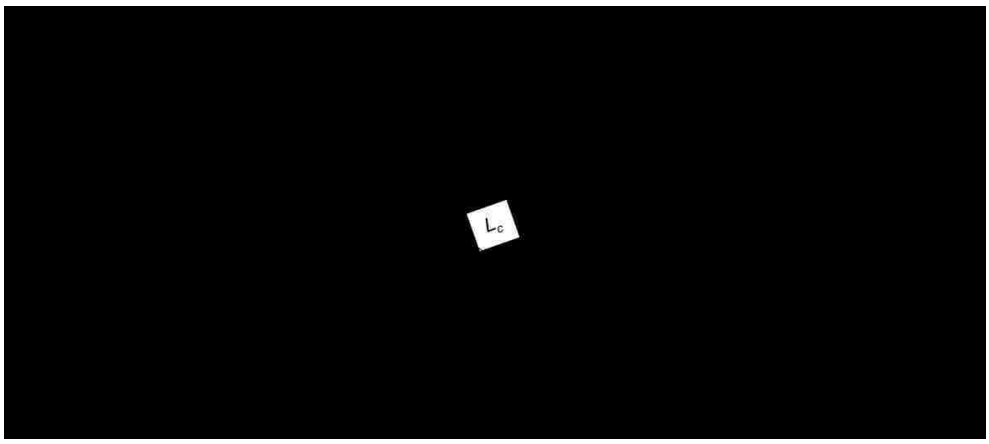

Figure 3-29 Backfill for abutment participating mass (wingwalls not shown, M_{Soil} in bold outline).

Table 3-8 Bridge section masses

Section	Mass (k-in./s^2)
Abutment A	7.98
Abutment A to Joint 1 (S1)	1.34
In-Span Hinge 1 to In-Span Hinge 2 (S2)	1.46
In-Span Hinge 2 to In-Span Hinge 3 (S3)	8.74
In-Span Hinge 3 to In-Span Hinge 4 (S4)	5.84
In-Span Hinge 4 to Abutment B (S5)	3.00
Abutment B	9.91
Total	38.3

3.5 DAMPING

Rayleigh damping is considered to define the damping property of the bridge system. As formulated in Equation 3-40, the damping matrix, $\boldsymbol{C}$, is a combination of stiffness- and mass-proportional damping.

$$\boldsymbol{C} = a_0\boldsymbol{M} + a_1\boldsymbol{K}_{Current} \tag{3-40}$$

where a_0 and a_1 are two constant parameters, $\boldsymbol{M}$ is the mass matrix, and $\boldsymbol{K}_{Current}$ is the stiffness matrix that considers stiffness degradation of a structure under seismic loading in real time.

The *rayleigh* and *region* commands are used to apply Rayleigh damping to all primary structural elements (all deck girders and columns). However, damping is not defined for the elements simulating local behaviors such as impact, bearing pads, abutment backwall/wingwall, etc. due to convergence problems and to avoid possible overdamping of the system. The constants a_0, for the mass matrix (Equation 3-41), and a_1, for the stiffness matrix (Equation 3-42), are determined from the natural frequencies of two different vibration modes, ω_i and ω_j, and an assumed damping ratio, ζ, of 5% (typical value for nonprestressed concrete structures).

$$a_0 = \frac{2\zeta\omega_i\omega_j}{\omega_i + \omega_j} \tag{3-41}$$

$$a_1 = \frac{2\zeta}{\omega_i + \omega_j} \tag{3-42}$$

According to Chopra (2007), the modes used to determine ω_i and ω_j should be chosen to ensure all modes that significantly affect the dynamic response are appropriately damped. Qin and Lou (2000) investigated different methods for defining damping and chose the first five modes of their studied bridge. Based on recommendations by Chopra (2007), the first and fourth modes are chosen to create a roughly equal damping ratio for the first five modes. Therefore, ω_i represents the first mode frequency and ω_j indicates the fourth mode frequency. Eigen value analysis, using the *eigen* command, is performed on Bridge G-953 to determine the bridge frequencies for the first and fourth modes. According to Charney (2008), the Rayleigh method can lead to over-damping for concrete structures due to non-uniform flexural deformation in columns, such as that in the plastic hinge zones. To overcome this problem, Charney (2008) recommended a reduction factor of $\sqrt{(2)}/2$ which is applied to ω_i and ω_j.

3.6 EARTHQUAKE LOAD

3.6.1 Ground Motion Records

Nevada is a highly seismic state, where the USGS (usgs.gov) predicts a 20-25% probability of an earthquake of at least magnitude 6 in the next 100 years (Lamichhane et al. 2014). The USGS, based on its national seismic hazard model (NSHM), calculates a PGA of 0.19g for a probability of 2% in 50 years (Lamichhane et al. 2014), the maximum considered earthquake (MCE). However, Lamichhane et al. (2014) investigated seismic risk in the Las Vegas Valley (LVV) and found that the seismic risk, as determined by USGS, may be underestimated. This conclusion was reached by using five different ground motion prediction equations (GMPEs) while considering additional

faults, including regional faults and several faults not deemed tectonic by the USGS, and a higher slip rate for the primary Eglington fault (0.6 mm/yr Lamichhane et al. [2014] vs. 0.1 mm/yr USGS). The comparison in PGA between the USGS and Lamichhane et al. (2014), for the MCE, can be seen in Figure 3-30. The USGS (Figure 3-30a) expects a PGA in the LVV of about 0.2-0.3g, while Lamichhane et al. (2014, Figure 3-30b) predicts the PGA near Bridge G-953 to be 0.35-0.45g, with a maximum of 0.52g in the north-central LVV. Lamichhane et al. (2014) stressed that their findings are not for design due to uncertainties, but more so to spur further investigation of the fault systems in determining the most accurate level of seismic risk in the LVV. According to Lamichhane et al. (2014), the USGS cautiously omitted several potential seismic contributions due to uncertainty and a lack of data. The analysis of Bridge G-953 under this new seismic data by Lamichhane et al. (2014) should further stress the importance of further studies.

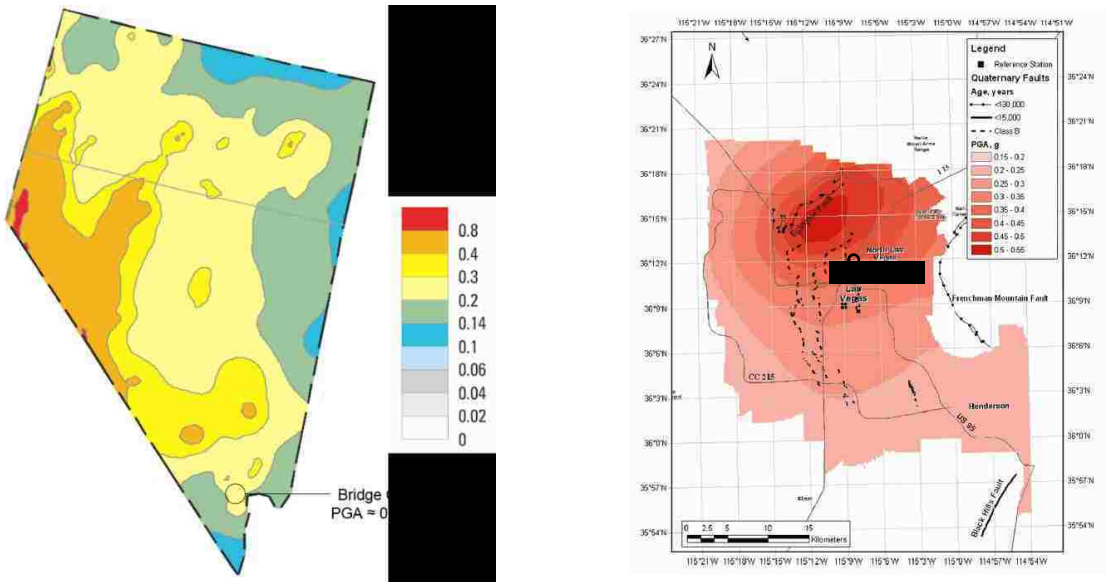

(a) USGS (USGS.gov) (b) Lamichhane et al. (2014)

Figure 3-30 Comparison of seismic hazard for the state of Nevada and Las Vegas Valley.

To reinforce their findings, a suite of 7 synthetic, site-specific ground motions for Bridge G-953 were developed by Lamichhane et al. (2014). A one-dimensional column of soil was used to project the bedrock motions to the surface. Depending on the properties of the soil and other factors, the ground motion intensity at the surface may be increased (amplification) or decreased (damping) from the ground motion at bedrock level. It was found that amplification of the bedrock ground motions occurred when projected to the surface location of Bridge G-953.

While running an extensive suite of ground motions is a typical analysis approach, it is desirable to find a robust method that can quickly determine seismic demands on a structure. Therefore, an additional ground motion, which is a single, spectrum-matched record, titled "Ground Motion RSP" for this paper, has been included. This ground motion is developed using the spectrum-matching approach by Hancock et al. (2006) which is implemented in the program *RspMatch 2005* (Ordóñez, 2012). Hancock et al. (2006) found that adding wavelets to an original "seed" ground motion record can provide a close match to the frequency and phasing of the smooth target spectrum. If effective, it is a robust method for obtaining the inelastic seismic effects on a structure. However, modifications of the seed record can cause undesirable effects, including altering the frequency content and phase.

When seven or more ground motions are selected for analysis, ASCE/SEI 7-10 (2010) specifies that the average of the peak responses from each ground motion can be used to obtain seismic demands. This average will be referenced as "Avg 1-7", that is, the average response of ground motions 1 through 7, for the remainder of this document. Results from Ground Motion RSP, now referenced as "RSP" for the remainder of this document, is not included in calculating the average response but is compared with "Avg 1-7" to see if RSP produces similar values. If the comparison is similar, the spectrum-matched record will be considered a quick, effective analysis.

Figure 3-31 plots the seven site-specific ground motion records (GM1 to GM7) for Bridge G-953 along with the spectrum-matched *RSP* record. Table 3-9 lists important values of each record, such as the PGA, time step (Δt), and duration.

Table 3-9 Properties of considered ground motions

Ground Motion	1	2	3	4	5	6	7	RSP
Max (g)	0.470	0.645	0.762	0.684	0.440	0.536	0.482	0.479
Min (g)	-0.662	-0.655	-0.513	-0.509	-0.601	-0.510	-0.602	-0.630
Duration (s)	25.98	39.975	22.32	21.24	39.03	29.94	39.93	25.98
Δt (s)	0.005	0.005	0.01	0.005	0.005	0.005	0.005	0.005
Data Points	5196	2232	2232	4248	7806	5988	7935	5196

3.6.2 Application of Ground Motions to Bridge G-953

Since a ground motion can act in any direction, several application directions, referred to as "seismic loadings" for the remainder of this document, are necessary in order to obtain the critical demand for every type of structural response (torsion, displacement, shear, etc.). For simplicity and to provide a general envelope of responses, the *Caltrans SDC* (2013) recommends four seismic loadings along the principal horizontal axes of the bridge. As previously mentioned, the global X-axis is specified by a line connecting the centers of the abutments (intersection of the inside edge of the abutment with the centerline of Carey Avenue) in the horizontal plane, while the global Y-axis is orthogonal to it.

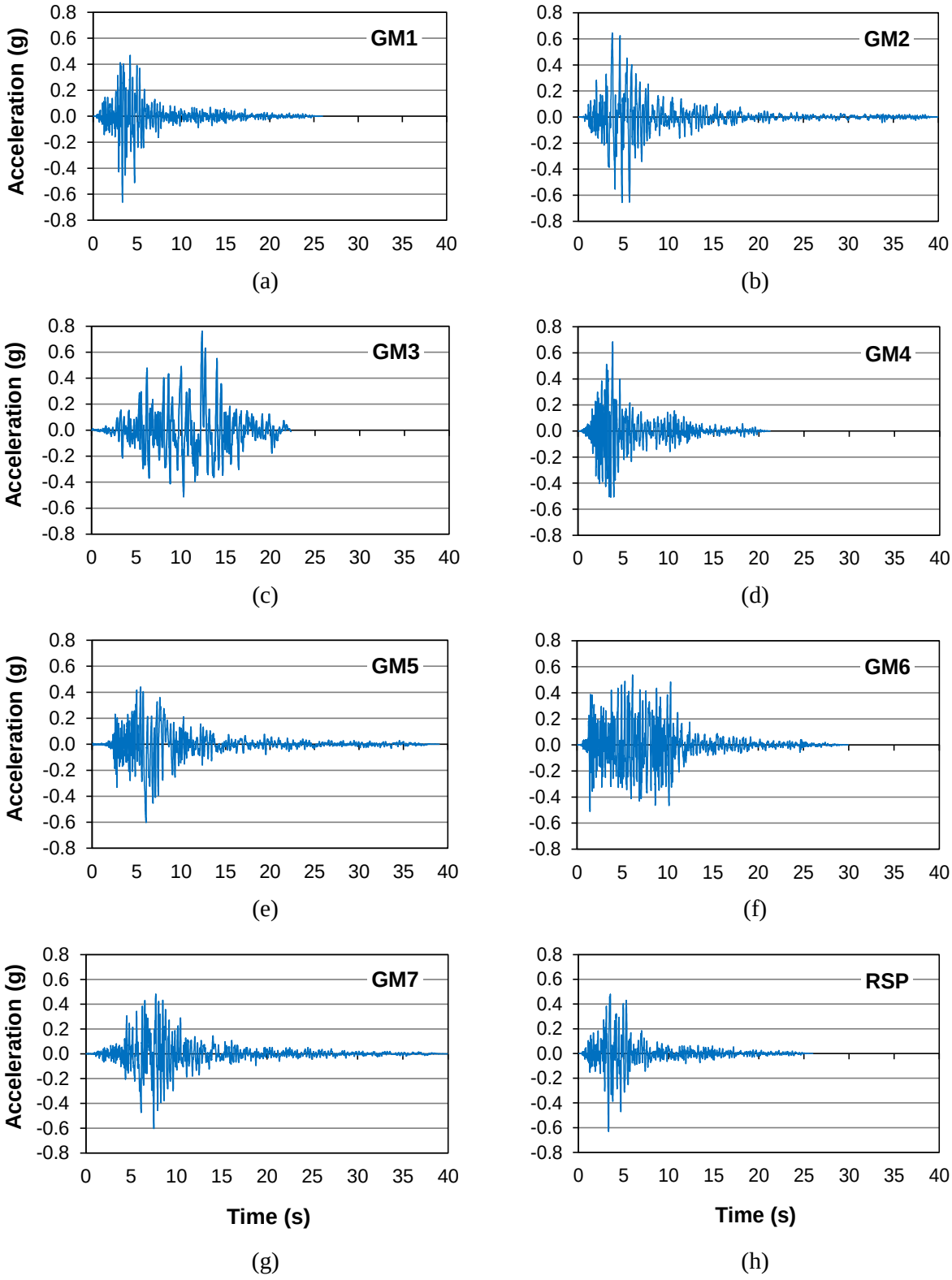

Figure 3-31 Ground motion time histories.

The first two seismic loadings are along the pure global X-axis (Figure 3-32a) and global Y-axis (Figure 3-32c). The other two will be applied bidirectionally, where the ground motion is fully applied along one horizontal global axis but scaled by a factor of 0.3 when applied simultaneously along the other axis. Thus, 100% X-30% Y in the X-Y axes (Figure 3-32b) means the full ground motion is applied along the global-X axis while the global-Y axis is only loaded with the same ground motion scaled by a factor of 0.3. Switching this loading gives the 100% Y-30% X application (Figure 3-32d). These loadings will be references as "100X-30Y" and "100Y-30X" for the remainder of this document. Bidirectional seismic loadings can be critical for columns, causing torsional effects and biaxial bending. The ground motion can be visualized as exciting the center-of-mass of each bridge segment in the global-X ($\ddot{u}_{g,X}$) and global-Y ($\ddot{u}_{g,Y}$) components, illustrated in Figure 3-32. The dashed outlines show the expected translational movement of the bridge under each seismic loading. Additionally, the approximate location of the center of mass is shown for each bridge segment and the magnitude is relatively scaled.

The *Caltrans SDC* (2013) analysis approach of the four seismic loadings in Figure 3-32 should provide a good envelope of responses. However, for the sake of completeness, several more seismic loadings were investigated. To reduce postprocessing, only two seismic loadings were chosen to generate the final analysis results. It was desired that both a longitudinal and transverse bridge loading were chosen in order to examine the critical responses along both global bridge axes. The bidirectional loadings, 100X-30Y and 100Y-30X, were generally more critical than the pure global-X, global-Y, and other bidirectional seismic loadings and thus will be used in the analysis.

(a) Pure longitudinal 100% X

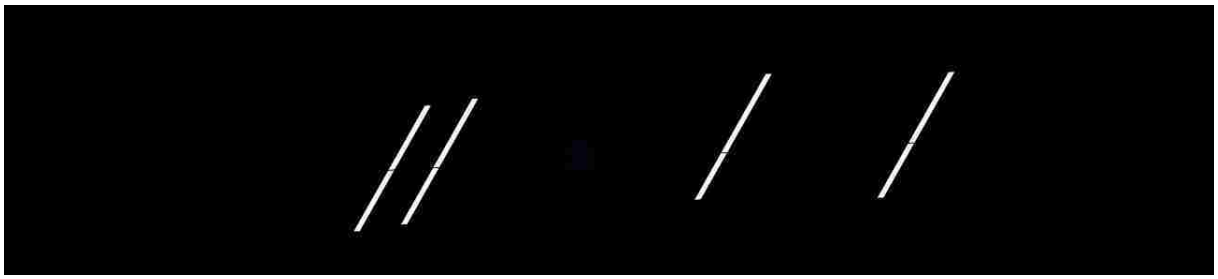

(b) Longitudinal 100% X – 30% Y

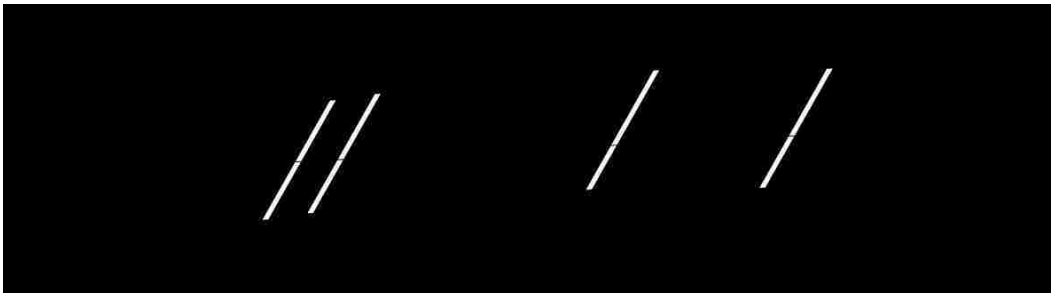

(c) Pure transverse 100% Y

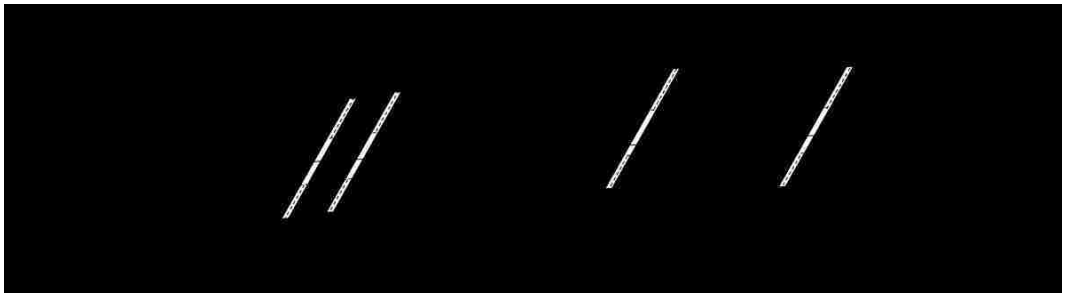

(d) Transverse 100% Y – 30% X

Figure 3-32 Seismic loadings recommended by *2013 Caltrans SDC*.

3.6.3 Settings for Running the Nonlinear Time History Analysis

To apply ground motions in OpenSEES (McKenna et al. 2010), the ground motion file must first be sourced into the *accelSeries* command and then implemented with the *UniformExcitation* command. The gravity load, equal to full dead and half live load, is applied and held constant for the duration of the nonlinear dynamic time-history analysis.

Each ground motion is applied for the full duration of the record, plus a few extra seconds to check residual post-earthquake values (i.e. will the structure re-center or are inelastic strains present?). Analysis commands utilized are the *UmfPack* system solver with *lvalueFact* of 15, *Transformation* constraints (typical for transient analysis), *RCM* numberer, a *Hilber-Hughes-Taylor (HHT) integrator* with α_{HHT} = 0.67 (Aviram et al. 2008b) for the transient analysis, and various iterative solvers used in a loop to ensure analysis convergence.

Three analyses of the two governing seismic loadings (100X-30Y and 100Y-30X) are ran for each ground motion record. The first is to determine the extent of superstructure cracking (Equation 3-7). The second analysis determines the amount of deck penetration at the in-span hinges in order to create a bilinear pounding spring from the initial linear model (Section 3.2.6). The third and final analysis creates the final, recorded responses for the bridge calibrated for superstructure cracking and nonlinear pounding.

CHAPTER 4

ANALYSIS RESULTS

4.1 DISPLACEMENT RESPONSE

4.1.1 Drift at the Top of Substructure Columns

Displacement response is one of the primary indicators of the seismic behavior of a structure. The analysis results indicate that the 100X-30Y seismic loading creates the maximum drift demands in the longitudinal direction (global-X), while 100Y-30X governs in the transverse direction (global-Y). The seismic responses of Bridge G-953 presented in this section include (1) lateral displacement and drift at the top of columns, and (2) the lateral displacement and in-plane rotation of the deck segments of the superstructure.

Figures 4-1 through 4-6 display the global-X/Y drift ratio demand for the first (northernmost) column of Piers 1, 3, and 5. The results for Piers 2 and 4 are omitted in most figures and tables in Chapter 4 for brevity; the response from Piers 1, 3, and 5 provide a representative envelope of responses for Bridge G-953. The drift plots are scaled differently for clarity. The most significant finding is the large drift demand caused by Ground Motions 3 and 5, where the maximum drift is many times higher than that due to other records. The average peak column drift for Ground Motions 1, 3, 4, 6, 7, and RSP is about 1-3%, but is as high as 16-23% for Ground Motions 3 and 5. Given that the analysis approach is the same for all ground motions, the magnitude and frequency component of the ground motions may have a significant effect.

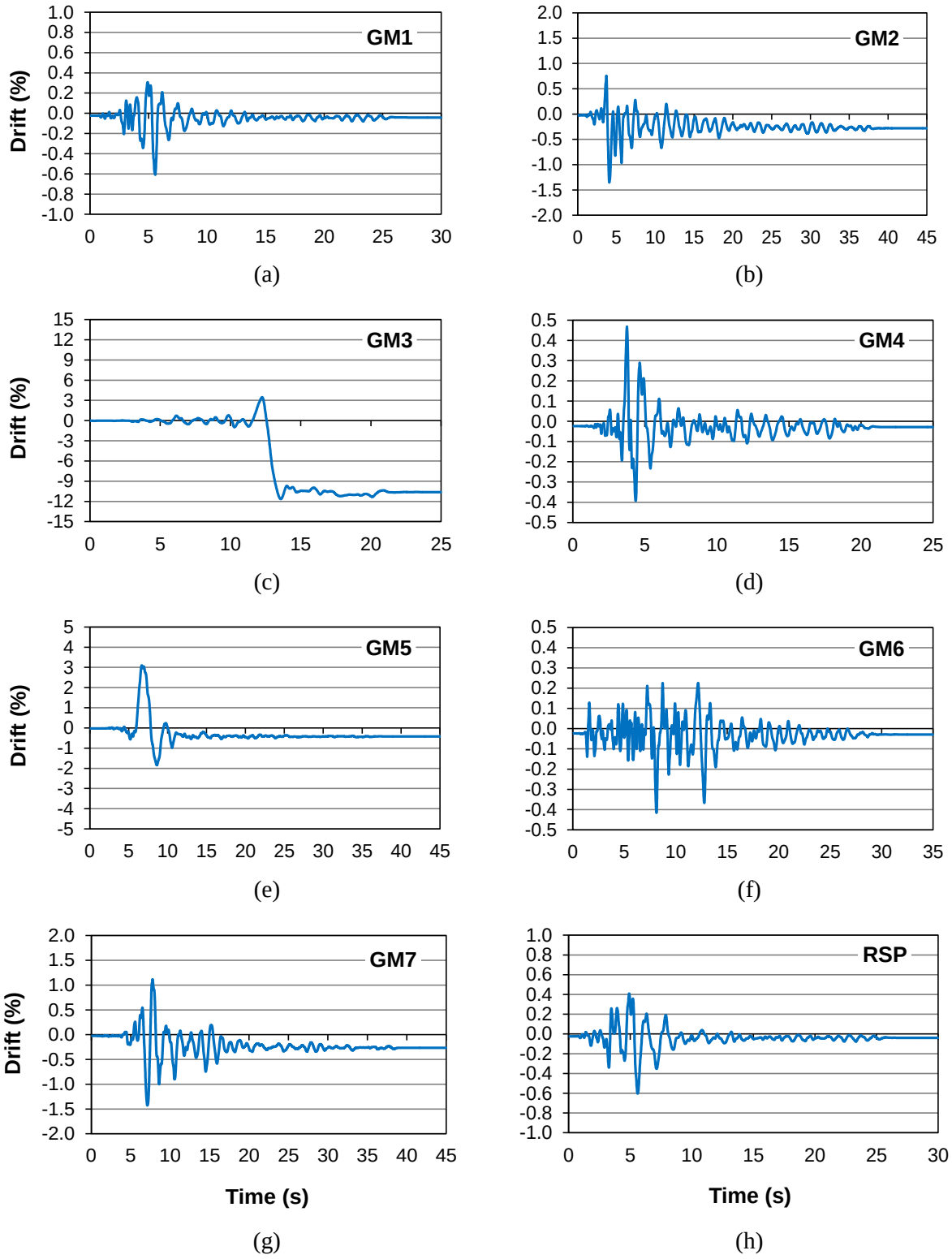

Figure 4-1 Time history of global-X drift ratio demand at Pier 1 (100X-30Y).

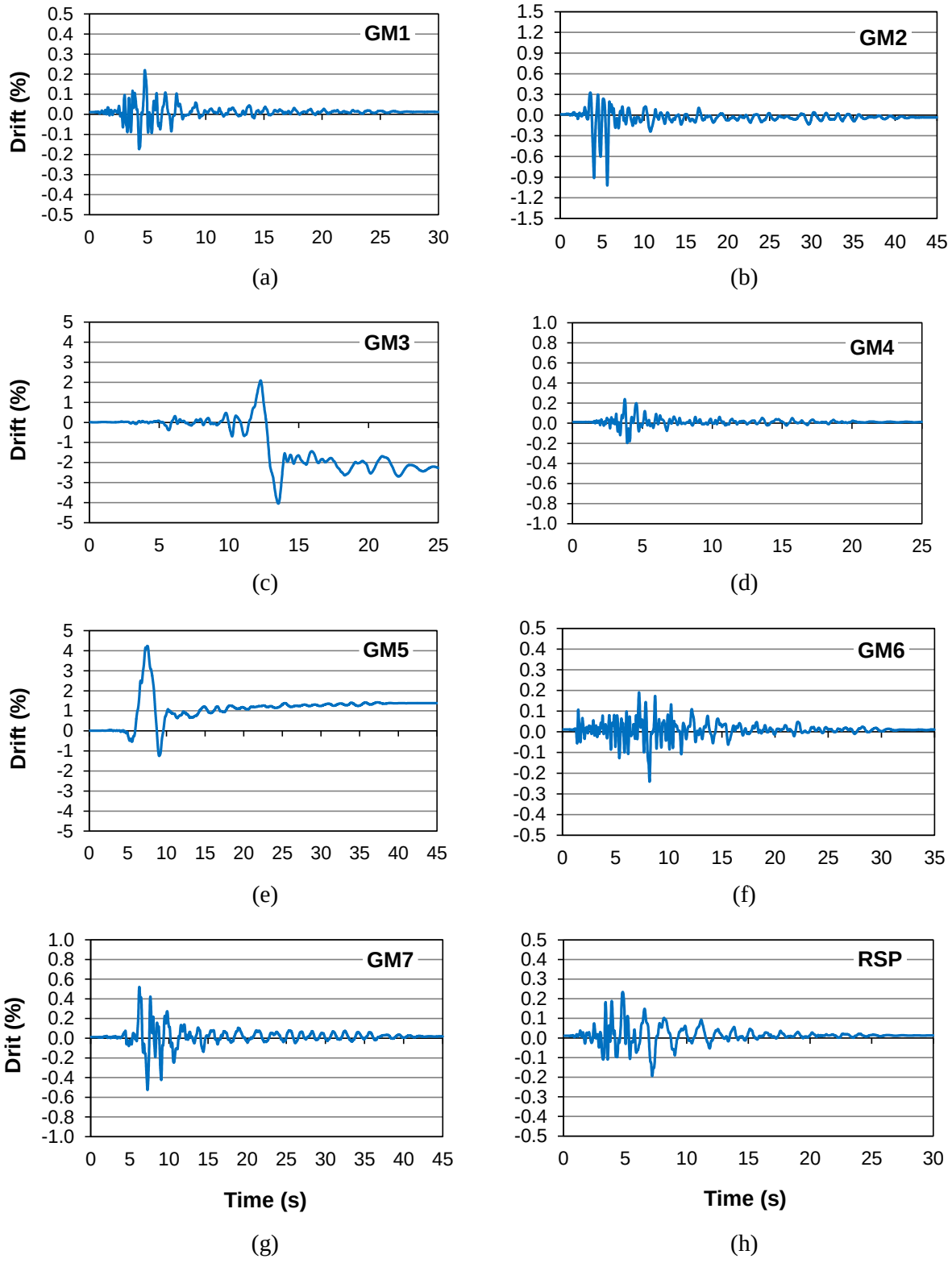

Figure 4-2 Time history of global-Y drift ratio demand at Pier 1 (100Y-30X).

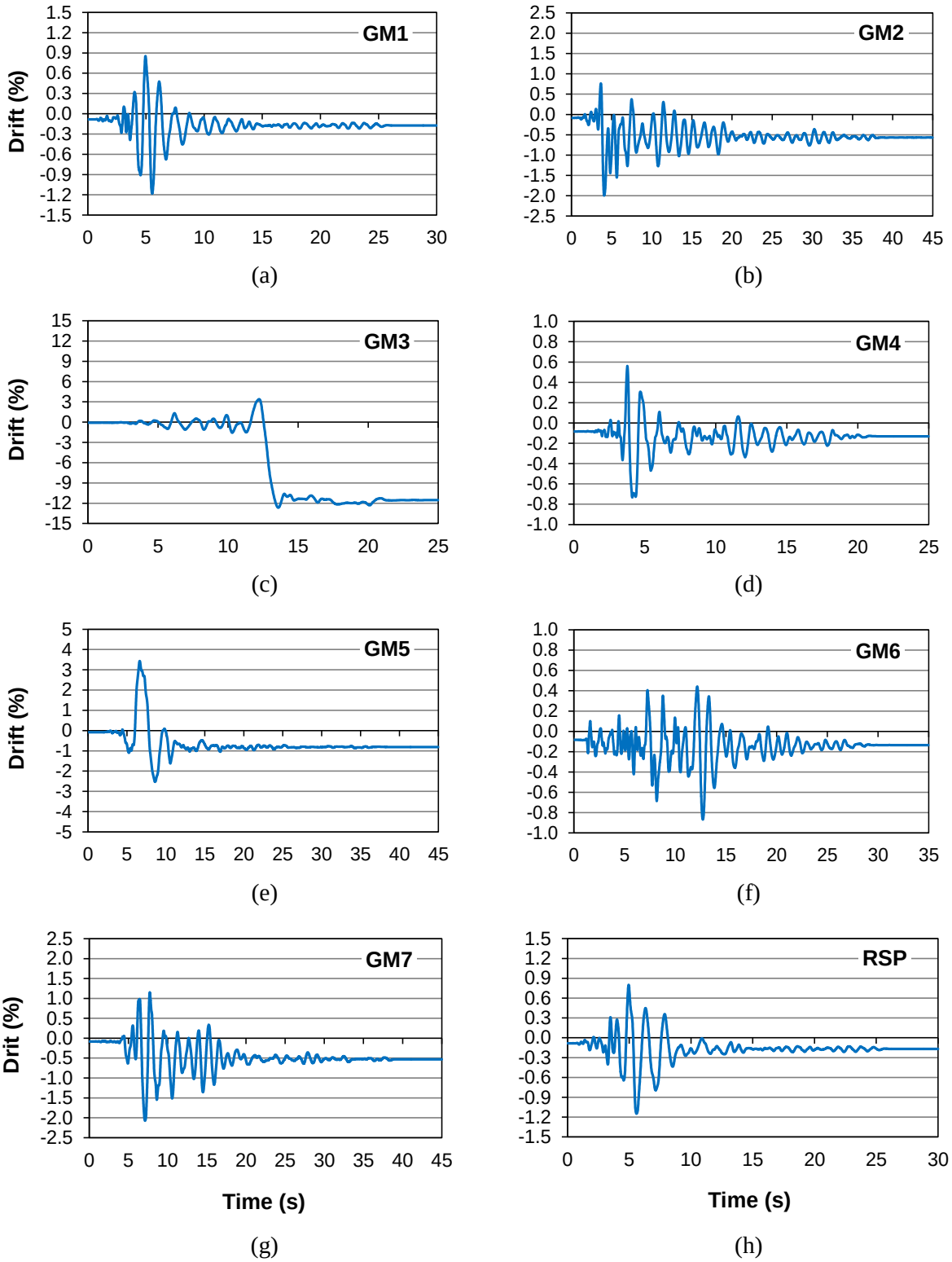

Figure 4-3 Time history of global-X drift ratio demand at Pier 3 (100X-30Y).

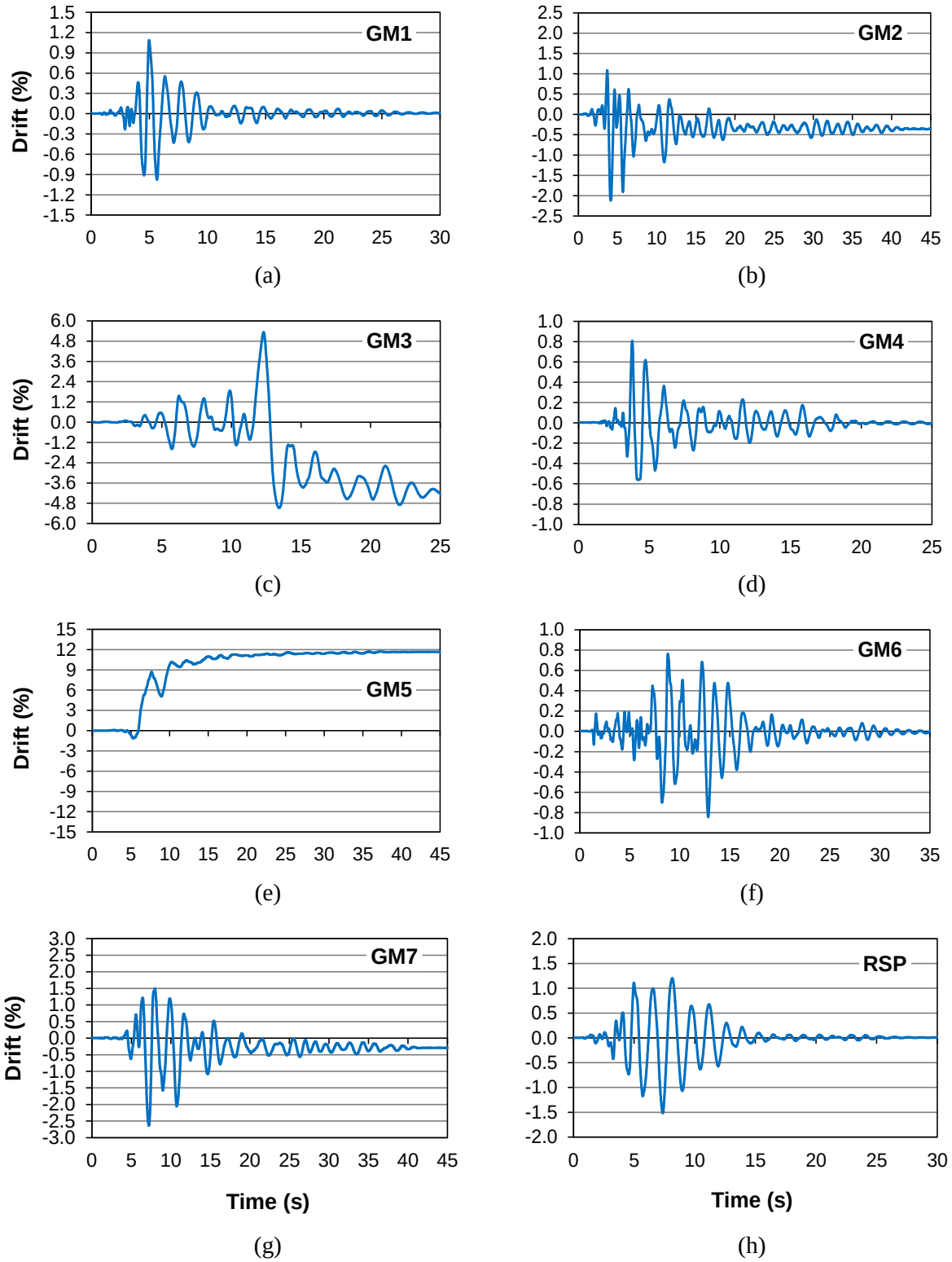

Figure 4-4 Time history of global-Y drift ratio demand at Pier 3 (100Y-30X).

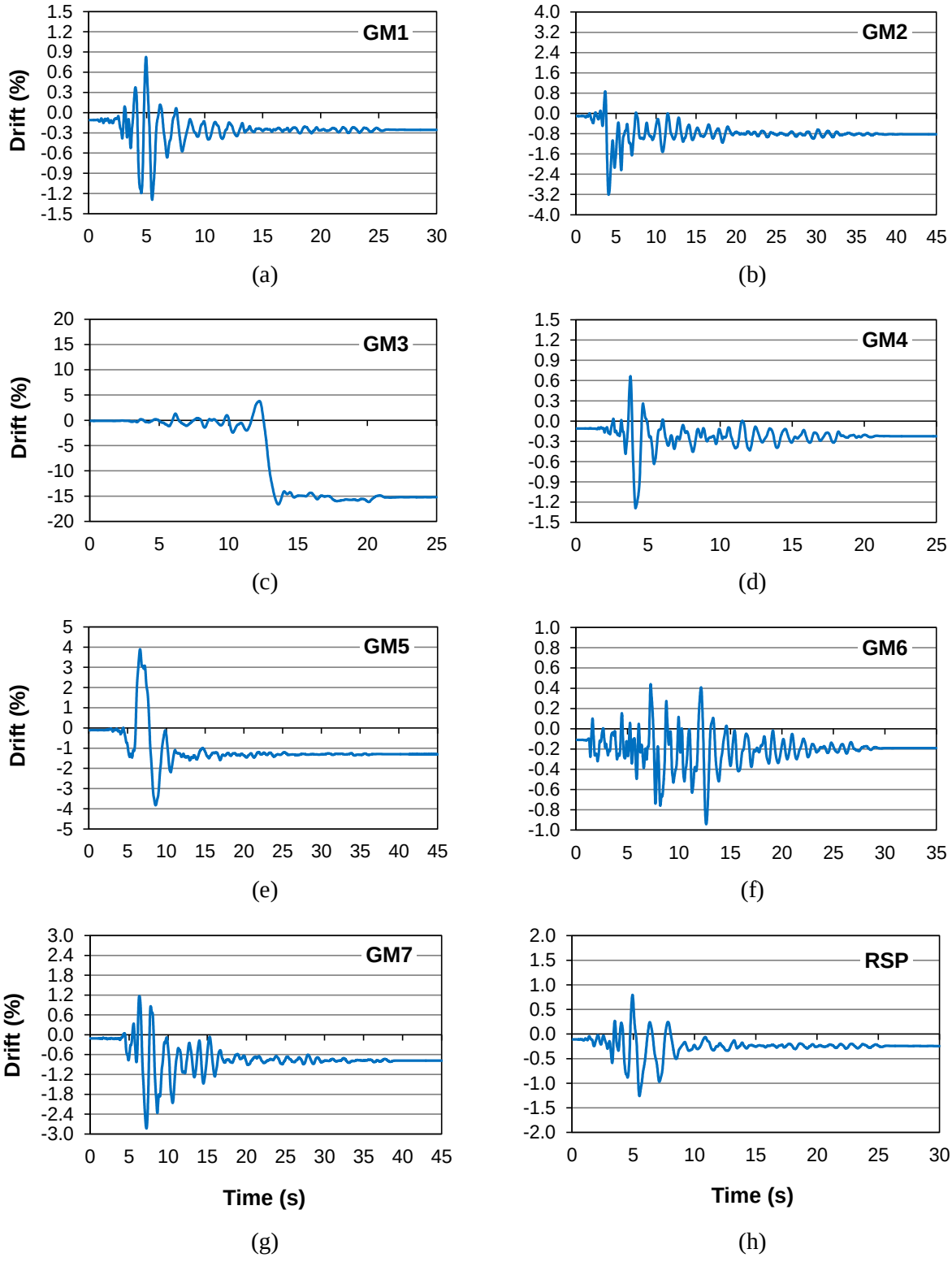

Figure 4-5 Time history of global-X drift ratio demand at Pier 5 (100X-30Y).

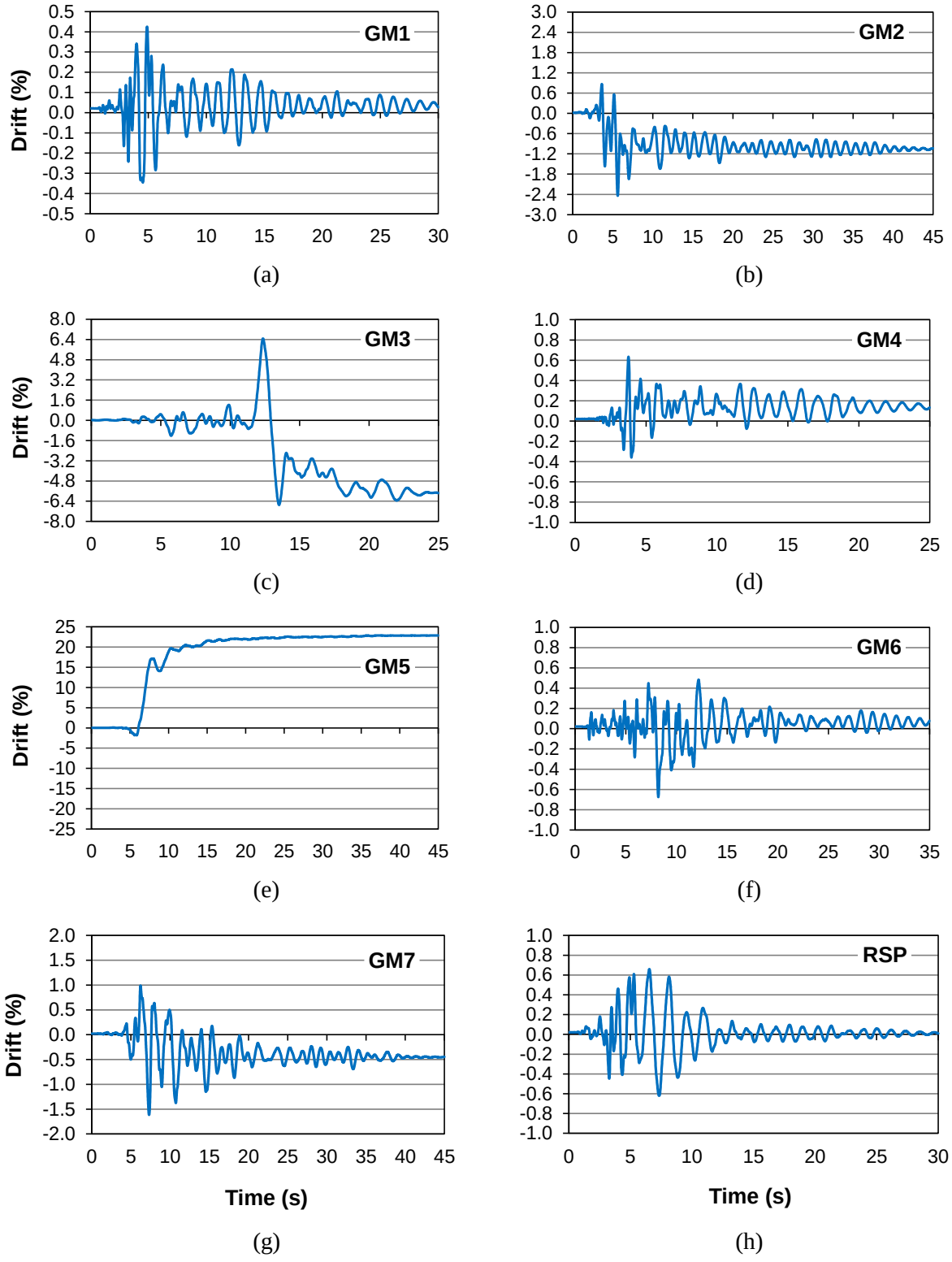

Figure 4-6 Time history of global-Y drift ratio demand at Pier 5 (100Y-30X).

Table 4-1 Column top resultant displacement demand (in.)

Pier	Seismic Loading	GM1	GM2	GM3	GM4	GM5	GM6	GM7	RSP	Avg 1-7
1	100X-30Y	2.64	5.31	42.1	1.66	11.0	1.50	5.90	2.55	10.0
	100Y-30X	0.782	3.62	16.1	0.881	17.2	1.07	2.85	1.02	6.06
3	100X-30Y	4.75	7.81	44.9	2.93	13.2	3.54	8.36	4.64	12.2
	100Y-30X	3.78	7.65	18.6	2.82	41.3	2.94	9.19	5.29	12.3
5	100X-30Y	3.60	9.03	46.8	3.60	11.5	2.61	8.26	3.51	12.2
	100Y-30X	1.98	7.00	19.0	1.87	63.4	2.15	5.89	3.00	14.5

Table 4-2 Column top resultant drift ratio demand (%)

Pier	Seismic Loading	GM1	GM2	GM3	GM4	GM5	GM6	GM7	RSP	Avg 1-7
1	100X-30Y	0.772	1.55	12.3	0.469	3.10	0.433	1.73	0.747	2.91
	100Y-30X	0.221	1.02	4.70	0.249	5.02	0.312	0.834	0.298	1.76
3	100X-30Y	1.37	2.25	12.9	0.843	3.79	1.02	2.40	1.33	3.51
	100Y-30X	1.09	2.20	5.34	0.810	11.9	0.845	2.64	1.52	3.54
5	100X-30Y	1.30	3.26	16.9	1.30	4.14	0.943	2.98	1.27	4.40
	100Y-30X	0.691	2.53	6.82	0.654	22.9	0.764	2.06	1.05	5.20

Tables 4-1 and 4-2 list the resultant column top displacement and drift, respectively, for all ground motions for comparison with “Avg 1-7”. It is seen that the average displacement and drift are heavily influenced by the large responses caused by Ground Motions 3 and 5. GM3 causes the highest drift for the 100X-30Y seismic loading (16.9%), while GM5 creates the absolute highest drift under 100Y-30X (22.9%). The tables show that, due to the considerably high drift demands from GM3 and GM5, RSP leads to significantly underestimated peak deformation demand, which is nearly three times lower than the average response. There is a trend of increasing displacement and drift demands from Pier 1 to Pier 5. This is most likely due to the combined effects of (1) the pin supports for the more slender Pier 5 columns, (2) the fixed base of the columns of Pier 1 (which supports deck Segment 2), and (3) Segment 4, which is supported by Piers 4 and 5, not being linked to the stiff Segment 2 as Segment 3, which contains Piers 2 and 3, is. This link is provided

via restrainers in the longitudinal direction and shear keys in the transverse direction. For "Avg 1-7", 100X-30Y governs for Pier 1, 100Y-30X controls for Pier 5, while Pier 3 sees a similar response to both seismic loadings.

Figure 4-7 summarizes the maximum lateral drift ratio demands at all bridge piers determined from the average responses, and the peak drift ratio demand associated with Ground Motion RSP. The governing seismic loading is listed below each bar graph. The 100X-30Y seismic loading governs the column displacement and drift for Piers 1 and 2, while 100Y-30X governs the responses of Piers 3 to 5. Given that a 3.0% lateral drift may indicate a global collapse (Mwafy et al. 2010), there is a high possibility of severe structural failure in Bridge G-953.

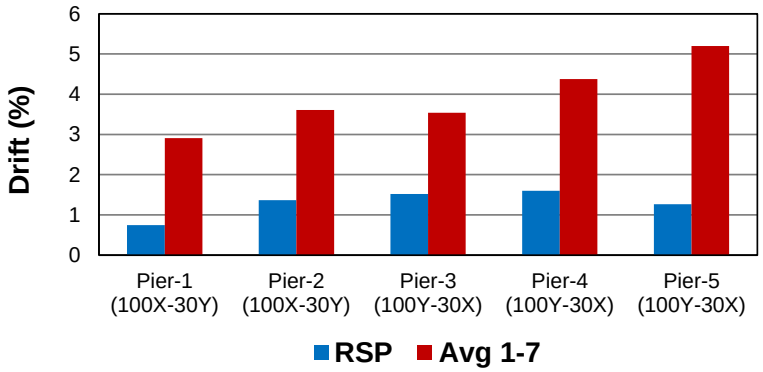

Figure 4-7 Comparison of drift ratios at the top of columns for RSP and "Avg 1-7".

4.1.2 Horizontal Displacements of Deck Segments

The responses of horizontal displacement and in-plane superstructure rotation at the five superstructure segments are checked to determine the trends in global seismic behavior of the bridge. The focus is given to Segments 2, 3, and 4 since the substructure is connected to these segments only. Analysis of only these segments will provide a representative envelope of demands that will have to be resisted primarily by the substructure.

Figure 4-8 shows the time-history of horizontal displacement at the four corners of a superstructure segment labeled in Figure 4-8a. This figure reports only the response caused by Ground Motion 5 under the 100X-30Y and 100Y-30X loading conditions. Figures 4-8b, 4-8d, and 4-8f display the global-X displacement for Segments 2, 3, and 4, respectively. Figures 4-8c, 4-8e, and 4-8g show the global-Y displacement for Segments 2, 3, and 4, respectively. The close match in global-X displacement response across Segments 2, 3, and 4 indicates the in-phase movement of the individual bridge segments in the longitudinal direction of the bridge. For the transverse displacement response (Figure 4-8c, 4-8e, and 4-8g), Segments 3 and 4 become out of phase with Segment 2 just after the peak ground acceleration (PGA) has been reached at around six seconds. A high residual displacement of almost 70 in. occurs for Segment 4 (northeast corner) under the 100Y-30X seismic loading, while only 7 in. is recorded for the stiffer Segment 2. Residual global-X displacements are much lower for Segments 2 to 4 under 100X-30Y, with 3 to 4 in. being the maximum. The large difference in residual displacements could be caused by excessive yielding of the column, the discontinuities at the in-span hinges and abutment expansion joints being more sensitive to the 100Y-30X loading, and/or a possible shear key failure.

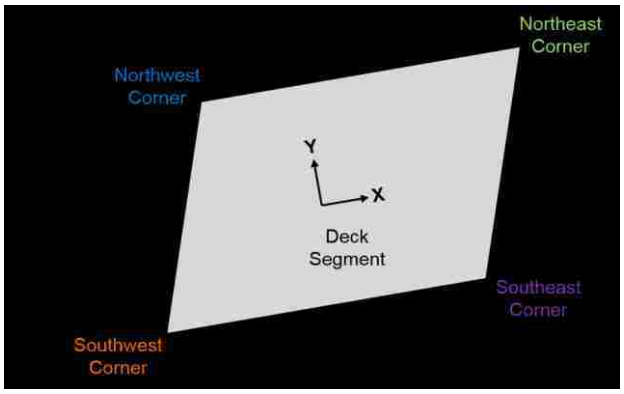

(a)

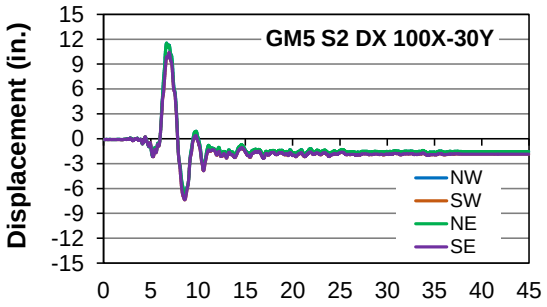

(b)

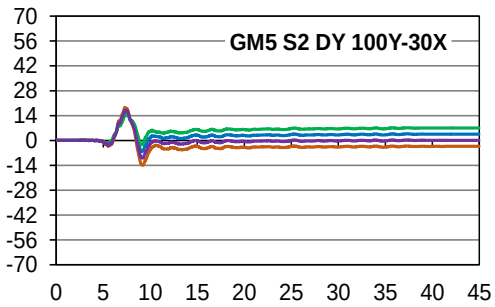

(c)

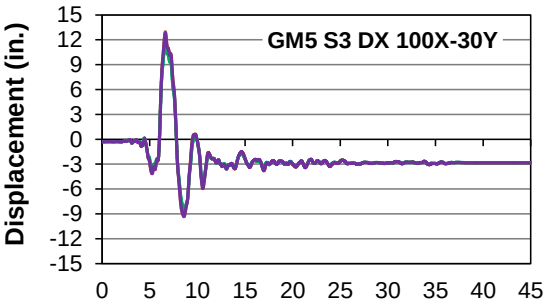

(d)

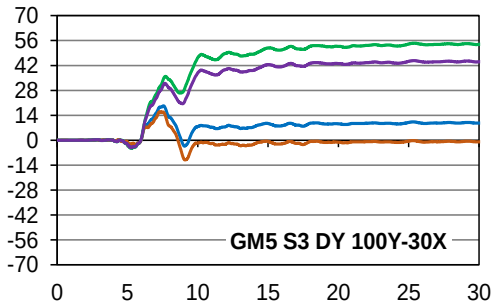

(e)

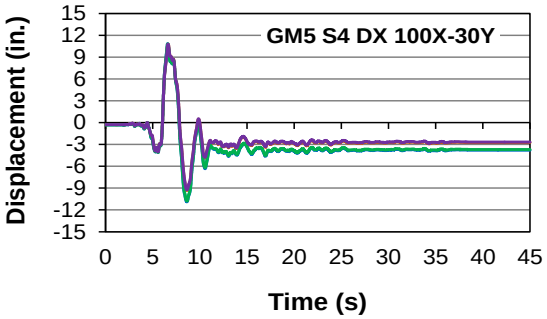

(f)

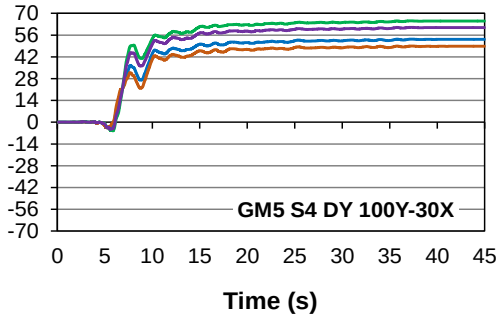

(g)

Figure 4-8 Longitudinal (global-X, 100X-30Y) and transverse (global-Y, 100Y-30X) displacement response for Segments 2, 3, and 4 under Ground Motion 5.

Table 4-3 lists the peak global-X/Y displacement for Segments 2 to 4 for all ground motions for comparison with "Avg 1-7". Only the maximum displacement of all four corners of a deck segment (Figure 4-8a) is shown. Figure 4-9 shows the maximum longitudinal (global-X) and transverse (global-Y) displacements of all corners of each deck segment for "Avg 1-7" and RSP. Similar to the lateral drift at the top of columns, there is a slight increase in displacement demand from the westernmost Segment 1 (S1) to the easternmost Segment 5 (S5) of the bridge for 100X-30Y. This trend is more dramatic for 100Y-30X, but drops from Segment 4 to Segment 5. As with the average displacement response at the top of columns, the average global-Y displacement demand is higher than that of global-X, except for Segment 2. RSP results in greatly underestimated displacement demand for all superstructure segments.

Table 4-3 Deck segments longitudinal (global-X) and transverse (global-Y) displacement demand (in.)

Deck Segment	Seismic Loading	GM1	GM2	GM3	GM4	GM5	GM6	GM7	RSP	Avg 1-7
2	100X-30Y (D_X)	2.72	5.64	42.2	1.79	11.5	1.60	6.28	2.64	10.3
	100Y-30X (D_Y)	0.857	3.94	17.1	0.89	18.4	1.00	3.37	1.16	6.51
3	100X-30Y (D_X)	4.75	7.63	44.2	3.02	13.0	3.56	8.27	4.68	12.1
	100Y-30X (D_Y)	5.10	9.28	22.3	3.00	55.1	4.11	11.9	7.01	15.8
4	100X-30Y (D_X)	3.74	8.97	46.2	3.73	10.9	2.76	7.98	3.64	12.0
	100Y-30X (D_Y)	4.27	7.36	21.5	2.64	65.1	3.30	10.8	5.68	16.4

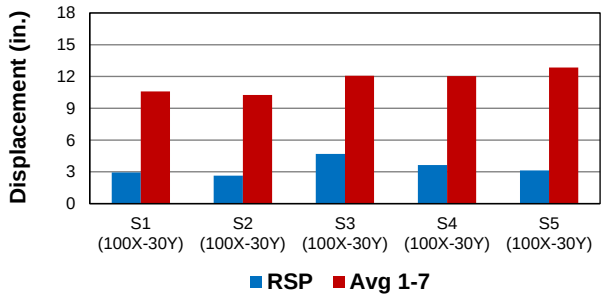

(a) Global-X displacement demand

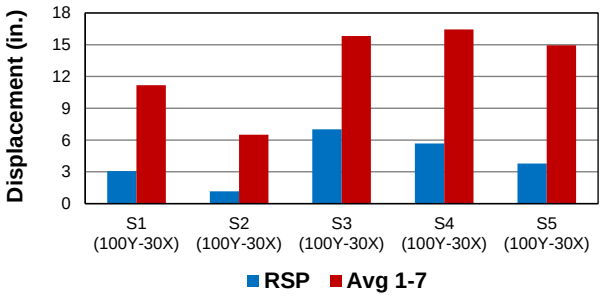

(b) Global-Y displacement demand

Figure 4-9 Displacement demand of superstructure segments for RSP and "Avg 1-7".

The bridge discontinuities caused by the in-span hinges and abutment expansion joints significantly affect the displacement response of the individual bridge segments. Likely due to pounding and other interactions at the gaps, the bridge is more able to "move together" as a unit under the primarily-longitudinal 100X-30Y seismic loading. This in-phase longitudinal motion may amplify shear demand and/or cause an exceedance of the longitudinal passive pressure of the abutments. However, the interaction across the gaps is reduced for 100Y-30X, and thus each segment responds more independent of adjacent bridge segments. If there was no skew in the bridge, or the ground motion was applied directly along the direction of the skew, the differences between the longitudinal and transverse loading would probably be even more pronounced.

4.1.3 Deck Segments In-Plane Rotation

The in-plane rotation (twist) of the bridge segments is investigated since skewed bridges are more prone to this behavior. Figure 4-10 shows the in-plane rotation of deck segments 2, 3, and 4 under Ground Motion 5 for both the 100Y-30X and 100X-30Y seismic loading. Due to deck rigid body rotation associated with its high in-plane stiffness, the twist response is represented by that obtained at the northwest corner (Figure 4-8a). Table 4-4 gives the maximum twist for both seismic loading under all ground motions, along with "Avg 1-7".

Ground Motion 5 causes the maximum twist in Segments 2, 3, and 4. Compared with 100X-30Y, the 100Y-30X seismic loading creates significantly higher in-plane rotations and leads to a residual twist larger than 0.015 radians at Segment 3. This twist could be significant, as Kaviani et al. (2012) cite a residual twist of 0.009 radians (about 0.5°) which offset a bridge by nearly 3.0 in. during the San Fernando earthquake. The dominance of twist by 100Y-30X could be explained by the combined effects of asymmetrical deck segments and possible shear key/abutment wingwall failures.

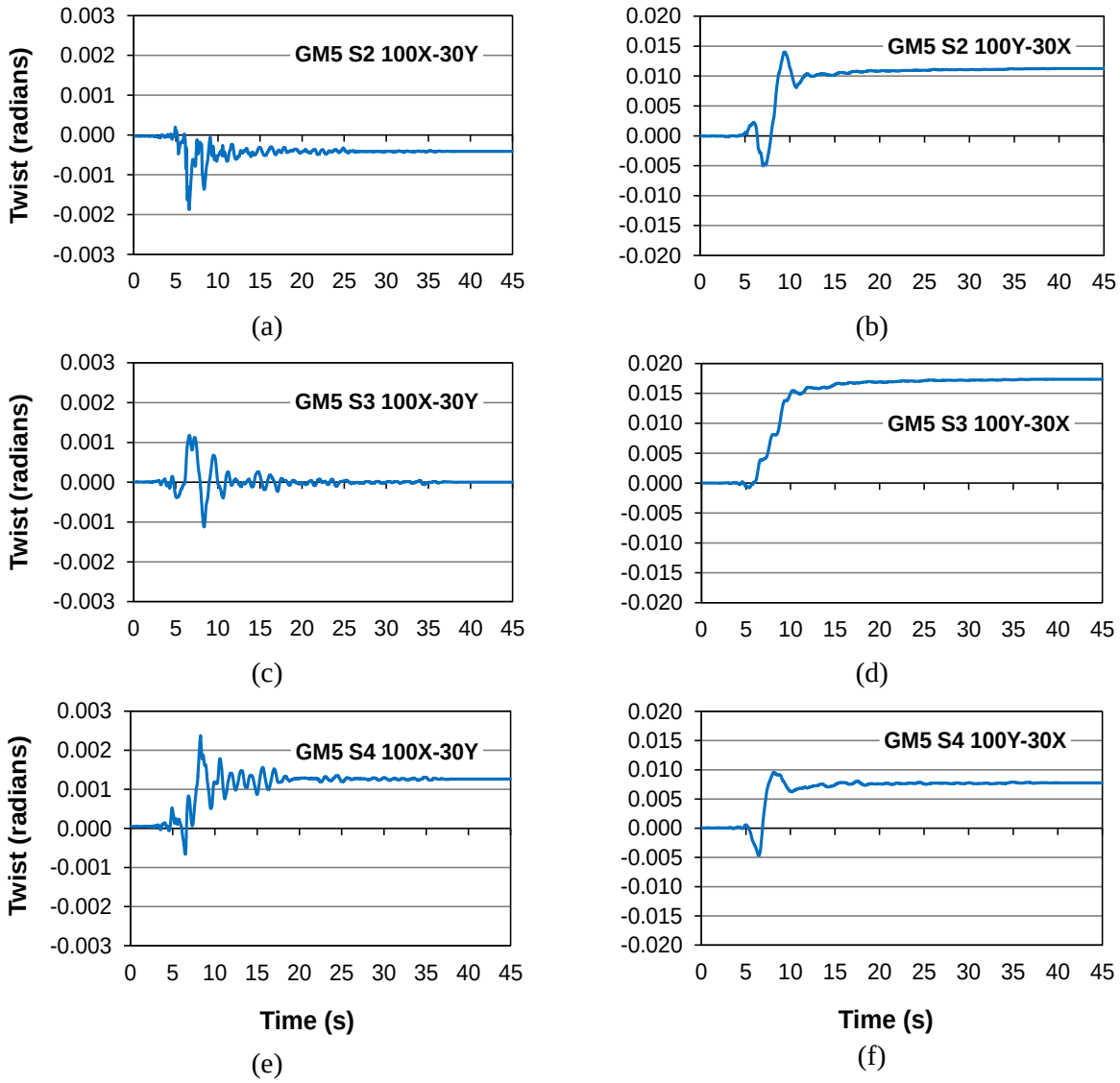

Figure 4-10 Deck in-plane rotation/twist response for Segments 2, 3, and 4 under Ground Motion 5 for 100X-30Y and 100Y-30X.

Table 4-4 Deck segment in-plane rotation/twist demand (unit: degrees)

Deck Segment	Seismic Loading	GM1	GM2	GM3	GM4	GM5	GM6	GM7	RSP	Avg 1-7
2	100X-30Y	0.0435	0.0607	0.174	0.0364	0.112	0.0292	0.131	0.0423	0.0839
	100Y-30X	0.0437	0.0892	0.340	0.0345	0.815	0.0897	0.212	0.0658	0.2320
3	100X-30Y	0.0512	0.0545	0.0995	0.0403	0.0675	0.0346	0.0888	0.0488	0.0623
	100Y-30X	0.118	0.169	0.282	0.0714	0.999	0.0810	0.192	0.122	0.273
4	100X-30Y	0.0388	0.0691	0.0863	0.0463	0.138	0.0386	0.0693	0.0393	0.0695
	100Y-30X	0.121	0.194	0.307	0.0949	0.549	0.0970	0.209	0.122	0.225

Figure 4-11 shows the in-plane rotation of each bridge segment for "Avg 1-7" and RSP. The twist demand is greatest on Segment 1 (S1). 100Y-30X still governs for all superstructure segments. RSP significantly underestimates deck rotation response, but by a smaller margin than for deck displacements (the average difference is about 205% for twist compared to 295% for displacements). The large transverse displacements and in-plane deck rotations identified in this study could signify shear key failure and possibly-high torsion demands in the columns of Pier 1.

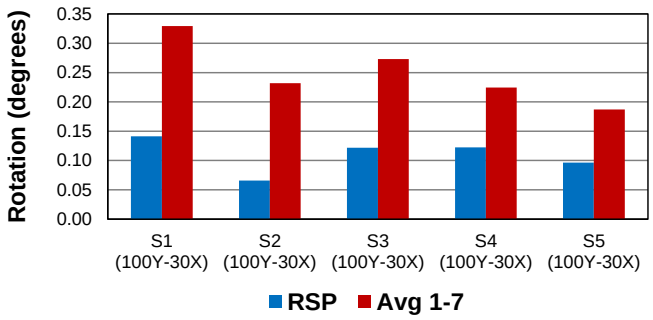

Figure 4-11 Maximum in-plane twist of deck segments for RSP and "Avg 1-7".

4.1.4 Risk of In-Span Hinge Unseating

The focus of unseating is given only to the four in-span hinges because the seat width at the abutments is 24 in., much larger than that of the in-span hinges (15-15.5 in.). The relative displacement between two adjacent decks is approximately calculated, using the global-X displacement of the two corner nodes at each side of an in-span hinge, as shown in Figure 4-12. This figure is also used to describe the displacement of the restrainer elements in Section 4.5.2.

Figure 4-13 shows the relative displacement time history between the northernmost (blue) and southernmost (red) pairs of nodes at each in-span hinge (ISH) (Figure 4-12). Only the governing response of the eight ground motions for both seismic loadings (100X-30Y and 100Y-30X) is shown. Positive values indicate that the bridge segments are moving toward each other

(penetration or “Pen” in Figures 4-12 and 4-13). This movement is mainly limited to the gap width at an in-span hinge (1.5 in. at hinges 1 and 4 and 2.0 in. at hinges 2 and 3). However, due to the penetration between deck segments predicted by the pounding model, the relative displacement can be slightly greater than the gap width. The flattened curve implies that two adjacent deck segments have contacted and are bearing against one another. Negative values in Figure 4-13 indicate that the bridge segments are moving away from each other at an in-span hinge (separation or “Sep” in Figures 4-12 and 4-13).

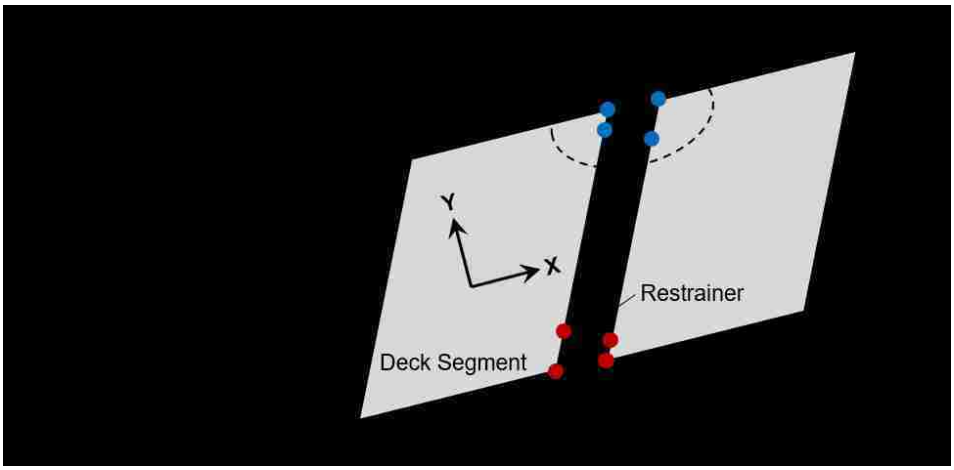

Figure 4-12 Explanation of in-span hinge displacement for unseating and restrainers.

The available seat width is 15.5 in. at In-Span Hinges 1 and 4 and 15.0 in. at In-Span Hinges 2 and 3. As seen in Figure 4-13, these values are not exceeded by the negative relative displacement/separation at any in-span hinge, indicating that the ground motions considered in this study do not cause unseating failure. Note that 100Y-30X governs separation for all in-span hinges. This is surprising, since intuition would lead one to assume the longitudinal seismic loading would causes the largest longitudinal separation of decks across the discontinuities. However, as discussed previously in Figure 4-8, the bridge “moves together” under the 100X-30Y seismic loading with little difference in relative displacement across the gaps.

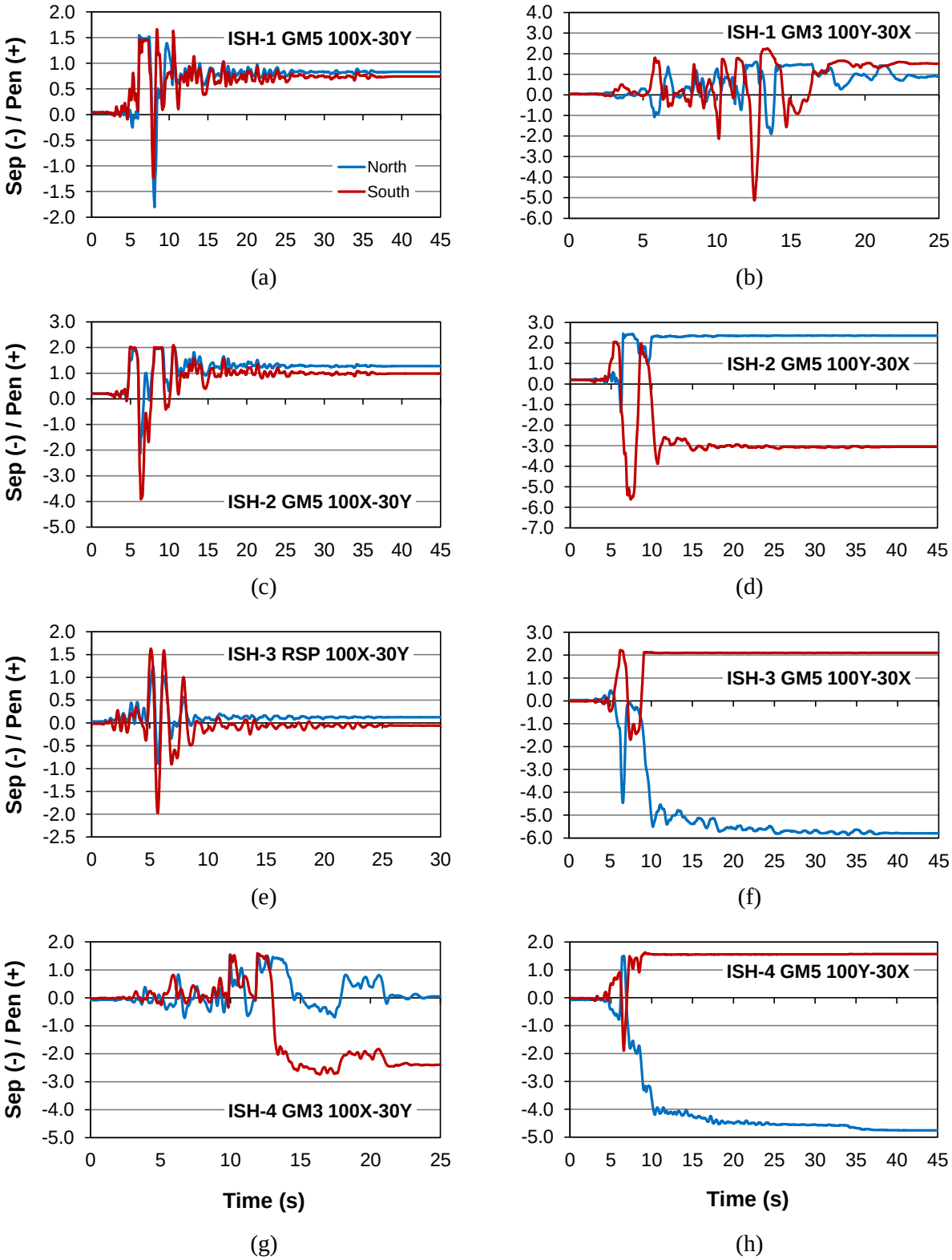

Figure 4-13 Time history of relative displacement between adjacent deck segments.

Also of note is the similar relative displacement behavior at the north and south ends of the deck for Hinges 1 to 3 under 100X-30Y. This means that both the north and south ends of the bridge segment are translating the same amount, indicating no in-plane rotation. Under the 100Y-30X seismic loading, however, the north and south responses diverge for all in-span hinges, indicating the effects of large in-plane rotation of the deck segments as previously shown in Figures 4-10b, 4-10d, and 4-10f.

Table 4-5 lists the minimum remaining seat width at all in-span hinges for all ground motions for comparison with "Avg 1-7". It is seen that the closest unseating risk exists at In-Span Hinge 2 due to Ground Motion 5 under 100Y-30X, which leads to a minimum remaining seat width of 8.98 in. The "Avg 1-7" value for this particular case shows a remaining seat width for In-Span Hinge 3 of 12.6 in., well within safe limits. Figure 4-14 shows the minimum remaining in-span hinge seat width, at any point in time during the seismic loading, for "Avg 1-7" and RSP. While Ground Motion RSP leads to severely underestimated displacement responses for columns and deck segments, it actually slightly overestimates the remaining seat width for all but In-Span Hinge 3. Therefore, the RSP method may be efficient in capturing certain categories of response.

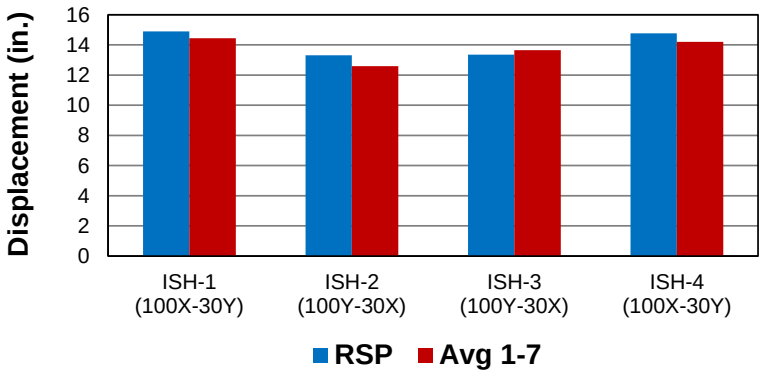

Figure 4-14 Approximate minimum remaining seat width at each in-span hinge for RSP and "Avg 1-7".

Table 4-5 Minimum remaining seat width at in-span hinges (in.)

In-Span Hinge	Seismic Loading	GM1	GM2	GM3	GM4	GM5	GM6	GM7	RSP	Avg 1-7
1	100X-30Y	14.8	14.5	13.8	15.1	13.8	14.1	14.5	14.9	14.4
	100Y-30X	14.6	13.6	10.5	14.6	11.5	14.6	13.7	14.3	13.3
2	100X-30Y	12.1	13.8	11.2	13.8	11.1	13.7	12.4	12.7	12.6
	100Y-30X	13.7	13.5	10.7	14.2	8.98	14.5	12.8	13.7	12.6
3	100X-30Y	13.0	14.3	14.0	14.4	13.3	13.4	13.3	12.9	13.7
	100Y-30X	13.1	12.2	9.83	13.6	9.53	13.7	10.8	13.2	11.8
4	100X-30Y	14.8	13.9	11.4	15.0	13.5	14.7	14.0	14.8	13.9
	100Y-30X	14.1	13.1	11.5	14.2	11.1	14.5	13.0	13.6	13.1

4.2 Shear Response

4.2.1 Shear Failure Potential Considering Force-Based Criteria

Both the force- and displacement-based shear failure criteria presented in Section 3.2.10.4 are used to evaluate the potential of shear failure in the columns. In this section, the evaluation results based on the force-based failure criterion are presented. Figures 4-15 to 4-20 show the time histories of the normalized shear demand/capacity ratio, V/V_u, for Column 1 (northernmost) of Piers 1, 3, and 5 associated with the 100X-30Y and 100Y-30X seismic loadings. The shear demand, V, is a resultant evaluated from the global-X and global-Y values. For Pier 1 (Figures 4-15 and 4-16), which has the only columns subjected to torsional loadings, the shear-torsion interaction discussed in Equation 3-38 is considered. The shear demand and capacity are evaluated at the topmost column section. The formulations for V_u given by both AASHTO (2011) (Equations 3-29 to 3-32) and Kowalsky and Priestley (2000) (Equations 3-33 to 3-35) are considered. The formulation that causes the more-conservative value (higher V/V_u) will be considered to govern for each case. A demand/capacity ratio greater than 1.0 indicates a potential force-based shear failure. For all figures in this chapter dealing with column capacities, focus is given to the northernmost column (column 1) of a pier for both seismic loadings (100X-30Y and 100Y-30X).

Note that, when it occurs, a red marker is placed on the plot to indicate the approximate time at which shear failure caused by plastic hinge rotation occurs ("Rotn-Lim" in the plot legend). After this point, the calculated bridge response is not reliable because the column failures would dramatically modify the bridge behavior. The ability to detect whether a force- or displacement-based failure mode occurs first in the columns can provide valuable insights into the behavior of the substructure. Force-based failures are brittle, while rotation-based failures are ductile. A full discussion of plastic hinge "rotation-based" shear failure is given in Section 4.2.2.

Just as Ground Motions 3 and 5 governed the lateral displacement (Section 4.1), they also control the shear demand at most piers. Among Piers 1, 3, and 5, Pier 1 has the highest demand/capacity ratio due to shear-torsion interaction (Figures 4-16e) at nearly 2.1 (GM5, 100Y-30X) for both the AASHTO (2011) and Kowalsky-Priestley (2000) shear strength calculation methods. Shear-torsion failure for Pier 1 also may occur under GM3 (100Y-30X). Apart from these maxima, all other ground motions and seismic loadings create a maximum demand/capacity ratio in the range of about 0.5-0.75 for Pier 1 (Figures 4-15 and 4-16).

Pier 5 (Figures 4-19 and 4-20) has the second-highest V/V_u value of about 0.35 (100Y-30X, GM1, GM5, GM7, RSP) based on the shear strength defined by Kowalsky and Priestley (2000) except for GM7 (Figure 4-20g), in which case the AASHTO (2011) method governs. In contrast, Pier 3 (Figures 4-17 and 4-18) has very low demand/capacity ratios not even exceeding 0.25 for any case. Notice in Figure 4-16 that the markers on the plots for GM3 (Figure 4-16c) and GM5 (Figure 4-16e) signify the onset of rotation-based shear failure, which occurs before the force-based shear failure is detected. This may indicate the substructure will be governed by nonlinear, ductile effects rather than brittle responses, even for the strong columns of Pier 1.

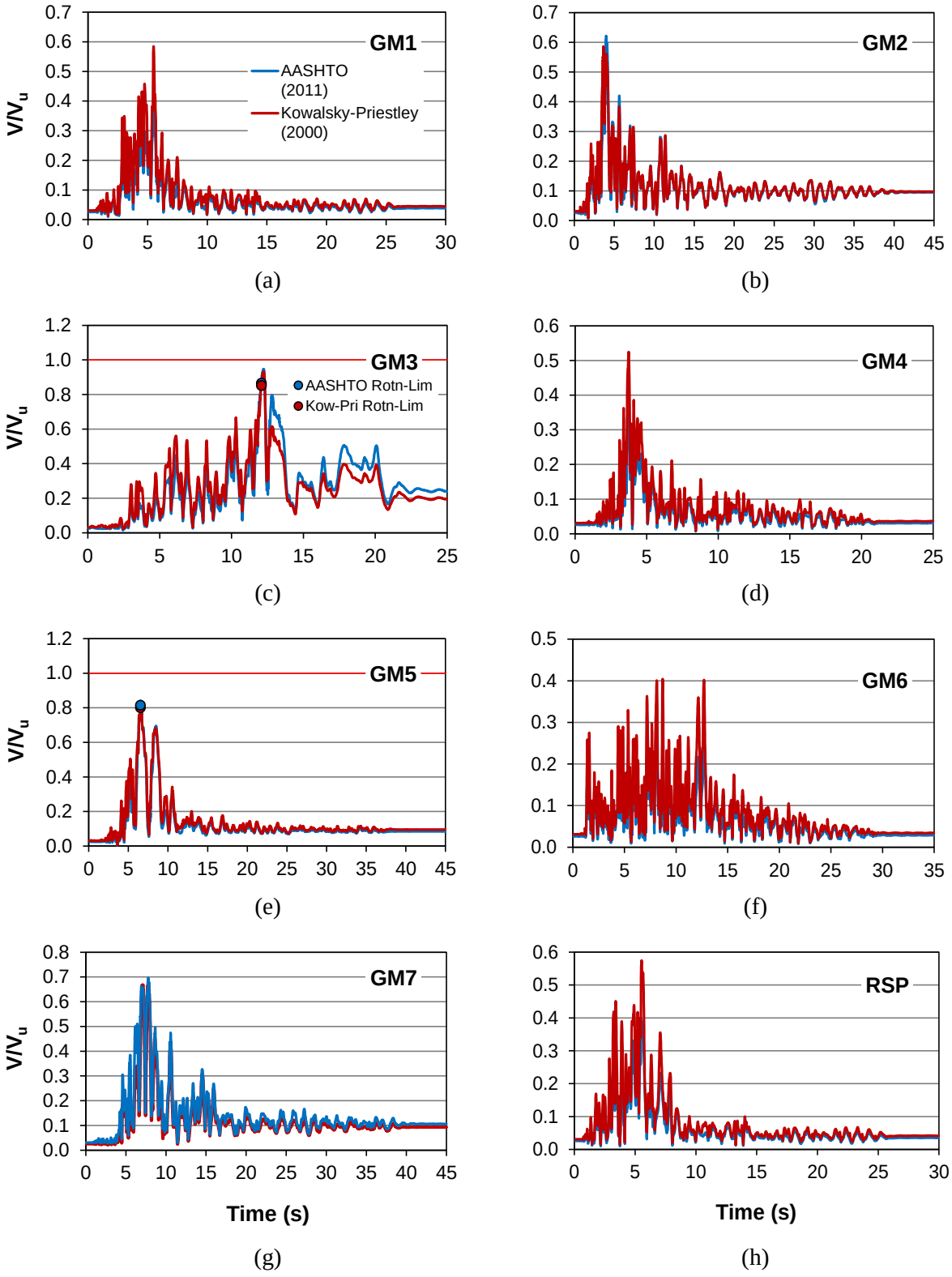

Figure 4-15 Time history of normalized resultant shear demand at Pier 1 column (100X-30Y).

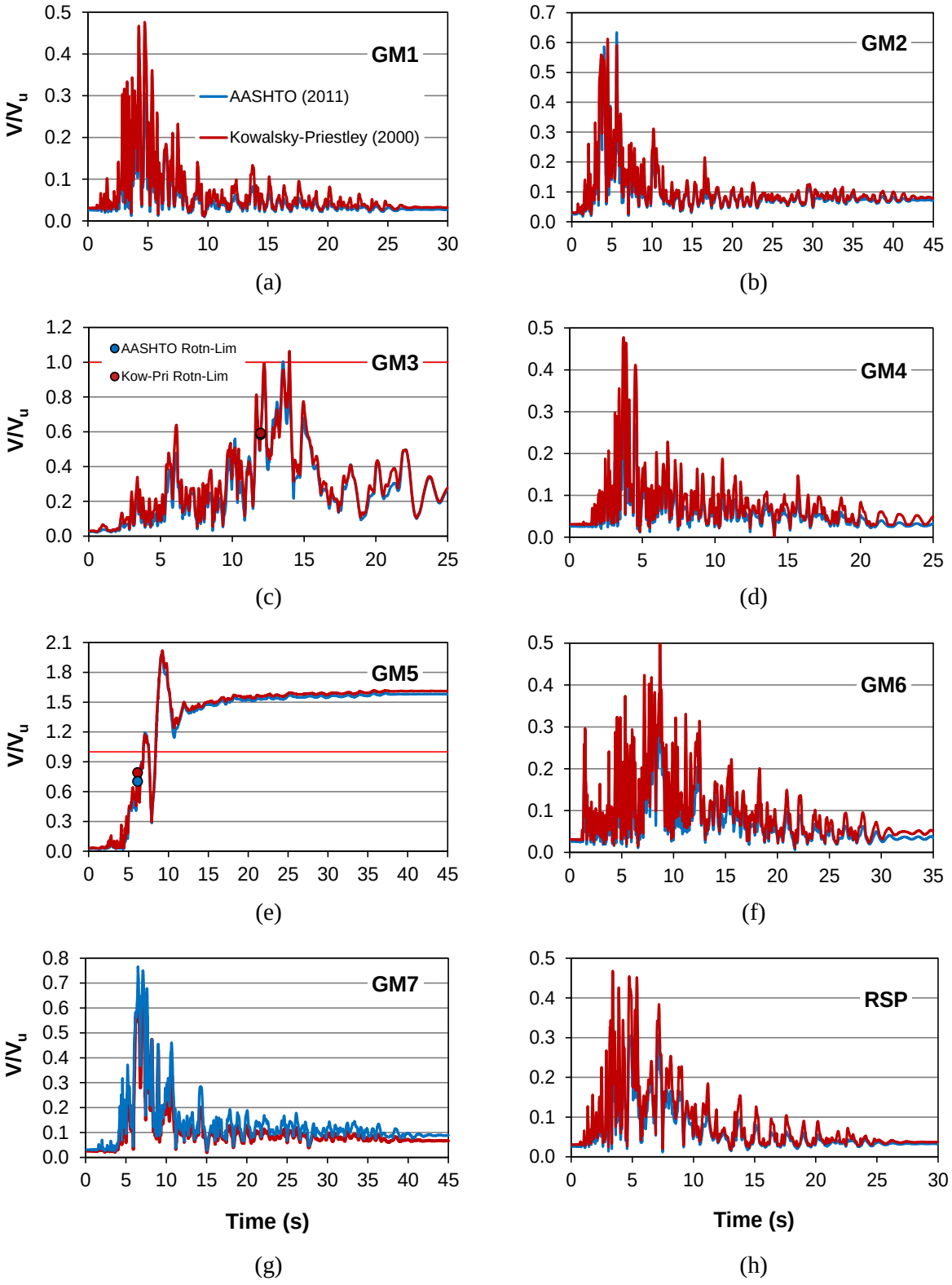

Figure 4-16 Time history of normalized resultant shear demand at Pier 1 column (100Y-30X).

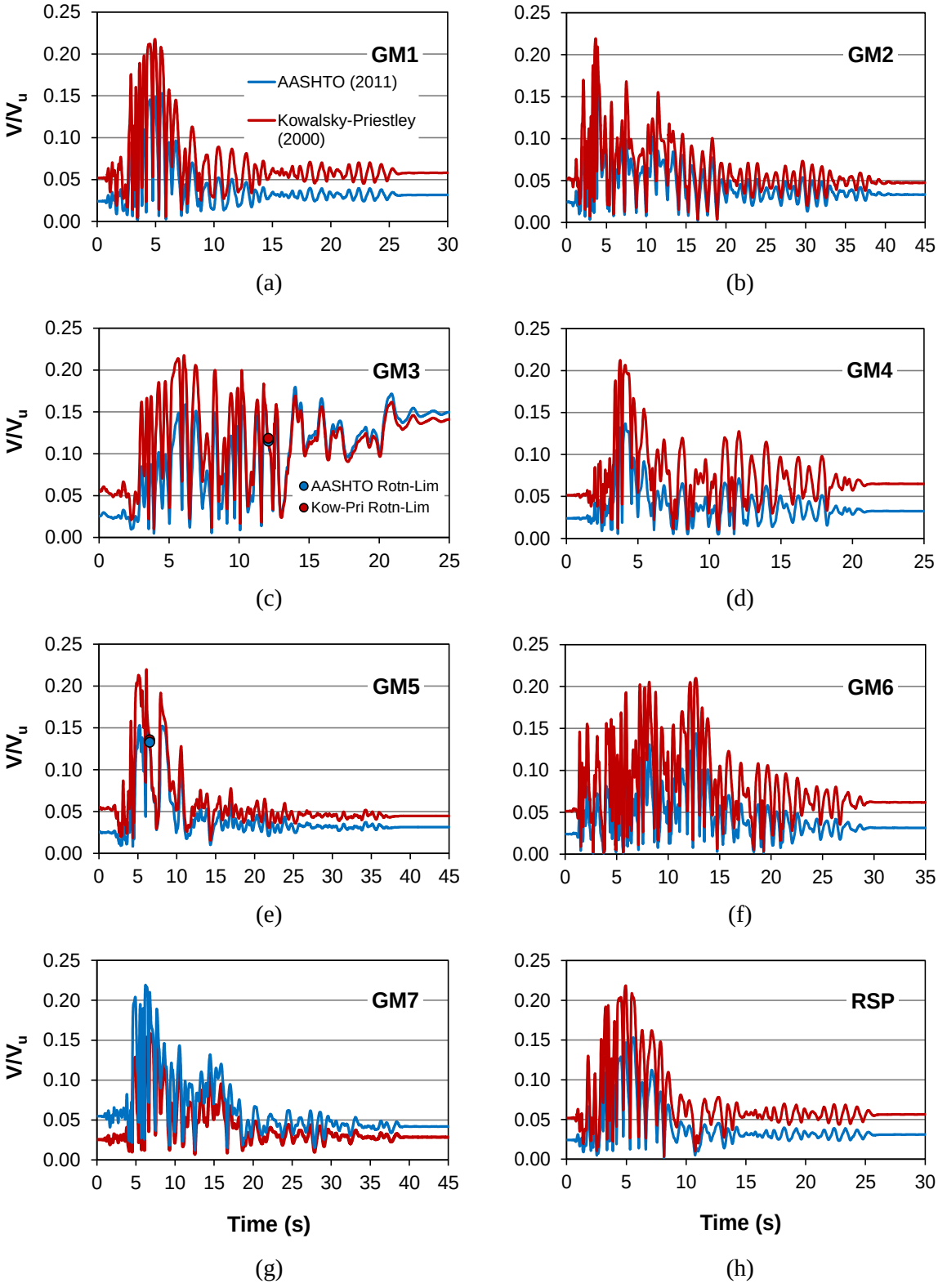

Figure 4-17 Time history of normalized resultant shear demand at Pier 3 column (100X-30Y).

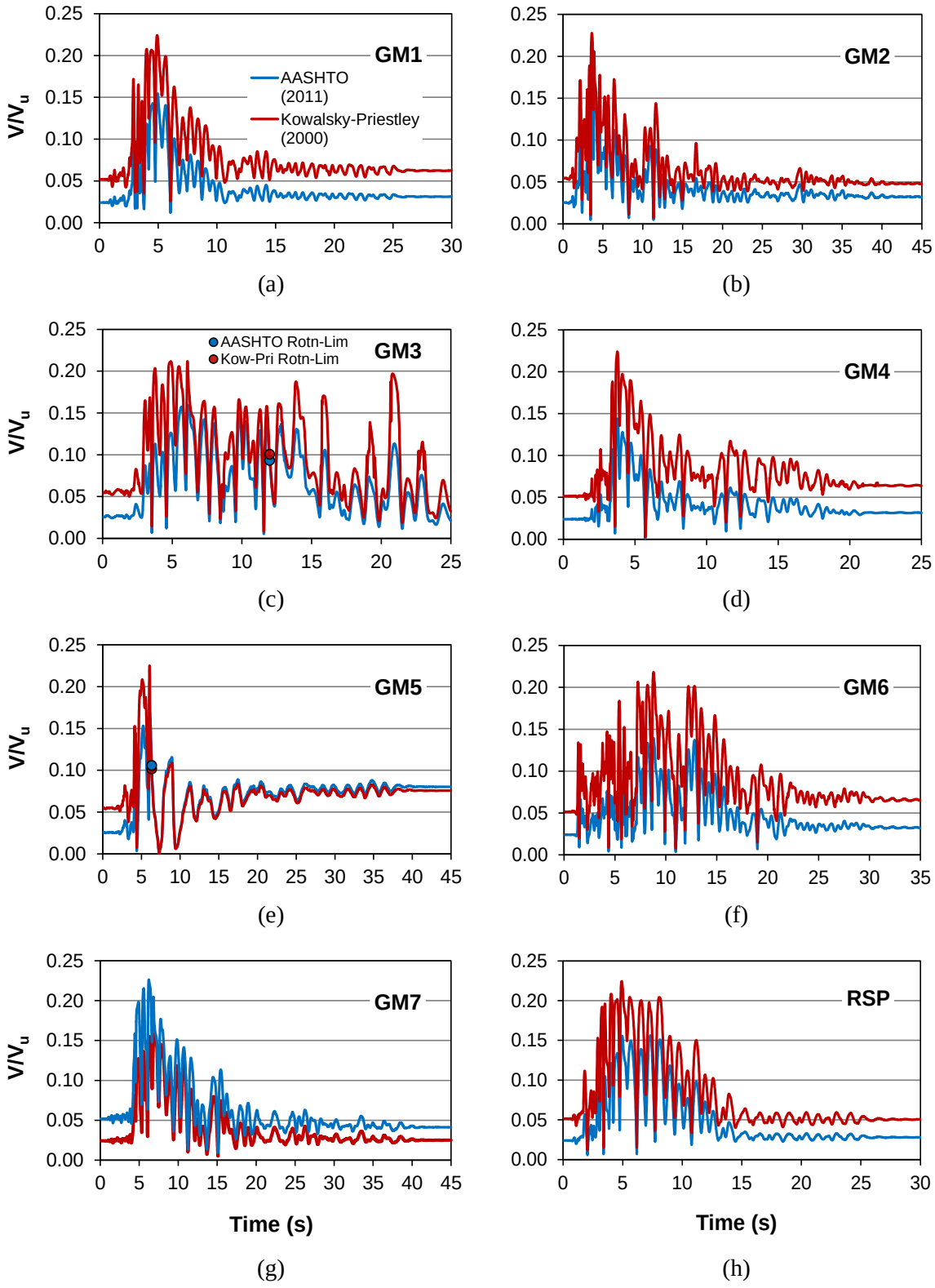

Figure 4-18 Time history of normalized resultant shear demand at Pier 3 column (100Y-30X).

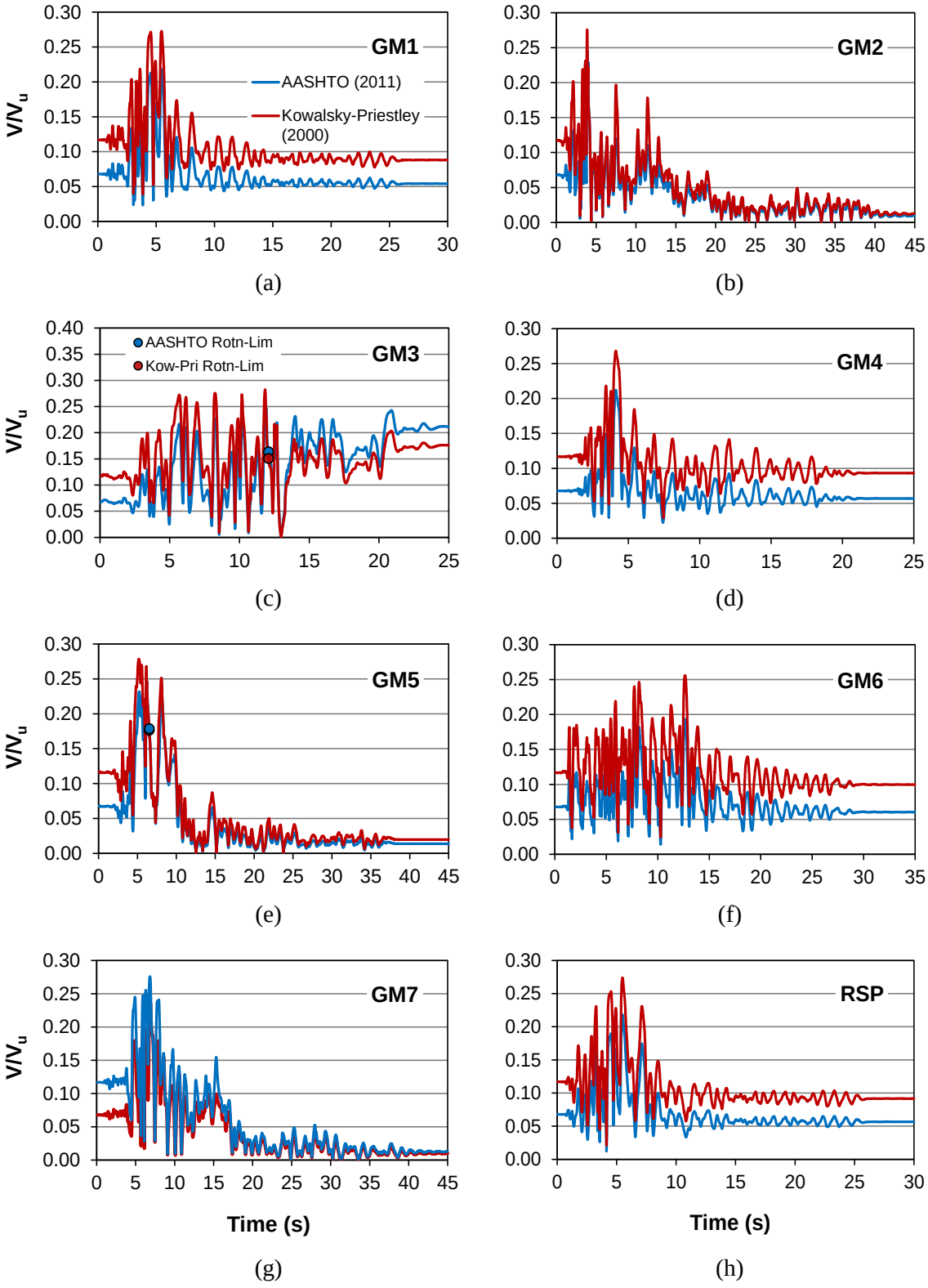

Figure 4-19 Time history of normalized resultant shear demand at Pier 5 column (100X-30Y).

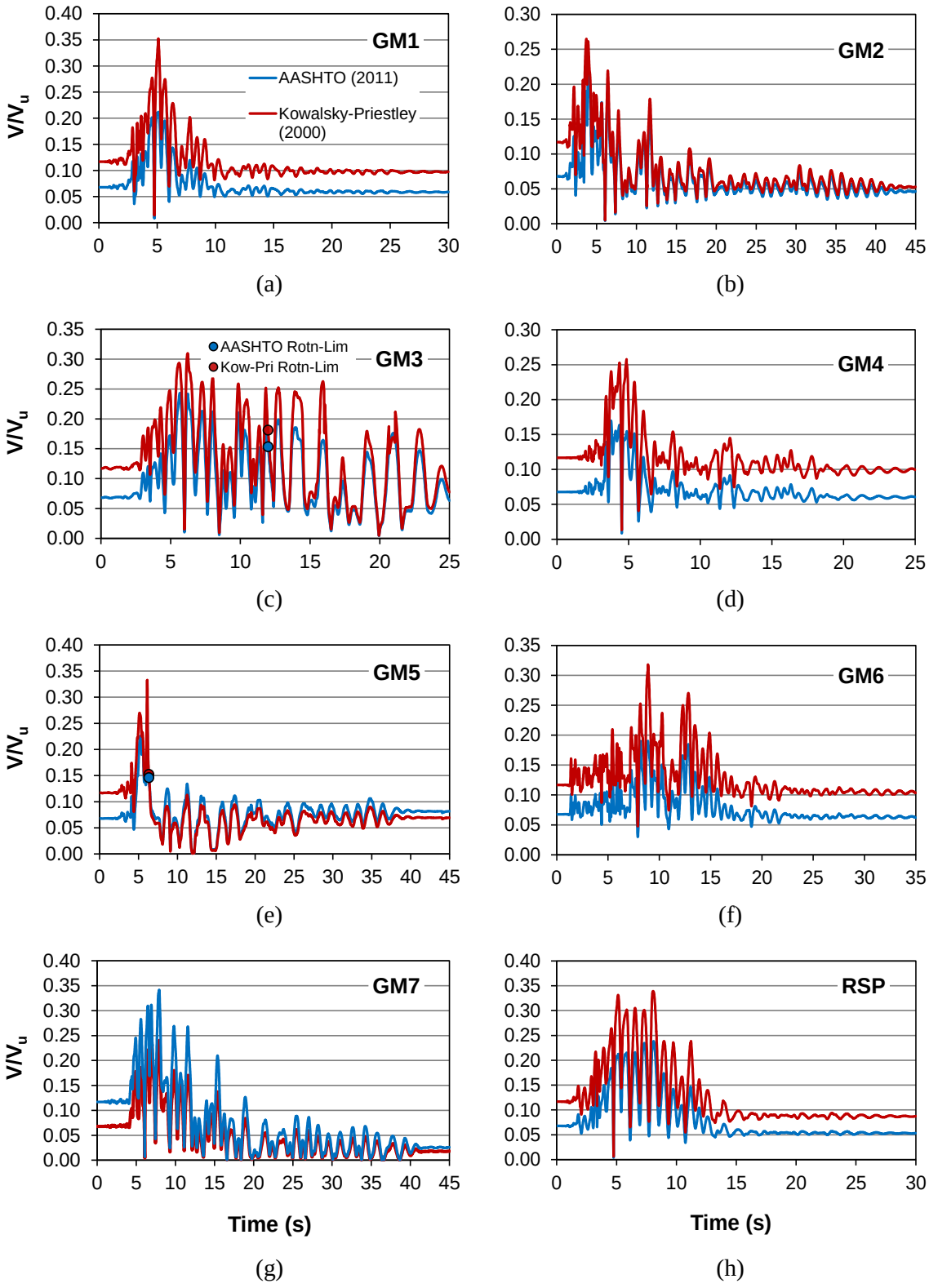

Figure 4-20 Time history of normalized resultant shear demand at Pier 5 column (100Y-30X).

Table 4-6 gives the resultant shear demand on the topmost column sections of Piers 1, 3, and 5 for all ground motions for comparison with "Avg 1-7". The difference in the demand/capacity ratio plots for the different piers can now be understood. Even though Piers 2 to 5 carry a massive superstructure and would thus experience a high seismic base shear demand, the force that can be carried is clearly limited by yielding and plastic hinging in the column critical sections. Pier 1, in comparison, has a much higher longitudinal reinforcement ratio at the column bases (4.6% average compared to the average of Piers 2 to 5 of 1.5% for the column topmost sections) and has stronger concrete, a larger cross section, and fixed supports. Thus, the columns of Pier 1 have a higher stiffness, attracting more seismic load, and can carry much more of that load prior to yielding. This will be further investigated later in Section 4.3, which deals with flexure.

Table 4-6 Maximum resultant shear demand of the four columns of a pier (unit: kips)

Pier	Seismic Loading	GM1	GM2	GM3	GM4	GM5	GM6	GM7	RSP	Avg 1-7
1	100X-30Y	155	248	288	137	259	120	221	153	204
	100Y-30X	119	201	254	132	279	110	189	126	183
3	100X-30Y	56.4	58.2	65.4	50.9	60.8	53.7	58.9	56.9	57.8
	100Y-30X	55.5	59.4	59.4	51.2	61.7	50.6	60.7	57.1	56.9
5	100X-30Y	97.4	112	147	96.4	116	83.5	109	97.1	109
	100Y-30X	75.4	110	106	79.3	135	86.2	107	88.5	100

Table 4-7 in turn presents the column shear capacity calculated using both the AASHTO (2011) and Kowalsky and Priestley (2000) methods. Each ground motion is recorded and compared to "Avg 1-7". Due to fluctuations in parameters that affect the strength, such as axial load on the columns, both the maximum and minimum recorded capacities are recorded. Additionally, the "Δ" value records the difference in capacity for the AASHTO (2011) method compared to the Kowalsky-Priestley (2000) method. While the columns of Pier 1 do have the

highest shear capacity, the columns of Piers 3 and 5 have maximum shear capacities of at least 300 kips but demands of less than 150 kips. This further reinforces the claim that flexural yielding is limiting the shear transferred to the columns.

Table 4-7 Summary of the governing shear capacity of the four columns of a pier
(unit: kips, Δ is change in AASHTO [2011] compared to Kowalsky-Priestley [2000])

Pier	Value	Seismic Loading	GM1	GM2	GM3	GM4	GM5	GM6	GM7	RSP	Avg 1-7
1	Max	AASHTO	430	431	431	431	431	429	426	431	430
		Kow-Pri	343	503	575	349	531	345	436	350	440
	Min	AASHTO	391	384	383	389	382	391	385	360	386
		Kow-Pri	213	213	213	213	213	213	213	213	213
	Δ (%)	Max	20.2	-16.7	-33.3	19.2	-23.0	19.7	-2.31	18.9	-2.35
		Min	45.6	44.6	44.4	45.3	44.2	45.6	44.6	40.8	44.9
3	Max	AASHTO	333	333	333	333	333	333	333	333	333
		Kow-Pri	331	331	442	330	444	329	332	331	363
	Min	AASHTO	314	313	313	314	313	314	314	314	314
		Kow-Pri	149	149	149	149	149	149	149	149	149
	Δ (%)	Max	0.569	0.470	-32.8	0.930	-33.5	1.02	0.103	0.534	-9.03
		Min	52.5	52.5	52.4	52.6	52.4	52.6	52.5	52.5	52.5
5	Max	AASHTO	333	333	333	333	333	333	333	333	333
		Kow-Pri	273	443	507	287	533	260	352	301	379
	Min	AASHTO	326	324	320	325	321	326	323	324	324
		Kow-Pri	192	192	190	192	192	192	192	192	192
	Δ (%)	Max	17.9	-33.1	-52.3	13.7	-60.3	21.9	-5.88	9.60	-14.0
		Min	41.1	40.7	40.7	41.0	40.0	41.1	40.7	40.9	40.8

Considering the maximum shear capacity, the AASHTO (2011) and Kowalsky-Priestley (2000) methods both calculate the higher capacity a similar amount of times. When looking at minimum column shear capacity, AASHTO (2011) gives a somewhat higher value for the shear capacity compared to the Kowalsky-Priestley (2000) method. This is primarily due to the fact that the steel and axial force contributions to shear strength as calculated in the Kowalsky-Priestley (2000) method are largely dependent on the depth of the concrete compression zone, *c* (Equations

3-34, 3-35). Therefore, in the beginning of a seismic loading, when intensities are low and the columns are not yielding (section largely in compression), the column section is primarily under compression from the gravity load. Therefore, the shear strength will be low since the column hoops are considered ineffective in compression. However, under ground motions that see the highest degree of inelastic deformation (i.e. GM3 and GM5), the column will experience flexure that puts some of the column section in tension, thus making the hoops effective and giving shear strengths oftentimes higher than AASHTO (2011).

Figure 4-21 compares the maximum shear demand for RSP and "Avg 1-7". As previously discussed, the columns of Pier 1 have the highest shear demand; this is likely due to higher flexural capacity. Pier 5 columns have the second-largest shear demand, being around 50% less than the shear demand for Pier 1. Piers 2 and 3 have the lowest shear demands, most likely limited by flexural yielding at plastic hinges. The columns of Piers 4 and 5 are more highly reinforced than those of Piers 2 and 3; this may explain the higher shear demand. Figure 4-22 compares the force-based shear demand/capacity ratios for the critical column of each pier for RSP and "Avg 1-7". The shear strength model by ASSHTO (2011, Figure 4-22a) and Kowalsky and Priestley (2000, Figure 4-22b) are both considered.

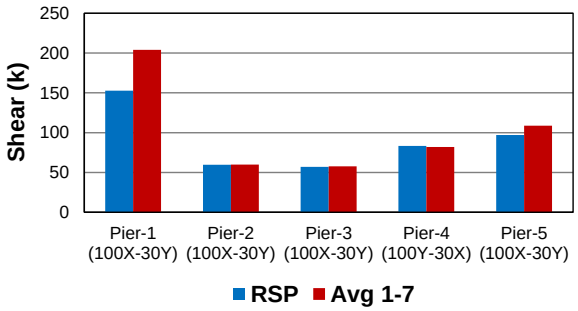

Figure 4-21 Maximum shear demand for columns associated with RSP and "Avg 1-7".

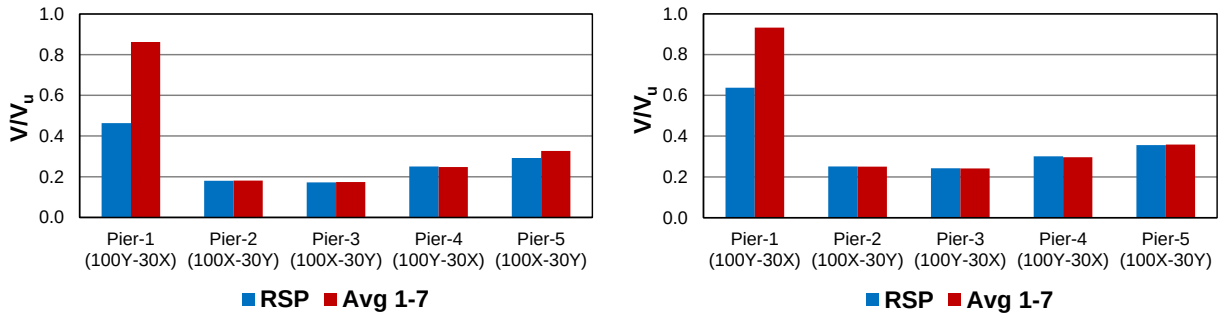

a) AASHTO (2011) Method

b) Kowalsky-Priestley (2000) Method

Figure 4-22 Maximum normalized shear demand for columns associated with RSP and Avg 1-7.

Piers 1 and 5 have the highest risk for force-based shear failure, but no actual failure is detected using either model for calculating pure shear resistance. While the absolute maximum V/V_u calculated by either method (AASHTO [2011] and Kowalsky and Priestley [2000]), with the addition of shear-torsion interaction (add T/T_u to V/V_u), is nearly 2.1 for Pier 1 100Y-30X (Figure 4-16e), the maximum "Avg 1-7" V/V_u for Pier 1 is only about 0.93. In conclusion to force-based shear failure, there is some threat to the columns of Pier 1. Pier 1 is much stiffer than the remaining substructure that it attracts more seismic force. While this bent may be adequate for pure shear or torsion alone, the interaction is cause for concern. Figures 4-21 and 4-22 indicate that the maximum shear demand produced by Ground Motion RSP is much closer to "Avg 1-7" than the displacement demand. Thus, RSP may adequately estimate force demands, especially if they are

limited by nonlinear effects such as flexural yielding. Investigation into other bridge responses is necessary to support this finding.

4.2.2 Shear Failure Potential Considering Plastic Hinge Rotation Capacity

While the columns of Bridge G-953 seem to be adequate for shear resistance based on the force-based failure criteria, concern still exists over the possibility of shear failure due to a high level of plastic hinge rotation. To capture this type of shear failure, Equation 3-36 proposed by Leborgne (2012) is used to determine the plastic hinge rotation at which shear failure may occur. Figures 4-23 through 4-28 display the time histories for the normalized plastic hinge rotation demand, θ/θ_{ult}, at Column 1 of Piers 1, 3, and 5. The demand is the governing total hinge rotation, either in the local-y or local-z axis of the section, $\theta_{y/z}$, at the top of a column. The capacity is the expected ultimate rotation at which shear failure at the topmost column section may occur, θ_{ult}. A $\theta_{y/z}/\theta_{ult}$ ratio greater than unity indicates a possible shear failure caused by excessive plastic hinge rotation.

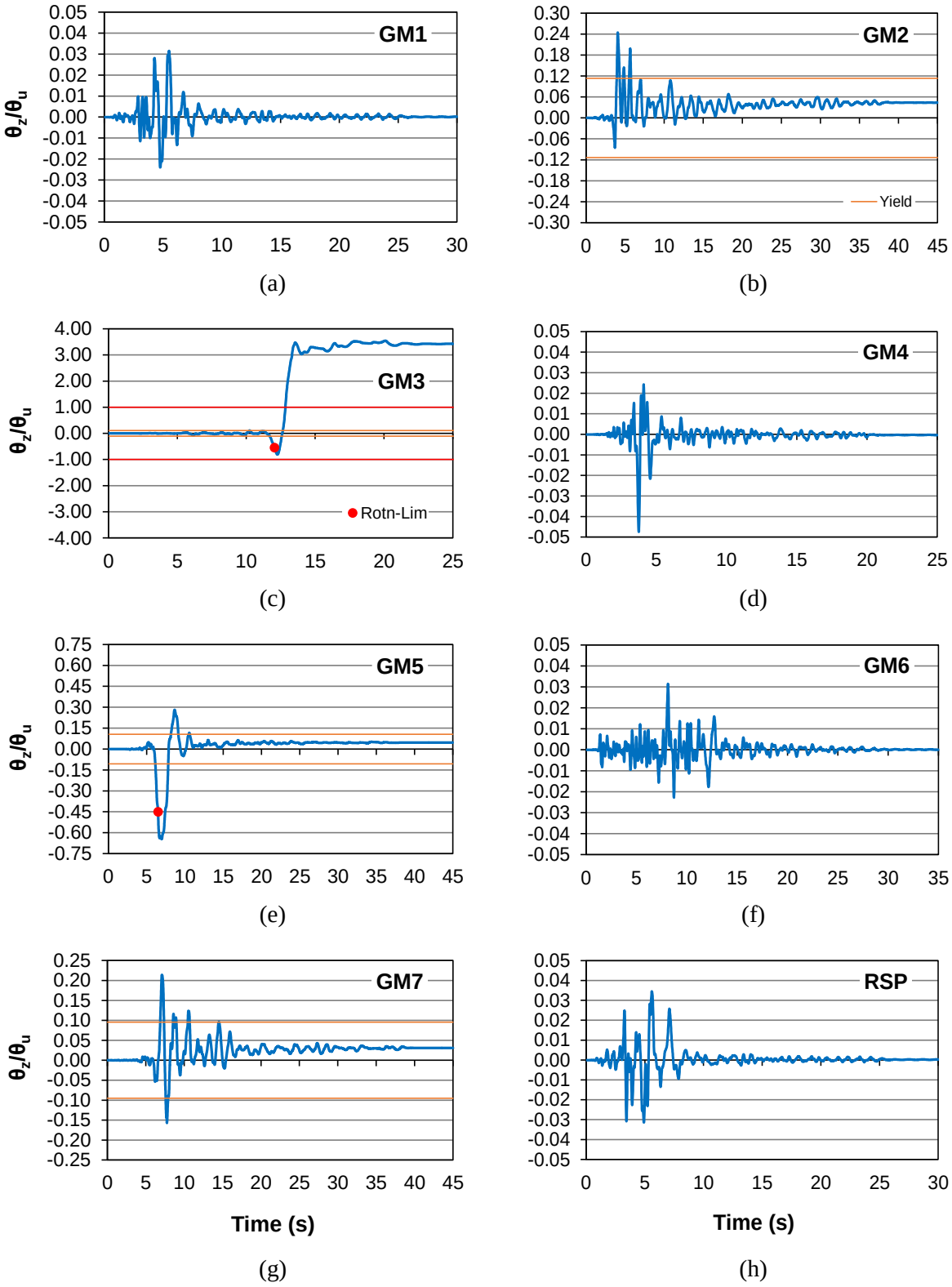

Figure 4-23 Time history of normalized plastic hinge rotation at Pier 1 column (100X-30Y).

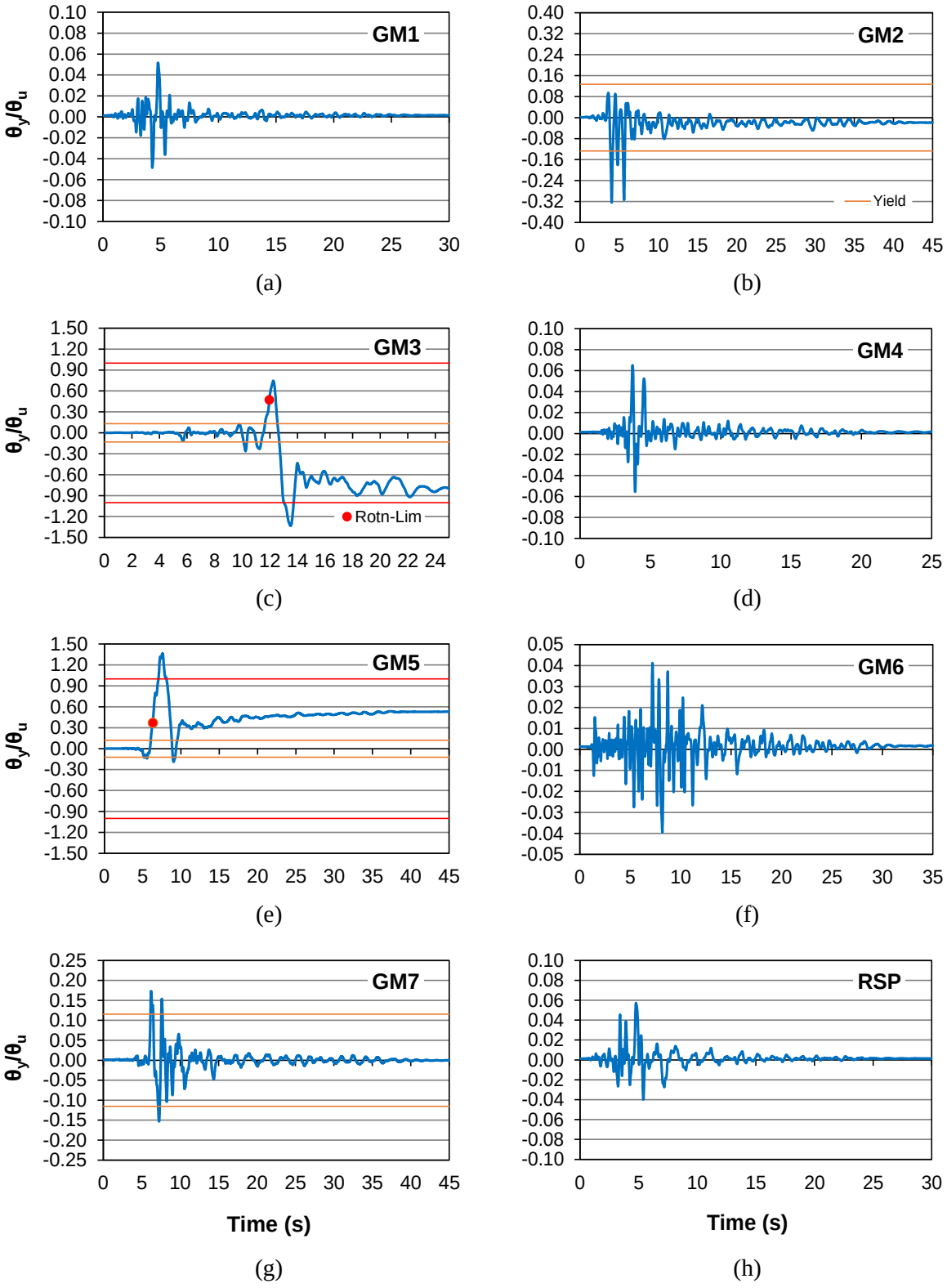

Figure 4-24 Time history of normalized plastic hinge rotation at Pier 1 column (100Y-30X).

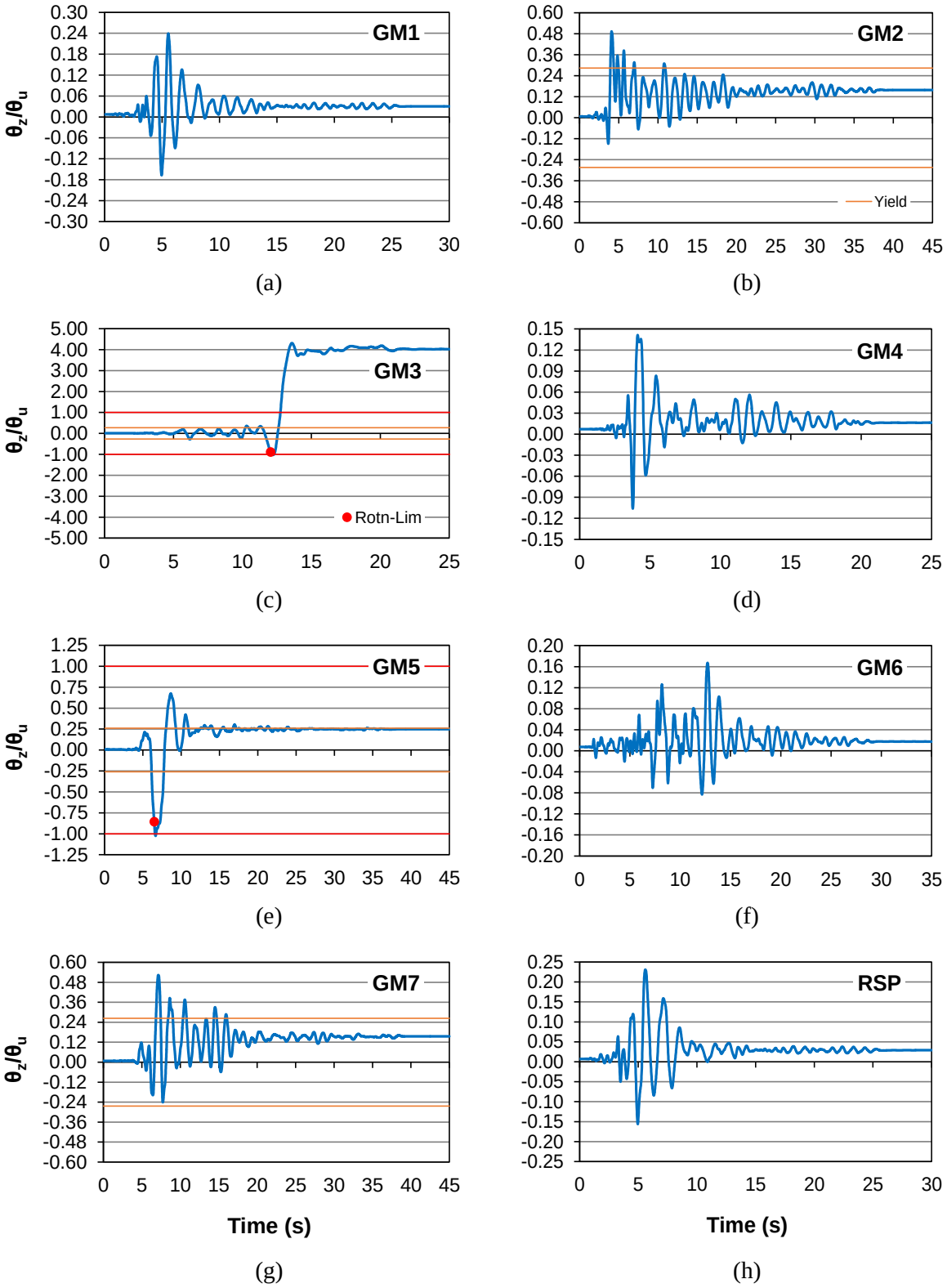

Figure 4-25 Time history of normalized plastic hinge rotation at Pier 3 column (100X-30Y).

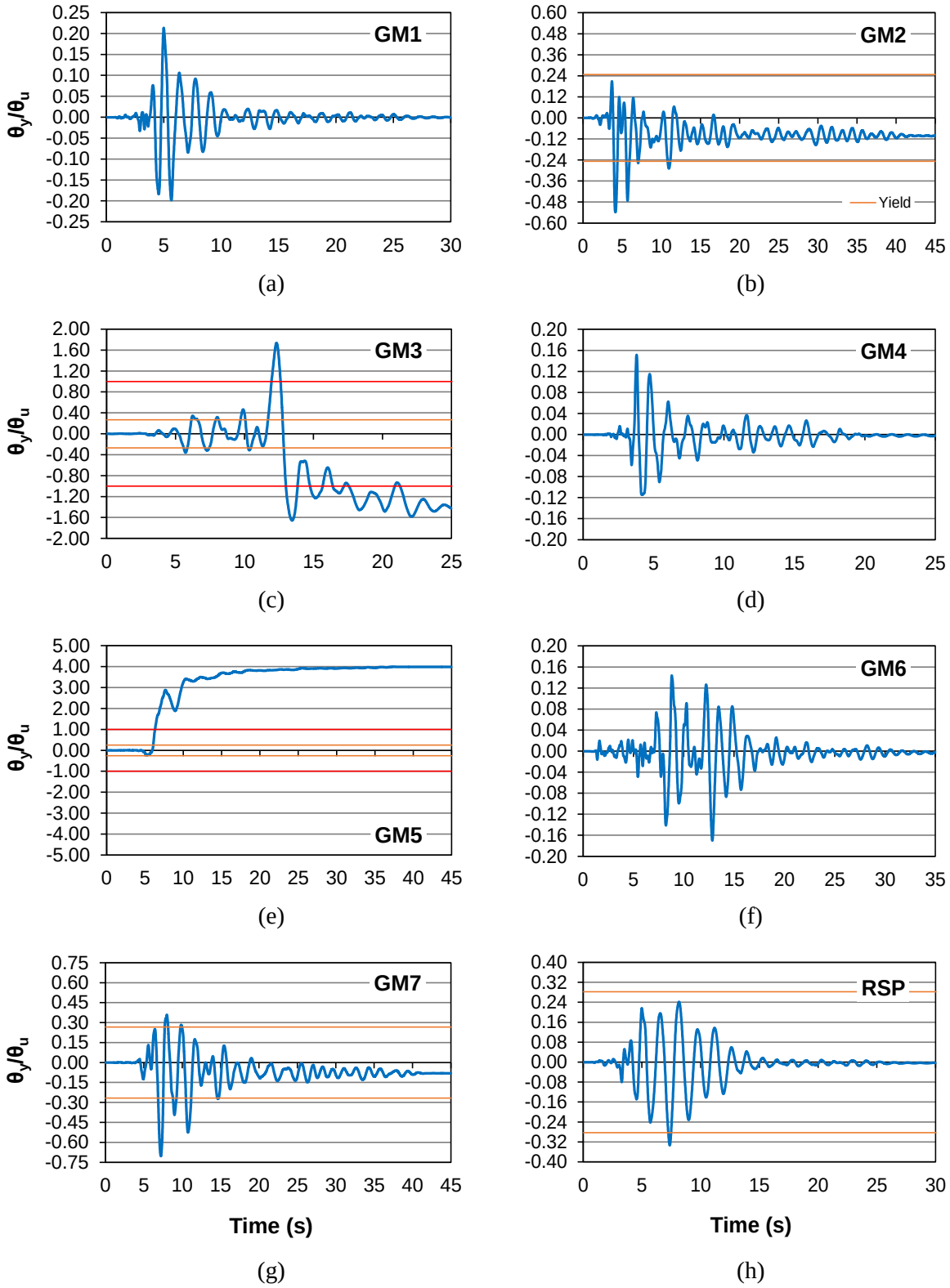

Figure 4-26 Time history of normalized plastic hinge rotation at Pier 3 column (100Y-30X).

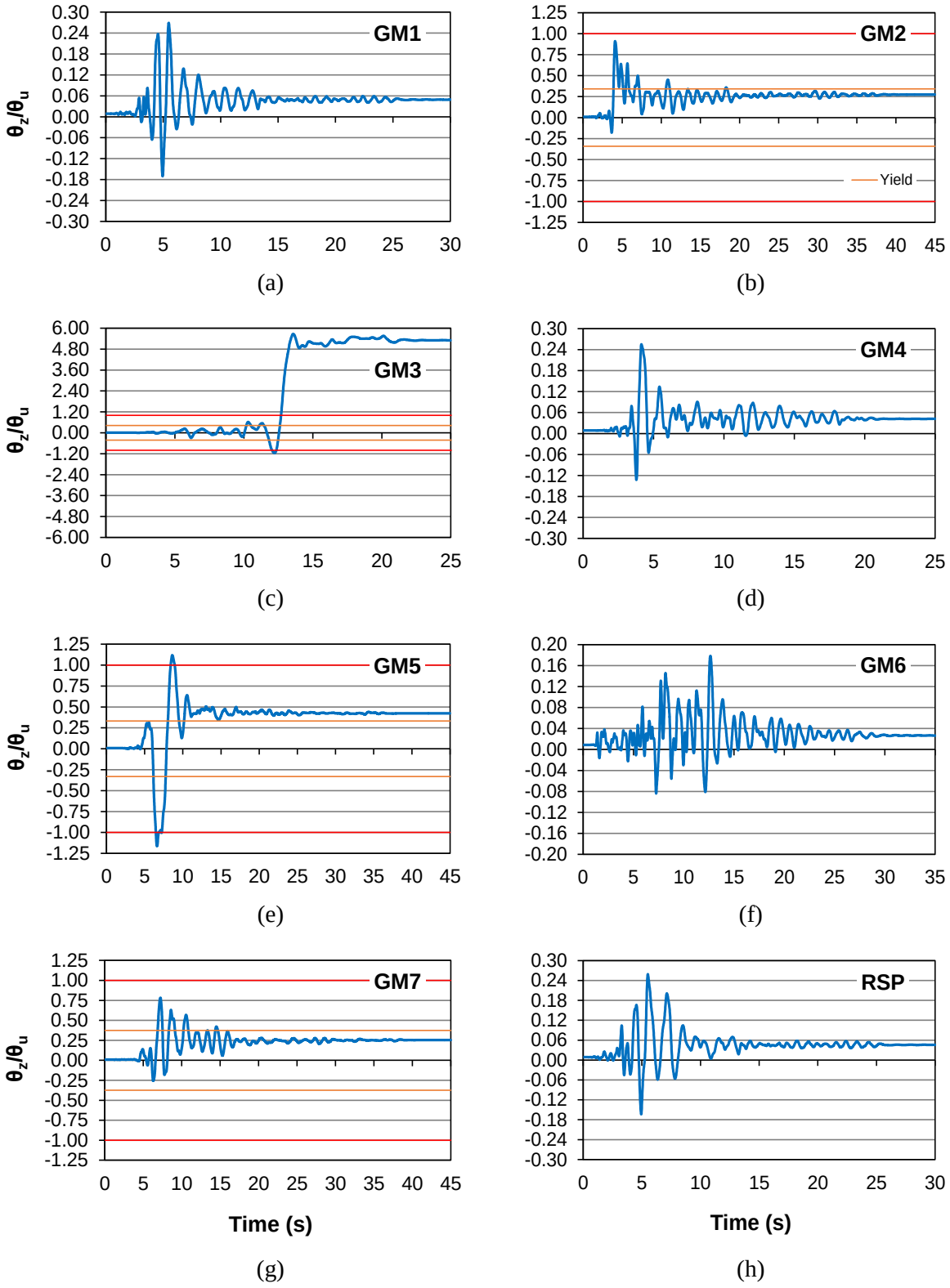

Figure 4-27 Time history of normalized plastic hinge rotation at Pier 5 column (100X-30Y).

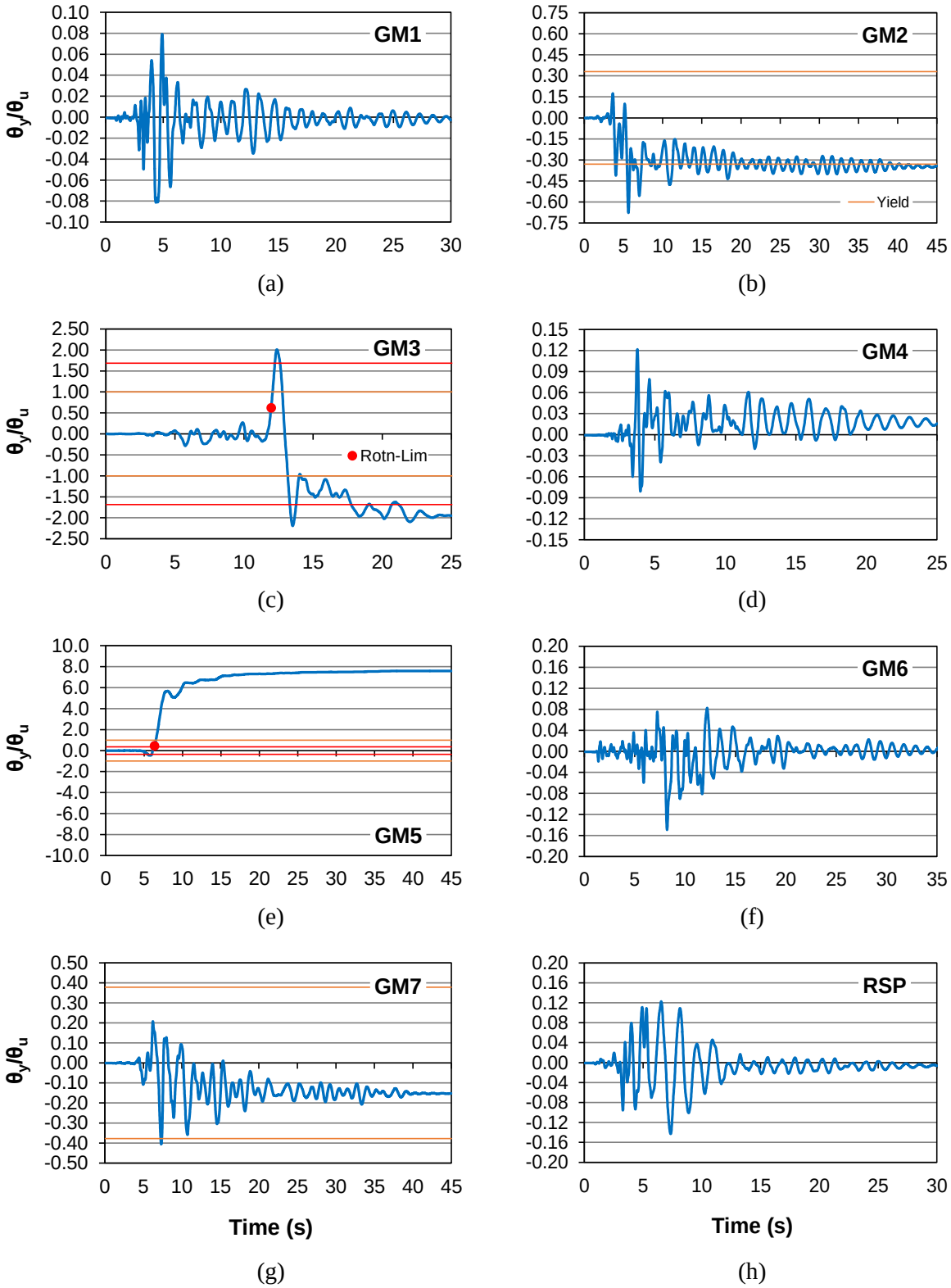

Figure 4-28 Time history of normalized plastic hinge rotation at Pier 5 column (100Y-30X).

The orange line indicates yielding of the longitudinal bars. The actual response of a column will be modified after shear failure. Thus, the plots following an identified shear failure may not be representative anymore. The rotation-based shear failure of a column is clearly displayed as the red line marking a demand/capacity ratio of unity. However, for Pier 1 and Pier 3 under GM3 for the 100X-30Y seismic loading (Figures 4-23c and 4-25c, respectively), the marker indicates the point in time where a rotation-based shear failure first occurred at another column for that ground motion and loading case. In this case, rotation-based shear failure first occurs for Pier 5 (Figure 4-27c); a marker is not used since shear failure occurs when the plot crosses the red line. These local failures can affect the global response of the bridge, which can then influence the behavior of the Pier 1 column (Figure 4-23c); thus, the marker is presented to indicate a possibly non-representative response after this point in time. Even if force-based shear failure discussed previously may not occur in the columns, this study indicates that rotation-based shear failure is possible for Bridge G-953. As shown in Figures 4-23 to 4-28, the θ/θ_{ult} ratio is greater than 1.0 under GM3 and GM5 for all cases except Pier 1 GM5 100X-30Y (Figure 4-23e). Rotation-based shear failure is approached for the Pier 5 column (100X-30Y) under GM2 (Figure 4-27b) and GM7 (Figure 4-27g).

Table 4-8 lists the maximum total hinge rotation demand at the exterior and interior columns for all ground motions for comparison with “Avg 1-7". Table 4-9 gives the total hinge rotation capacity, limited by ductile shear failure, for the exterior and interior columns, which ranges from 1.3 to 1.7 degrees. Values for all ground motions are listed for both tables and compared to “Avg 1-7”. As can be seen, the total hinge rotation under GM3 and GM5 is excessive, consistent with the high horizontal displacement and drift demands shown in Tables 4-1 and 4-2. GM3 creates a 9.18° rotation under 100X-30Y, while GM5 causes a 12.8° rotation for 100Y-30X;

both rotation demands were recorded at the exterior (northernmost/southernmost) columns of Pier 5. However, the remaining ground motions create much more moderate demands, either under or just exceeding the capacity of the column. The "Avg 1-7" maximum demand is 2.70° (100Y-30X), which is only a bit over the minimum capacity of 1.43° and suggests that a retrofitting strategy may be sufficient to prevent collapse.

Table 4-8 Column top sections total hinge rotation demand (in degrees)

Pier	Seismic Loading	GM1	GM2	GM3	GM4	GM5	GM6	GM7	RSP	Avg 1-7
1-Ext	100X-30Y	0.0796	0.471	5.57	0.0966	0.957	0.0726	0.424	0.0783	1.10
	100Y-30X	0.0772	0.469	2.27	0.0971	2.38	0.0623	0.310	0.0853	0.809
1-Int	100X-30Y	0.0780	0.465	5.44	0.0970	0.908	0.0630	0.391	0.0759	1.06
	100Y-30X	0.0772	0.469	2.27	0.0971	2.38	0.0623	0.310	0.0853	0.809
3-Ext	100X-30Y	0.433	0.859	6.96	0.243	1.71	0.294	0.978	0.417	1.64
	100Y-30X	0.341	0.822	2.80	0.241	6.40	0.257	1.08	0.505	1.71
3-Int	100X-30Y	0.432	0.918	7.03	0.230	1.77	0.285	1.01	0.411	1.67
	100Y-30X	0.324	0.914	2.74	0.239	5.94	0.244	1.16	0.513	1.65
5-Ext	100X-30Y	0.428	1.45	9.18	0.409	1.94	0.284	1.24	0.411	2.13
	100Y-30X	0.180	1.06	3.51	0.202	12.8	0.244	0.882	0.332	2.70
5-Int	100X-30Y	0.400	1.49	9.16	0.384	1.97	0.263	1.25	0.385	2.13
	100Y-30X	0.165	1.14	3.60	0.203	12.4	0.246	0.867	0.297	2.66

Table 4-9 Column top sections total hinge rotation capacity limited by ductile shear failure (in degrees)

Pier	Seismic Loading	GM1	GM2	GM3	GM4	GM5	GM6	GM7	RSP	Avg 1-7
1-Ext	100X-30Y	1.45	1.45	1.44	1.45	1.44	1.46	1.45	1.45	1.45
	100Y-30X	1.45	1.45	1.44	1.45	1.43	1.38	1.44	1.45	1.43
1-Int	100X-30Y	1.45	1.45	1.44	1.45	1.43	1.38	1.44	1.45	1.43
	100Y-30X	1.50	1.49	1.48	1.49	1.47	1.38	1.49	1.50	1.47
3-Ext	100X-30Y	1.53	1.54	1.54	1.54	1.54	1.54	1.54	1.54	1.54
	100Y-30X	1.52	1.51	1.51	1.52	1.51	1.37	1.52	1.51	1.49
3-Int	100X-30Y	1.60	1.59	1.56	1.60	1.58	1.60	1.59	1.60	1.59
	100Y-30X	1.60	1.59	1.55	1.60	1.57	1.37	1.59	1.60	1.55
5-Ext	100X-30Y	1.60	1.60	1.60	1.60	1.59	1.60	1.59	1.60	1.60
	100Y-30X	1.58	1.56	1.56	1.58	1.56	1.37	1.56	1.57	1.54
5-Int	100X-30Y	1.65	1.65	1.62	1.65	1.65	1.66	1.65	1.65	1.65
	100Y-30X	1.66	1.65	1.65	1.66	1.64	1.37	1.65	1.66	1.61

4.3 FLEXURAL RESPONSE OF COLUMNS

4.3.1 Moment-Curvature Behavior

Large plastic hinge rotations were discussed in section 4.2, indicating severe nonlinearity and stressing the need for an analysis of the flexural response. The moment-curvature response for the critical top section of Column 1 at Pier 1, 3, and 5 is recorded in Figures 4-29 to 4-34. The bending about the local-z axis of the column section governs for the 100X-30Y seismic loading, while the local-y axis governs for 100Y-30X. Since the column sections are circular and symmetric, the flexural capacity is similar for the local-y and local-z axes. When a flattening of the response curve is observed, yielding has occurred and initiated plastic hinge rotation. While GM3 and GM5 record very high curvatures, a fair number of ground motions only cause near-yielding or small inelastic deformations. GM2, GM3, GM5 and GM7 all create yielding in the columns, while the remaining ground motions, including RSP, come close to reaching the yield limit. The yield moment for the top section of the concrete columns appears to be approximately 24,000 k-in. for Pier 1, 23,000 k-in. for Pier 3, and 36,000 k-in. for Pier 5. This is consistent with the amount of longitudinal reinforcement provided for each section.

Tables 4-10 and Table 4-11 summarize the maximum moment and curvature demand, respectively, for the critical column top sections for Piers 1, 3, and 5 for all ground motions for comparison with "Avg 1-7". The 100Y-30X seismic loading governs most of the responses for Piers 1 and 3, while 100X-30Y causes large deformations in Pier 5 columns. As Table 4-11 proves, only some ground motions, especially GM3 and GM5, capture severe flexural deformations. With average curvatures as high as 0.0420 $in.^{-1}$ (100X-30Y) and 0.0445 $in.^{-1}$ (100Y-30X), the reason for rotation-based shear failure, and most likely flexural failure, is clear.

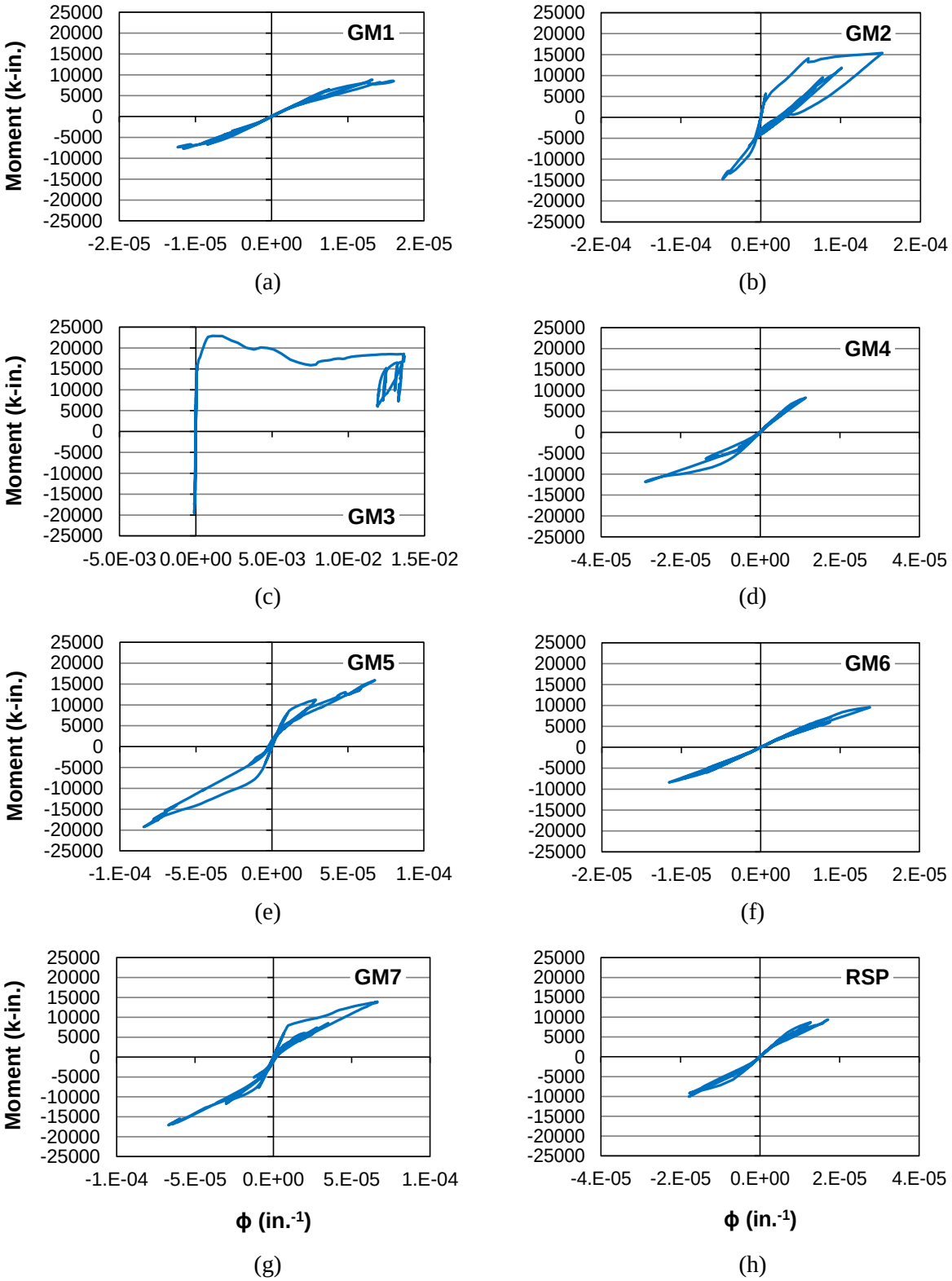

Figure 4-29 Moment-curvature demand for local-z axis for Pier 1 column top (100X-30Y).

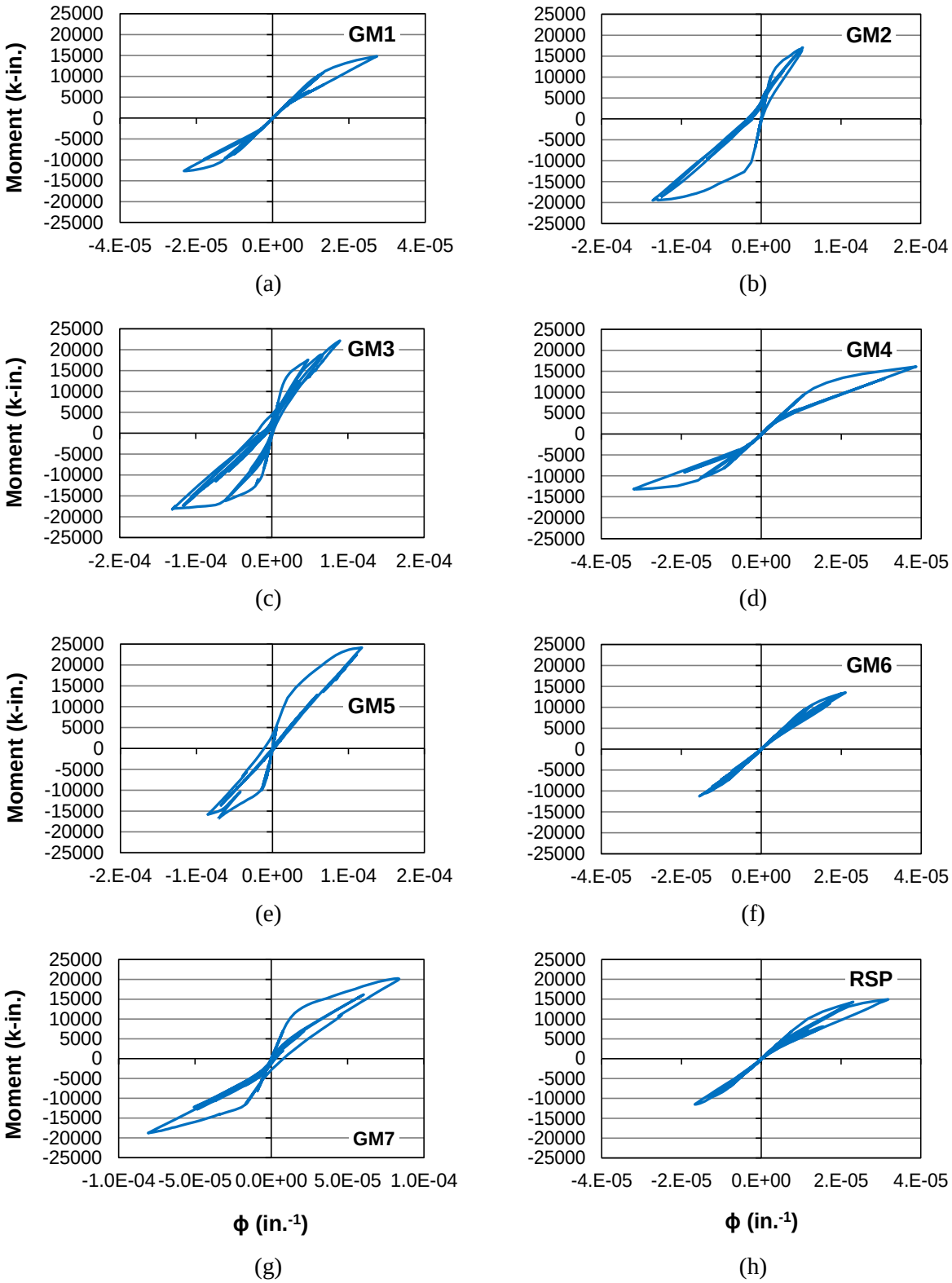

Figure 4-30 Moment-curvature demand for local-y axis for Pier 1 column top (100Y-30X).

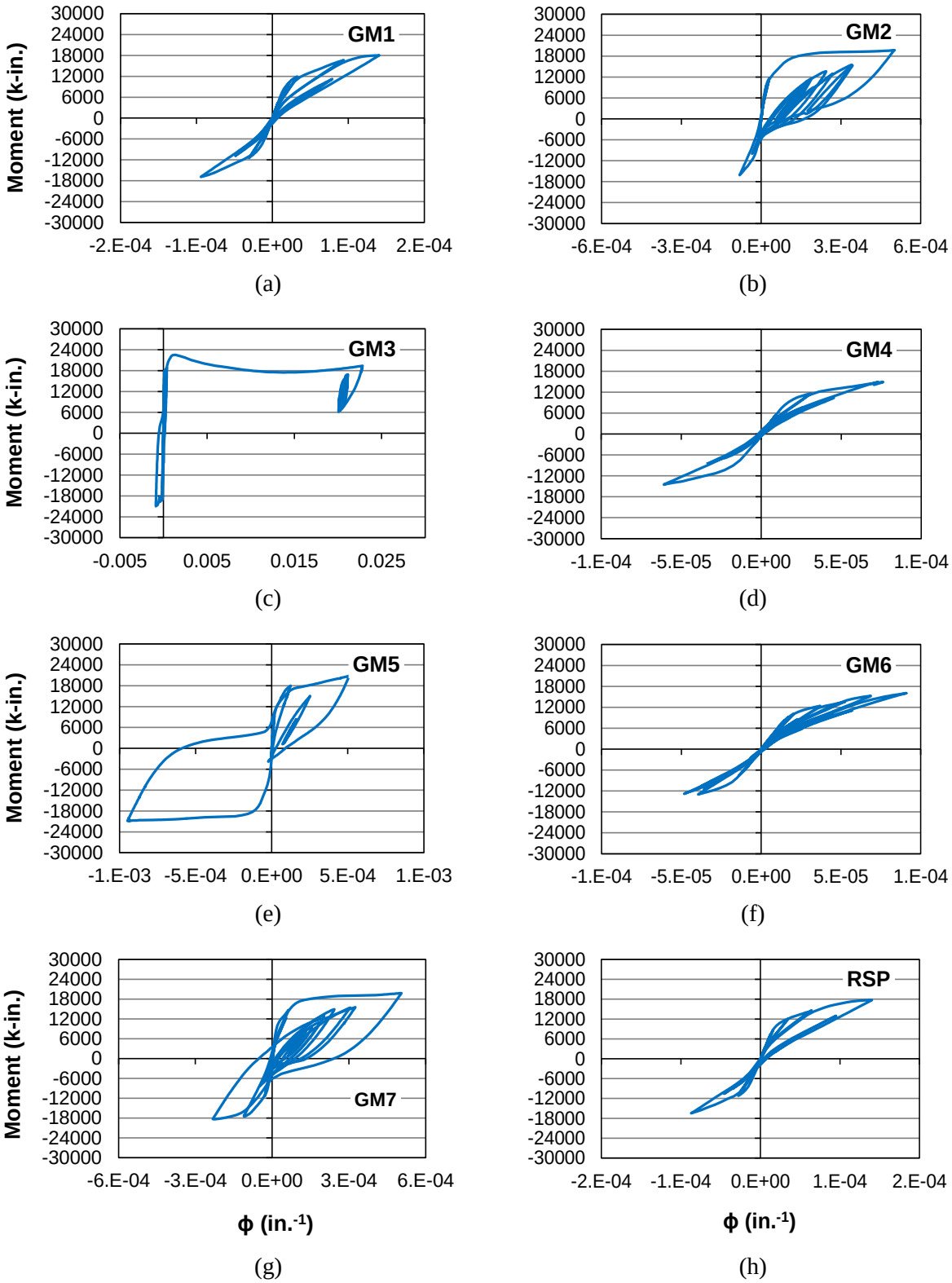

Figure 4-31 Moment-curvature demand for local-z axis for Pier 3 column top (100X-30Y).

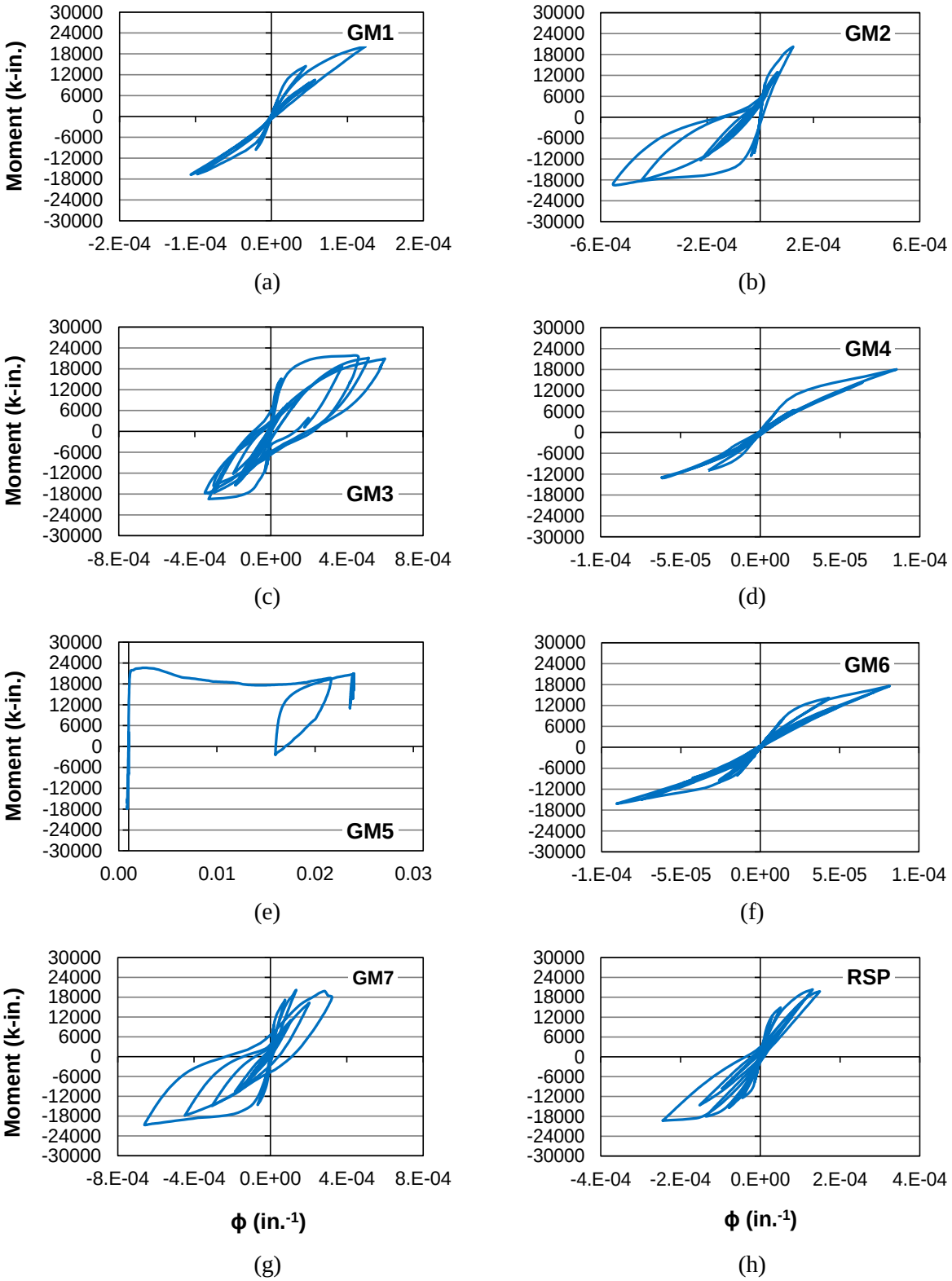

Figure 4-32 Moment-curvature demand for local-y axis for Pier 3 column top (100Y-30X).

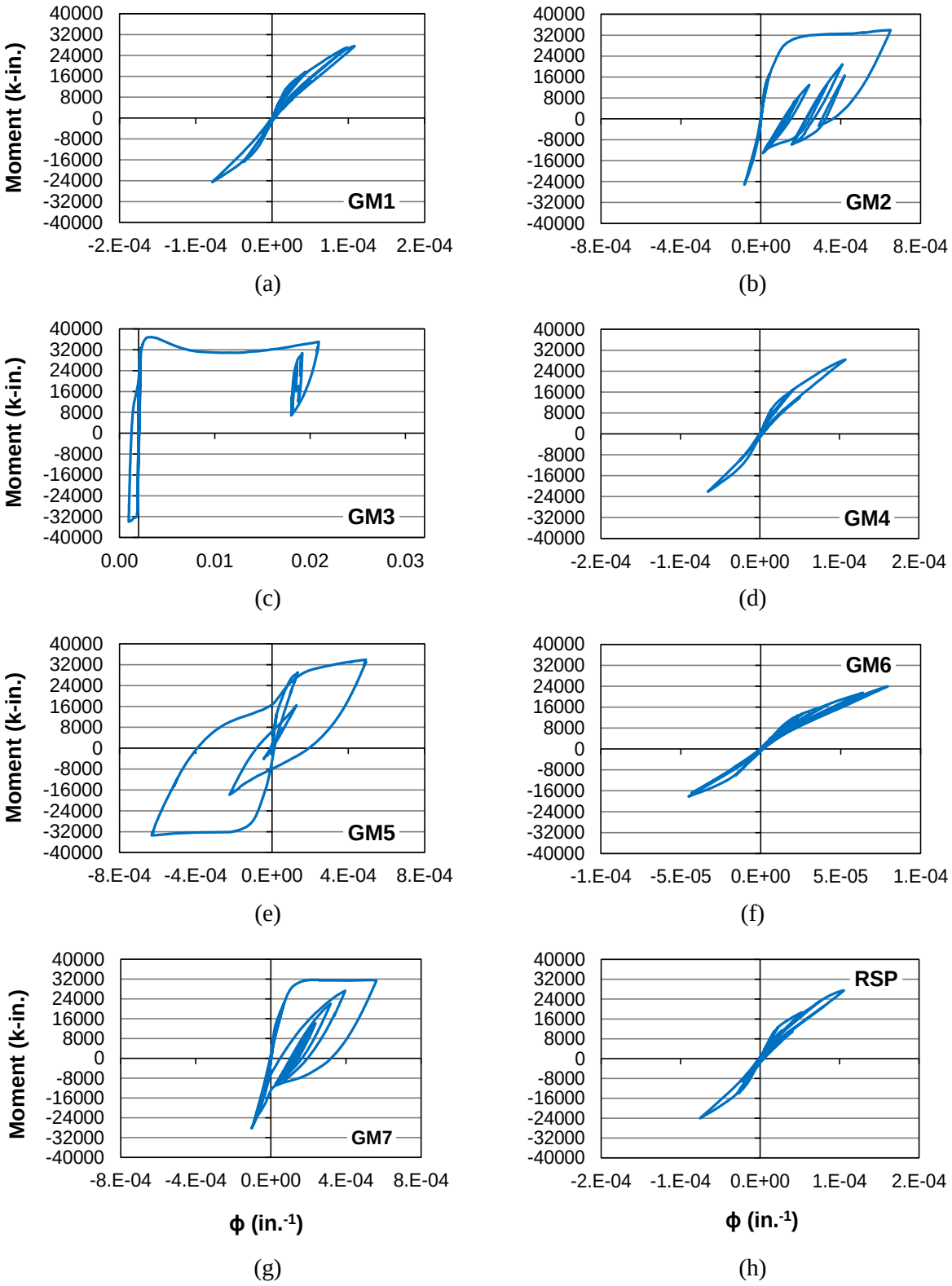

Figure 4-33 Moment-curvature demand for local-z axis for Pier 5 column top (100X-30Y).

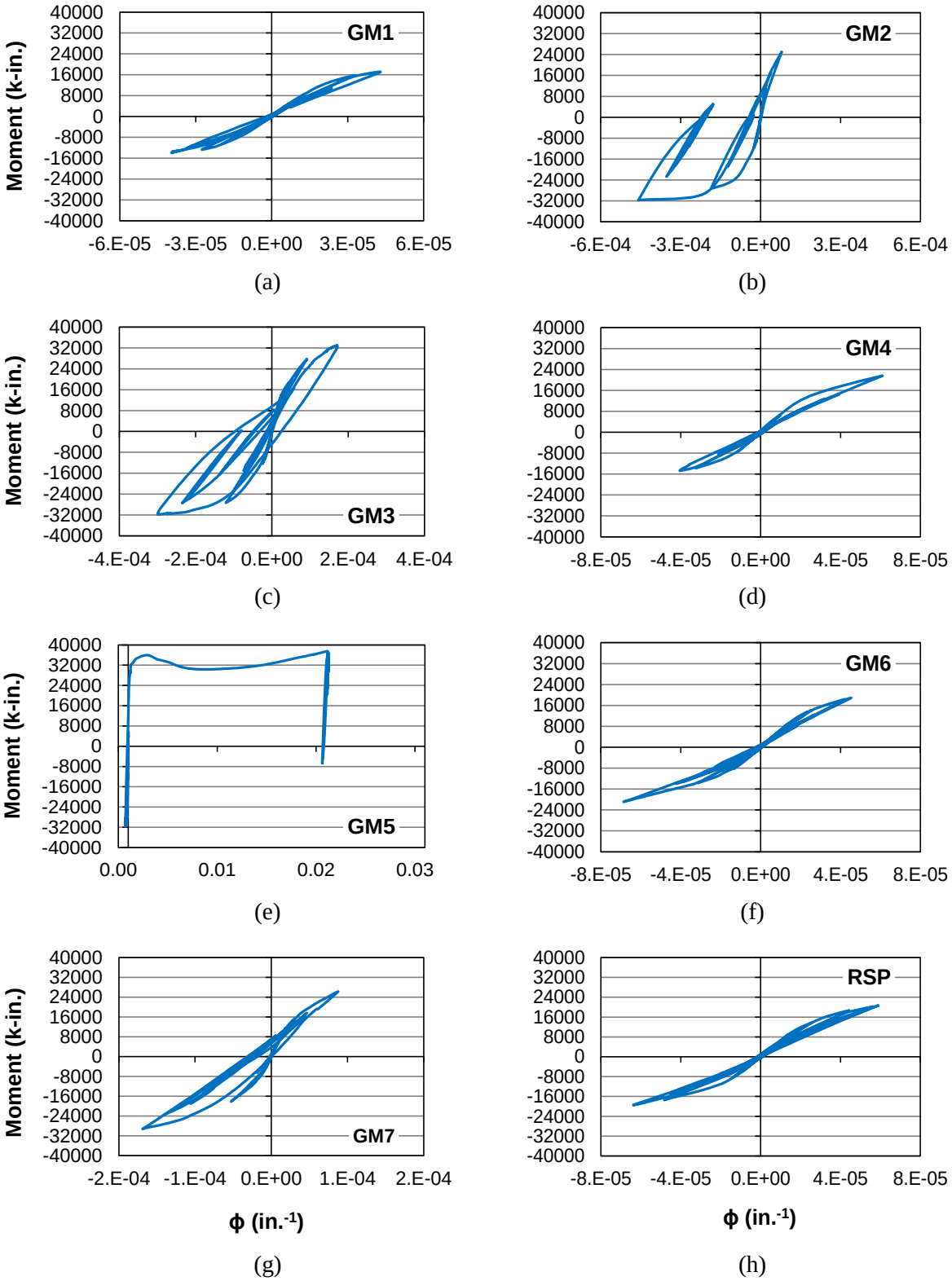

Figure 4-34 Moment-curvature demand for local-y axis for Pier 5 column top (100Y-30X).

Table 4-10 Maximum moment at column top critical sections (k-in.)

Pier	Seismic Loading	GM1	GM2	GM3	GM4	GM5	GM6	GM7	RSP	Avg 1-7
1	100X-30Y	13100	17800	23000	12300	19300	11200	17900	13000	16400
	100Y-30X	15700	23000	22900	17000	24900	14600	23500	16400	20200
3	100X-30Y	21700	23000	27100	18300	23700	19700	22800	21600	22300
	100Y-30X	21300	21900	24100	19300	24800	19300	23400	23100	22000
5	100X-30Y	29200	36600	39400	29800	36300	24800	34700	29000	33000
	100Y-30X	20900	34700	37100	22800	40000	24100	34100	26800	30500

Table 4-11 Maximum curvature at column top critical sections ($in.^{-1} \times 10^{-4}$)

Pier	Seismic Loading	GM1	GM2	GM3	GM4	GM5	GM6	GM7	RSP	Avg 1-7
1	100X-30Y	0.298	2.83	168	0.349	4.09	0.195	1.28	0.304	25.3
	100Y-30X	0.359	2.22	2.71	0.477	6.09	0.254	2.06	0.416	2.02
3	100X-30Y	1.63	5.23	262	0.843	17.6	1.06	5.34	1.60	42.0
	100Y-30X	1.24	5.83	7.02	0.854	289	0.906	6.60	2.44	44.5
5	100X-30Y	1.08	6.50	257	1.08	6.32	0.794	5.62	1.05	39.8
	100Y-30X	0.553	4.59	8.16	0.610	219	0.692	1.69	0.843	33.7

4.3.2 Response of Flexural Reinforcement of Columns

Since yielding is apparent from the moment-curvature discussion (Section 4.3.1), it is worthwhile to analyze the stress-strain behavior of the longitudinal reinforcing steel. Figures 4-35 to 4-40 display the normalized strain demand, $\varepsilon_s/\varepsilon_{s,u}$, for the steel at the topmost column section for the first column of Piers 1, 3, and 5. Strain capacity, $\varepsilon_{s,u}$, is the assumed ultimate strain at fracture or bucking as defined in Section 3.2.2. Positive values are for tension and negative values show compression. Additionally, the "Rotn-Lim" marker is shown to approximately indicate when rotation-based shear failure likely occurs, after which the recorded response is not reliable.

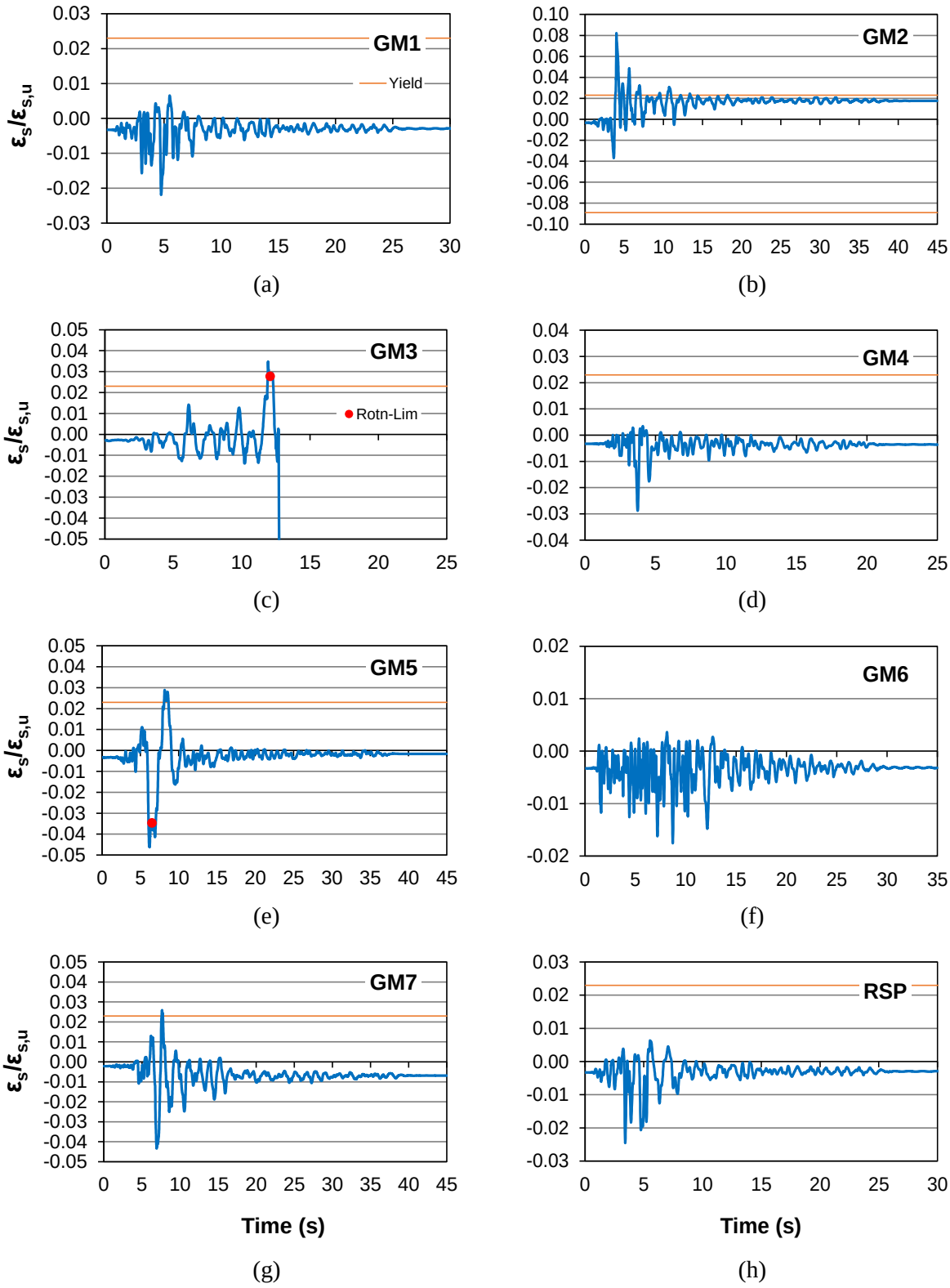

Figure 4-35 Time history of normalized strain of longitudinal bars in Pier 1 column top (100X-30Y).

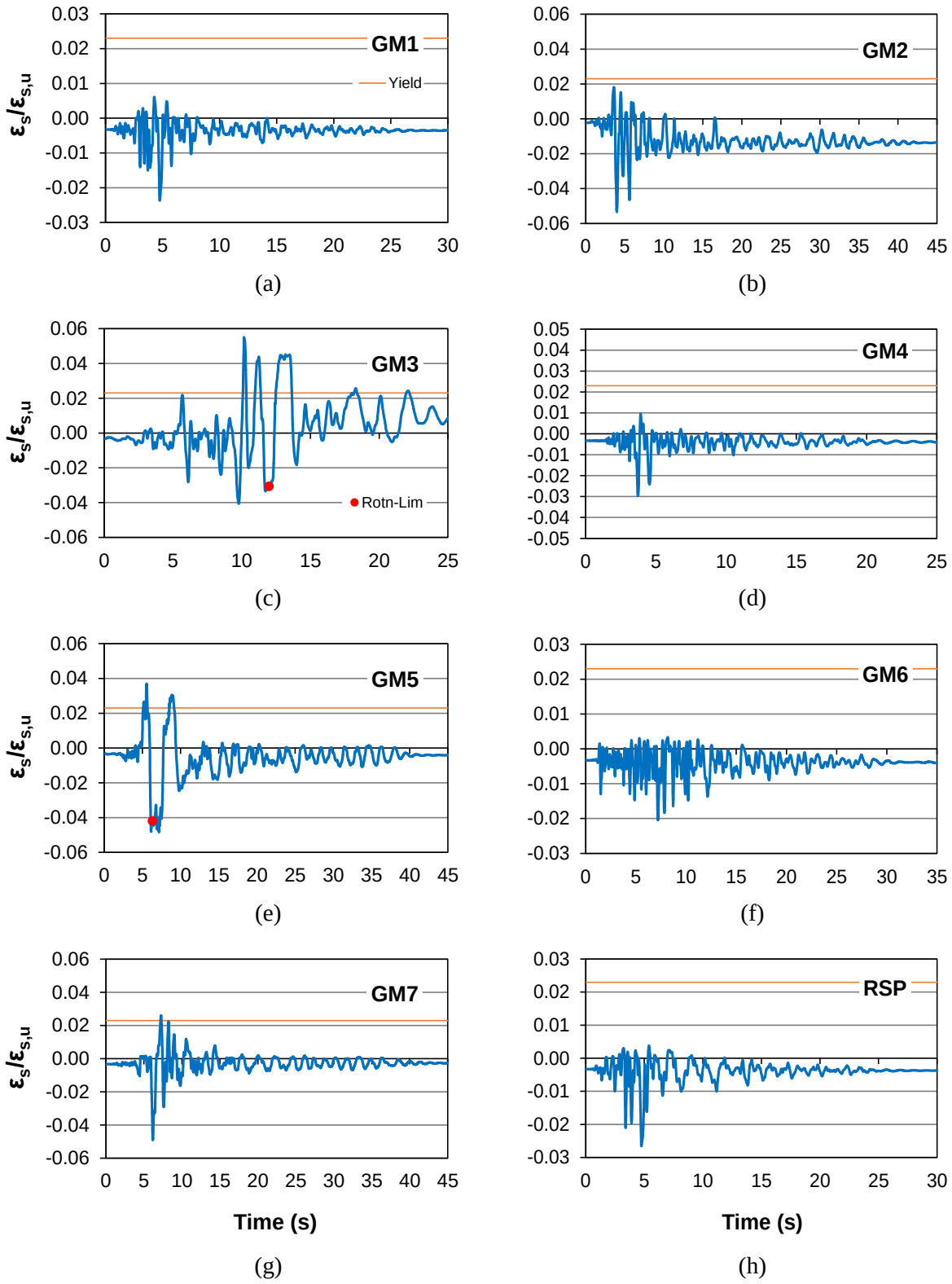

Figure 4-36 Time history of normalized strain of longitudinal bars in Pier 1 column top (100Y-30X).

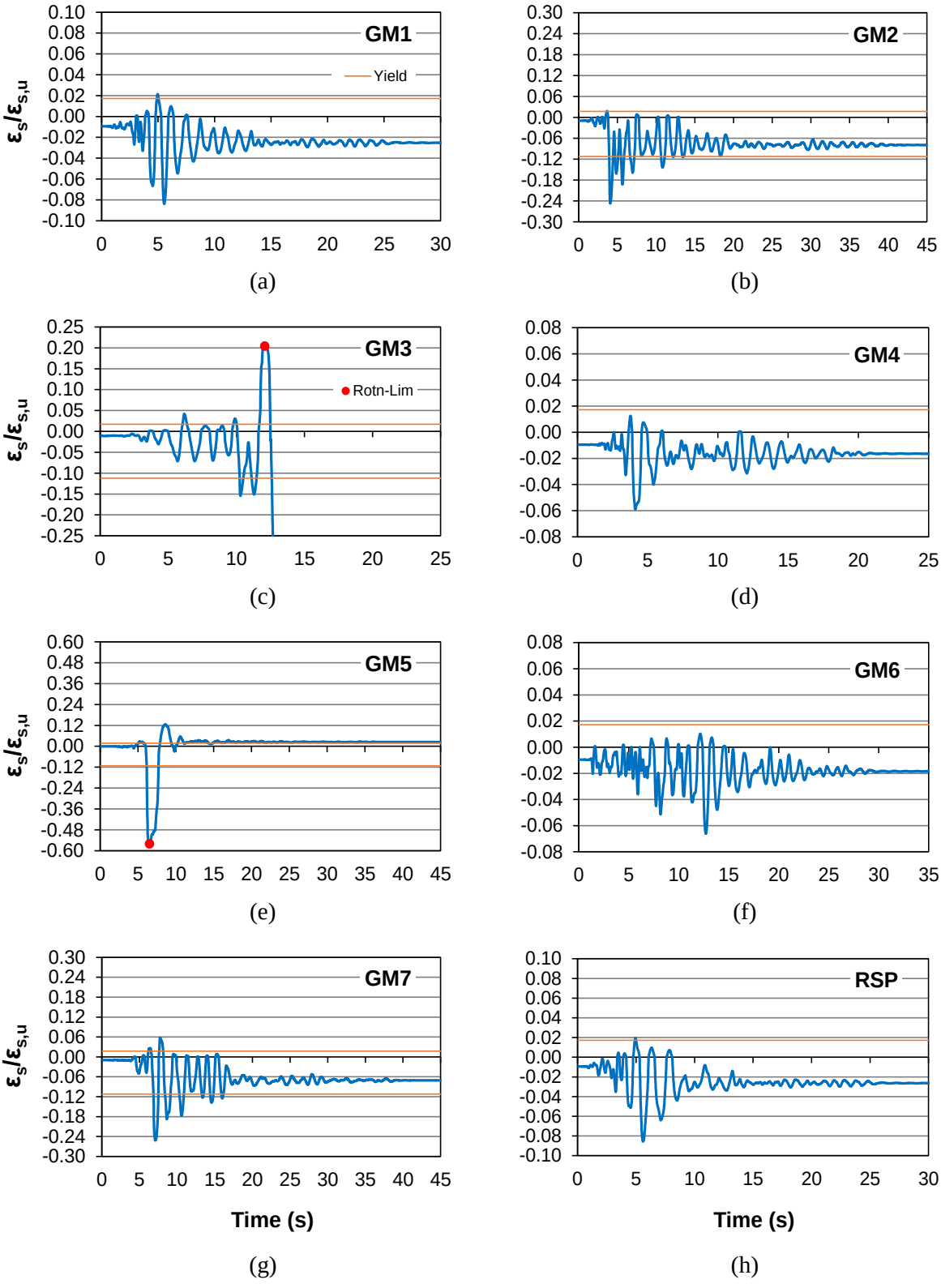

Figure 4-37 Time history of normalized strain of longitudinal bars in Pier 3 column top (100X-30Y).

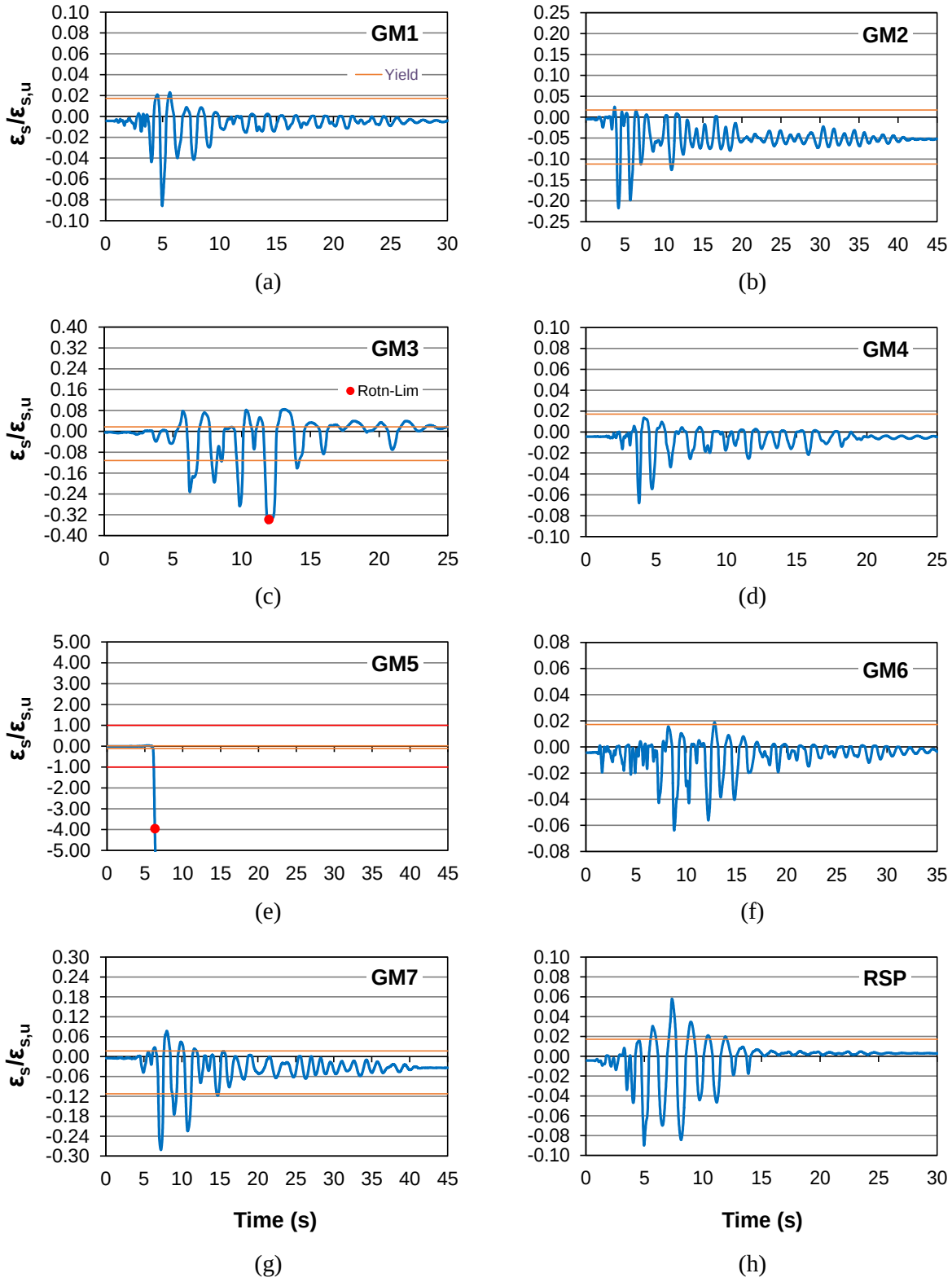

Figure 4-38 Time history of normalized strain of longitudinal bars in Pier 3 column top (100Y-30X).

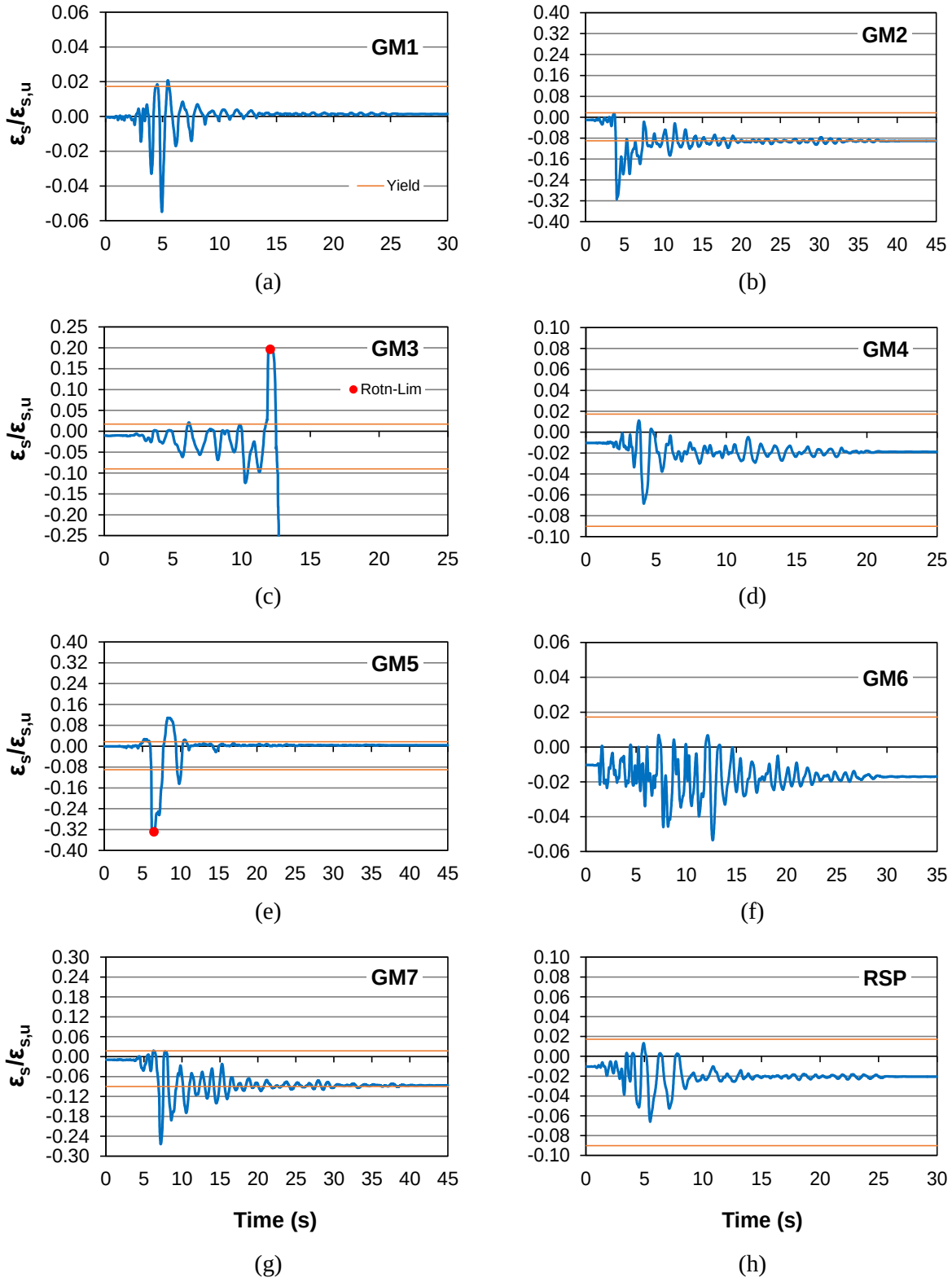

Figure 4-39 Time history of normalized strain of longitudinal bars in Pier 5 column top (100X-30Y).

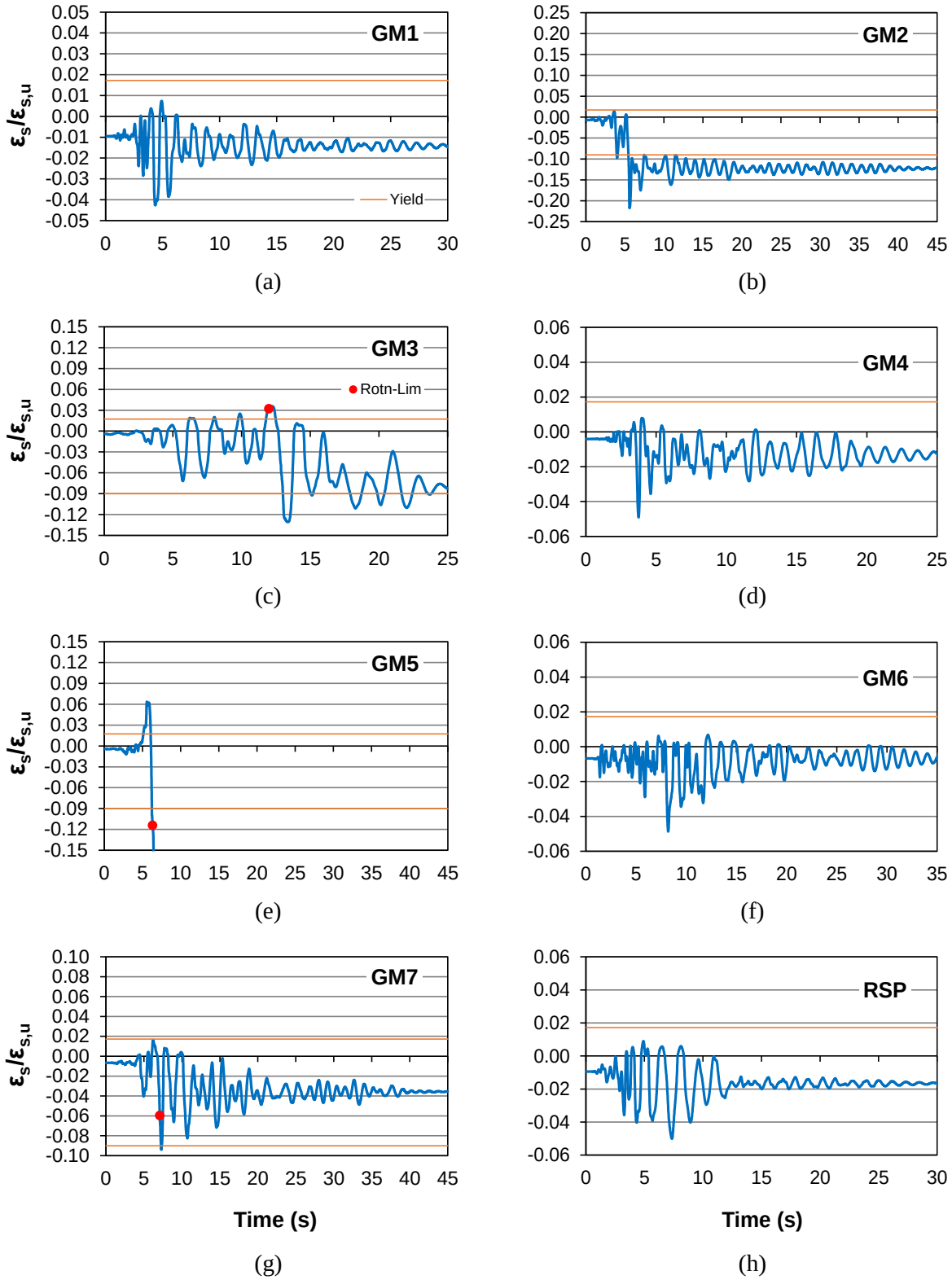

Figure 4-40 Time history of normalized strain of longitudinal bars in Pier 5 column top (100Y-30X).

From figures 4-35 to 4-40, it is seen that there is only a slight degree of yielding in Pier 1, but much more extensive yielding and for more ground motions in Piers 3 and 5. Pier 5 has the largest demands, and buckling in compression generally governs. Some of the plots for GM3 and GM5 show a dramatic increase in the demand/capacity ratio (not completely shown on the plot). These occurrences correlate with the high drift demands discussed in section 4.1 and explain the exceptionally high curvatures recorded. For these failure cases, the rotation-based shear failure occurs before the steel buckles or fractures except for Figure 4-38e (Pier 3 GM5 100Y-30X).

Table 4-12 the maximum compressive/tensile strain for all ground motions for comparison with "Avg 1-7". Yielding ($\varepsilon_s = 2.07 \times 10^{-3}$) occurs under many ground motions, and RSP does in fact detect yielding for some columns in Pier 3, but the large extent of inelastic deformations is not captured. Inelastic flexural failure in Bridge G-953 is indeed likely under GM3 and GM5, with buckling of the longitudinal reinforcement being significantly more likely than fracture.

Table 4-12 Strain demand for the longitudinal steel at the column top critical section (in./in. x 10^{-3}, T = tension, C = compression, yield at approximately 2.07 x 10^{-3} in./in.)

Pier	State	Seismic Loading	GM 1	GM 2	GM 3	GM 4	GM 5	GM 6	GM 7	RSP	Avg 1-7
1	T	100X-30Y	0.942	13.4	313	1.31	17.5	0.592	5.40	0.958	50.3
		100Y-30X	0.928	7.51	9.92	1.34	20.6	0.562	7.16	1.09	50.1
	C	100X-30Y	-0.683	-2.86	-393	-0.783	-3.59	-0.564	-1.56	-0.681	-57.6
		100Y-30X	-0.670	-1.83	-2.01	-0.778	-3.80	-0.548	-1.72	-0.716	-57.5
3	T	100X-30Y	4.46	15.7	473	2.13	46.0	2.76	15.9	4.41	80.0
		100Y-30X	3.00	17.5	19.7	1.92	479	2.26	19.3	6.95	142.4
	C	100X-30Y	-1.69	-5.06	-506	-1.19	-19.7	-1.36	-4.97	-1.73	-77.1
		100Y-30X	-1.59	-4.63	-6.48	-1.25	-599	-1.18	-5.20	-2.12	-159.8
5	T	100X-30Y	2.50	17.0	483	2.45	16.0	1.74	15.1	2.42	76.8
		100Y-30X	1.22	12.6	21.1	1.33	387	1.63	4.44	1.76	127.4
	C	100X-30Y	-1.54	-7.40	-478	-1.57	-7.75	-1.23	-6.05	-1.51	-71.9
		100Y-30X	-1.05	-5.00	-9.67	-1.13	-432	-1.25	-2.16	-1.42	-131.4

Figure 4-41 gives bar graphs of the maximum tension (Figure 4-41a) and compression (Figure 4-41b) strain demand/capacity ratios for the longitudinal steel at the column critical sections (including the fixed base of Pier 1); results are presented for RSP and "Avg 1-7". As can be seen, the strongly-reinforced Pier 1 does fairly well, while both fracture and buckling failures are highly likely for Piers 3 to 5. The response of RSP in comparison to the average is barely visible, once again indicating the inability of RSP to detect nonlinear deformation demand.

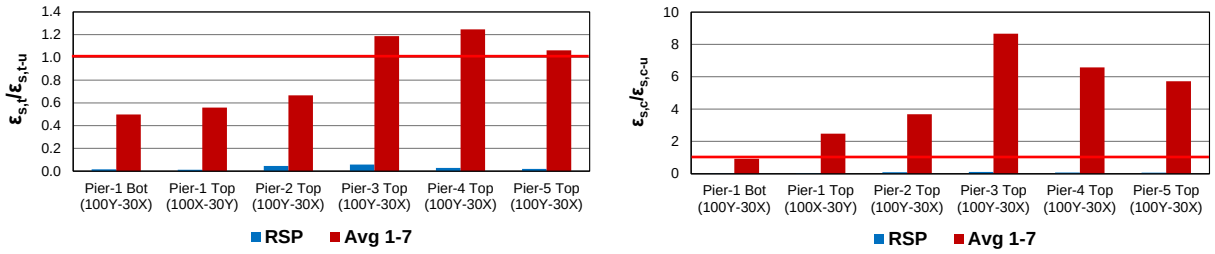

(a) Steel tension demand/capacity (b) Steel compression demand/capacity

Figure 4-41 Maximum normalized strain of longitudinal steel in column top for RSP and "Avg 1-7".

4.3.3 Columns Concrete Flexural Behavior

The compressive strain of concrete at the extreme fiber of confined core is studied. Figures 4-42 to 4-47 present the normalized compressive strain demand/capacity ratio, $\varepsilon_c/\varepsilon_{c,u}$, for concrete in the first column of Piers 1, 3, and 5 under 100X-30Y and 100Y-30X. The strain in the outermost fiber of the core concrete is recorded. Since the cover concrete lies just beyond this point, the orange line in several plots indicates the approximate strain at which spalling can be expected in the cover concrete (outermost cover fiber will have a strain larger than that recorded at the outermost core fiber). The marker on several plots indicates the point of possible rotation-based shear failure at some location in the substructure, after which the results cannot be considered reliable.

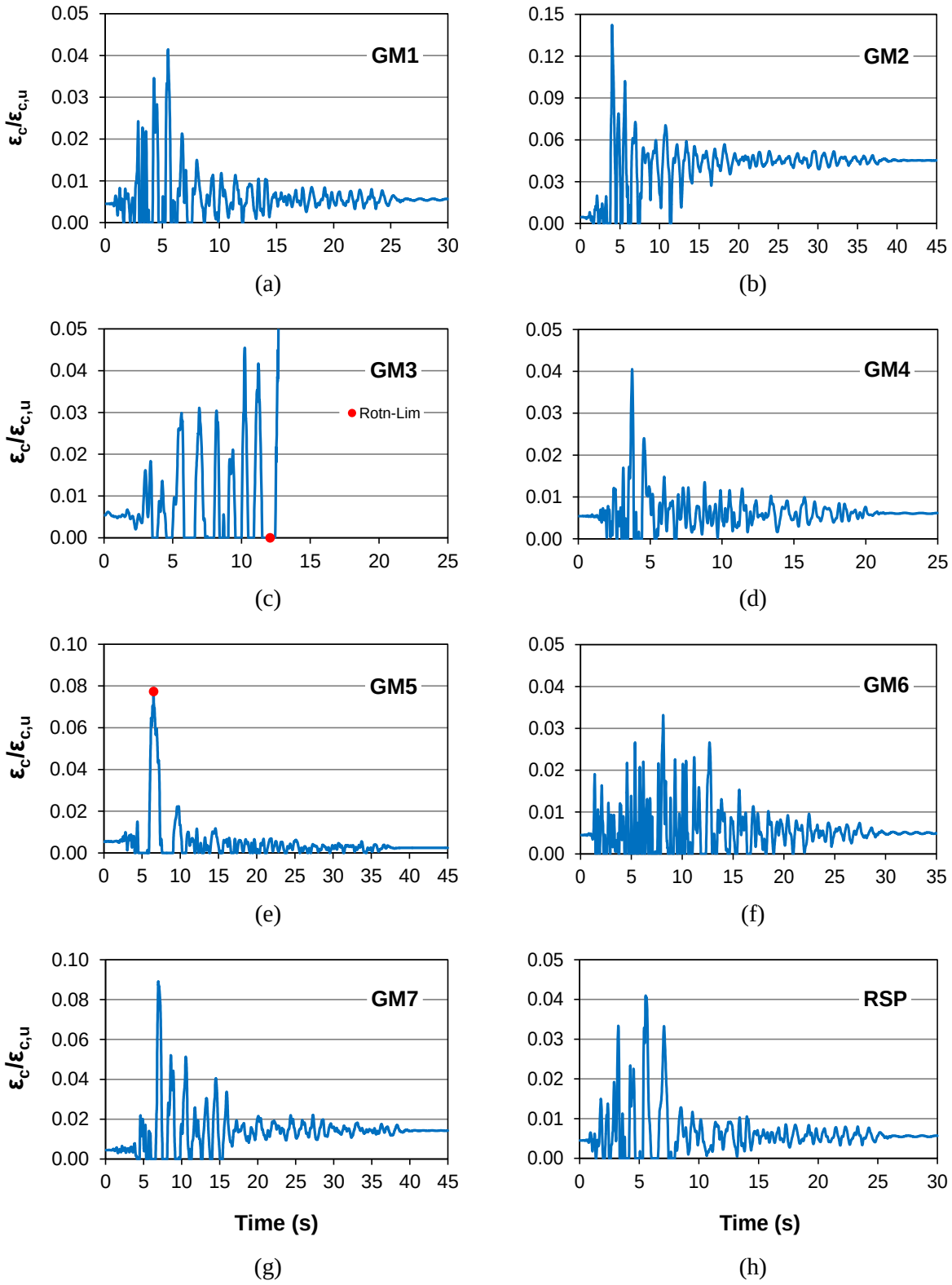

Figure 4-42 Time history of normalized strain of concrete in Pier 1 column top (100X-30Y).

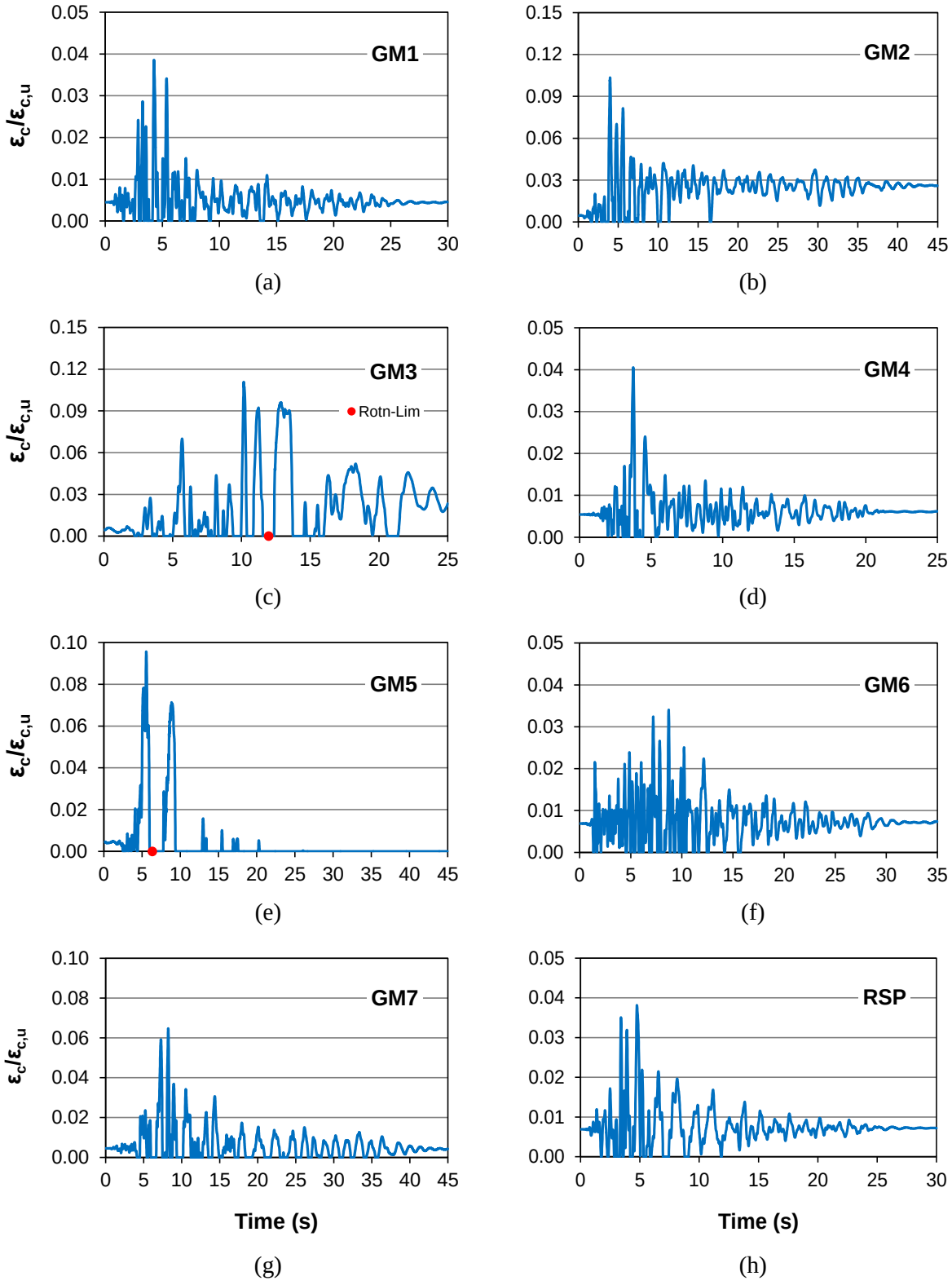

Figure 4-43 Time history of normalized strain of concrete in Pier 1 column top (100Y-30X).

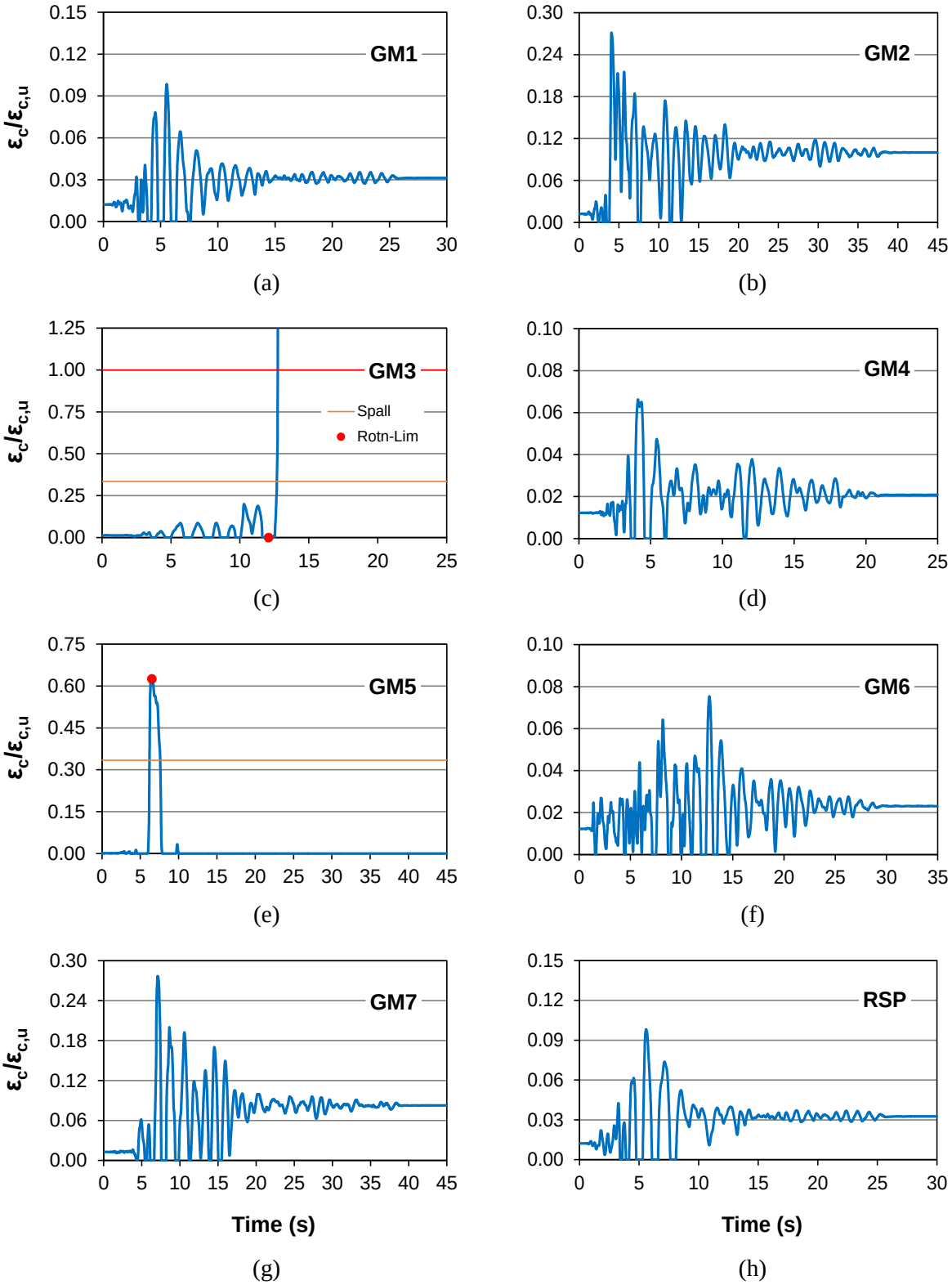

Figure 4-44 Time history of normalized strain of concrete in Pier 3 column top (100X-30Y).

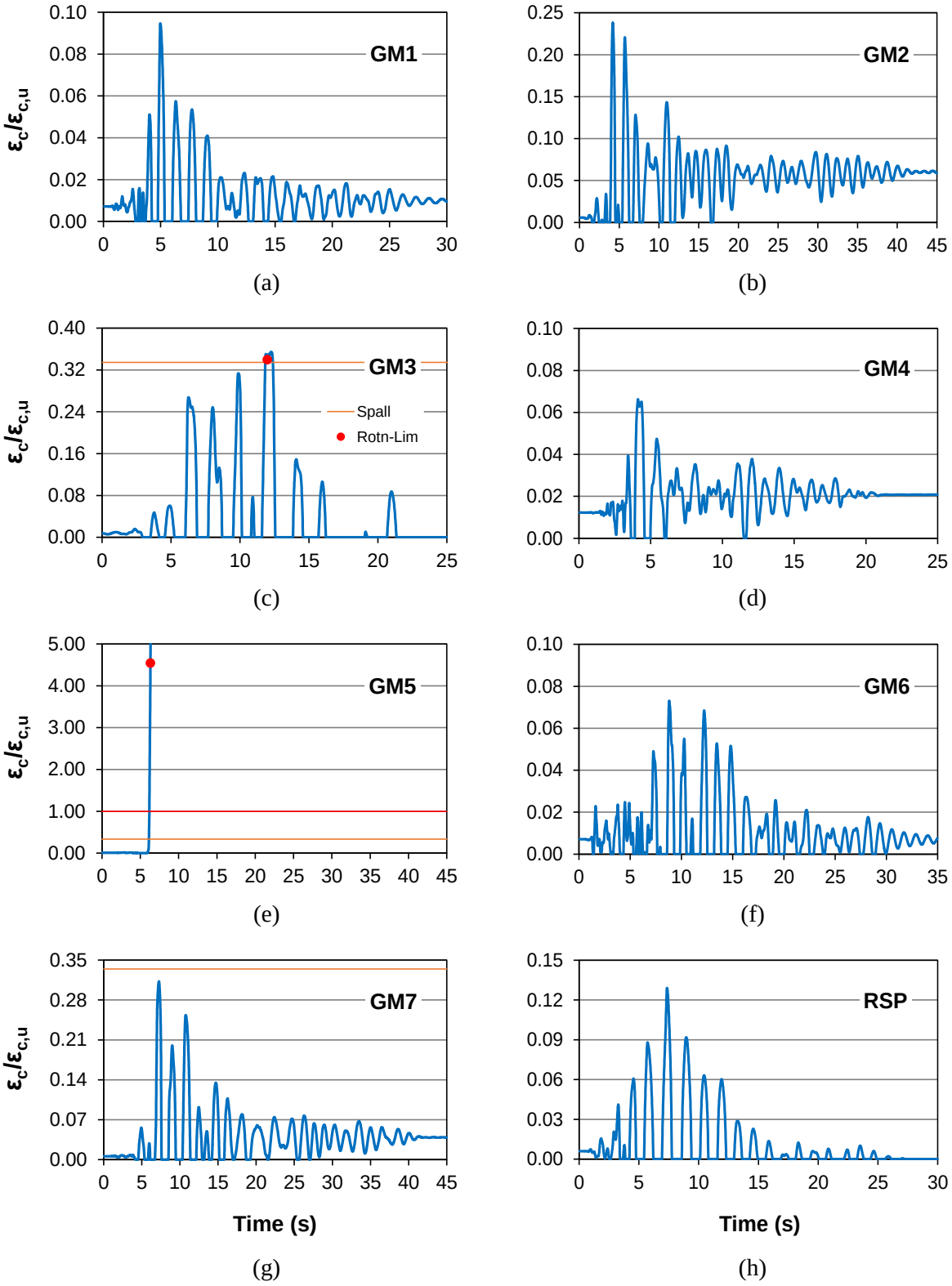

Figure 4-45 Time history of normalized strain of concrete in Pier 3 column top (100Y-30X).

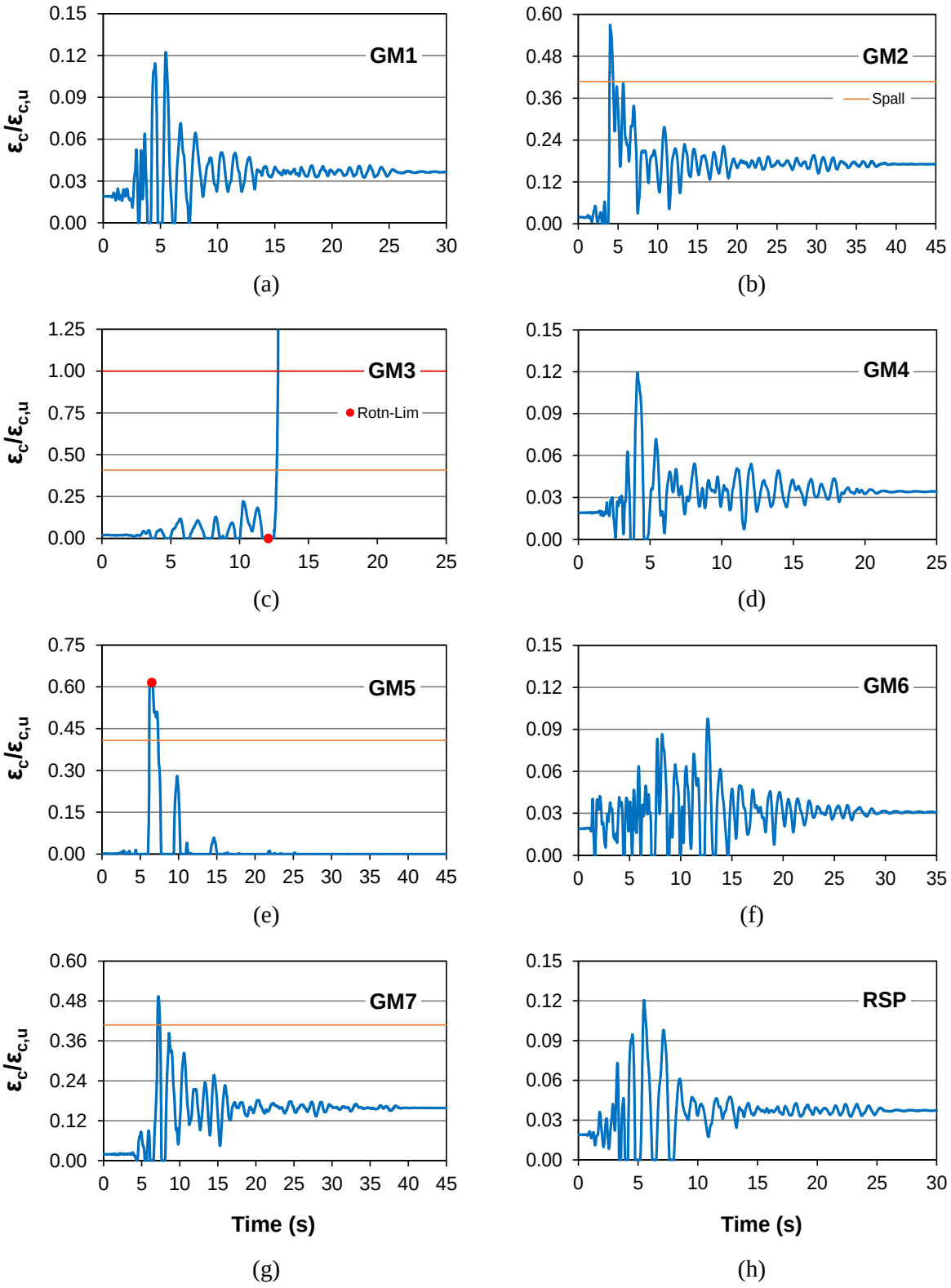

Figure 4-46 Time history of normalized strain of concrete in Pier 5 column top (100X-30Y).

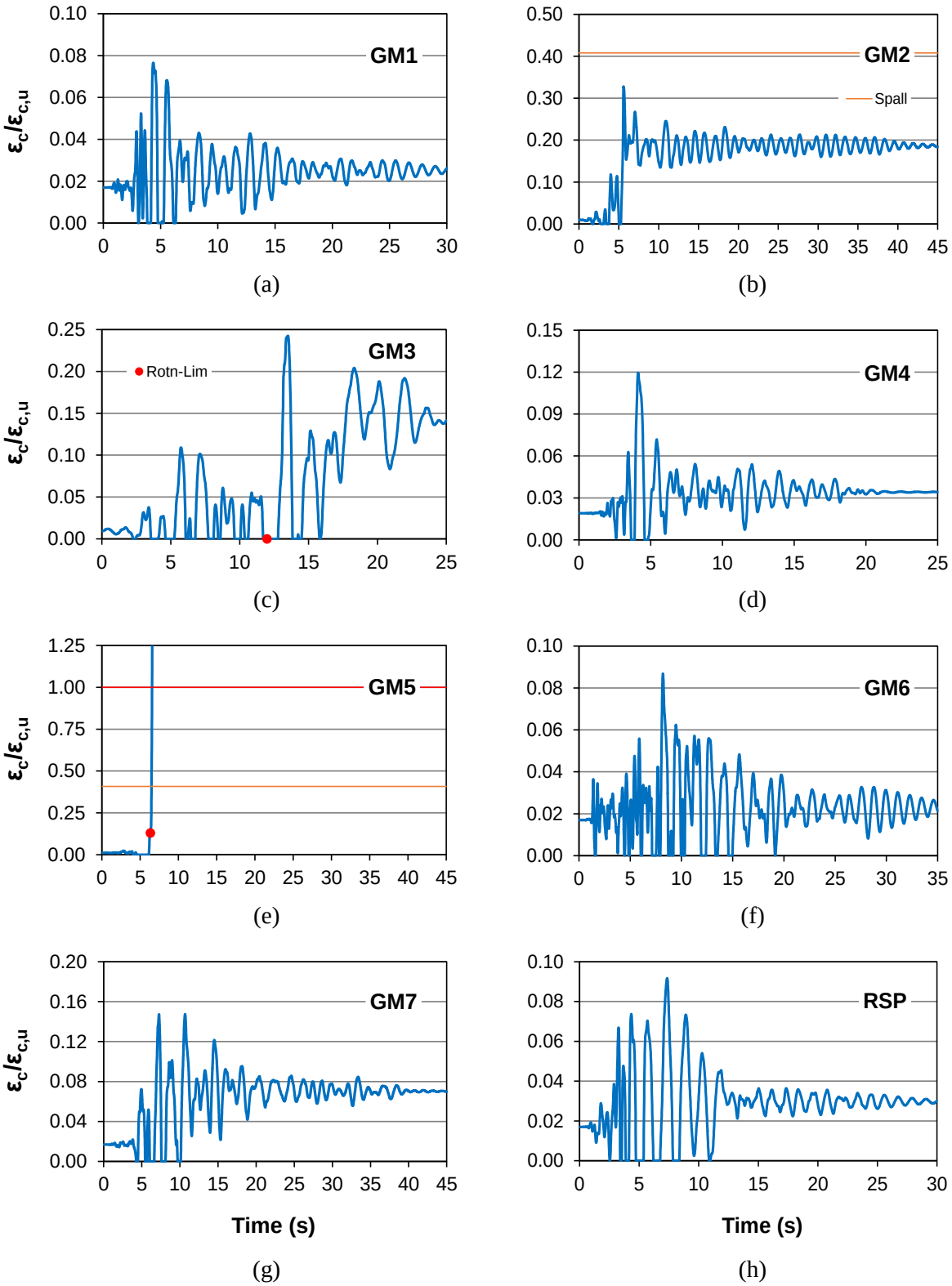

Figure 4-47 Time history of normalized strain of concrete in Pier 5 column top (100Y-30X).

Piers 3 and 5 have a significantly higher concrete core strain demand than Pier 1. The robust columns of Pier 1 have stronger concrete (f'_c of 5 ksi compared to 3 ksi for Piers 2 to 5) and do not even exceed a demand/capacity ratio of 0.15. The concrete of Piers 3 and 5 experiences crushing under GM3 for 100X-30Y and GM5 for 100Y-30X. It seems that the concrete and steel in the columns fail together. For the first column of Pier 1, under GM3 (100X-30Y), the steel (Figure 4-35c) and concrete (Figure 4-42c) strain demand both show a rapid increase at about 13s.

Table 4-13 gives the concrete strain demands for all ground motions for comparison with "Avg 1-7". The core concrete strain capacity is provided in parentheses, where "Ext" and "Int" denote the capacity for the exterior (northernmost/southernmost Column 1 and 4) and interior (Column 2 and 3) columns, respectively. Table 4-13 shows great differences between the ground motion records. GM3 and GM5 once again govern; where concrete strains exceeding -0.5 in./in. well exceed the maximum capacity of only -0.0118 in./in. to -0.0149 in./in.. The "Avg 1-7" value is highest for Pier 3 at -0.0855 in./in. for 100Y-30X, indicating that the average response still detects crushing of the concrete core by at least a factor of 5 (capacity is -0.0138 in/in. to -0.0149 in./in.). Interestingly, Pier 1 is much more sensitive to the 100X-30Y seismic loading, having an average strain demand of -0.0609 in./in. compared to only -0.00171 in./in. for 100Y-30X.

Table 4-13 Strain demand for the extreme fiber of the concrete core at the column top critical section (in./in. x 10^{-3}, capacity in parentheses)

Pier	Seismic Loading	GM1	GM2	GM3	GM4	GM5	GM6	GM7	RSP	Avg 1-7
1 (Ext: -11.6) (Int: -12.0)	100X-30Y	-0.704	-3.04	-416	-0.815	-3.50	-0.573	-1.65	-0.704	-60.9
	100Y-30X	-0.680	-1.85	-2.05	-0.815	-4.15	-0.564	-1.83	-0.746	-1.71
3 (Ext: -14.9) (Int: -13.8)	100X-30Y	-1.71	-4.64	-498	-1.12	-19.8	-1.32	-4.71	-1.70	-75.9
	100Y-30X	-1.42	-5.27	-5.30	-1.12	-578	-1.09	-5.76	-1.93	-85.5
5 (Ext: -12.2) (Int: -11.8)	100X-30Y	-1.50	-7.28	-474	-1.47	-7.78	-1.20	-6.06	-1.48	-71.4
	100Y-30X	-1.02	-4.02	-8.57	-1.47	-424	-1.15	-2.02	-1.35	-63.1

4.4 TORSIONAL RESPONSE

Only Pier 1 has fixed connections at the base and top of its columns, and is thus the only pier to experience torsion. Figures 4-48 and 4-49 plot the pure normalized torsion demand, T/T_u, on Column 1 of Pier 1 for the 100X-30Y and 100Y-30X seismic loadings, respectively. T_u was determined according to Section 3.2.10.5.

In general, the torsional demand is not high; however, GM3, GM5, and GM7 all impose significant torsional demand, and the maximum torsion on the columns of Pier 1 is much greater for the transverse 100Y-30X seismic loading. GM5 under 100Y-30X (Figure 4-49) actually causes torsional failure by a significant margin. This is the same loading case that causes force-based shear failure for the Pier 1 column due to shear-torsion interaction (Figure 4-16e).

Table 4-14 provides the maximum torsion demand and torsion demand/capacity ratio for all ground motions for comparison with "Avg 1-7". In Figure 4-10 it was shown that the 100Y-30X seismic loading causes much larger in-plane rotation of the superstructure. This can lead to increased torsion demand in the columns of Pier 1. While a failure is possible under GM5 (100Y-30X), the average demand is only at 50% of the column capacity. As previously stated, the effect of force-based shear or torsion alone on Pier 1 is not of concern, but the interaction of both could cause a serious limit state.

Table 4-14 Pier 1 columns torsion

Pier	Seismic Loading	GM1	GM2	GM3	GM4	GM5	GM6	GM7	RSP	Avg 1-7
Torsion (k-in.)	100X-30Y	288	400	1169	241	752	195	877	277	560
	100Y-30X	287	590	2300	228	5511	605	1418	436	1563
Torsion Dem/Cap	100X-30Y	0.09	0.13	0.38	0.08	0.24	0.06	0.28	0.09	0.18
	100Y-30X	0.09	0.19	0.74	0.07	1.77	0.19	0.46	0.14	0.50

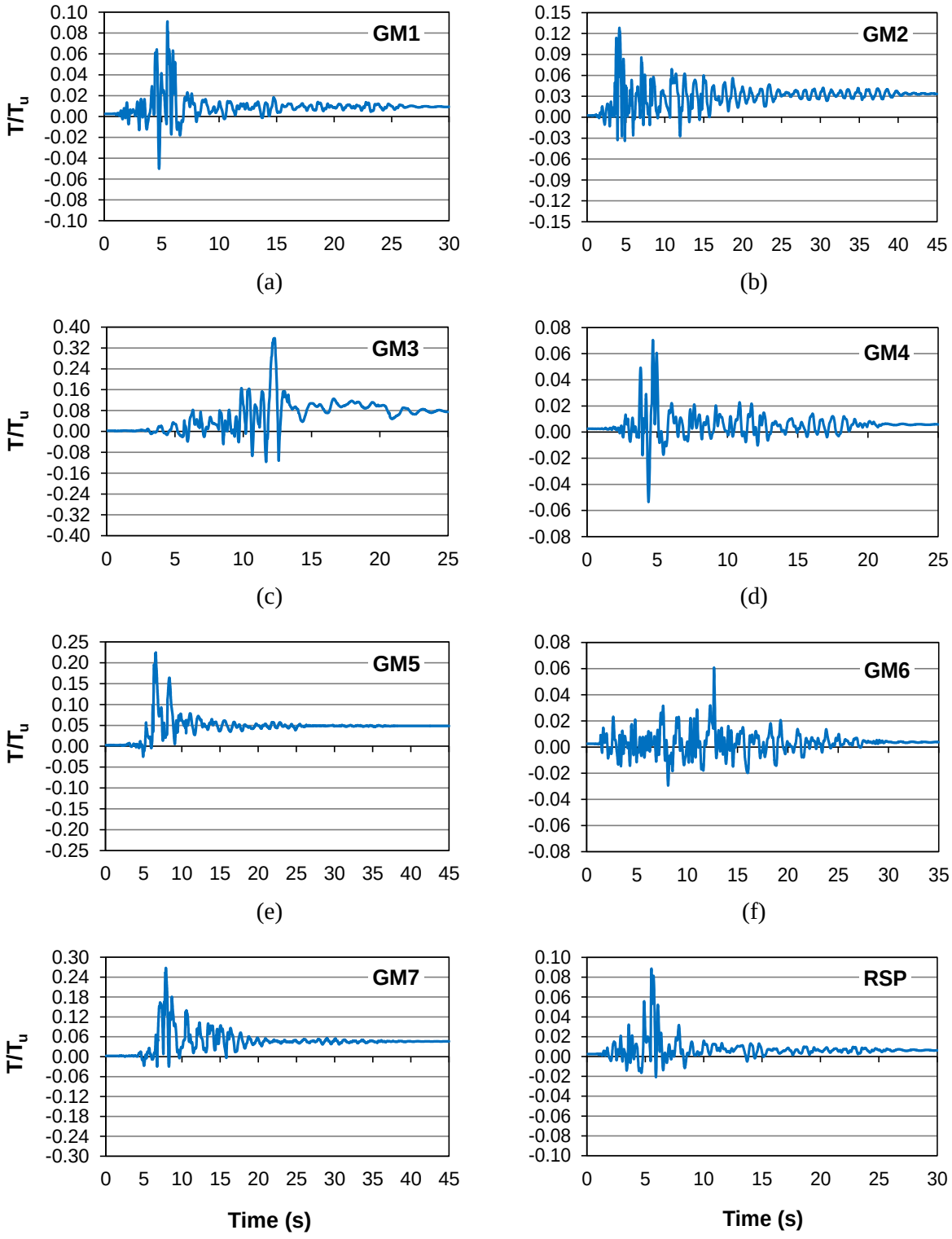

Figure 4-48 Normalized torsion for Pier 1 column (100X-30Y).

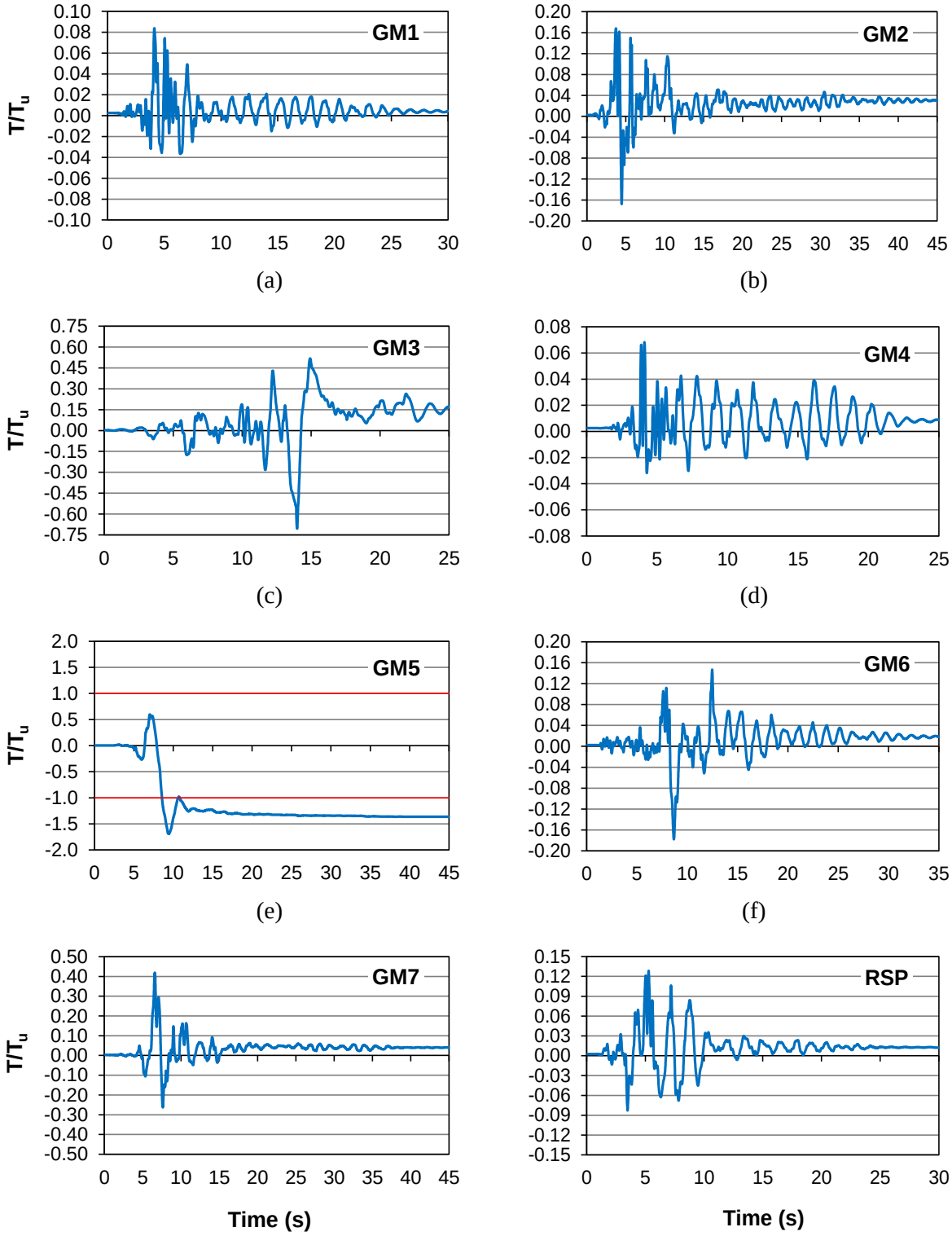

Figure 4-49 Normalized torsion for Pier 1 column (100Y-30X).

4.5 In-Span Hinges and Abutment Expansion Joints

4.5.1 Pounding

Given the large displacements of the bridge segments discovered in Section 4.1.2, pounding is likely to occur. Gaps are located at the in-span hinges and abutment expansion joints, for a total of 6 discontinuities for the bridge. Bearing failure by pounding was found to not be of concern, but the additional force created by this action may have substantial effects on the bridge. Figures 4-50 to 4-53 plot the relative global-X displacement across In-Span Hinges 2 and 3 for the 100X-30Y and 100Y-30X seismic loadings. The relative displacement between the northernmost nodes of adjacent deck segments is shown in blue, while the southernmost nodes are plotted in red. This can provide an approximate measurement of the opening and closing of the gap at each in-span hinge. Positive values indicate the adjacent bridge segments are separating, while a value of zero, shown as a red line, indicates where pounding occurs. The governing pounding response was recorded at In-Span Hinges 2 and 3 and is representative; plots for In-Span Hinges 1 and 4 are excluded for brevity. A look at abutment-superstructure pounding can be found in Section 4.6.

Interestingly, pounding occurs under all ground motions, occurring much more frequently under the ground motions that have been found to cause higher drifts (GM2, GM3, GM5, and GM7). For In-Span Hinge 2, pounding occurs for each ground motion under the 100X-30Y seismic loading (Figure 4-50). This is most likely because of out-of-phase vibration, since Segment 2 and Segment 3, which border In-Span Hinge 2, are vastly different in size and stiffness. Comparing the pounding response under 100X-30Y of In-Span Hinge 2 (Figure 4-50) to that of In-Span Hinge 3 (Figure 4-52) supports this finding, as GM1, GM4, GM6, and RSP do not cause pounding at In-Span Hinge 3. Segment 3 and segment 4, which border In-Span Hinge 3, are much more similar in size and stiffness and should tend to stay in-phase more often under seismic excitations.

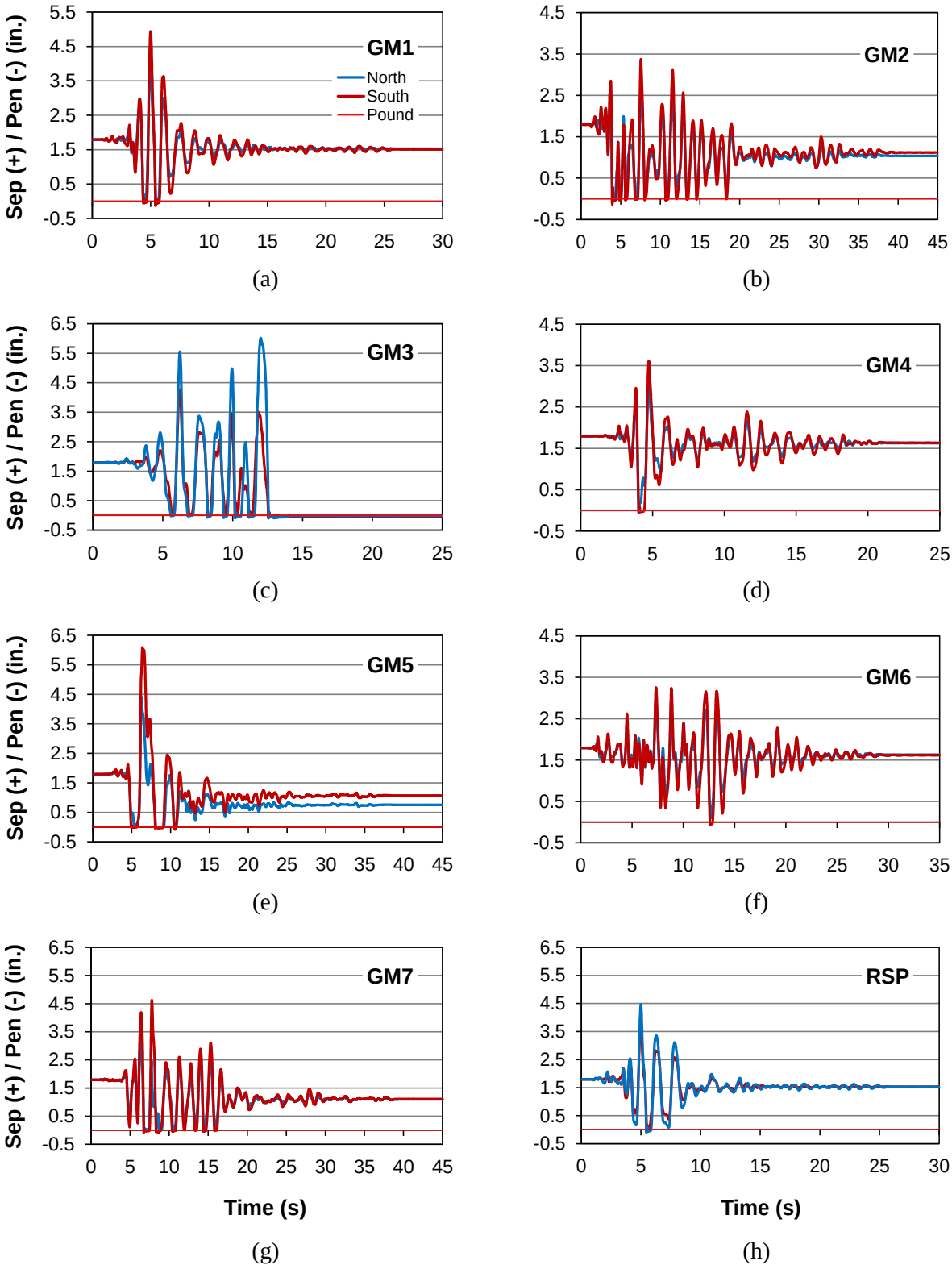

Figure 4-50 Time history of global-X relative displacement across In-Span Hinge 2 (100X-30Y).

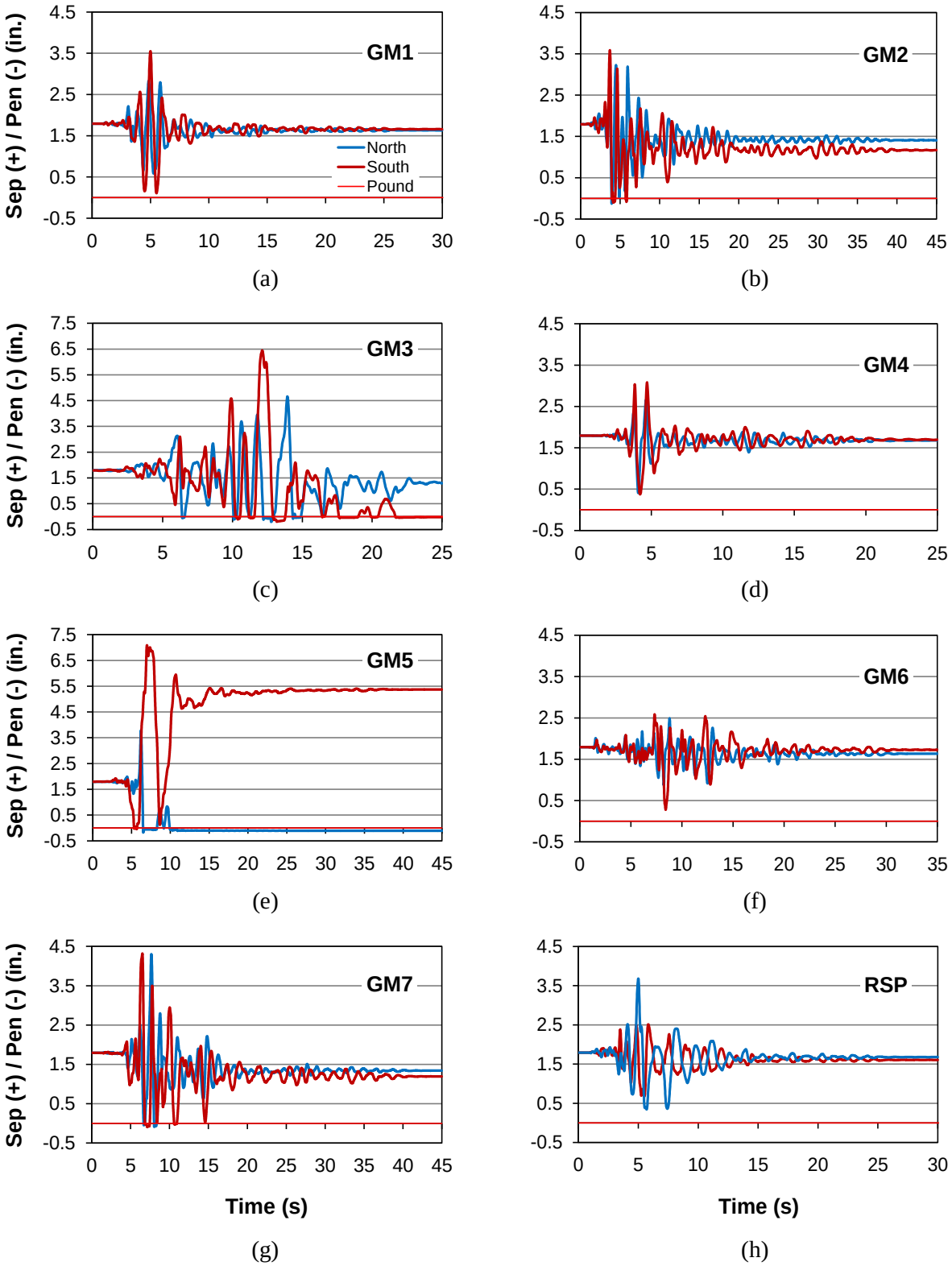

Figure 4-51 Time history of global-X relative displacement across In-Span Hinge 2 (100Y-30X).

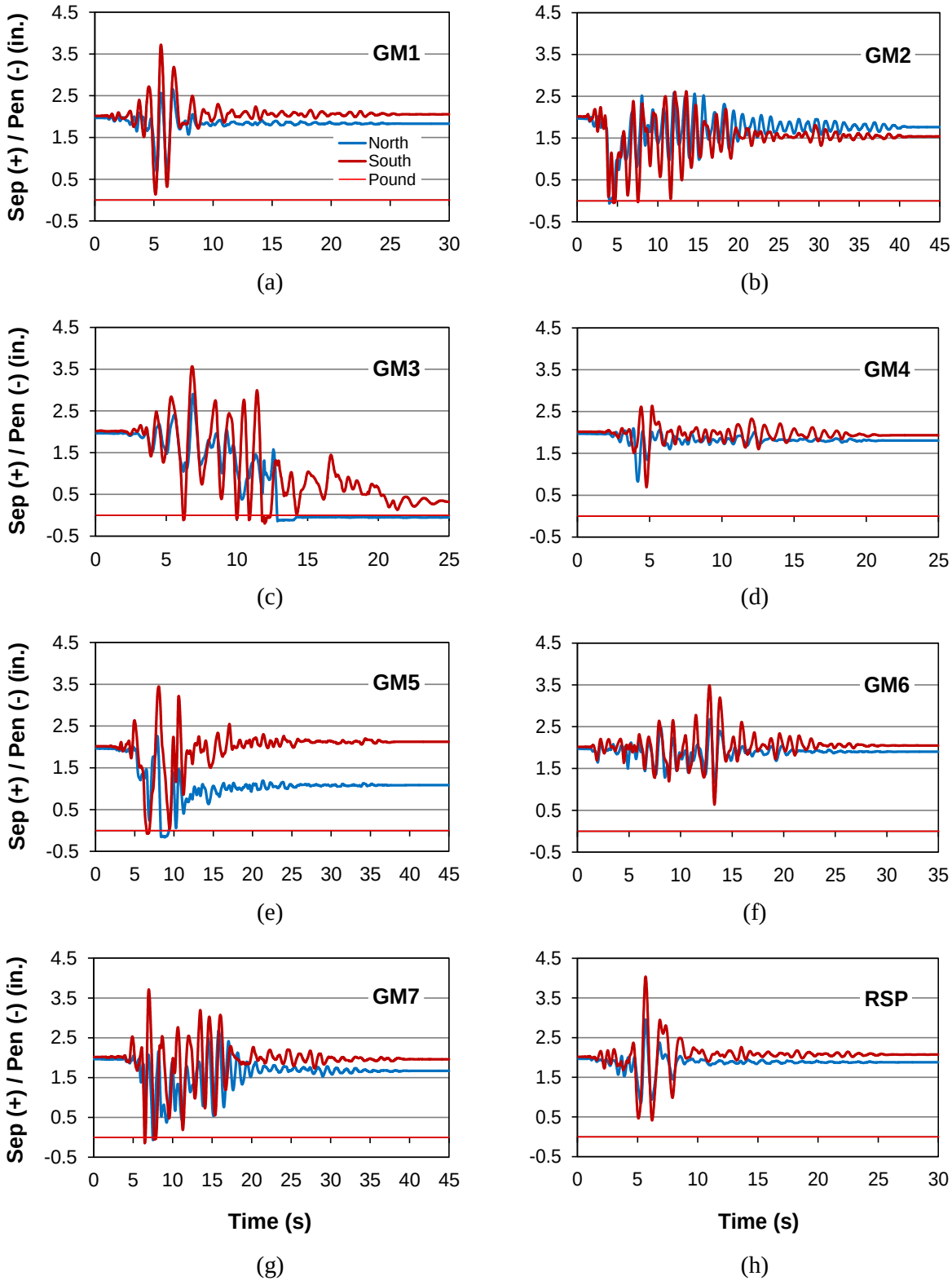

Figure 4-52 Time history of global-X relative displacement across In-Span Hinge 3 (100X-30Y).

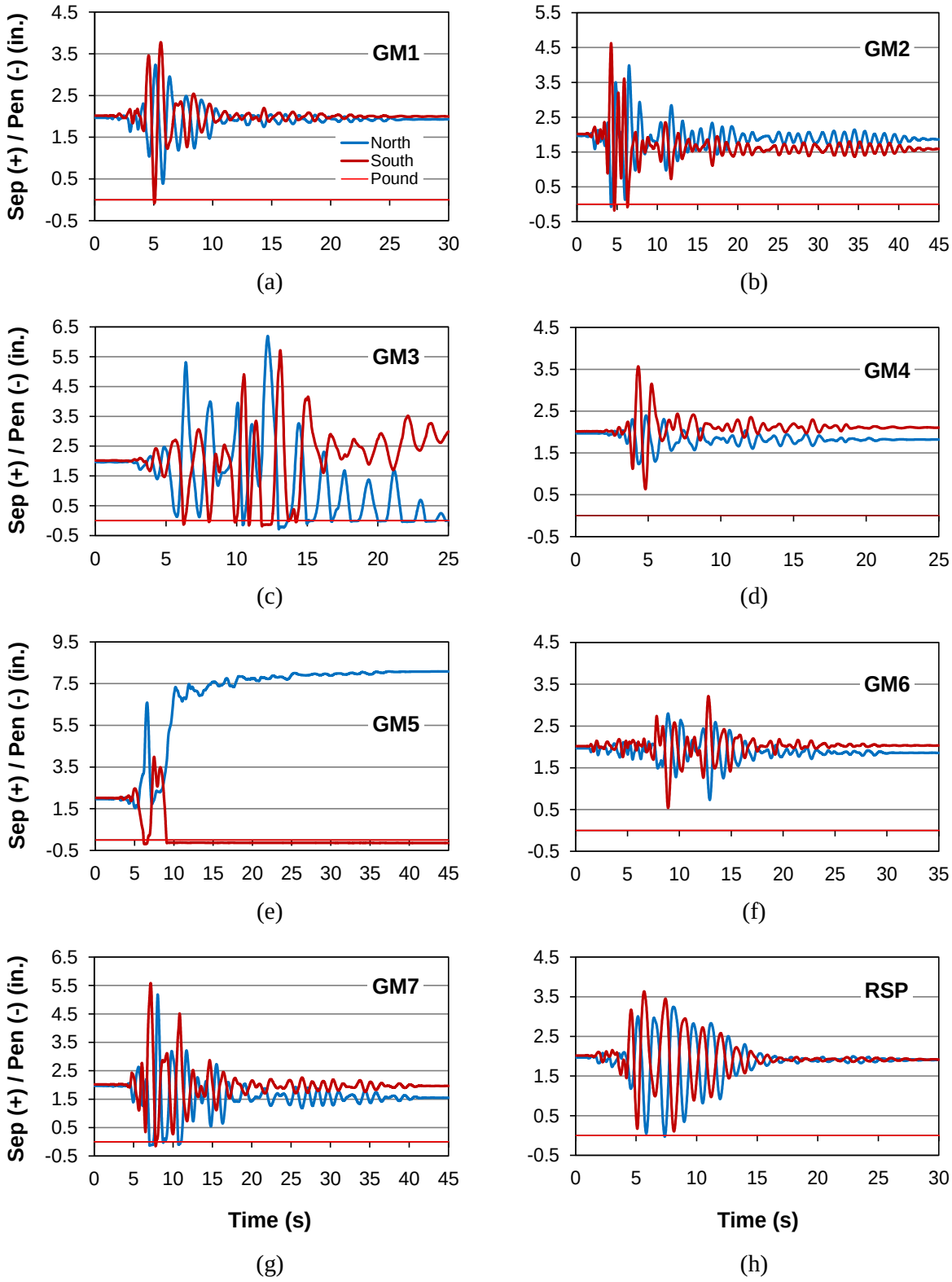

Figure 4-53 Time history of global-X relative displacement across In-Span Hinge 3 (100Y-30X).

Another notable behavior is seen under the 100Y-30X seismic loading of GM5 for In-Span Hinge 2 (Figure 4-51e) and In-Span Hinge 3 (Figure 4-53e). As was discussed previously, Ground Motion 5 causes a purely-torsional failure for the 100Y-30X application (Figure 4-49e). This torsional loading is caused by twisting of the superstructure, where even a degree of rotation can lead to an inch or more of additional lateral displacement. Analyzing these figures further, if in-plane rotation of the deck had not occurred, both the north and south ends of the bridge segments would have similar relative displacements. This is not the case, however, as one end of the adjacent bridge segments pound against one another while the other end separates. Additionally, most likely due to inelastic deformations, the adjacent bridge segments (Segments 2 and 3 for Figure 4-51e, Segments 3 and 4 for Figure 4-53e) stay stuck together at one end after pounding. After inelastic behavior causes permanent residual deformations, it is difficult for the columns to re-center and thus restore the in-span hinges to the original gap width (1.5 in. for In-Span Hinge 1 and 4, 2.0 in. for In-Span Hinge 2 and 3).

Table 4-15 lists the maximum pounding force of the ten pounding springs at each in-span hinge for all ground motions for comparison with "Avg 1-7". Table 4-16 similarly gives the percent-reduction in pounding force with the modified bilinear spring (Muthukumar and DesRoches 2006) over the linear spring with 25,000 k/in. stiffness. As can be seen, the modified spring model reduces the pounding force for every occurrence, in some cases by more than 200%. However, even with the bilinear pounding spring model, the less-severe ground motions (i.e. not GM3 or GM5) still cause several hundred kips of pounding force to be transferred between bridge segments. GM3 sees as much as 1480 kips for ISH-3, and the 100Y-30X seismic loading can cause higher pounding forces than 100X-30Y, possibly emphasizing the dramatic effect of bridge skew on the in-plane rotation of the superstructure and its resulting effects. RSP and the other ground

motions that do not cause significant column yielding (GM1, GM4, GM6) see very little pounding force. This may indicate that nonlinear effects greatly change the frequency response of the bridge to the ground motions. For example, adjacent bridge segments that were in-phase in the elastic range can become out-of-phase if the substructure of one of the segments shifts into the nonlinear range.

Table 4-15 Maximum pounding force at in-span hinges (kip)

In-Span Hinge	Seismic Loading	GM1	GM2	GM3	GM4	GM5	GM6	GM7	RSP	Avg 1-7
1	100X-30Y	314	361	1090	244	483	0	753	258	463
	100Y-30X	0	559	1270	0	543	158	276	0	400
2	100X-30Y	688	875	586	236	334	207	575	536	500
	100Y-30X	0	627	954	0	643	0	391	0	374
3	100X-30Y	0	266	915	0	459	0	641	0	326
	100Y-30X	243	890	1480	0	627	0	621	40	551
4	100X-30Y	0	325	425	412	508	0	290	0	280
	100Y-30X	0	382	601	0	414	0	196	0	228

Table 4-16 Change in pounding force using nonlinear over linear pounding spring model (%)

In-Span Hinge	Seismic Loading	GM1	GM2	GM3	GM4	GM5	GM6	GM7	RSP	Avg 1-7
1	100X-30Y	-113	-271	-37.4	100	-112	0	-214	-188	-108
	100Y-30X	0	-129	-127	0	-14.2	-121	-130	0	-104
2	100X-30Y	-124	-132	-192	-240	-189	-177	-220	-161	-182
	100Y-30X	0	-123	-43.4	0	-37.7	0	-176	0	-95.1
3	100X-30Y	0	-231	-51.0	0	-17.9	0	-85.2	0	-96.3
	100Y-30X	-119	-68.3	-15.0	0	-11.2	0	-62.7	-194	-55.2
4	100X-30Y	0	-193	-178	-113	-70.7	0	-149	0	-141
	100Y-30X	0	-138	-117	0	16.1	0	-73.3	0	-78.1

Figure 4-54 displays the pounding force at each in-span hinge (Figure 4-54a) as well as the percent-reduction in pounding force using the nonlinear spring over the linear model (Figure 4-54b). While RSP does not cause frequent pounding, the magnitude of the pounding force is similar

to “Avg 1-7” at In-Span Hinges 1 and 2. There is at least 100% reduction in pounding force for all in-span hinges using the modified bilinear spring stiffness, which should help produce analysis results that are not overly conservative. Even with the reduction, however, the transfer of hundreds of kips between deck segments across these discontinuities could have a significant effect on the substructure. For example, if a column was already yielding prior to the occurrence of pounding during a ground motion, the additional force could greatly amplify the nonlinear deformations and induce flexural or rotation-based shear failure. Larger initial gaps and more symmetric bridge segments may have helped to further reduce the pounding forces. Additionally, the restrainers may have failed and were unable to control the relative displacement, which will be investigated in the next section.

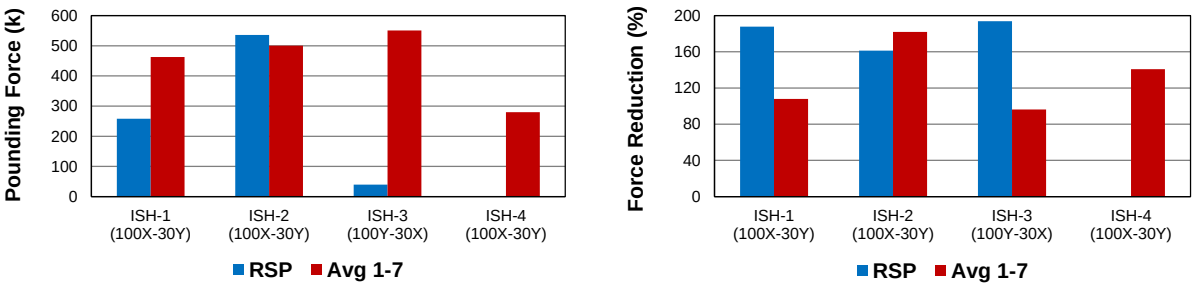

(a) Maximum pounding force (b) Pounding force reduction

Figure 4-54 In-span hinges pounding response for RSP and “Avg 1-7”.

4.5.2 Response of Restrainers

The restrainers were not part of the original bridge design and were installed as a retrofitting measure. Figures 4-55 to 4-58 plot the deformation response of the restrainer elements at In-Span Hinge 2 and 3. Just as for pounding, the governing responses are recorded at these two expansion joints and the responses at In-Span Hinge 1 and 4 are omitted for brevity. Nine restrainers were installed at each in-span hinge, and only the restrainers at the northernmost (blue line) and southernmost (red line) ends of the bridge are plotted for clarity (Figure 4-12 illustrates the

displacement of the restrainer elements). Positive values of displacement indicate separation between adjacent bridge segments (likelihood for restrainer extension/activation), while negative values indicate closing of the gap causing the restrainers to contract. The green line signifies restrainer activation (all restrainers are modeled with an assumed slack of 0.5 in. from Section 3.1.3), the orange line signals the onset of restrainer yielding, and the red line shows the maximum restrainer extension of 1.8 in. which will cause restrainer fracture (1.8 in. extension + 0.5 in. slack = 2.3 in. shown as limit in figures).

As can be seen, many of the ground motions cause yielding of the restrainers; this will reduce their effectiveness significantly. A restrainer is designed to have a high elastic stiffness to limit displacement across the gap. After yielding, however, the restrainer is much softer. Every ground motion at least activates the restrainers, signifying that adjacent bridge segments become at least slightly out-of-phase with another during the seismic loading. Referencing the previous discussion on deck in-plane rotation in Section 4.5.1, a look at the restrainers under 100Y-30X for GM3 and GM5 at In-Span Hinge 2 (Figure 4-56c,e) and In-Span Hinge 3 (Figure 4-58c,e) is warranted. The skewed nature of the bridge once again comes into play, twisting adjacent bridge segments enough to pound each other at one end and separate and fail the restrainer at another end. This failure is explicitly modeled and can be seen in the figures as the flat line right at 2.3 in., the local deformation of the restrainer element required to reach its maximum force capacity of 53 kips. After failure, the recorded deformation of the restrainer element is locked at 2.3 in., the failure limit specified. It is inferred that the restrainers were only designed to handle uniform separations at the in-span hinges, where the north and south ends displaced equally together. The amplified separation caused by in-plane deck rotation easily fails the restrainers or at least causes yielding, which is unfavorable for seismic performance.

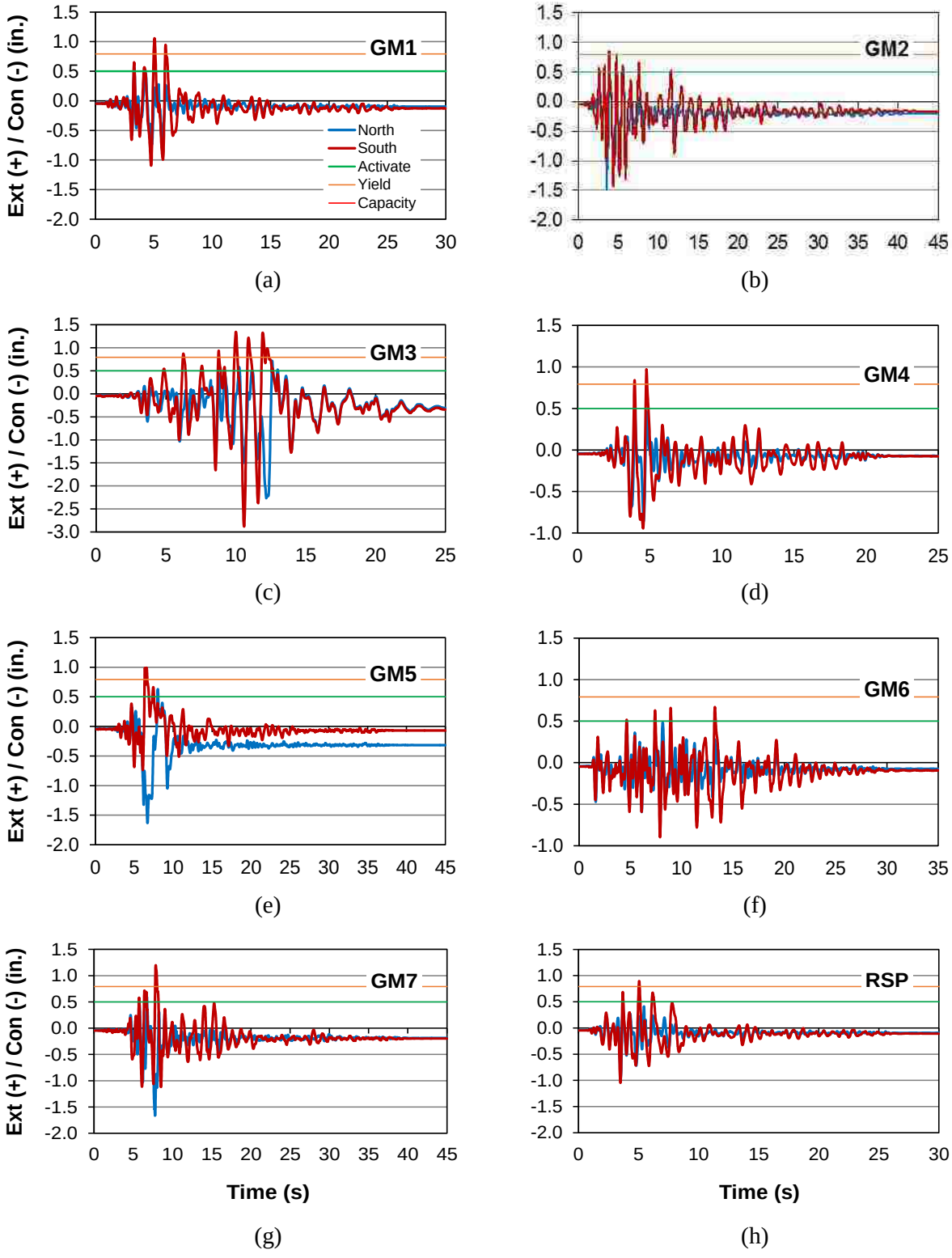

Figure 4-55 Time history of restrainer deformation at In-Span Hinge 2 (100X-30Y).

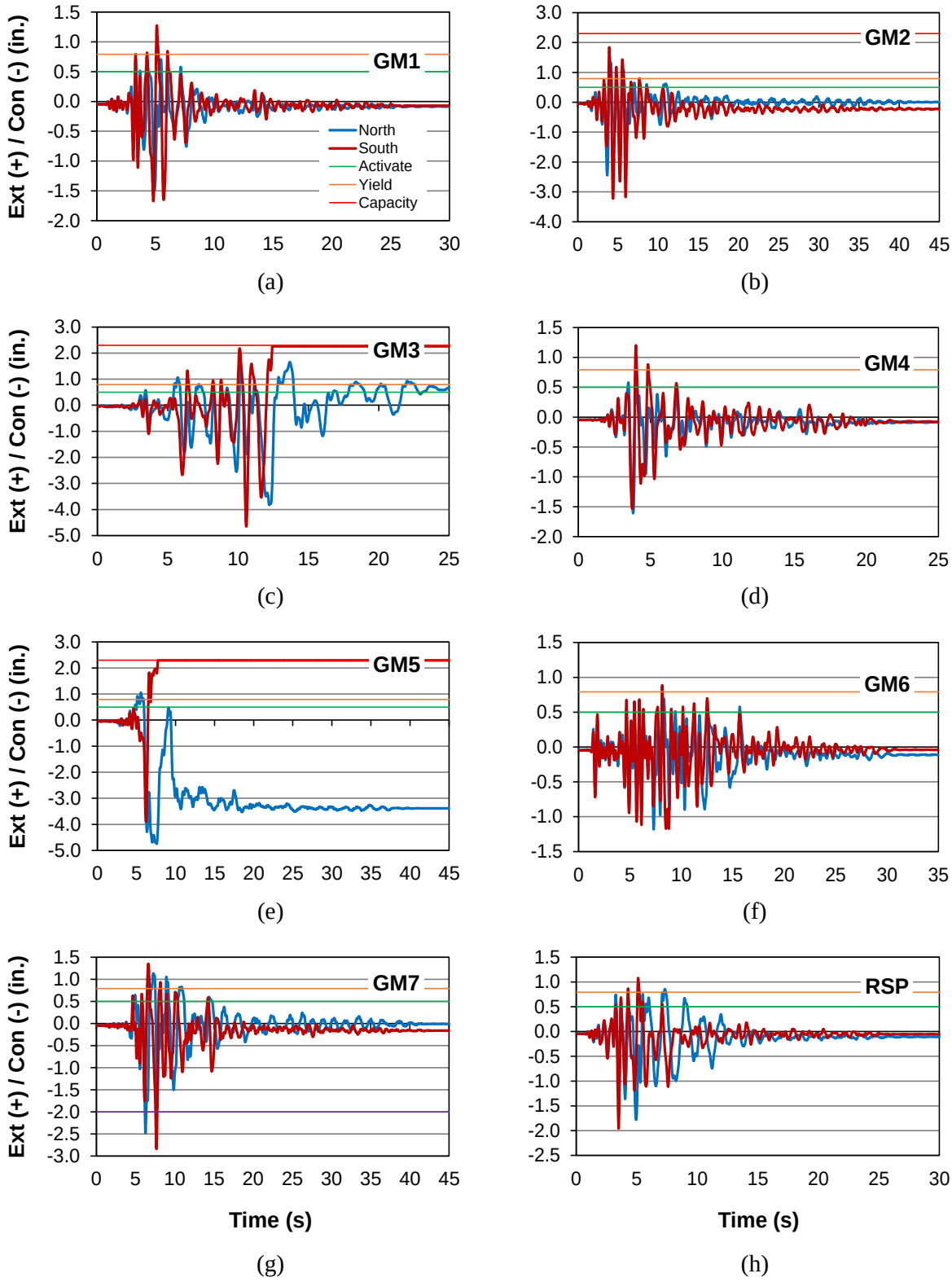

Figure 4-56 Time history of restrainer deformation at In-Span Hinge 2 (100Y-30X).

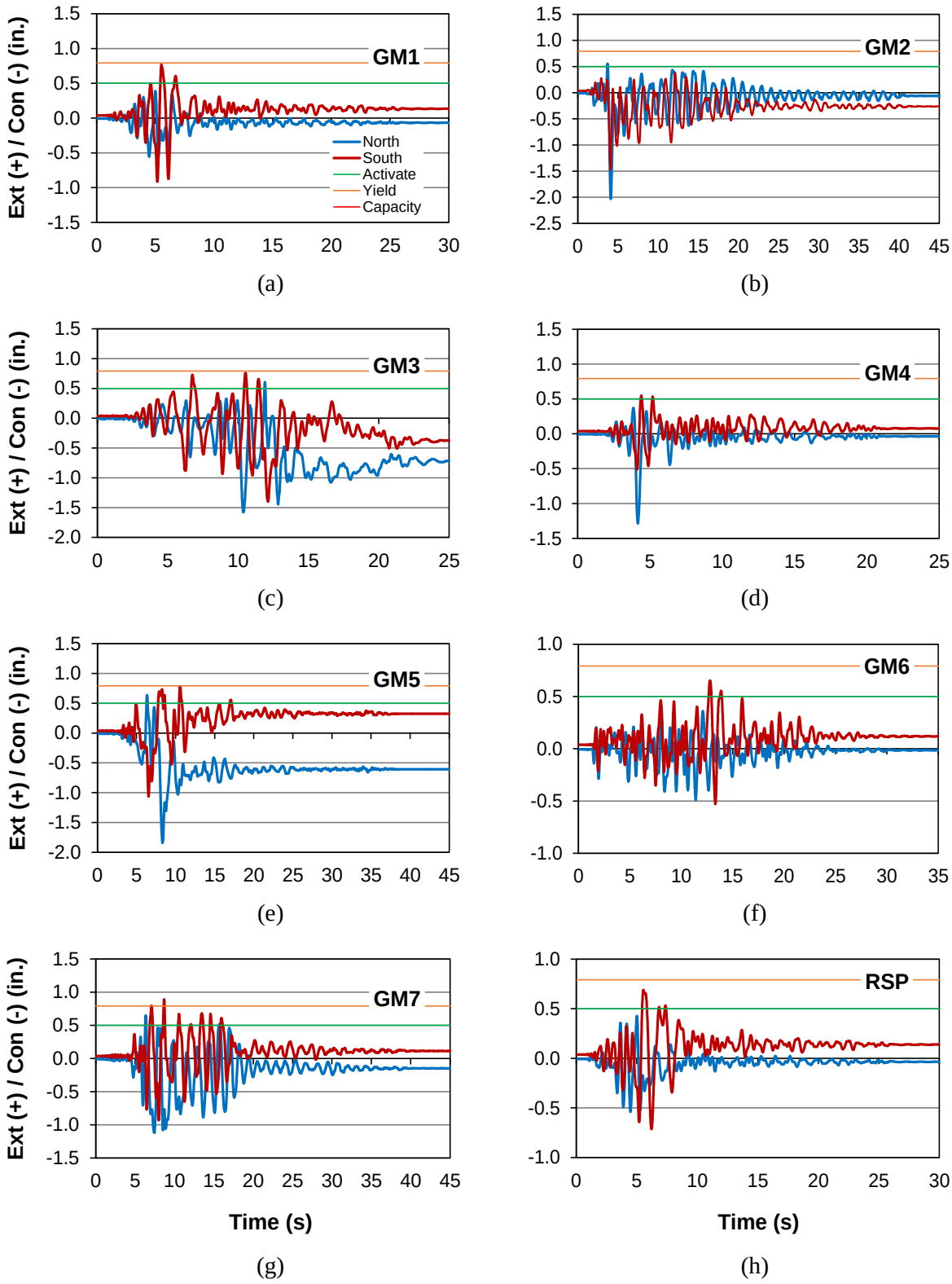

Figure 4-57 Time history of restrainer deformation at In-Span Hinge 3 (100X-30Y).

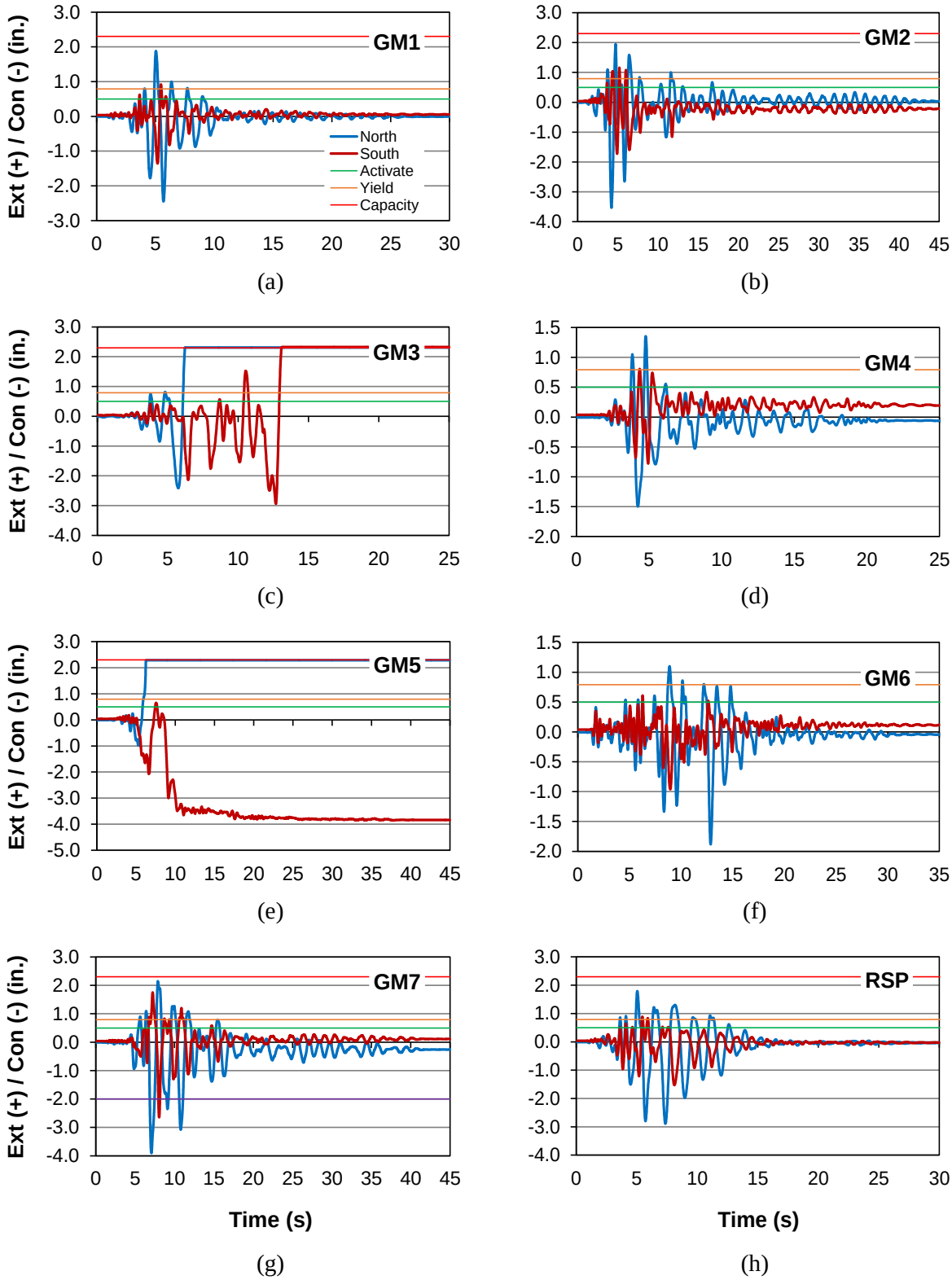

Figure 4-58 Time history of restrainer deformation at In-Span Hinge 3 (100Y-30X).

Table 4-17 provides the governing normalized restrainer force demand, with respect to the ultimate force of 53 kips, of the nine restrainers at each in-span hinge. The results for all ground motions are compared to "Avg 1-7". As discussed previously, GM3 and GM5 cause failures for the 100Y-30X seismic loading. The 100Y-30X seismic loading causes more distress in the restrainers than 100X-30Y for all ground motions. Many cases stress the restrainer beyond the yield point of 0.736.

Table 4-17 Restrainer force demand/capacity ratios (yield at 0.736 [39 kips], fail at 1.00 [53 kips])

In-Span Hinge	Seismic Loading	GM1	GM2	GM3	GM4	GM5	GM6	GM7	RSP	Avg 1-7
1	100X-30Y	0.741	0.195	0.752	0.239	0.689	0.112	0.629	0.169	0.480
	100Y-30X	0.751	0.789	1.00	0.659	1.00	0.745	0.957	0.809	0.843
2	100X-30Y	0.784	0.750	0.834	0.769	0.772	0.428	0.809	0.756	0.735
	100Y-30X	0.822	0.921	0.999	0.810	0.995	0.754	0.835	0.788	0.877
3	100X-30Y	0.648	0.124	0.631	0.102	0.700	0.364	0.753	0.454	0.475
	100Y-30X	0.925	0.935	1.00	0.833	0.996	0.789	0.970	0.909	0.921
4	100X-30Y	0.241	0.512	0.866	0.000	0.740	0.309	0.646	0.000	0.473
	100Y-30X	0.778	0.887	0.955	0.801	1.00	0.756	0.785	0.788	0.852

Figure 4-59 compares the governing restrainer force for RSP and "Avg 1-7" for all four in-span hinges. The red line marks the ultimate capacity (53 kips) and the orange line marks the yield capacity (39 kips). RSP slightly underestimates the force demand compared to "Avg 1-7", but does capture yielding and some nonlinearity in the response. The average response captures the greater extents of yielding better than RSP, but no failure is expected. The failures caused by the extreme twisting of adjacent deck segments, combined with extensive yielding in other cases, most likely has caused reduced pounding mitigation, in-span hinge unseating control, force balance between adjacent superstructure segments, and other possible effects.

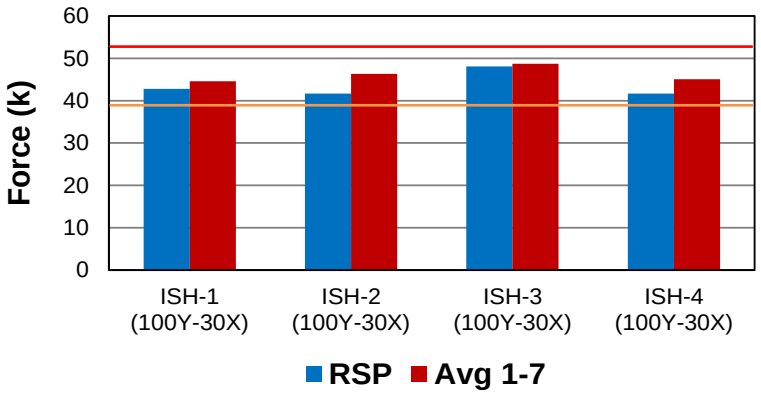

Figure 4-59 Restrainer force demand for RSP and "Avg 1-7".

4.5.3 Response of Shear Keys

Figures 4-60 to 4-65 provide the time histories for the normalized force demand, $V_{SK}/V_{SK,u}$, for the shear key at In-Span Hinges 2 and 3 and the northernmost of four shear keys at Abutment A. The plots for In-Span Hinges 1 and 4 and Abutment B are omitted for brevity. While the shear keys technically have a residual capacity up to an ultimate displacement of 4.5 in., the interest is primarily in whether the initial linear-elastic force capacity, $V_{SK,u}$ (Section 3.2.8), is reached. The brittle failure of the shear keys is demonstrated for some ground motions. There is high force demand for the shear keys at both the in-span hinges and abutment expansion joints under both seismic loadings (100X-30Y and 100Y-30X). The high stiffness of the shear key model and possible numerical errors causes some plots to record forces much higher than capacity, but the residual capacity is recorded soon after. The 100Y-30X loading generally governs for most ground motions, most likely due to this loading placing more demand directly on the shear keys at the gaps instead of translating the force longitudinally through the bearing pads, pounding, or restrainers. For the Abutment A shear key under GM3 100X-30Y, however (Figure 4-64c), the demand is substantially higher than that caused by the 100Y-30X seismic loading (Figure 4-65c); pounding at the abutments that can cause in-plane rotation of the deck may explain this.

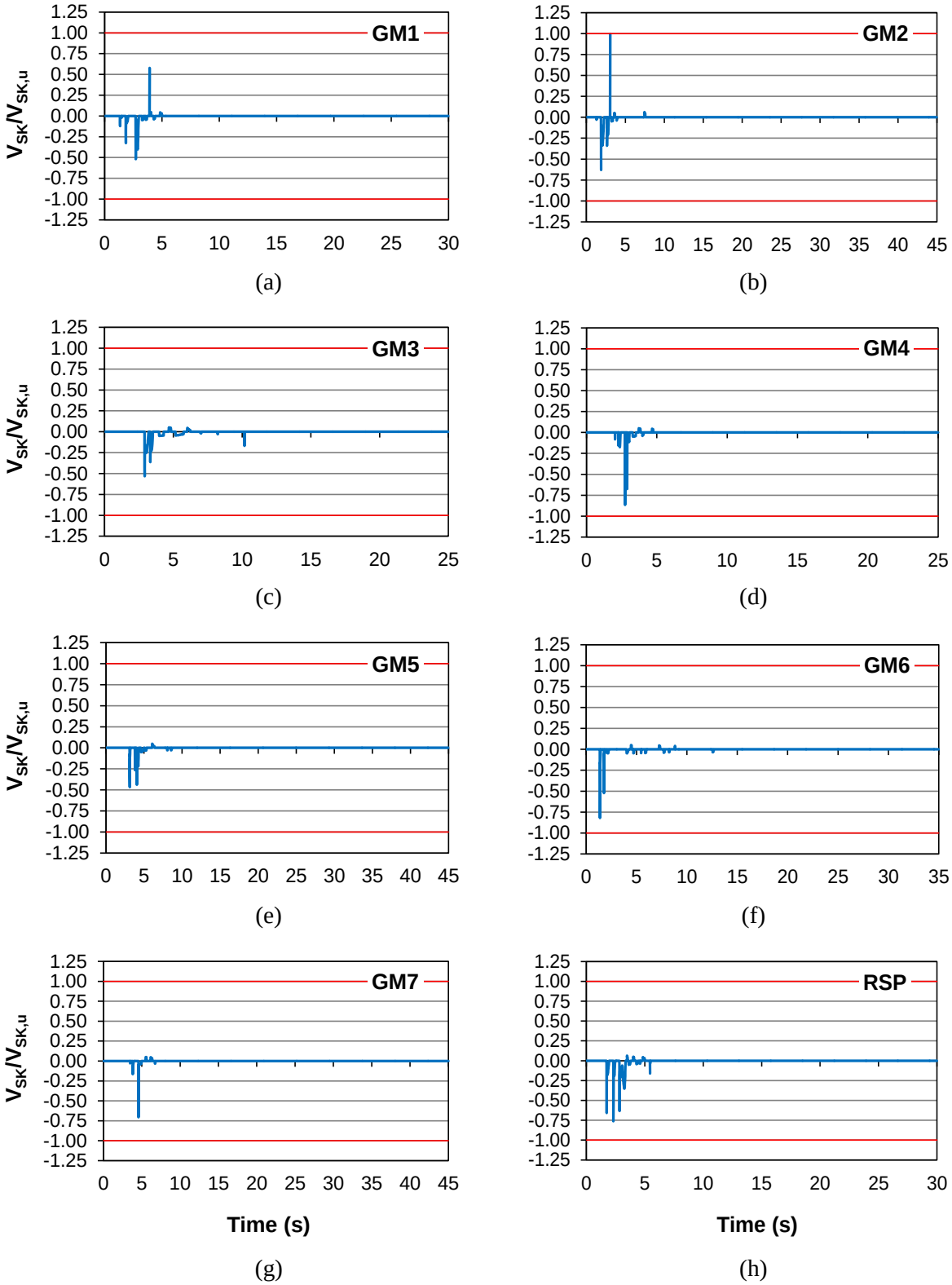

Figure 4-60 Time history of normalized force for shear key at In-Span Hinge 2 (100X-30Y).

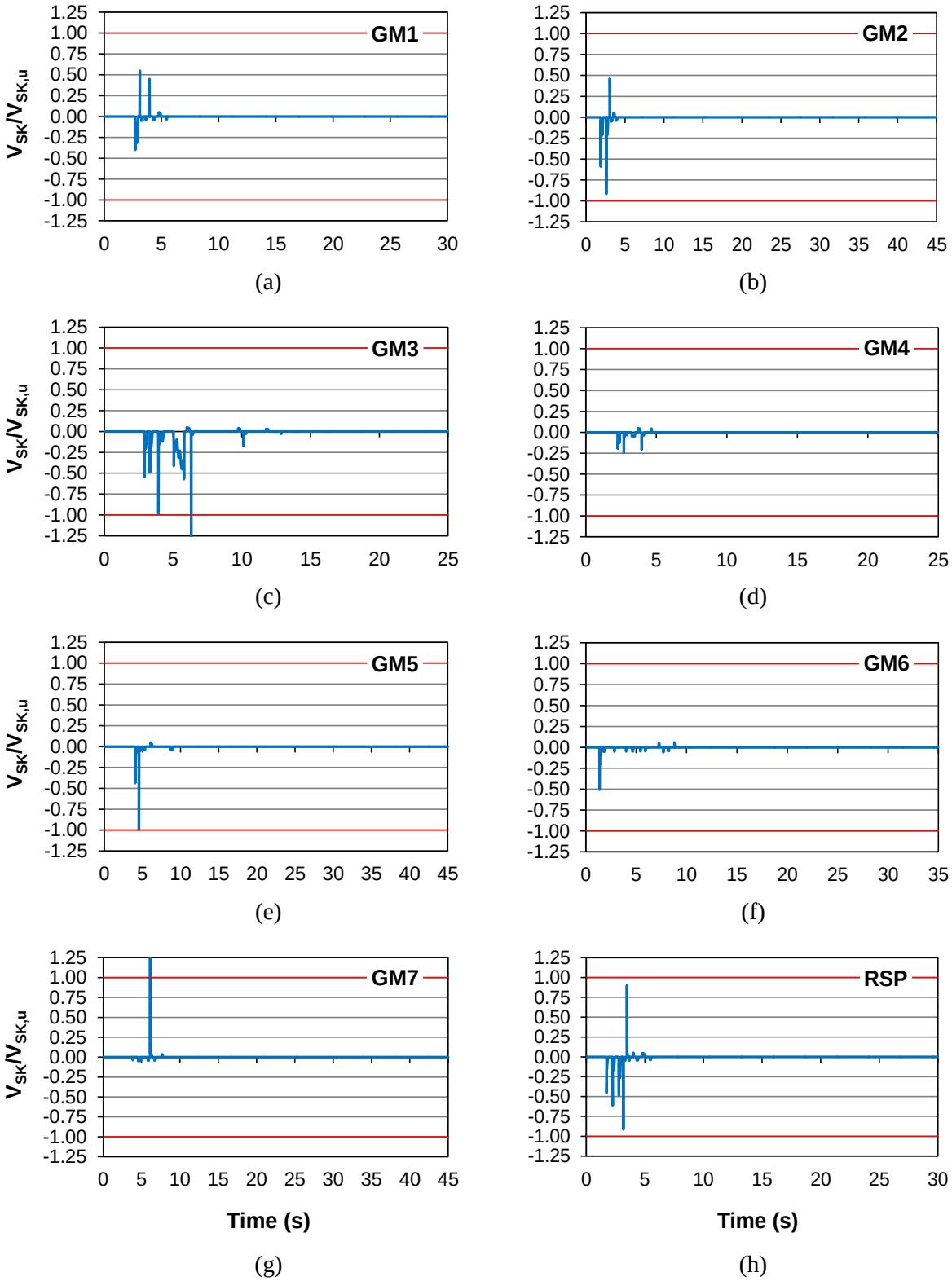

Figure 4-61 Time history of normalized force for shear key at In-Span Hinge 2 (100Y-30X).

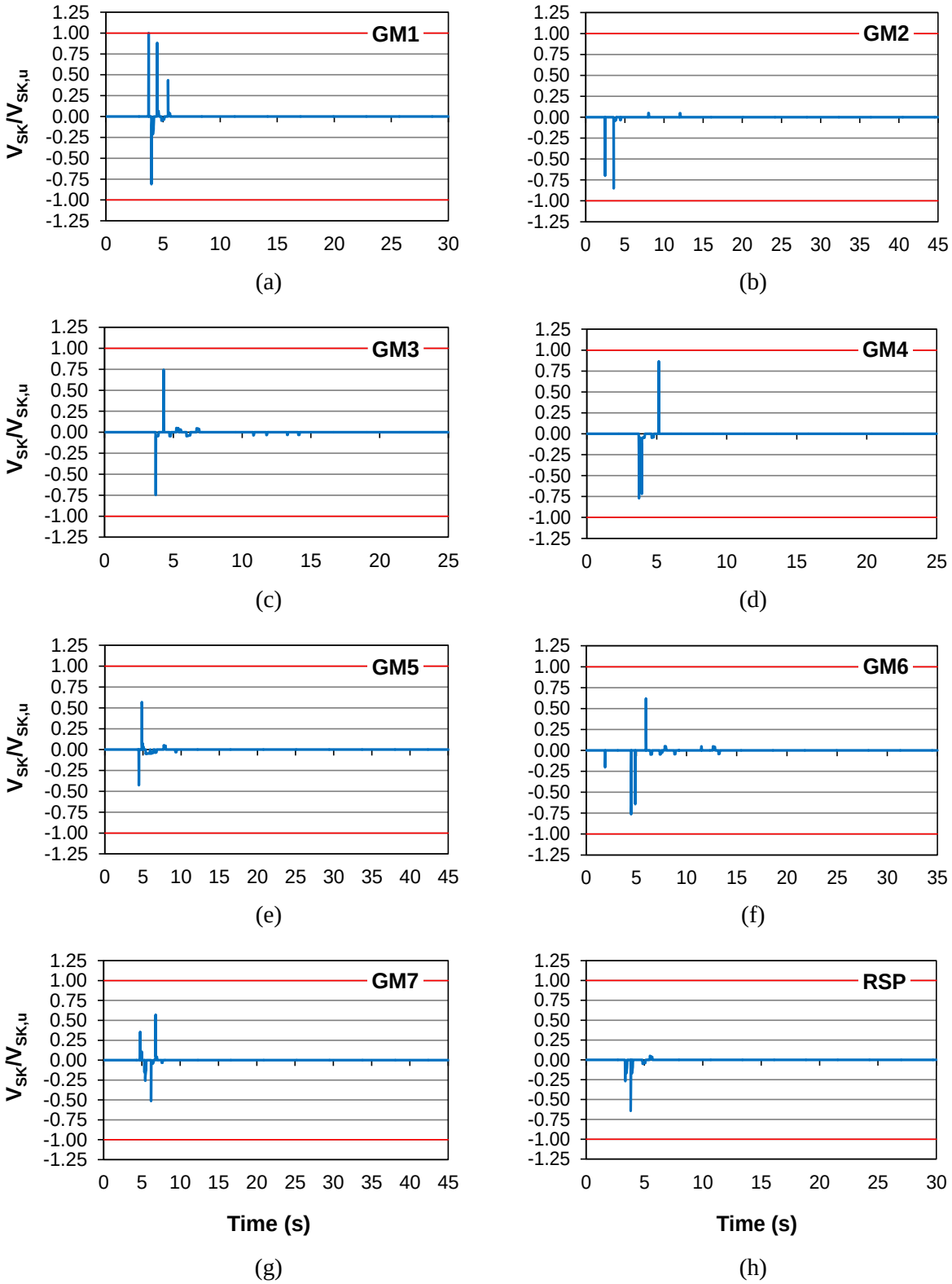

Figure 4-62 Time history of normalized force for shear key at In-Span Hinge 3 (100X-30Y).

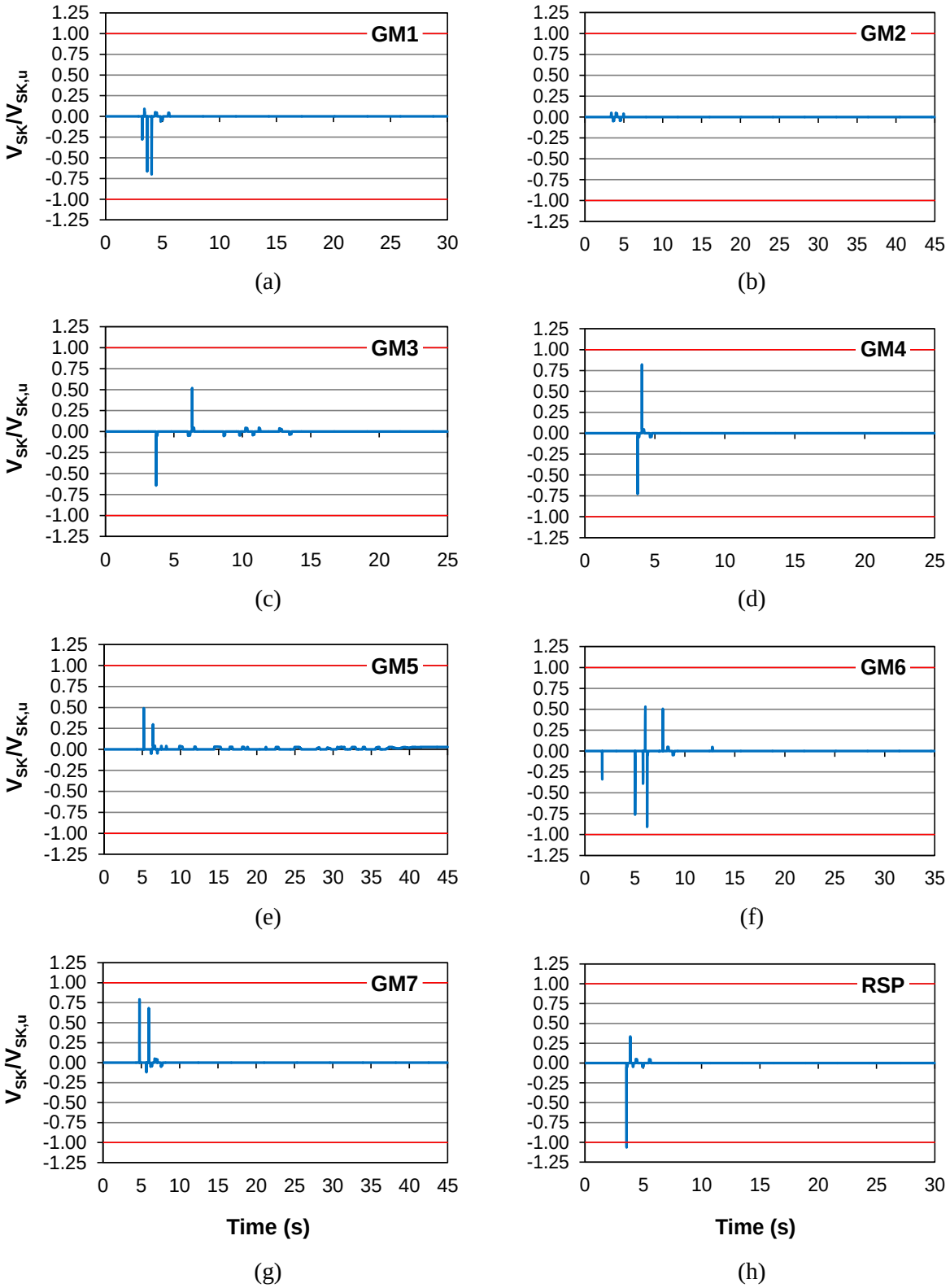

Figure 4-63 Time history of normalized force for shear key at In-Span Hinge 3 (100Y-30X).

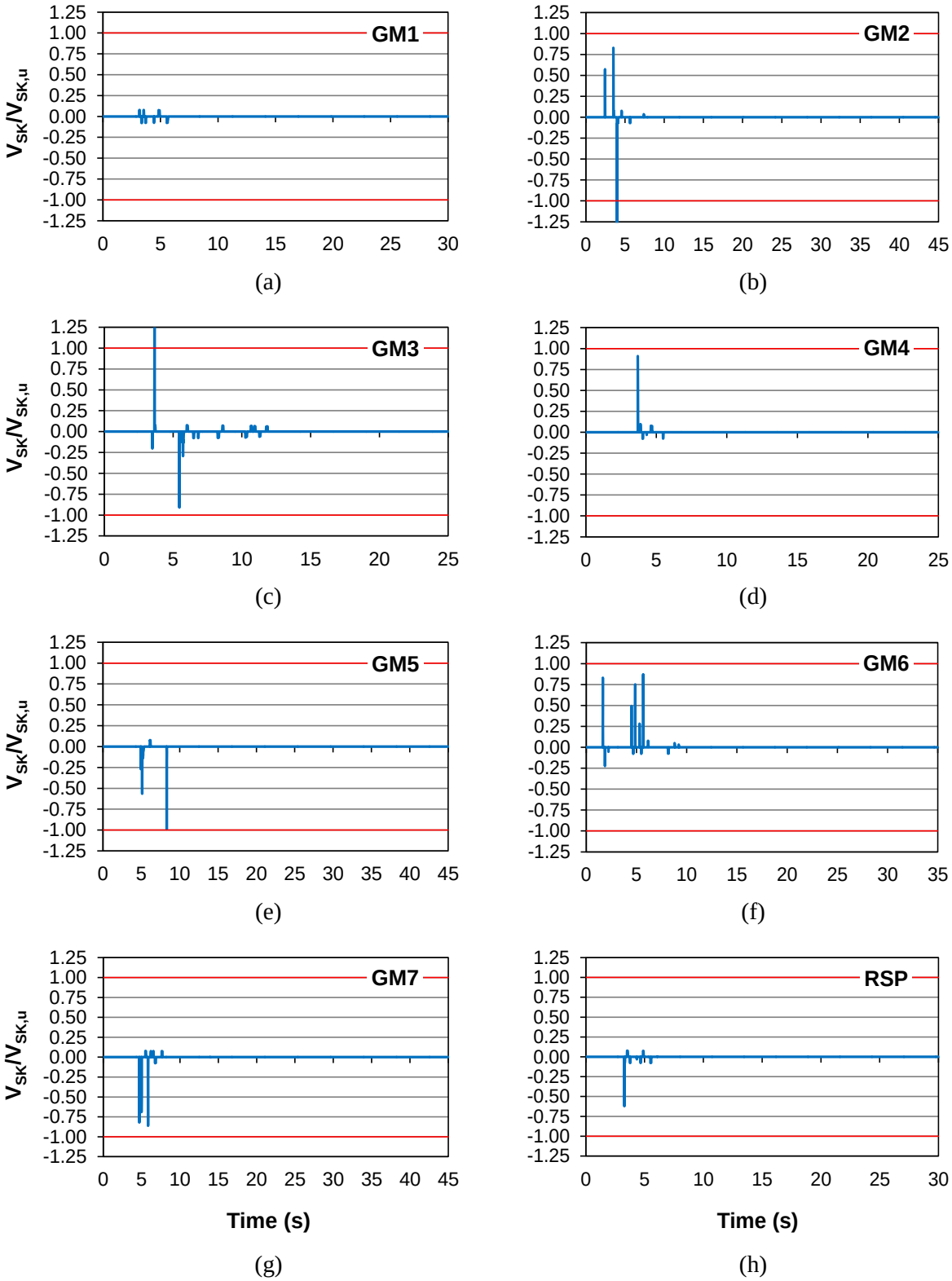

Figure 4-64 Time history of normalized force for northernmost shear key at Abutment A (100X-30Y).

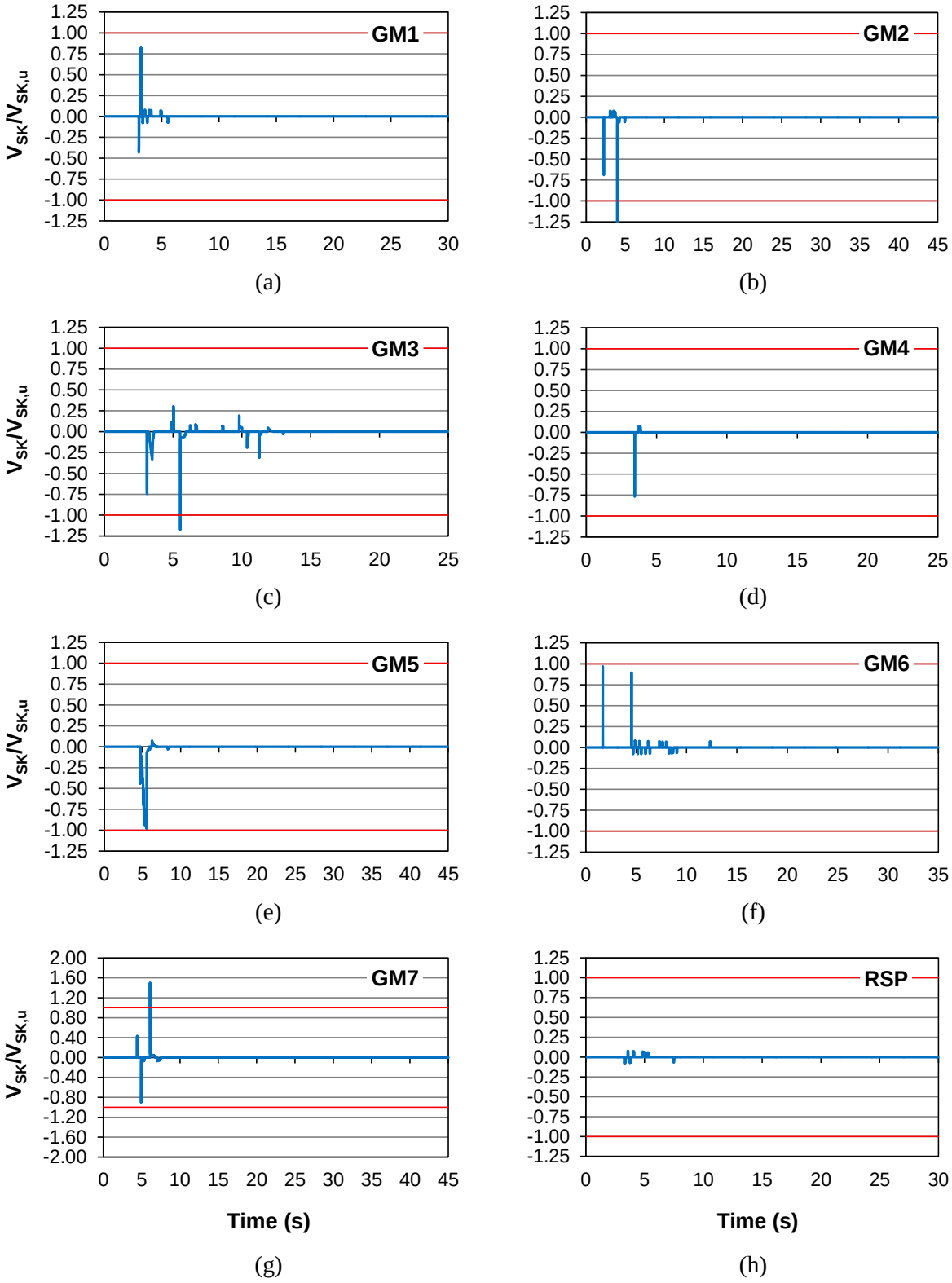

Figure 4-65 Time history of normalized force for northernmost shear key at Abutment A (100Y-30X).

Table 4-18 summaries the force demand for all shear keys (in-span hinges and abutments) under all ground motions for comparison with "Avg 1-7" (shear key strength is given in parentheses). While some cases recorded force demands higher than capacity, only the maximum capacity given by Equation 3-18 is listed. While failure is only detected in a handful of cases, many are at 75% of capacity or more. The minimum "Avg 1-7" demand is 393 kips for Abutment B (100X-30Y), but is still 82% of capacity since the four smaller shear keys at the abutments have less strength then those at the in-span hinges (479 kips vs. 644 kips). For the average response at the in-span hinges, the lowest demand is 406 kips for In-Sapn Hinge 3 (100Y-30X), which is 63% of capacity. Even though a shear key may not reach its ultimate capacity, cracking and stiffness/strength degradation can still be expected with cyclic loadings as discussed in Section 2.1.4. Many of these interior shear keys will probably have to be replaced following a major seismic event, but they are generally designed to be sacrificial.

Table 4-18 Shear key force demand (kips)

Shear Key	Seismic Loading	GM1	GM2	GM3	GM4	GM5	GM6	GM7	RSP	Avg 1-7
ISH-1 (644)	100X-30Y	645	32.2	638	645	645	538	436	68.0	511
	100Y-30X	153	645	645	645	546	392	635	210	523
ISH-2 (644)	100X-30Y	372	642	343	558	300	529	455	492	457
	100Y-30X	354	592	645	155	642	326	645	590	480
ISH-3 (644)	100X-30Y	644	549	482	558	368	492	368	415	495
	100Y-30X	451	32.2	415	530	317	585	510	645	406
ISH-4 (644)	100X-30Y	472	498	645	179	560	54.1	543	624	422
	100Y-30X	508	32.2	544	533	495	434	472	633	431
Abut-A (479)	100X-30Y	348	480	480	470	475	418	480	342	450
	100Y-30X	395	480	480	368	470	465	480	419	448
Abut-B (479)	100X-30Y	344	422	480	431	452	139	480	421	393
	100Y-30X	437	480	414	440	478	423	467	455	448

4.6 RESPONSE OF ABUTMENTS

4.6.1 BACKWALL/WINGWALL FORCE/DISPLACEMENT DEMAND

Abutments can stabilize the bridge superstructure against longitudinal and transverse ground motions. The abutments of Bridge G-953 do not have pile foundations; therefore, the transverse strength is fairly limited in comparison to the longitudinal passive strength of the backfill soil. Figures 4-66 and 4-67 present the normalized longitudinal displacement demand, D/D_u, of Abutment A and Abutment B, respectively, under the 100X-30Y seismic loading. Figures 4-68 and 4-69 display D/D_u for the transverse direction under 100Y-30X.

As can be seen, most ground motions exceed the maximum longitudinal passive pressure of the backfill and fail the abutment by excessive displacement. More ground motions cause a failure associated with transverse displacement due to the weak wingwall stiffness and strength (generally one-tenth of the backwall capacity). The same ground motions that cause large column displacements, namely GM2, GM3, GM5, and GM7, also cause abutment failure. RSP, even with relatively low column drift demands (less than 2%), also fails the abutment by a small margin (demand/capacity greater than 1.1) considering the longitudinal (Figure 4-66h) and transverse (Figures 4-68h and 4-69h) displacement, but not for Abutment B under 100X-30Y (Figure 4-67h).

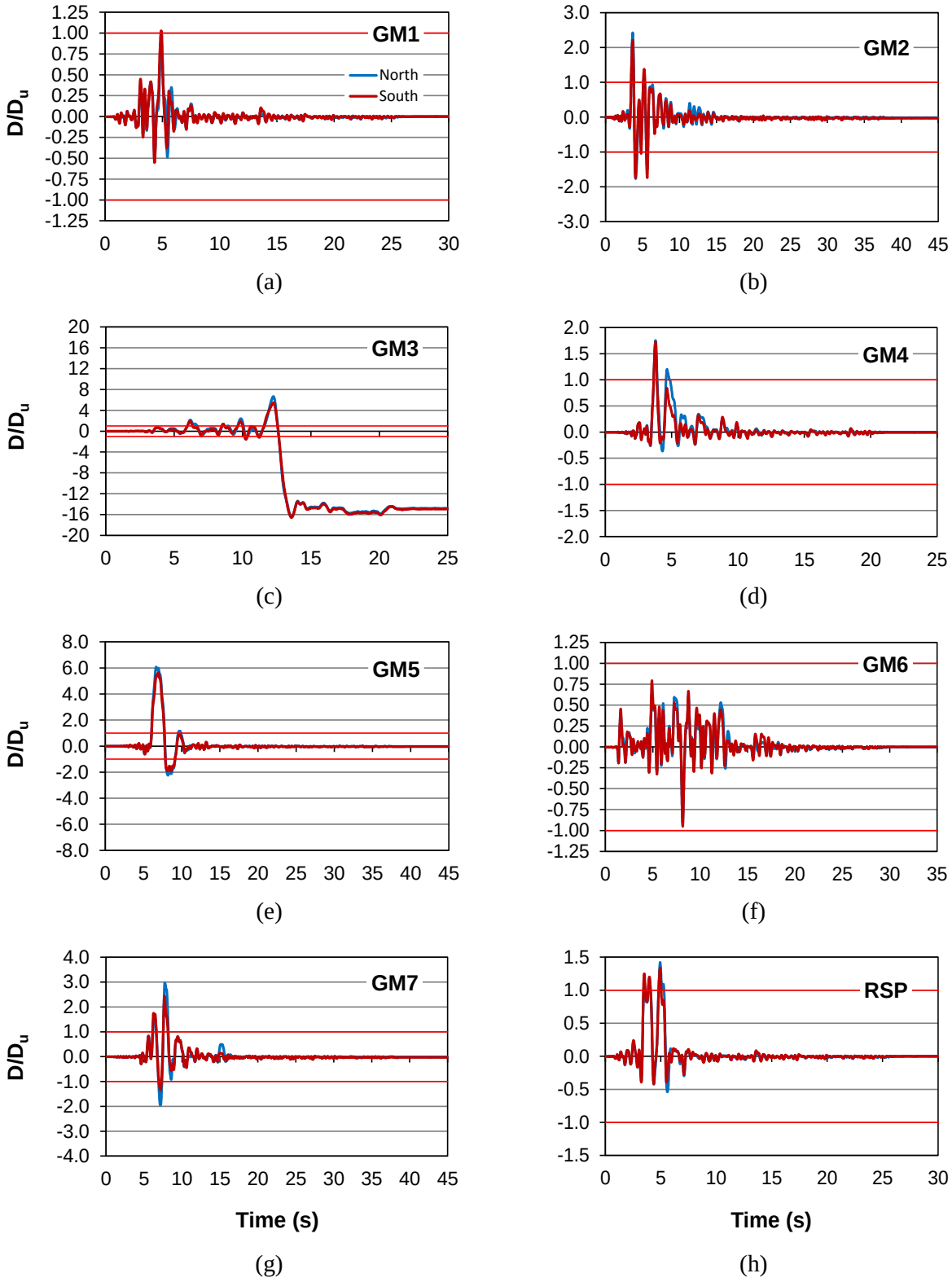

Figure 4-66 Time history of normalized longitudinal displacement at Abutment A (100X-30Y).

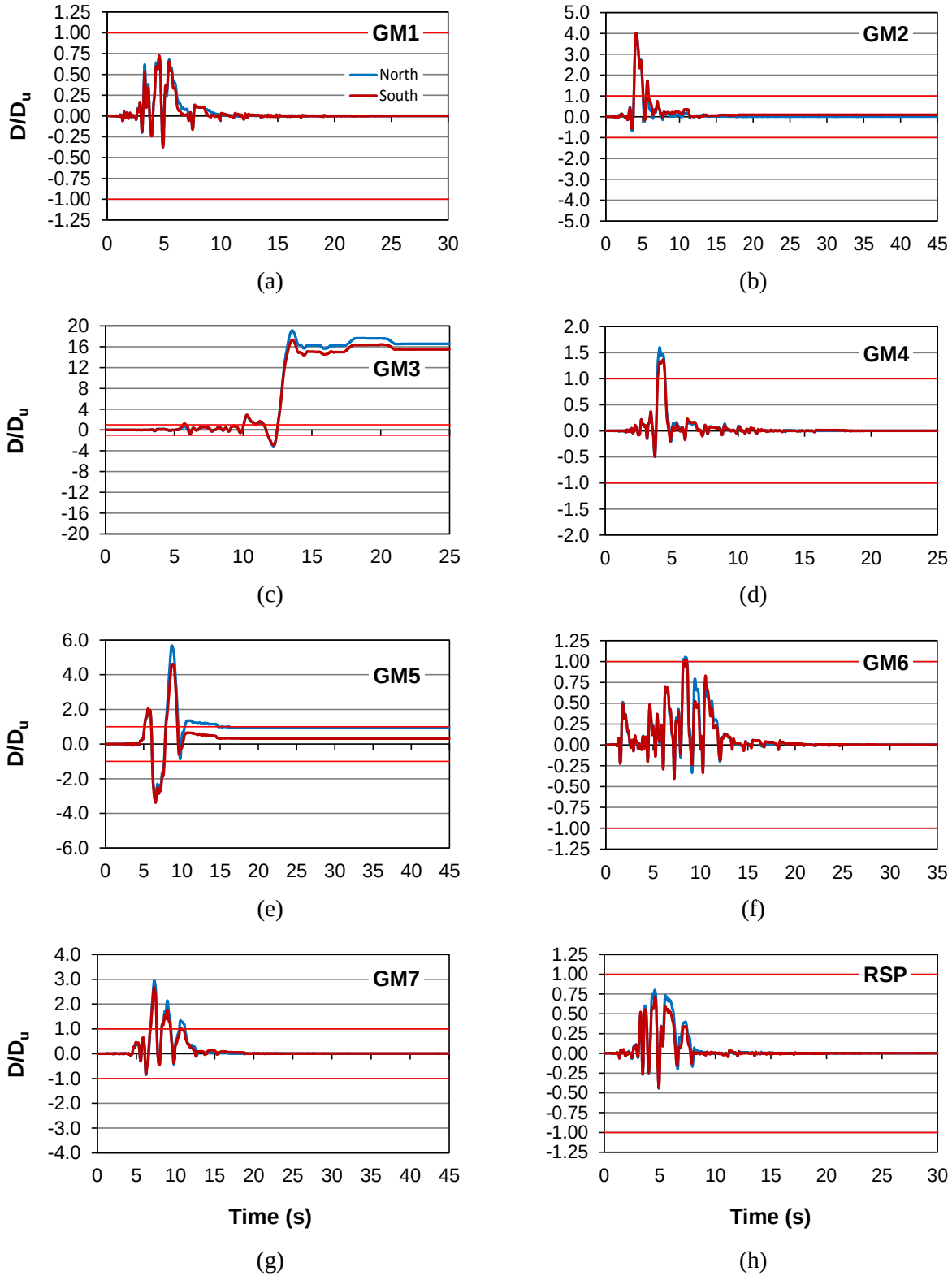

Figure 4-67 Time history of normalized longitudinal displacement at Abutment B (100X-30Y).

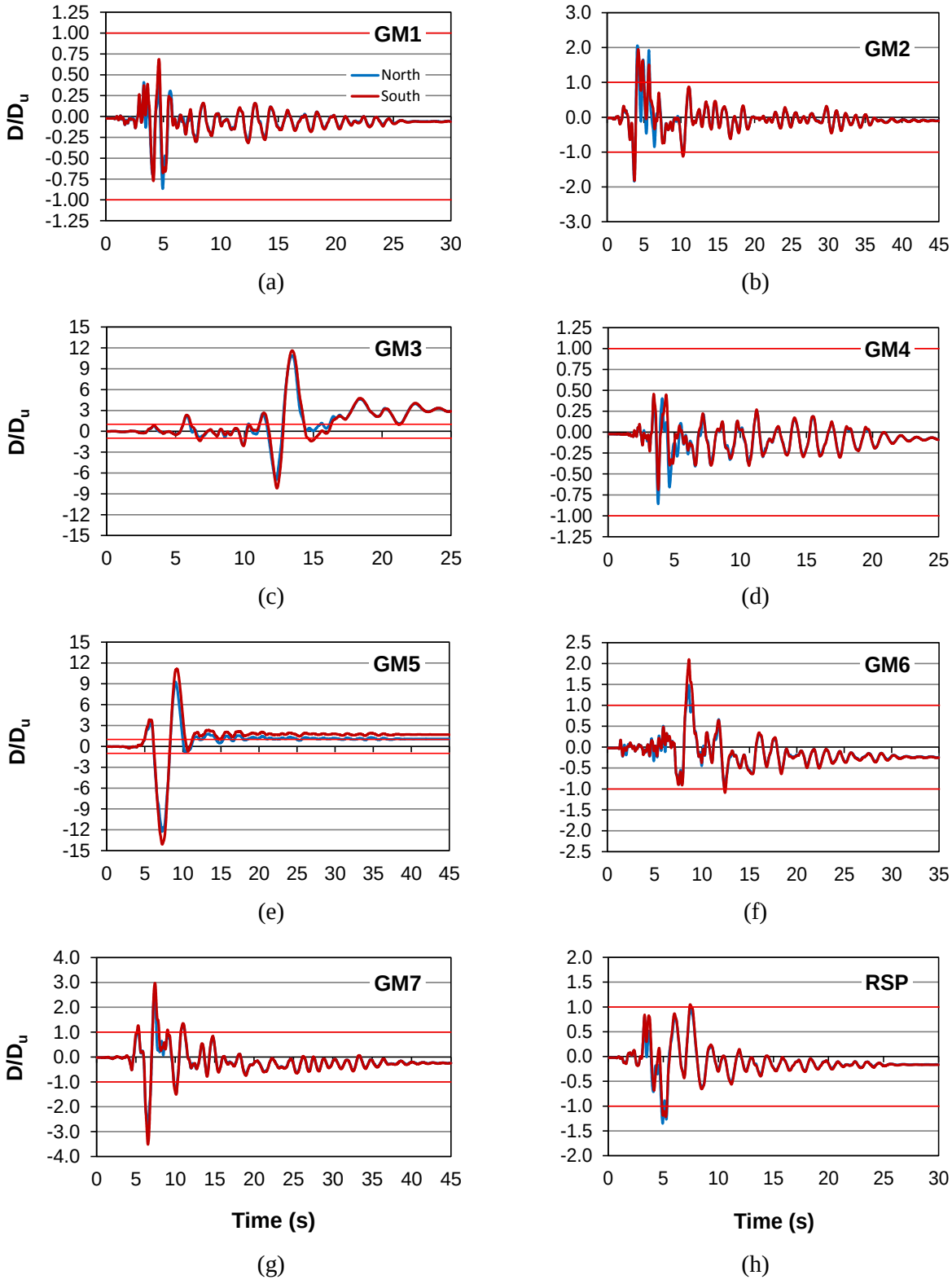

Figure 4-68 Time history of normalized transverse displacement at Abutment A (100Y-30X).

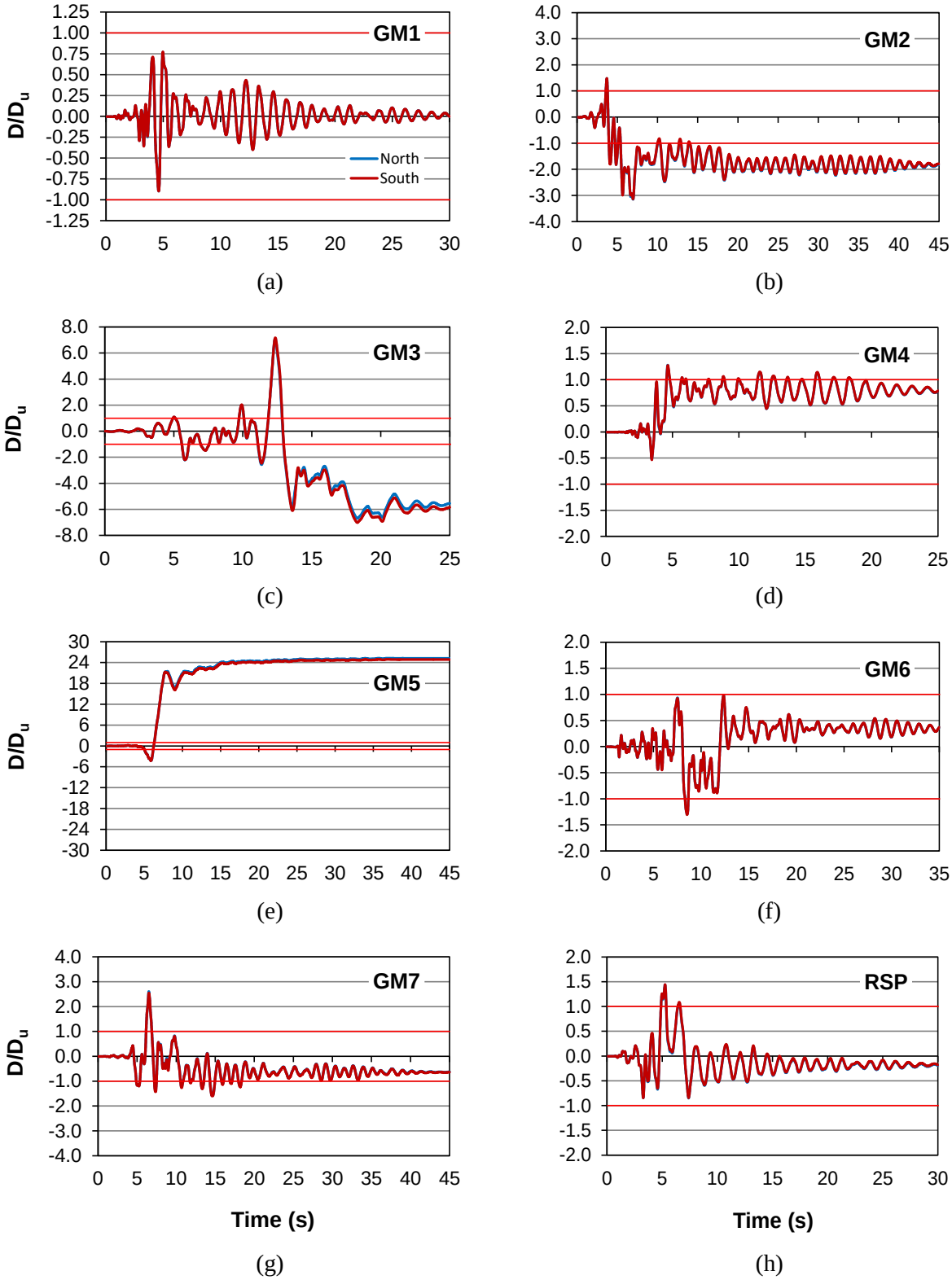

Figure 4-69 Time history of normalized transverse displacement at Abutment B (100Y-30X).

Table 4-19 lists the force and displacement demand for the backwalls, while Table 4-20 provides these demands for the wingwalls. Both tables present results for all ground motions for comparison with "Avg 1-7". As can be seen, the 100X-30Y seismic loading clearly governs the backwall response, and many of the ground motions create force demands that exceed the force capacity of both backwalls. Abutment B is stronger than Abutment A and generally sees slightly higher displacement demands. Abutment B is more massive than Abutment A, and the seismic force caused by the participating mass modeled in the abutment alone could be enough to cause this higher displacement demand. Another cause could be the more massive Segments 3 and 4 being closer to Abutment B. As the weaker columns of Piers 2 to 5 yield excessively, large deformations can translate across the discontinuities by pounding. Pounding at the abutments has been observed, and the extra force transmitted may be enough to cause failure of the backwall. Pier 1 is much stiffer and Segment 1 and 2 are much less massive, on the other hand, and probably do not carry as much load to Abutment A in the longitudinal direction.

Table 4-19 Abutment backwall force/displacement demand (capacity given in parentheses)

Response	Seismic Loading	GM1	GM2	GM3	GM4	GM5	GM6	GM7	RSP	Avg 1-7
Abut.-A Force (1020 k)	100X-30Y	1020	1020	1020	941	1020	1020	1020	1020	1010
	100Y-30X	637	1020	1020	960	589	934	512	667	808
Abut.-A Disp (2.4 in.)	100X-30Y	2.47	5.82	41.6	3.78	13.8	2.28	6.52	2.76	10.9
	100Y-30X	1.05	3.28	8.07	1.42	6.75	1.88	1.81	1.70	3.47
Abut.-B Force (1590 k)	100X-30Y	1340	1590	1590	1590	1590	1540	1590	1590	1570
	100Y-30X	252	370	800	215	751	240	498	310	446
Abut.-B Disp (2.4 in.)	100X-30Y	1.74	9.61	46.0	3.85	13.4	2.53	6.89	1.93	12.0
	100Y-30X	0.276	0.324	3.39	0.349	2.71	0.191	0.597	0.355	1.12

Table 4-20 Abutment wingwall force/displacement demand (capacity given in parentheses)

Response	Seismic Loading	GM1	GM2	GM3	GM4	GM5	GM6	GM7	RSP	Avg 1-7
Abut-A Force (90.8 k)	100X-30Y	80.1	90.8	90.8	64.0	90.8	66.2	90.8	70.1	81.9
	100Y-30X	90.8	90.8	90.8	90.8	90.8	90.8	90.8	90.8	90.8
Abut-A Disp (2.4 in.)	100X-30Y	1.00	1.66	4.33	0.881	2.53	0.618	2.65	0.746	2.0
	100Y-30X	2.06	4.93	27.9	2.06	33.7	5.04	8.24	3.24	12.0
Abut-B Force (323 k)	100X-30Y	323	323	323	320	323	323	323	323	323
	100Y-30X	323	323	323	323	323	323	323	323	323
Abut-B Disp (2.4 in.)	100X-30Y	1.64	3.60	8.68	1.08	6.76	1.54	2.48	1.73	3.68
	100Y-30X	2.16	7.57	17.2	3.07	62.1	3.13	6.25	3.47	14.5

Figure 4-70 illustrates the comparison of RSP with "Avg 1-7" for the abutment backwall and wingwall force (Figure 4-70a) and displacement (Figure 4-70b) normalized demand. RSP again successfully predicts the linear-elastic force demand on both the backwall and wingwalls, with both RSP and "Avg 1-7" exceeding the ultimate passive pressures of the backfill soil. While the displacement demand/capacity ratio is still underestimated for RSP, it can still detect that excessive abutment displacement is a possible failure mode.

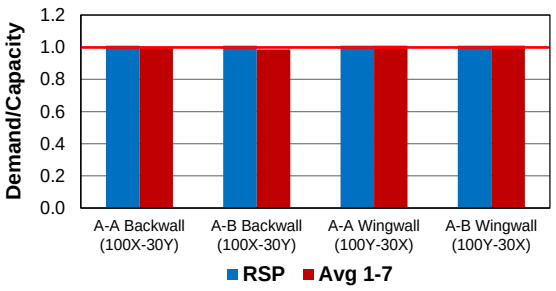

(a) Force demand/capacity

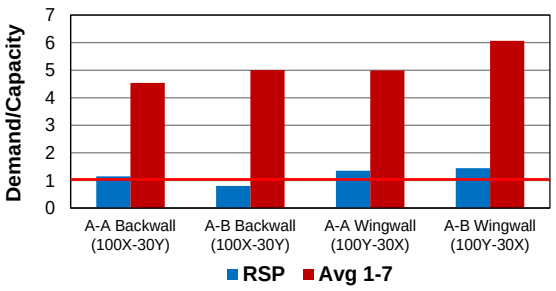

(b) Displacement demand/capacity

Figure 4-70 Abutment response for RSP and "Avg 1-7".

4.6.2 BACKWALL-SUPERSTRUCTURE POUNDING

To complement the investigation of abutment displacement demand, the pounding interaction between the abutment backwall and the adjacent superstructure of the bridge should be discussed. Figures 4-71 to 4-74 provide the time histories of the relative longitudinal (global-X) displacement across this gap, where the red line at -1.5 in. signifies that pounding occurs. Both the northernmost and southernmost displacements are shown.

Comparing the 100X-30Y relative displacement in Figures 4-71 and 4-73 to the abutment backwall displacement (Figures 4-66 and 4-67), a correlation between the occurrence of pounding and backwall displacement failure can be seen. For example, under GM1 (100X-30Y), the maximum normalized displacement demand at Abutment A (Figure 4-66a) occurs at about the same time (just after 5s) that pounding does for Abutment-A (Figure 4-71a).

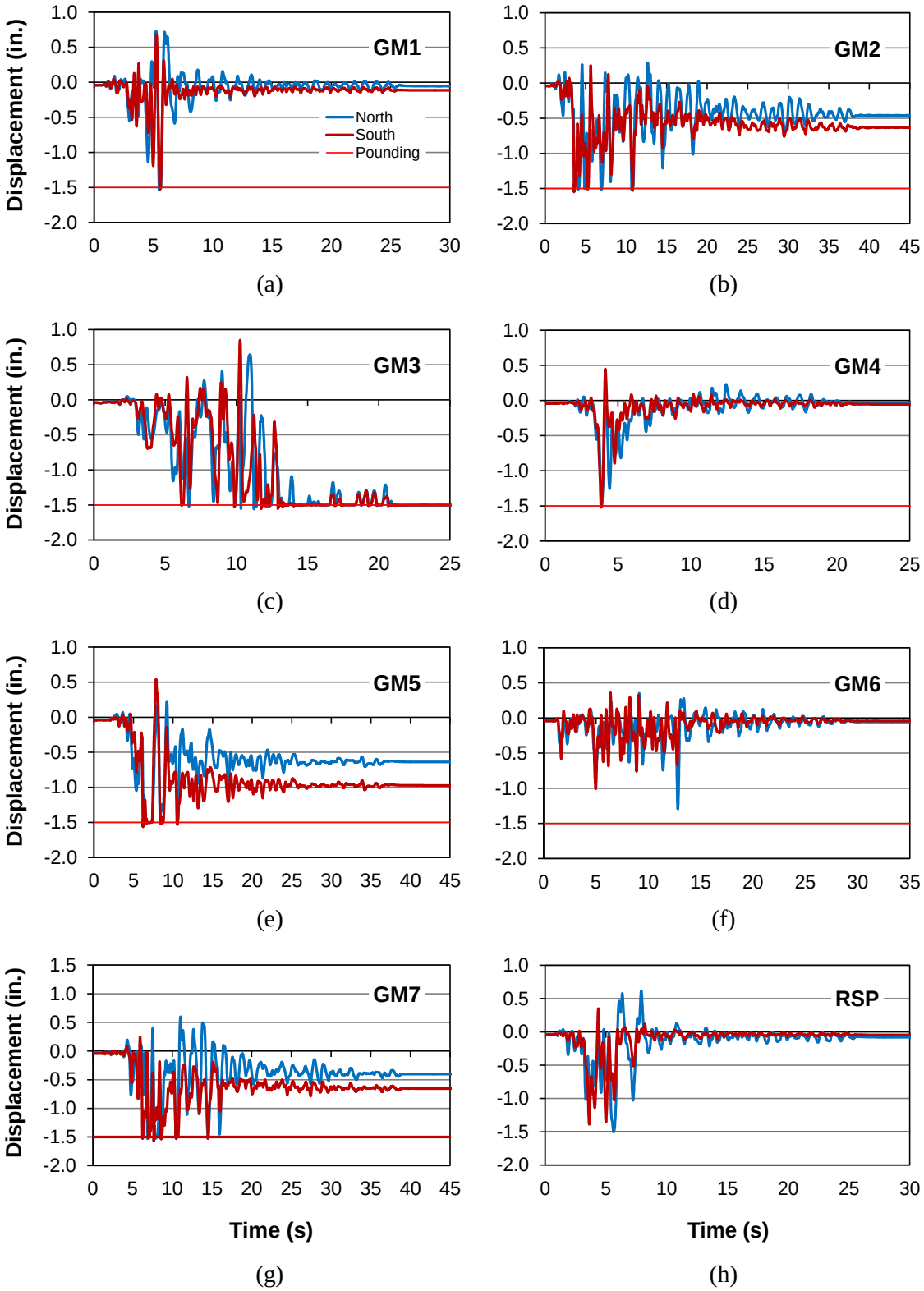

Figure 4-71 Time history of global-X relative displacement between Abutment-A and the superstructure (100X-30Y).

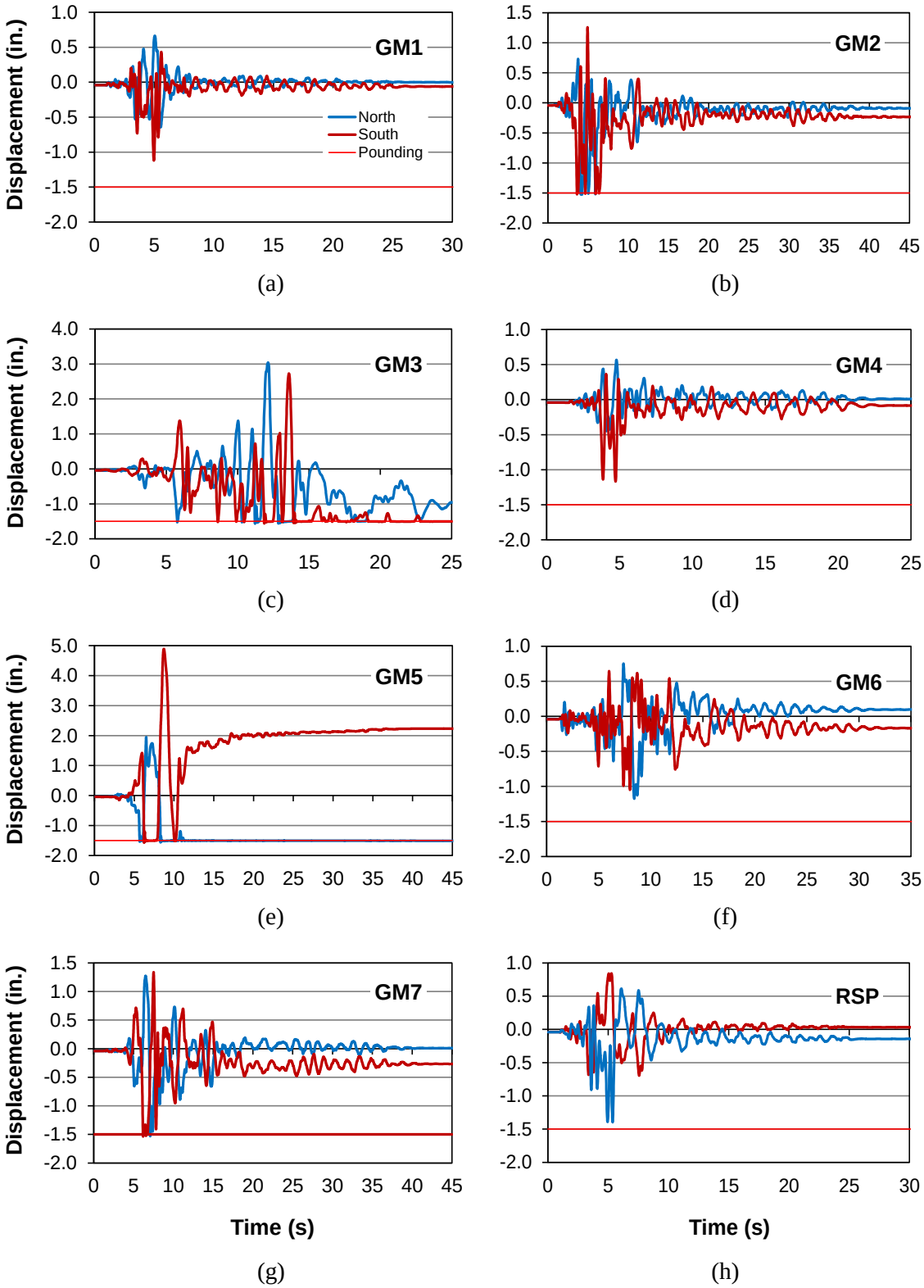

Figure 4-72 Time history of global-X relative displacement between Abutment-A and the superstructure (100Y-30X).

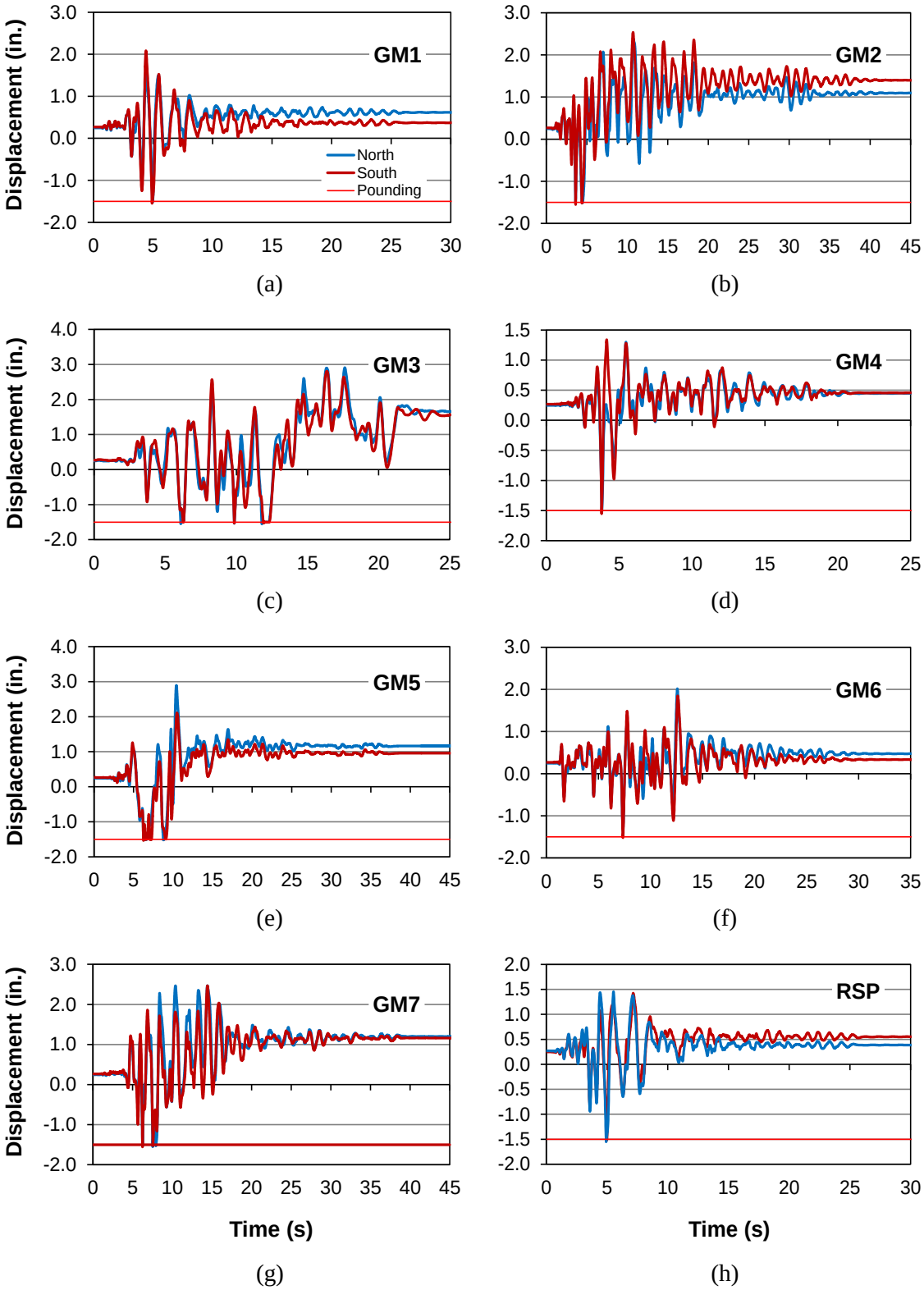

Figure 4-73 Time history of global-X relative displacement between Abutment-B and the superstructure (100X-30Y).

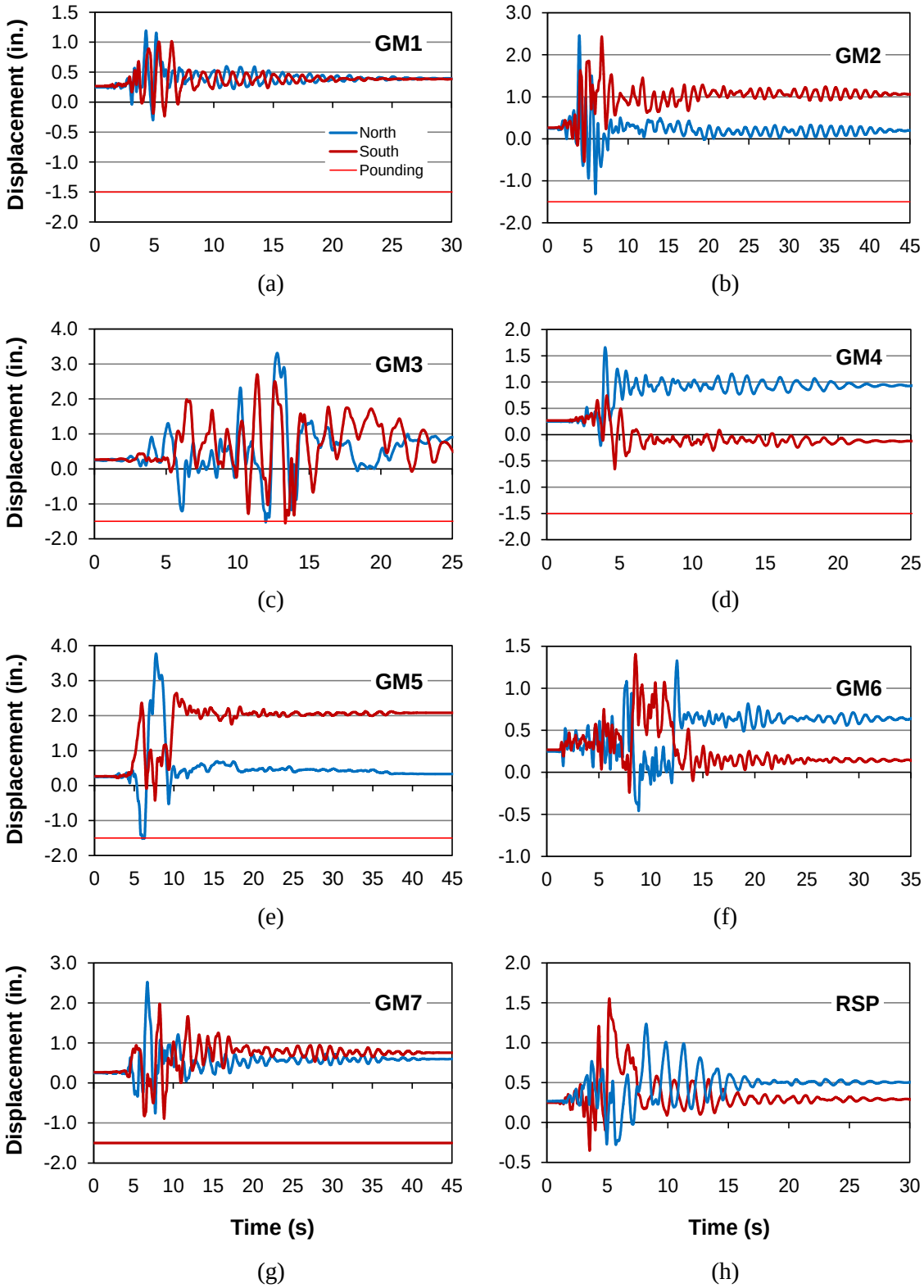

Figure 4-74 Time history of global-X relative displacement between Abutment-B and the superstructure (100Y-30X).

Table 4-21 gives the maximum pounding force that occurs under all ground motions for comparison with "Avg 1-7". As can be seen, pounding between the abutment backwall and the superstructure is shown to transfer large amounts of force. For example, for GM1 (100X-30Y) at Abutment A, over 1000 kips of force is transferred from the superstructure to the backwall of Abutment A. Without this level of pounding force, the maximum displacement capacity may have been not exceeded at Abutment-A (Figure 4-66a). Figure 4-75 compares the pounding force for RSP and "Avg 1-7". RSP captures the force demand well for Abutment B, but underestimates the Abutment A demand.

Table 4-21 Abutment-superstructure pounding demand (kips)

Abutment	Seismic Loading	GM1	GM2	GM3	GM4	GM5	GM6	GM7	RSP	Avg 1-7
A	100X-30Y	1050	1250	1440	581	1630	0.0	1760	102	1110
	100Y-30X	0.0	653	1670	0.0	1780	0.0	952	0.0	722
B	100X-30Y	1200	1290	1420	1350	846	540	1330	1260	1140
	100Y-30X	0.0	0.0	1340	0.0	510	0.00	0.0	0.0	264

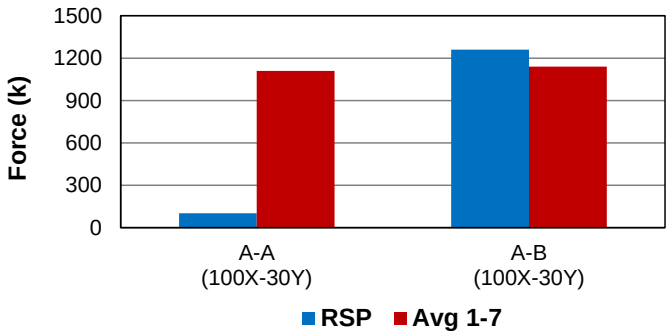

Figure 4-75 Abutment pounding force for RSP and "Avg 1-7".

CHAPTER 5

CONCLUSIONS

5.1 SUMMARY

The goal of this research was to determine the seismic performance of an older bridge (Bridge G-953) in southern Nevada under maximum considered earthquake (MCE). A detailed nonlinear finite element model was developed for this bridge and subjected to a suite of eight site-specific ground motions scaled for MCE. All major components of the bridge were accounted for, including an elastic superstructure, nonlinear columns with bond slip, localized interactions at the in-span hinges, and participation of the passive soil stiffness at the abutments. The ground motions were applied bidirectionally for two seismic loadings, the first being 100% global-X and 30% global-Y and the second switched as 100% global-Y and 30% global-X. Each ground motion record was used for both seismic loadings for a total of 16 cases. Included in the set of ground motions is a spectrum-matched "RSP" record developed to capture an envelope of critical responses without the need for an extensive suite of ground motions. The demands created by "RSP" were compared to the average response from the other seven records, labeled "Avg 1-7". The records were all scaled to MCE based on the updated seismic hazard in southern Nevada.

The following conclusions are reached from the simulation results:

(1) Lateral drift demand – The average column drift ranged from 3% for Pier 1 to 5% for Pier 5, indicating that high levels of nonlinearity can be expected during the ground motions. The discontinuities in the superstructure lead to the 100Y-30X seismic loading causing larger displacements since the individual bridge segments move more independently of one another. Unseating was not found to be a significant concern, and the

available seat width of about 15 in. for the in-span hinges indicates that this bridge may have accounted for certain seismic vulnerabilities.

(2) Shear demand – The very strong columns of Pier 1 allowed large average shear demands in excess of 200 kips per column, while the lightly reinforced and pinned-base columns of Piers 2 to 5, were limited by flexural yielding and experienced less than 125 kips. The fixed base columns of Pier 1 are susceptible to torsional loadings, and while shear-torsion interaction does cause failure during two ground motions, the normalized shear-torsion demand is over 0.9 but less than unity. Flexural yielding in the columns with pinned bases ensures that force-based shear is not of concern. Additionally, the pinned bases do not allow torsional loadings.

(3) Nonlinear, rotation-based shear failure – The large column drifts equate to large amounts of nonlinearity and the formation of plastic hinges at the column critical sections, which can then lead to shear failure. Average rotations in excess of 2.5° were recorded for the columns of Pier 5, which only exceeds their capacity of about 1.6° by a moderate amount. The 100Y-30X seismic loading causes a noticeably higher rotation demand than 100X-30Y (difference between average maxima is about 0.57°). Comparison of the force-based and rotation-based shear demand/capacity graphs shows that deformation-controlled shear failure may occur in some columns.

(4) Column flexural behavior – Large plastic hinge rotations means high states of flexural distress at the column critical sections. For the average response, curvatures in excess of 0.004 $in.^{-1}$ cause yielding and fracture/buckling of the longitudinal reinforcement, spalling of the cover concrete, and crushing of the core concrete. Flexural deformation capacities, limited by buckling of the longitudinal reinforcement, are exceeded by a factor of about 6

to 8 for the average response at the most critical column sections. Bar buckling is likely due to the large spacing of the transverse reinforcement. Comparison of the concrete and steel strain demand/capacity ratios show that rotation-based shear failure occurs just before or right after flexural failure.

(5) In-span hinges – Pounding is experienced under a majority of the ground motions, most likely due to asymmetrical bridge segments becoming "out-of-phase" with adjacent segments during the excitations. However, pounding forces are not large enough to exceed the bearing stress of the in-span hinges, avoiding a possible unseating threat. The restrainers are activated under most of the ground motions and reach their yield capacity. Restrainer fracture is detected in several ground motions, which is mostly caused by in-plane rotations of the superstructure that the restrainers were probably not designed for.

(6) Shear keys – The shear keys at both the in-span hinges and abutment expansion joints experienced significant average force demand, about 60-80% of their capacity. While the average response does not detect total failure, some cracking is expected. Moreover, the maximum shear key demand occurs simultaneously with column shear and flexural demand spikes. This may show that individual bridge segments do work together somewhat, especially during the 100Y-30X seismic loading, prior to cracking of the shear keys.

(8) Abutments – The passive soil pressure in the longitudinal direction is exceeded and the displacement is beyond acceptable limits under both 100X-30Y and 100Y-30X. The seat-type abutments lack the necessary stiffness and can displace an unacceptable amount under the excitation of their own mass alone. Additionally, pounding between the abutment backwall and the superstructure occurs frequently and can amplify the force and

displacement demand on the backwall of the abutment. For an MCE-level event, however, the failure of the abutments is more of a localized response and may be acceptable.

(9) RSP vs. "Avg 1-7" – RSP is proven effective in estimating the linear-elastic *force* demands on the bridge, including maximum shear and yield moment in the columns, and some shear key, pounding, abutment, and restrainer interaction. However, the average response dictates that nonlinear *displacement* demands govern the limit states of the structure, such as rotation-based shear failure, crushing of the core concrete, and fracture/buckling of the longitudinal reinforcement. RSP fails to predict these critical limit states and thus cannot be recommended for use for this individual study.

5.2 Recommended Future Research

To better understand the need for retrofitting, it is recommended to analyze the model with increased confinement and shear strength in the columns. The literature contains research on calculating the effectiveness of CFRP wraps, and more robust restrainer types have been developed. Achieving a design that prevents rotation-based shear and flexural failures in the columns would be the goal, which has a high possibility of being met without replacement of the structure.

This analysis was performed for the maximum considered earthquake, for which collapse prevention is the priority. However, it may prove useful to analyze the structure under design level (10% probability of exceedance in 50 years) acceleration time histories. Additionally, a parametric study of the various local elements could give more insights into the behavior of skew-type bridges. In particular, the restrainers could be removed to gauge their effectiveness, or the abutments ignored to better analyze their contributions. More study is needed on the behavior of structures with irregular geometries, and the skew and slight vertical and horizontal curves of Bridge G-953 makes it an ideal candidate for study.

APPENDIX

BRIDGE G-953 ORIGINAL DRAWINGS

Original drawings for Bridge G-953, including new expansion joints and restrainers, are located in attachment one of supplemental materials in ProQuest.

REFERENCES

Abdel Raheem, S. E. (2009). Pounding mitigation and unseating prevention at expansion joints of isolated multi-span bridges. *Engineering Structures, 31*(10), 2345-2356.

American Association of State and Highway Transportation Officials. (1998). *1998 interim revisions to standard specifications for highway bridges* Washington, DC.

American Association of State and Highway Transportation Officials. (2011). *AASHTO guide specifications for LRFD seismic bridge design, 2nd edition* (2nd ed.). Washington, DC:

American Concrete Institute. (2014). *ACI 318-14* American Concrete Institute.

Andrawes, B., & Desroches, R. (2005). Unseating prevention for multiple frame bridges using superelastic devices. *Smart Materials and Structures, 14*(3), S60-S67. doi:10.1088/0964-1726/14/3/008

ASCE/SEI Standard 7-10. (2010). *Minimum design loads for buildings and other structures* American Society of Civil Engineers.

Attarchian, N., Kalantari, A., & Moghadam, A. S. (2012). Seismic assessment of monolithic vs. pin column top connections in R/C skewed bridges. Paper presented at the *6th International Conference on Bridge Maintenance, Safety and Management, IABMAS 2012,* Stresa, Lake Maggiore. 2743-2749.

Aviram, A., Mackie, K. R., & Stojadinovic, B. (2008a). Effect of abutment modeling on the seismic response of bridge structures. *Earthquake Engineering and Engineering Vibration, 7*(4), 395-402. doi:10.1007/s11803-008-1008-3

Aviram, A., Mackie, K. R., & Stojadinovic, B. (2008b). *Guidelines for nonlinear analysis of bridge structures in california.* (Technical Report No. UCB/PEER 2008/03). Berkeley, CA: Pacific Earthquake Engineering Research Center. . (bridges, reinforced concrete, finite element modeling, nonlinear analysis,)

Belarbi, Q., L., & Suriya Prakash, S. (2009). Torsional effects on seismic performance of square vs. circular RC bridge columns. *25th US-Japan Bridge Work Shop,*Tsukuba Science City, Japan. (25)

Berry, M. P., & Eberhard, M. O. (2008). *Performance modeling strategies for modern reinforced concrete bridge columns.* (No. 2007/07). Berkeley, CA: Pacific Earthquake Engineering Research Center.

Bridge of the Week. (2016). Retrieved from http://www.bridgeofweek.com

Buckle, I., Friedland, I., Mander, J., Martin, G., Nutt, R., & Power, M. (2006). *Seismic retrofitting manual for highway structures: Part I - bridges.* (Technical Report No. FHWA-HRT-06-032).Federal Highway Administration.

Button, M. R., Cronin, C. J., & Mayes, R. L. (2002). Effect of vertical motions on seismic response of highway bridges. *Journal of Structural Engineering, 128*(12), 1551-1564. doi:10.1061/(ASCE)0733-9445

California Department of Transportation. (2013). *Caltrans Seismic Design Criteria, Version 1.7* (1.7th ed.). Sacramento, CA: California Department of Transportation.

CEB-FIP-1990, model code 1990: Design code. (0000).

Charney, F. A. (2008). Unintended consequences of modeling damping in structures. *Journal of Structural Engineering, 134*(4), 581-592. doi:10.1061/(ASCE)0733-9445(2008)134:4(581)

Chen, W., & Scawthorn, C. (2003). In Chen W., Scawthorn C. (Eds.), *Earthquake engineering handbook* (1st ed.). Boca Raton, FLA: CRC Press. doi:0-8493-0068-1 (ISBN)

Chen, W., & Duan, L. (2000). In Chen W., Duan L. (Eds.), *Bridge engineering handbook* (1st ed.). Boca Raton, FL: CRC Press.

Chopra, A. K. (2007). 11.4 classical damping matrix. In W. J. Hall (Ed.), *Dynamics of structures: Theory and applications to earthquake engineering* (Third ed., pp. 457). Upper Saddle River, New Jersey: Pearson Prentice Hall. doi:ISBN - 0-13-156174-X

Chouw, N., & Hao, H. (2008). Significance of SSI and nonuniform near-fault ground motions in bridge response I: Effect on response with conventional expansion joint.*Engineering Structures, 30*(1), 141-153. doi:10.1016/j.engstruct.2007.03.002

Das, B. M. (2006). In Das B. M. (Ed.), *Principles of geotechnical engineering* (6th ed.). Toronto, Ontario, Canada: Thomson. doi:ISBN 13: 978-0-534-55144-5; ISBN 10: 0-534-55144-0

Degenkolb, O. (1977). *Concrete box girder bridges* (Monograph No. 10 ed.). Ames, Iowa; Detroit, Michigan: The Iowa State University Press, American Concrete Institute.

Dimitrakopoulos, E. G. (2011). Seismic response analysis of skew bridges with pounding deck-abutment joints. *Engineering Structures, 33*(3), 813-826. doi:10.1016/j.engstruct.2010.12.004

Dowell, R. (2004). Seismic analysis of the sylmar interstate 5 and highway 14 connector bridge. *SMIP04 Seminar on Utilization of Strong-Motion Data,* p. 41 - 60.

Earthquake Engineering Research Center, University of California-Berkeley. (2016). Retrieved from http://peer.berkeley.edu

Earthquake Engineering Research Institute. (2016). Retrieved from http://www.eeri.org

Elgamal, A., Yan, L., Yang, Z., & Conte, J. P. (2008). Three-dimensional seismic response of humboldt bay bridge-foundation-ground system. *Journal of Structural Engineering,134*(7), 1165-1176. doi:10.1061/(ASCE)0733-9445(2008)134:7(1165)

Elicegui, M., Stefonowicz, T., & Severns, D. (2008). *NDOT Structures Manual* Nevada Department of Transportation: Structures Division.

Elwood, K. J. (2004). Modelling failures in existing reinforced concrete columns. *Canadian Journal of Civil Engineering, 31*(5), 846-859. doi:10.1139/L04-040

Elwood, K. J., & Moehle, J. P. (2008). Dynamic collapse analysis for a reinforced concrete frame sustaining shear and axial failures. *Earthquake Engineering and Structural Dynamics, 37*(7), 991-1012. doi:10.1002/eqe.787

EQE (1995). *The January 17, 1995 Kobe Earthquake: An EQE Summary Report,*

Gomes, A., & Appleton, J. (1997). Nonlinear cyclic stress-strain relationship of reinforcing bars including buckling. *Engineering Structures, 19*(10), 822-826.

Hancock, J., Watson-Lamprey, J., Abrahamson, N. A., Bommer, J. J., Markatis, A., McCoy, E., & Mendis, R. (2006). An improved method of matching response spectra of recorded earthquake ground motion using wavelets. *Journal of Earthquake Engineering, 10*(SPEC. ISS. 1), 67-89. doi:10.1142/S1363246906002736

Jennings, P. C., Housner, G. W., Hudson, D. E., Trifunac, M. D., Frazier, G. A., & Wood, J. H. (1971). *Engineering features of the san fernando earthquake of february 9, 1971.* (No. EERL 71-02). California Institute of Technology, Pasadena: EERL.

Johnson, R., Padgett, J. E., Maragakis, M. E., Desroches, R., & Saiidi, M. S. (2008). Large scale testing of nitinol shape memory alloy devices for retrofitting of bridges. *Smart Materials and Structures, 17*(3) doi:10.1088/0964-1726/17/3/035018

Kaviani, P., Zareian, F., & Taciroglu, E. (2012). Seismic behavior of reinforced concrete bridges with skew-angled seat-type abutments. *Engineering Structures, 45*, 137-150. doi:10.1016/j.engstruct.2012.06.013

Kowalsky, M. J., & Priestley, M. J. N. (2000). Improved analytical model for shear strength of circular reinforced concrete columns in seismic regions. *ACI Structural Journal,97*(3), 388-396.

Lamichhane, S., Luke, B., & Taylor, W. J. (2014). An alternative analysis of the probabilistic seismic hazard for las vegas valley, nevada. *Bulletin of the Seismological Society of America, 104*(2), 741-768. doi:10.1785/0120120268

LeBorgne, M. R., & Ghannoum, W. M. (2014). Calibrated analytical element for lateral-strength degradation of reinforced concrete columns. *Engineering Structures, 81*, 35-48. doi:10.1016/j.engstruct.2014.09.030

Mander, J. B., Priestley, M. J. N., & Park, R. (1988). Theoretical stress-strain model for confined concrete. *Journal of Structural Engineering New York, N.Y., 114*(8), 1804-1826.

Maroney, B. H., & Chai, Y. H. (1994). Seismic design and retrofitting of reinforced concrete bridges. *Proceedings of 2nd International Workshop, Earthquake Commission of New Zealand,*

McCallen, D. B., & Romstad, K. M. (1994). - Dynamic analyses of a skewed Short-Span, Box-Girder overpass. - *Earthquake Spectra, 10*(- 4), - 729. doi:- 10.1193/1.1585795

McDonald, J., Heymsfleld, E., & Avent, R. R. (2000). Slippage of neoprene bridge bearings. *Journal of Bridge Engineering, 5*(3), 216-223. doi:10.1061/(ASCE)1084-0702(2000)5:3(216)

McKenna, F., Scott, M. H., & Fenves, G. L. (2010). Nonlinear finite-element analysis software architecture using object composition. *Journal of Computing in Civil Engineering, 24*(1), 95-107. doi:10.1061/(ASCE)CP.1943-5487.0000002

Megally, S. H., Silva, P. F., & Seible, F. (2002). *Seismic response of sacrificial shear keys in bridge abutments.* (Final Report No. SSRP-2001/23). Sacramento, CA: California Department of Transportation.

Memari, A. M., Harris, H. G., Hamid, A. A., & Scanlon, A. (2011). Seismic evaluation of reinforced concrete piers in low to moderate seismic regions. *Electronic Journal of Structural Engineering, 11,* 57-68.

Menegotto, M., & Pinto, P. E. (1973). Method of analysis for cyclically loaded reinforced concrete plane frames including changes in geometry and non-elastic behavior of elements under combined normal force and bending. *IABSE Symposium on Resistance and Ultimate Deformability of Structures Acted on by Well Defined Repeated Loads,*Lisbon, Portugal. 15-15-22.

Mitoulis, S. A. (2012). Seismic design of bridges with the participation of seat-type abutments. *Engineering Structures, 44,* 222-233. doi:10.1016/j.engstruct.2012.05.033

Moustafa, K. F., Sanders, D., Saudi, M. S., & El-Azazy, S. (2011). Seismic performance of reinforced concrete bridge bents. *ACI Structural Journal, 108*(1), 23-33.

Muthukumar, S., & DesRoches, R. (2006). A hertz contact model with non-linear damping for pounding simulation. *Earthquake Engineering and Structural Dynamics, 35*(7), 811-828. doi:10.1002/eqe.557

Muthukumar, S. (2003). *A contact element approach with hysteresis damping for the analysis and design of pounding in bridges* (Ph.D.). Available from ProQuest Dissertations & Theses

(PQDT). (305330117). Retrieved from http://search.proquest.com/docview/305330117?accountid=3611

Mwafy, A., Kwon, O.-S., & Elnashai, A. (2010). Seismic assessment of an existing non-seismically designed major bridge-abutment-foundation system. *Engineering Structures,32*(8), 2192-2209.

Mylonakis, G., & Gazetas, G. (2000). Seismic soil-structure interaction: Beneficial or detrimental? *Journal of Earthquake Engineering, 4*(3), 277-301.

Mylonakis, G., Simeonov, V., Reinhorn, A. M., & Buckle, I. G. (1999). Implications of spatial variation of ground motion on collapse of SR 14/I-5 southbound and overhead bridge in northridge earthquake. *Seismic Response of Concrete Bridges.SP-187 Special Publication of the American Concrete Institute.*, , 299-325.

Naeim, F., & Kelly, J. M. (1999). *Design of seismic isolated structures: From theory to practice* (1st ed.). New York, NY: John Wiley & Sons, Inc. doi:ISBN: 0-147-14921-

National Center for Transportation and Industrial Productivity. (2016). Retrieved from http://www.transportation.njit.edu

Nevada Department of Transportation. (2015). *State highway preservation report.* ().Nevada Department of Transportation.

Nielson, B. G., & Desroches, R. (2007). Seismic performance assessment of simply supported and continuous multispan concrete girder highway bridges. *Journal of Bridge Engineering, 12*(5), 611-620. doi:10.1061/(ASCE)1084-0702(2007)12:5(611)

Nobles Catalogue Section 2: Wire Rope. (2016). Retrieved from http://www.nobles.com.au/3dissue/section02/index.html

O'Connor, C., & Shaw, P. A. (2000). Chapter 7: Dynamic vehicle loads 12.5: Earthquake loads. In C. O'Connor, & P. A. Shaw (Eds.), *Bridge loads: An international perspective* (1st ed., pp. 182-182-216, 316-323). New Fetter Lane, London; New York, NY: Spon Press. doi:ISBN: 0-419-24600-2

Ordóñez, G. A. (2012). *A pre-processor and post processor for RspMatch2005 & RspMatch2009*. Lacey, Washingtion, USA: Geomotions, LLC.

Otsuka, H., Wang, Y., Takata, T., & Yoshimura, T. (2003). Experimental study on the parameters effecting the hysteresis loop of RC members subjected to pure torsion. *Journal of Structural Mechanics and Earthquake Engineering, 739*(60), 93-104.

Pamuk, A., Kalkan, E., & Ling, H. I. (2005). Structural and geotechnical impacts of surface rupture on highway structures during recent earthquakes in turkey. *Soil Dynamics and Earthquake Engineering, 25*(7-10), 581-589. doi:10.1016/j.soildyn.2004.11.011

Papazoglou, A. J., & Elnashai, A. S. (1996). Analytical and field evidence of the damaging effect of vertical earthquake ground motion. *Earthquake Engineering and Structural Dynamics, 25*(10), 1109-1137.

Park, R., & Paulay, T. (1975). In Park R., Paulay T. (Eds.), *Reinforced concrete structures* John Wiley and Sons, Inc.

Prakash, S., Belarbi, A., & You, Y. -. (2010). Seismic performance of circular RC columns subjected to axial force, bending, and torsion with low and moderate shear. *Engineering Structures, 32*(1), 46-59. doi:10.1016/j.engstruct.2009.08.014

Priestley, M. J. N., Seible, F., & Calvi, G. M. (1996). *Seismic design and retrofit of bridges* (First ed.). New York, NY: John Wiley & Sons, Inc.

Priestley, M. J. N., Verma, R., & Yan Xiao. (1994). Seismic shear strength of reinforced concrete columns. *Journal of Structural Engineering - ASCE, 120*(8), 2310-2329.

Qin, Q., & Lou, L. (2000). Influence of non-classical damping on the seismic response of suspension bridges. *Advances in Structural Engineering, 3*(2), 163-171.

Roeder, C. W., Stanton, J. F., & Taylor, A. W. (1987). *Performance of elastomeric bearings.* (). Retrieved from SCOPUS

Saad, A. S. (2009). *Seismic evaluation of clark county critical bridges using nonlinear static procedures* (M.S.E.). Available from Dissertations & Theses @ University of Nevada Las Vegas. (305088548). Retrieved from http://search.proquest.com/docview/305088548?accountid=3611

Saadeghvaziri, M. A., & Yazdani-Motlagh, A. R. (2008). Seismic behavior and capacity/demand analyses of three multi-span simply supported bridges. *Engineering Structures,30*(1), 54-66. doi:http://dx.doi.org/10.1016/j.engstruct.2007.02.017

Scott Derr Painting Company, LLC. (2007). Retrieved from http://www.derrpainting.com

Seible, F., & Priestley, M. J. N. (1999). Lessons learned from bridge performance during northridge earthquake. *Seismic Response of Concrete Bridges.SP-187 Special Publication of the American Concrete Institute.*, , 29-55.

Selna, L. G., Malvar, L. J., & Zelinski, R. J. (1989a). Box girder bar and bracket seismic retrofit devices. *ACI Structural Journal, 86*(5), 532-540.

Selna, L. G., Malvar, L. J., & Zelinski, R. J. (1989b). Bridge retrofit testing. hinge cable restrainers. *Journal of Structural Engineering New York, N.Y., 115*(4), 920-934.

Siddharthan, R. V., & El-Gamal, M. (1999). Investigation of performance of bridge abutment fills in 1994 northridge earthquake. *Seismic Response of Concrete Bridges.SP-187 Special Publication of the American Concrete Institute.*, , 69-88.

Taylor, A. W. (1999). Performance of reinforced concrete bridges in january 1995 hyogoken nanbu (kobe) earthquake. *Seismic Response of Concrete Bridges.SP-187 Special Publication of the American Concrete Institute.*, , 57-67.

Tensar. (2016). Retrieved from http://www.tensar.co.uk

Timosidis, D., & Pantazopoulou, S. J. (2007). Limit state model for R.C. bridge joints under seismic loading. *Bulletin of Earthquake Engineering, 5*(3), 391-423. doi:10.1007/s10518-007-9035-4

Tirasit, P., Kawashima, K., & Watanabe, G. (2006). Effect of combined cyclic flexural-torsional loading on the seismic performance of RC columns. Paper presented at the *8th US National Conference on Earthquake Engineering 2006,* San Francisco, CA. *, 1* 199-208.

Tsuchiya, S., Maekawa, K., & Kawashima, K. (2007). Three-dimensional cyclic behavior simulation of RC columns under combined flexural moment and torsion coupled with axial and shear forces. *Journal of Advanced Concrete Technology, 5*(3), 409-421. doi:10.3151/jact.5.409

United States Geographical Survey. (2014). Usgs. Retrieved from http://www.usgs.gov/

Urmson, C. R., & Mander, J. B. (2012). Local buckling analysis of longitudinal reinforcing bars. *Journal of Structural Engineering (United States), 138*(1), 62-71. doi:10.1061/(ASCE)ST.1943-541X.0000414

U.S. Department of Transportation Federal Highway Administration. (2016). Retrieved from http://www.fhwa.dot.gov

Vlassis, A. G., Maragakis, E., & Saiidi, M. (2004). Experimental evaluation of longitudinal seismic performance of bridge restrainers at in-span hinges. *Journal of Testing and Evaluation, 32*(2), 96-105.

Wakefield, R. R., Nazmy, A. S., & Billington, D. P. (1991). Analysis of seismic failure in skew RC bridge. *Journal of Structural Engineering New York, N.Y., 117*(3), 972-986.

Werner, S. D. (1994). Study of caltrans seismic evaluation procedure for short bridges. *Proceedings of the 3rd Annual Seismic Research Workshop,*

Wibowo, H., Smith, D. M., Buckle, I. G., & Sanders, D. H. (2012). Live load effects on response of bridges during earthquakes. Paper presented at the *Structures Congress 2012,* Chicago, IL. 591-602. doi:10.1061/9780784412367.053

Wight, J. K., & MacGregor, J. G. (2009). 3-14: Reinforcement. In J. K. Wight, & J. G. MacGregor (Eds.), *Reinforced concrete: Mechanics and design* (pp. 90-93). Upper Saddle River, NJ: Pearson Prentice Hall.

Wilson, J. C., & Tan, B. S. (1990). Bridge abutments. assessing their influence on earthquake response of meloland road overpass. *Journal of Engineering Mechanics, 116*(8), 1838-1856.

World of Stock. (2015). Retrieved from http://www.worldofstock.com (website shut down)

Xanthakos, P. (1996). In Xanthakos P. (Ed.), *Bridge substructure and foundation design* Prentice Hall.

Xiao, Y., Priestley, M. J. N., & Seible, F. (1999). Seismic performance of bridge footings designed to current standards. *Seismic Response of Concrete Bridges.SP-187 Special Publication of the American Concrete Institute.,* , 131-157.

Yi Meng, J., & Lui, E. M. (2000). Seismic analysis and assessment of a skew highway bridge. *Engineering Structures, 22*(11), 1433-1452. doi:10.1016/S0141-0296(99)00097-8

Zhang, J., & Makris, N. (2002). Kinematic response functions and dynamic stiffnesses of bridge embankments. *Earthquake Engineering and Structural Dynamics, 31*(11), 1933-1966. doi:10.1002/eqe.196

Zhao, J., & Sritharan, S. (2007). Modeling of strain penetration effects in fiber-based analysis of reinforced concrete structures. *ACI Structural Journal, 104*(2), 133-141.

CURRICULUM VITAE

Graduate College
University of Nevada, Las Vegas

Contact:

E-mail: isaacrt915@gmail.com

Education:

Bachelor of Science in Civil Engineering with Structural Emphasis, 2009

University of Nevada, Reno

Master of Science in Civil Engineering with Structural Emphasis, 2016

University of Nevada, Las Vegas

Employment:

Project Intern — November 2015 – Present

Kordt Engineering Group — Las Vegas, Nevada

Technical Intern — Summer 2008

PBS&J (now Atkins) — Las Vegas, Nevada

Thesis Title:

Seismic Response of an Older Bridge in Nevada Under Maximum Considered Earthquake (2016)

Thesis Examination Committee:

Chairperson, Dr. Ying Tian, Ph.D.

Committee Member, Dr. Aly Said, Ph.D.

Committee Member, Dr. Samaan Ladkany, Ph.D.

Graduate Faculty Representative, Dr. Zhiyong Wang, Ph.D.